

## Ultrathin InAs/GaAs quantum wells : electronic structure, excitonic effects and carrier capture

**Citation for published version (APA):**

Brübach, J. (2001). *Ultrathin InAs/GaAs quantum wells : electronic structure, excitonic effects and carrier capture*. [Phd Thesis 1 (Research TU/e / Graduation TU/e), Applied Physics and Science Education]. Technische Universiteit Eindhoven. <https://doi.org/10.6100/IR539984>

**DOI:**

[10.6100/IR539984](https://doi.org/10.6100/IR539984)

**Document status and date:**

Published: 01/01/2001

**Document Version:**

Publisher's PDF, also known as Version of Record (includes final page, issue and volume numbers)

**Please check the document version of this publication:**

- A submitted manuscript is the version of the article upon submission and before peer-review. There can be important differences between the submitted version and the official published version of record. People interested in the research are advised to contact the author for the final version of the publication, or visit the DOI to the publisher's website.
- The final author version and the galley proof are versions of the publication after peer review.
- The final published version features the final layout of the paper including the volume, issue and page numbers.

[Link to publication](#)

**General rights**

Copyright and moral rights for the publications made accessible in the public portal are retained by the authors and/or other copyright owners and it is a condition of accessing publications that users recognise and abide by the legal requirements associated with these rights.

- Users may download and print one copy of any publication from the public portal for the purpose of private study or research.
- You may not further distribute the material or use it for any profit-making activity or commercial gain
- You may freely distribute the URL identifying the publication in the public portal.

If the publication is distributed under the terms of Article 25fa of the Dutch Copyright Act, indicated by the "Taverne" license above, please follow below link for the End User Agreement:

[www.tue.nl/taverne](http://www.tue.nl/taverne)

**Take down policy**

If you believe that this document breaches copyright please contact us at:

[openaccess@tue.nl](mailto:openaccess@tue.nl)

providing details and we will investigate your claim.

# **Ultrathin InAs/GaAs Quantum Wells: Electronic Structure, Excitonic Effects and Carrier Capture**

## **PROEFSCHRIFT**

ter verkrijging van de graad van doctor aan de Technische  
Universiteit Eindhoven, op gezag van de Rector Magnificus,  
prof.dr. M. Rem, voor een commissie aangewezen door het  
College voor Promoties in het openbaar te verdedigen op  
maandag 15 januari 2001 om 16.00 uur

door

**Jörg Brübach**

geboren te Hannover

Dit proefschrift is goedgekeurd door de promotoren:

prof.dr. J.H. Wolter

en

prof.dr. G.H. Döhler

Copromotor:

dr. A. Yu. Silov

CIP-DATA LIBRARY TECHNISCHE UNIVERSITEIT EINDHOVEN

Brübach, Jörg

Ultrathin InAs/GaAs Quantum Wells: Electronic Structure, Excitonic Effects and Carrier Capture / by Jörg Brübach. - Eindhoven : Technische Universiteit Eindhoven, 2001. -

Proefschrift.

ISBN 90-386-1679-1

NUGI 812

Trefw.: quantumputten, indiumarsenide, elektronische structuur, excitonen, ladingsdragerinvangst

Subject headings: quantum wells, indium arsenide, electronic structure, excitons, carrier capture

The work described in this thesis was carried out at the COBRA Inter-University Research Institute on Communication Technology of the Department of Physics of the Eindhoven University of Technology and was part of the research program of the Dutch Foundation for Fundamental Research on Matter (FOM), which is financially supported by the Dutch Organization for the Advancement of Research (NWO).

# *Contents*

<b>1. Introduction</b>	<b>1</b>
<i>References</i>	17
<b>2. Electronic Structure in Ultrathin InAs/GaAs Quantum Wells</b>	<b>23</b>
2.1 Impact of Strain on the Band Alignment	23
2.2 Quantum Size Effects in Ultrathin InAs Layers	33
2.3 Coupling of Ultrathin InAs Layers:	42
A New Method for the Determination of Band Offsets	
2.3.1 Confined States in Coupled Ultrathin InAs Layers	45
2.3.2 Sample Growth and Structural Characterization	50
2.3.3 Successive Band Offset Determination from PL, PLE	54
and Cleaved Side PLE Spectra of Coupled Ultrathin InAs Layers	
2.4 Validation of the InAs/GaAs Band Offsets and Band Offset Ratio	62
2.5 hh-lh Level Crossing in Coupled Ultrathin InAs Layers	66
<i>References</i>	68
<b>3. Excitonic Effects in Ultrathin InAs/GaAs Quantum Wells</b>	<b>71</b>
3.1 Excitons in Ultrathin InAs Layers	71
3.1.1 Ideal 3D and 2D Excitons	72
3.1.2 Excitons in Single Ultrathin InAs Layers	78
3.1.2.1 Calculation of the Exciton Binding Energy and	78
Exciton Dimensionality	
3.1.2.2 Experimental Determination of the Exciton Binding Energy	80
3.1.3 Excitons in Coupled Ultrathin InAs Layers	84
3.2 Doubly Resonant Raman Scattering and Resonant Luminescence	87
3.2.1 Sample Growth and Characterization	90
3.2.2 Observation of Resonant Excitonic Effects in CW Experiments	91

3.2.3 Distinction of the Resonant Excitonic Effects by Time-Resolved Experiments	94
3.2.4 Temperature Dependence of the Resonant Excitonic Effects	101
3.2.5 Linewidth of Exciton Transitions in Ultrathin InAs Layers	107
<i>References</i>	111
<b>4. Carrier Capture in Ultrathin InAs/GaAs Quantum Wells</b>	<b>115</b>
4.1 Sample Growth and Characterization	117
4.2 Time-Resolved Two-Wavelength Pump-Probe Phototransmission	117
4.3 Phototransmission in Ultrathin InAs/GaAs Quantum Wells	121
4.3.1 Phase-Space-Filling	125
4.3.2 Exciton Screening	126
4.3.3 Coupled Rate Equation Model	130
4.4 Experimental Results for the Carrier Capture	135
4.5 Evaluation of the Capture Times by Rate Equation Analysis	138
<i>References</i>	144
<b>5. Summary</b>	<b>147</b>
Samenvatting	151
Acknowledgements	157
List of Publications	159
Curriculum Vitae	161

---

# 1. Introduction

The progress in the development of sophisticated growth techniques like Molecular Beam Epitaxy (MBE), Chemical Beam Epitaxy (CBE), and Metal Organic Chemical Vapour Deposition (MOCVD) over the past two decades offered the possibility to deposit single atomic layers of different specific semiconductor materials in a controllable way. These artificially synthesized semiconductor structures on one hand exhibit new basic phenomena as for instance the Integer<sup>1</sup> and Fractional Quantum Hall Effect<sup>2</sup>. Moreover, due to the dimensionality reduction in the motion of electrons and holes, novel physical effects, which were already theoretically predicted during the development of quantum mechanics, became accessible for experimental study. Concerning the latter, an important milestone in the development of modern semiconductor physics and technology is marked by the year 1974, when Esaki and Chang<sup>3</sup> reported for the first time on resonant electron tunnelling through a semiconductor potential barrier, and when Dingle<sup>4</sup> experimentally demonstrated the quantization of energy levels in semiconductor quantum wells. On the other hand, the layer sequence and the choice of the semiconductor materials has a tremendous impact on the electronic and optical properties of semiconductor heterostructures. By engineering the band structure in a controlled way, novel devices like semiconductor lasers<sup>5</sup>, optoelectronic modulators<sup>6</sup>, optical switches<sup>7</sup> and high speed transistors<sup>8</sup> for the explosively growing field of communication technology have been developed.

One of the semiconductor heterostructures most intensively studied in the past with respect to the electronic structure, excitonic effects and carrier dynamics are GaAs/Al<sub>x</sub>Ga<sub>1-x</sub>As quantum wells. Since this material system is lattice matched, no limitations by the growth with respect to the well thickness or the Al concentration in the barrier occur. The evolution of the electronic structure therefore can be continuously traced from an energy quasi-continuum, as in the bulk case, down to a few discrete energy levels when the well thickness becomes considerably smaller than the de Broglie wavelength of the carriers. Quantum wells were classified as so-called bi-dimensional systems<sup>9</sup>, because due to the energy quantization in the well region they can be distinguished from bulk material, but quantum wells also differ from an ideal two-

dimensional system, which consists of a well inserted between infinitely high barriers. However, the application of AlGaAs/GaAs quantum well structures in optoelectronic devices is somewhat limited, because the achievable operation wavelength in those devices do not meet the requirements of optical fibers used in long-distance communication networks. The two preferred windows for operation wavelength of optoelectronic devices are determined by the minima in the absorption spectrum of quartz fibers<sup>10</sup> located at 1550 nm and 1300 nm. In contrast to that, the operation wavelength of devices based on AlGaAs/GaAs quantum wells is limited by the lowest lying optical transition in the GaAs quantum well, i.e. it is always smaller than the bandgap wavelength of bulk GaAs at 870 nm.

Motivated by the demand for optoelectronic devices at 1550 nm and 1300 nm in the last decade new binary, ternary or even quaternary material systems<sup>10</sup> like InAs/GaAs<sup>11</sup>, InAs/InP<sup>12</sup>, InGaAs/GaAs<sup>13</sup>, InGaAs/InP<sup>14</sup> or InGaAsP/InP<sup>15</sup> have been studied. Except in particular cases for the composition, these material systems all have in common that they are not lattice matched. Due to the different lattice constant of well and barrier material the atomic arrangement in the unit cell of the well material is distorted and the well material incorporates strain. Strain can be either tensile or compressive depending on whether the lattice constant of the well material is smaller or larger than the one of the barrier material. Regardless of whether the strain is tensile or compressive, it has two important consequences. The first one is that strained layers cannot be grown with a thickness up to any extent<sup>16</sup>. From the so-called critical layer thickness on, strain cannot be accommodated in an elastic deformation of the unit cell anymore and the lattice relaxes by the incorporation of dislocations. Since dislocations severely degrade the morphological and optical quality of the strained layers<sup>17</sup>, the thickness of strained quantum wells has to be kept below the critical layer thickness. In highly strained material systems like InAs/GaAs the critical layer thickness can be as small as 2-3 monolayers<sup>18</sup>. Evidently, in strained quantum wells the limitations in the composition of the well material, and subsequently the critical layer thickness, drastically reduce the tuneability of their optical properties.

The second consequence of strain is a drastic modification of the band structure in the strained material<sup>19, 20</sup>. Even in the bulk case the hydrostatic strain component leads to a considerable change of the bandgap, and the shear strain component is known to lift

the degeneracy of the hh and lh subbands. The strain induced band structure modifications are exactly opposite for compressive and tensile strain. In the former case the bandgap is increased and, taking the top of the valence band of the unstrained material as reference point, the strain induced splitting lowers the lh valence band edge more than the hh subband edge, so that the bandgap is formed with the hh valence band. In the case of tensile strain the bandgap is reduced and formed with the lh valence band, because the shear strain raises the lh subband edge more than hh band edge. When a quantum well consists of strained material, the band structure modifications due to strain are combined with the changes in the electronic structure as a consequence of the confinement<sup>21</sup>. Interesting structures in the valence band depending on the well width and the amount of strain in the well material like negative effective masses<sup>22</sup> or a cross-over between hh and lh subbands<sup>23</sup> can be observed. Thus, by tailoring the valence band structure using strain, interesting ideas to improve the performance of semiconductor lasers or new concepts for polarization independent electro-optic modulators have been developed.

Most of the experimental and theoretical work about the electronic structure and optical properties in strained quantum wells is concerned with a strain percentage of the order of 1 % or below. For highly strained systems, however, like InAs/GaAs, which exhibits a lattice mismatch of approximately 7 %<sup>24, 25</sup>, only very few experimental data concerning the band alignment at the heterointerface are available<sup>26-28</sup>. Nevertheless, highly strained semiconductor systems are particularly interesting to study, because the strain induced splitting between the hh and lh subbands becomes as large as the energy of the split-off band, and elasticity theory predicts for this regime additional considerable modifications of the valence band structure.

A recent development in the field of semiconductor heterostructures is the reduction of the quantum well width down to a single monolayer, i.e. to embed a single layer of isoelectronic impurities inside a host material. This situation of so-called isoelectronic  $\delta$ -doping<sup>29, 30</sup> clearly has to be distinguished from the conventional  $\delta$ -doping. In commonly used  $\delta$ -doped structures<sup>31</sup> like GaAs:Si the group III atoms are replaced by a group IV element, so that extra free carriers and strong long-range Coulomb-fields are introduced. Although the doping atoms are deposited in ideally one atomic plane, the confining potential is extended over a few tens of nanometers<sup>31, 32</sup>. In contrast to that, in



isoelectronic  $\delta$ -doping, atoms with similar chemical properties are replaced, so that the confinement potential of the impurity layer is localized within one lattice constant, i.e. within a few Ångströms. Therefore, isoelectronic  $\delta$ -layers mediate between single impurities and quantum wells. In the quantum well picture they represent - at least from the structural point of view - the case of an ideal two-dimensional semiconductor system which provides only one bound electron, hh, and lh state with confinement energies almost as large as the confinement potential and exciton binding energies four times higher than in bulk material. In the impurity picture isoelectronic  $\delta$ -layers are the limit of large planar impurity clusters. Both quantum wells and single isoelectronic impurities have been studied intensively in the past with respect to their electronic structure, excitonic effects and the trapping of carriers. However, at the borderline of ultrathin quantum wells and isoelectronic  $\delta$ -layers, only few experimental and theoretical studies are available.

In this thesis we focus in a comprehensive experimental and theoretical study on the electronic structure, excitonic effects and carrier capture in ultrathin highly strained InAs layers embedded in a GaAs matrix. The investigation of these subjects in ultrathin InAs/GaAs quantum wells is very interesting and demanding for various reasons. Firstly, isolated In impurities in GaAs, as for instance realized in InGaAs alloys, do not induce a localized state in the GaAs bandgap<sup>30, 33</sup>. As opposed to that, if the In coverage approaches one monolayer strong optical transitions approximately 60 meV below the GaAs bandgap are observed<sup>34</sup>. Recent theoretical studies<sup>29</sup> show, that a monolayer of isoelectronic impurities always binds a hole or electron regardless of the binding strength of an isolated impurity. Secondly, as mentioned above, the growth of InAs on GaAs is governed by the large lattice mismatch. At a layer thickness of around 1.6 - 2 monolayers, depending on the actual growth conditions, the InAs layer either starts to relax<sup>18</sup> or self-assembled quantum dots are formed<sup>35</sup>, which both changes the optical properties drastically. Therefore, ultrathin InAs layers in GaAs are the only possibility to study the band alignment at the highly strained InAs/GaAs heterointerface. As a consequence of the large compressive strain, the alignment of the lh subband and the existence of a confined lh state in ultrathin InAs layers attracts particular interest. Due to the large shear strain component the lh subband edge is, on one hand, expected to approach the GaAs valence bandedge. On the other hand the strain induced splitting

between hh and lh subbands is in the order of the energy of the split-off band, which in turn influences the lh confinement drastically<sup>36</sup>. Furthermore, InAs monolayer insertions in GaAs are often described as highly strained ultrathin quantum wells. According to the contradicting results in literature concerning effective masses, confinement energies and localization of the confined InAs states<sup>26-28, 37</sup>, rather fundamental questions arise, namely whether the quantum well model is still a physically correct description for the case of a two-dimensional system where the atomic potential is modified on the length scale of one lattice constant, and if continuum elasticity theory as well as the concept of band offsets still apply for those ultrathin layers. The third important aspect of ultrathin InAs layers are excitonic effects, which have been found to dominate their optical properties<sup>27, 28</sup>. Excitons bound to ultrathin InAs layers are expected to be different from excitons in usual quantum wells. In conventional quantum wells the increase of the exciton binding energy with decreasing well width demonstrates the bi-dimensional character of the excitons, but the “character” of the excitons is still determined by the well material<sup>38</sup>. In contrast, the character of the excitons bound to ultrathin InAs layers is entirely determined by the surrounding GaAs barrier. However, the dimensionality of the excitons and in particular the question, whether in ultrathin InAs layers a bound lh exciton exists<sup>39</sup>, still had to be clarified. Beyond that, the resonant excitation of excitons can efficiently be used to investigate the exciton-phonon interaction and the dominant mechanism for exciton dephasing, i.e. the decay in their initially fixed phase relation and macroscopic polarization imprinted by a driving electric laser field. Concerning the latter, the magnitude of the dephasing time allows, in terms of the length scale of potential fluctuations due to disorder and microscopic strain distribution, important conclusions about the growth of the InAs layer<sup>40</sup>. Finally, the most important property of ultrathin InAs embedded in a GaAs matrix is the strong photoluminescence emerging below the GaAs bandgap. This unexpected strong emission line makes ultrathin InAs layers very interesting for application in semiconductor lasers with an operation wavelength at 980 nm. Typically, the emission from a single InAs layer has a hundred times higher intensity than the bandedge photoluminescence of a 100 nm GaAs barrier<sup>41</sup>, which indicates a very efficient trapping of photogenerated carriers by the InAs layer. To our knowledge, until now there were neither experimental data available

for the capture times in ultrathin quantum wells nor a detailed analysis of the capture mechanism.

A detailed experimental and theoretical study of the electronic structure in ultrathin InAs layers embedded in a GaAs matrix is presented in Chapter 2 of this thesis. Previously, Wilke and Hennig<sup>30</sup> calculated the electronic level positions for isoelectronic InAs  $\delta$ -layers in GaAs within the tight-binding scheme. This model describes the InAs layer in the impurity picture, and the changes in the atomic level positions leading to the formation of a deep level in the GaAs bandgap were calculated by taking into account interaction up to second nearest neighbours. Since this method is based on the calculation of atomic orbitals and not on the concept of band offsets it is certainly favourable to describe the transition between an isolated In impurity and InAs layers of submonolayer coverage. However, in this model only the hydrostatic strain component of the biaxial deformation in the InAs layer is considered, whereas the tetragonal distortion, i.e. the shear strain component, is neglected. Therefore, the tight-binding model gives a reasonable agreement with the experimental results for the hh related transitions in accordance with elasticity theory, which predicts that the hh levels are predominantly affected by the hydrostatic strain. In contrast, the tight-binding model does not allow any predictions for the lh levels, because the degeneracy of hh and lh states is entirely lifted due to the shear strain. Moreover, to place the electronic structure of the InAs layer in relation to the GaAs matrix a value for the conduction band offset  $\Delta E_c$  is required, which by itself was not reliably known until now.

An alternative method for the calculation of the electronic structure of ultrathin InAs layers is the quantum well model, which is based on the concept of band offsets. Strain has been considered either explicitly by using an eight-band k-p type model<sup>28</sup> or implicitly in so-called strain modified band offsets<sup>26, 27</sup>, i.e. conduction and hh valence band offsets are decreased with respect to the (hypothetical) unstrained values resulting in an increased bandgap, and hh and lh band offsets are different as a consequence of the shear strain. Although this model allows to fit the experimental data for the optical transitions as a function of InAs coverage rather well, it implies very strong physical assumptions which are violated if applied to ultrathin layers. The most important assumption in the square well model is that the envelope wavefunction smoothly varies with respect to the periodicity of the Bloch wavefunctions<sup>42</sup>. In the case of a monolayer

thick InAs layer, however, the slope of the envelope function would even change the sign within one lattice constant, which is in clear contradiction to the assumption.

In Chapter 2 a new model for the description of the electronic structure is formulated which is based on the concept of band offsets but which solves the fundamental problems of the square well model as described above, and which is in good agreement with the tight-binding model for the transition region of submonolayer coverages. Motivated by the fact that the insertion of a monolayer thick InAs layer induces a confinement potential on the length scale of one lattice constant, in this model the confinement potential of the InAs layer is described by a  $\delta$ -potential<sup>43</sup>. This approach naturally takes into account, that the wavefunction of a confined state cannot be constructed inside the ultrathin InAs layer, but that it extends entirely into the GaAs barrier. As a consequence, by using the  $\delta$ -potential there is no freedom to adjust the effective masses of the confined states: they are solely determined by the GaAs barrier. However, we will demonstrate, by means of calculating the effective masses with the two-band Luttinger-Hamiltonian in spherical approximation<sup>44</sup>, that the effective masses considerably differ from the GaAs bulk values and that for the in-plane effective masses a reversal between hh and lh masses takes place. It should be emphasized that both effects are a pure consequence of the strong quantization due to the InAs layer. A further inherent property of the  $\delta$ -potential is that it always binds one electron, hh, and lh state no matter how weak the binding strength of the potential is. This is consistent with the results of the tight-binding calculations<sup>29</sup>, which show that isoelectronic impurity layers always bind a hole or electron regardless of the strength of the short-range perturbation.

The magnitude of the band offsets, which enters the tight-binding model as well as the square well model, is the subject of recent interest. In an early experimental work<sup>45</sup>, the conduction and valence band discontinuities were determined from the core level positions found in X-ray photoelectron spectroscopy measurements in strain-relaxed samples, where the impact of the lattice mismatch on the core level position was not considered. In pseudomorphically grown InAs layers, spectroscopic techniques, namely PL and PLE, have been used for the determination of the band alignment at the highly strained InAs/GaAs heterointerface. The observed optical transition energies were subsequently matched with the quantum well calculations by fitting the band offsets. Since this method is not sensitive to the band offset ratio, for unstrained quantum wells

it is already questionable whether this method can provide reliable values for the band offsets, because the transition energies depend on both the confinement energies of the electron state and of the hh or lh state. In highly strained layers the situation becomes even more troublesome: due to the strain induced splitting of the hh and lh subbands one needs to determine three band offsets independently from only two optical transitions. This problem is reflected by the large spreading in the values for the band offsets and band offset ratio reported previously, although the same model and effective masses were used<sup>26-28, 46</sup>. Furthermore, the excitonic character of the observed optical transitions and the strong dependence of the exciton binding energies on the InAs layer thickness<sup>47</sup>, which adds additional uncertainty to the band offsets, had not been considered. As a result, the band offsets and the band offset ratio determined earlier seemed to contradict elasticity theory, and further lead to the conclusion that ultrathin InAs layers do not provide a confined lh state and a bound lh exciton state.

In Chapter 2 a novel technique for the determination of band offsets by means of spectroscopy is also introduced<sup>48</sup>, which allows to determine conduction and valence band offsets independently. Thus, this is the first optical method for the band offset determination, which is explicitly sensitive to the band offset ratio. In this method the band offsets are extracted from the coupling induced splitting between the symmetric and antisymmetric states in two coupled ultrathin InAs layers separated by a GaAs barrier with different width exploiting the large difference between electron and hh effective masses. Because the band offsets are determined from the energy difference of the observed transitions rather than from their absolute spectral position, substantial errors due to excitonic effects are eliminated. It is important to note, that this method has general validity. The band offsets are equal to the depth of the confining potential in the conduction and valence band, which implicitly take strain into account. Therefore, this method is not restricted to ultrathin strained layers and it does not have principle limitations with respect to the material system. By exchanging the  $\delta$ -potential model with the square well model it can easily be applied to conventional quantum wells.

The band offsets and band offset ratio we find for the highly strained InAs/GaAs heterointerface agree for the first time with elasticity theory and calculations performed in the local density approximation<sup>49</sup>. Moreover, they also allow a consistent qualitative and quantitative explanation of the experimental results of other groups. Our values

show, that until now the confinement energy of the electrons had been underestimated, whereas the confinement energies of the hh and lh states were overestimated. This experimental finding is of particular relevance for the discussion about whether ultrathin InAs layers can bind a lh exciton or not. The magnitude of the lh band offset we find, unambiguously provides a localized lh state at cryogenic temperatures with an effective confinement energy being ten times higher than the one previously reported by other groups. As it will turn out in Chapter 4 of this thesis, the existence of a localized lh state plays a key role in the efficient carrier capture by the InAs layer.

Based on the results about the electronic structure and effective masses, in Chapter 3 of this thesis an experimental and theoretical study of excitonic effects in ultrathin InAs layers is presented. Previous PLE measurements and a lineshape analysis of the photorefectivity spectra<sup>50</sup> revealed that excitonic transitions dominate the optical properties of ultrathin InAs layers. It had also been shown that the strong photoluminescence from the InAs layers results from the recombination of hh excitons localized by the InAs layer. Additionally, Wang et al. found in magneto-PLE measurements<sup>26</sup> an increase of the hh exciton binding energy with increasing average InAs layer thickness. However, according to the contradicting interpretations<sup>26, 27, 36</sup> of excitons related to the InAs layer, there seemed to be a fundamental problem in unifying the GaAs character of the excitons and their large binding energies. As a consequence of their GaAs character the excitons were interpreted as three-dimensional<sup>51</sup> and their large binding energies were attributed to the “strong localization”. The existence of a bound lh exciton was doubted by several authors<sup>26, 39, 40</sup> although optical transitions suggesting to originate from lh excitons were observed in PLE or modulation spectra. As will be explained in Chapter 2, most of the trouble in understanding excitons in ultrathin layers results from the use of the quantum well model, which has lead to wrong band offsets and wrong effective masses and which suggests that a part of the envelope function is confined in the “well” region.

In Chapter 3 the character and dimensionality of excitons in ultrathin InAs layers is clarified. The hh and lh exciton binding energies are determined by PLE and temperature dependent PL measurements and they are calculated by means of the zero-radius potential model. In this model excitons are not bound to single atoms as in the case of isolated impurities, but bound to the InAs layer as a whole, i.e. they can freely

move in the InAs plane, but their motion is restricted in the growth direction. The character of the excitons is fully determined by the reduced effective mass as the only material sensitive parameters entering the calculation of the binding energy and Bohr-radius. Since the wavefunctions of the confined states to which the excitons are bound extend entirely into the GaAs matrix, the effective masses are solely determined by the barrier material. Consequently, excitons bound to the InAs layer are GaAs-like. Calculations and experiments consistently show an enhancement of the hh exciton binding energy by a factor of 2.5 with respect to the bulk value, whereas the lh exciton binding energy is increased by only a factor 1.2. The hh exciton is thus almost 2D, whereas the lh exciton is 3D. The dimensionality reduction of the hh exciton is a direct consequence of the strong confinement of the hh's by the InAs layer and the resulting barrier penetration length of only 20 Å. However, what makes the hh excitons in ultrathin InAs layers really special is the fact that, although they are almost 2D, their character is purely GaAs barrier-like. As opposed to that, in a conventional GaAs/Al<sub>0.3</sub>Ga<sub>0.7</sub>As quantum well<sup>52</sup> an increase of the exciton binding energy by a factor of 2.5 is observed for a well thickness of 50 Å. At this well thickness the integrated probability of finding the electron or hole in the barrier is still below 10 %, i.e. the exciton character is dominated by the well material. The unique property of ultrathin InAs layers, namely the coexistence of a 2D hh exciton and a 3D lh exciton both bound to the InAs layer, results from the fact that InAs layers in GaAs are highly compressively strained. In unstrained quantum wells lh states are always slightly less confined than hh states due to the lower lh effective mass, so that the lh excitons have intrinsically a more 3D character than hh excitons. Under high compressive strain, where the shear strain component significantly reduces the lh band offset and the lh confinement, this difference in dimensionality becomes more pronounced.

The unambiguous experimental proof for a bound lh exciton is found in cw and time-resolved resonant excitation experiments, which are also presented in Chapter 3. Under selective excitation of the lh exciton transition one discovers a new sharp emission line<sup>40,51</sup>, which emerges close to the hh exciton photoluminescence band exactly one LO phonon below the excitation energy. The striking features of this line are as follows: (i) the spectral width of the line is as small as the laserline, (ii) the spectral position of the sharp line rigidly shifts with a detuning of the excitation energy always one GaAs

LO phonon below the excitation energy, (iii) the sharp line vanishes when the excitation energy is completely detuned from the lh exciton transition, (iv) its intensity is exactly proportional to the excitation density, and (v) the intensity of the sharp line dramatically decreases when the temperature is increased from 4 K to 18 K, where the line has disappeared.

Sharp lines with similar properties have previously been observed in conventional quantum well structures. Stanley et al.<sup>53</sup> reported about sharp emission lines due to hot exciton relaxation under LO phonon emission in II-VI semiconductor quantum wells, which later was also discovered in GaAs/AlGaAs quantum wells<sup>54</sup>. Resonant Raman scattering under the emission of one LO phonon was used by Zucker et al.<sup>55</sup> to determine the degree of confinement of excitons in GaAs/AlGaAs multiple quantum wells, and Nakamura et al.<sup>56</sup> demonstrated for the first time transformation between resonant Raman scattering and resonant luminescence in semiconductors, which had been discovered in molecular iodine long before<sup>57</sup>. Doubly resonant Raman scattering<sup>58</sup>, where incoming and outgoing photons are both resonant with excitonic transitions, has been observed in specific GaAs/AlGaAs quantum wells. By changing the resonance conditions it has been used to distinguish exciton-phonon coupling via deformation potential- and Fröhlich-interaction. However, hot exciton relaxation, resonant luminescence, resonant Raman scattering and doubly resonant Raman scattering are distinct processes which can hardly be distinguished in cw experiments in particular if they involve the same number and type of phonons.

Ultrathin InAs layers of a thickness between 1.2 and 1.6 monolayers give rise to the observation of hot exciton relaxation, resonant luminescence and doubly resonant Raman scattering when they are resonantly excited at the lh exciton transition, because the energy difference between hh and lh exciton states is approximately one GaAs LO phonon. The interaction with GaAs optical phonons in all three processes is not too surprising, since the confined states forming the excitons extend entirely into the GaAs barrier and the GaAs phonon mode is only weakly perturbed by the thin InAs layer. In the hot exciton relaxation process the initial lh exciton population relaxes rapidly (within a few picoseconds) under LO phonon emission to unoccupied hh exciton states. This process involves both a lh and a hh exciton population and occurs over the hh exciton lifetime. A similar process having an identical transient behaviour is the creation



of hh excitons at  $k \neq 0$  which subsequently relax to  $k=0$ . Resonant luminescence is the incoherent succession of two single photon processes, namely, the absorption followed by re-emission in a resonant Raman process. This process only involves a lh exciton population and occurs over the lh exciton lifetime. In contrast, doubly resonant Raman scattering is a coherent single photon scattering process in which initial, final, and virtual intermediate state are resonant with real states. Thus, incoming and outgoing photons are correlated over the dephasing time of the lh exciton state. Consequently, as long as hh exciton lifetime, lh exciton lifetime and lh exciton dephasing time are different, they can be distinguished by studying the transient behaviour of the sharp line, because the decay time of the sharp line acts as an individual “fingerprint” of each process.

From the results of our time-resolved experiments on the decay time of the sharp line and the hh exciton lifetime using time-correlated single-photon-counting, which are presented in Chapter 3, we can rule out hot exciton relaxation as the origin for the sharp line. By additionally measuring the lh exciton lifetime we will demonstrate, that resonant luminescence and doubly resonant Raman scattering are simultaneously present and that the origin of the sharp line continuously transforms from resonant luminescence for excitation on resonance to doubly resonant Raman scattering for off resonant excitation. Under resonant excitation we additionally performed temperature dependent measurements of the intensity of the sharp line. We observe a dramatic decrease of the intensity when the temperature is increased from 4 K to 18 K. Since the observation of doubly resonant Raman scattering requires the existence of both a bound hh and lh exciton state, the thermal quenching of the sharp line directly proves for the first time the existence of a bound lh exciton<sup>59</sup>.

For the special case of excitation on resonance our results for the lh exciton lifetime in combination with a polarization analysis of the sharp line<sup>51</sup> enable us to deduce the lh exciton dephasing time, because exciton-phonon coupling via deformation potential interaction was found to be negligible. Moreover, the polarization analysis reveals that for excitation on resonance the Raman component contributes less than 10 % to the total intensity of the sharp line, which strongly supports our results described above. For the lh exciton dephasing time we find a value of 40 ps, which is relatively long<sup>40</sup>. Under selective excitation coherent exciton wavefunctions only exist in a finite lateral region

of the InAs layer, which provides an effective confinement potential for the electronic states. In turn, the dephasing of excitons by thickness fluctuations, the formation of InAs islands or local strain fields at local steps, where the InAs coverage changes from 1 to 2 monolayers, strongly depends on the length scale of the fluctuations in the effective potential in comparison with the exciton Bohr-radius. Therefore, the long dephasing time provides strong evidence that short-range potential fluctuations, on a length scale smaller than the lh exciton Bohr-radius, are weak. Considering that the lh excitons were found to be almost 3D and having a Bohr-radius of approximately 120 Å, this suggests an almost perfectly two-dimensionally grown InAs layer. This is in excellent agreement with our results for the structural characterization by double crystal high-resolution X-ray diffraction, which revealed that the InAs layers are coherently strained and that more than 80 % of the deposited InAs is confined in a single atomic plane.

In Chapter 4 of this thesis we focus on the carrier capture in ultrathin InAs layers embedded in a GaAs matrix in order to explain the surprisingly strong photoluminescence below the GaAs bandgap. The capture times we obtain from picosecond time-resolved two-wavelength pump-probe phototransmission measurements are to our knowledge the first experimental data reported for quantum well structures thinner than 25 Å. In general, it is impossible to extrapolate the data for the capture times in conventional quantum wells to the case of ultrathin layers, because they are strongly dependent on the structural parameters such as well width, barrier width and heights or number of wells. Blom et al.<sup>60</sup> demonstrated that the capture time in GaAs/AlGaAs single quantum wells oscillates between 20 and 3 ps when the well width is increased from 26 to 90 Å. Oscillating capture times between 30 ps and 1 ns were theoretically predicted by Brum and Bastard<sup>61</sup>, who developed a state-of-the-art quantum mechanical capture model. They also demonstrated that the quantum mechanical nature of the capture process is preserved for thickness of the barrier layers of more than 1 μm. Therefore, their model implies in the sense of the correspondence principle the classical description of the capture process in early theoretical studies<sup>62, 63</sup> as a succession of diffusion and local capture. A decrease of the capture time down to 1-10 ps was found by Babiker and Ridley<sup>64</sup> for GaAs/AlGaAs superlattices, and in InGaAs/InP multiple quantum well structures electron capture times shorter than 1 ps were reported depending on the barrier width<sup>65</sup>. Furthermore, the capture times are known to depend

strongly on the experimental conditions like carrier excess energy and excitation density. Increasing the excitation density is known to reduce the capture time due to additional carrier-carrier scattering. At densities of  $10^{11} \text{ cm}^{-2}$  the capture time is already reduced by a factor two with respect to its value when the capture is dominated by LO phonon scattering<sup>66</sup>. As significant is the dependence of the capture times on the carrier excess energy, i.e. the energy difference between the initially created carrier distribution and the lowest lying barrier state. As soon as the excess energy exceeds the threshold energy for LO phonon emission the capture times were found to decrease by more than a factor of five<sup>67</sup>.

As an analogy from the classical regime of acoustic phonons, large capture rates leading to a strong fluorescence have also been found in the past for isolated impurities acting as deep traps or recombination centers<sup>68-70</sup>. Lax<sup>71</sup> demonstrated that the capture rates of charged centers are high when carriers can relax to the ground state by a multiphonon cascade. Capture cross sections as high as  $10^{-11} \text{ cm}^2$  were always found for traps introducing a long-range Coulomb attractive potential which in addition to the ground state also possesses bound excited states within  $k_B T$  close to the bandedges of the host material. The large capture cross section of those so-called ‘giant traps’ is explained by the large extension of the excited Coulomb states into the host material. The capture rate of the ground state is additionally limited by the rate at which carriers, once captured by an excited state, can relax from the excited state to the ground state. This transition may require a cascade of phonon emission or the emission of radiation. A large capture cross section of the trap only leads to a high luminescence from the ground state if the relaxation from the excited state is much more efficient than thermal emission of carriers from the excited state or non-radiative recombination.

In Chapter 4 it will be experimentally demonstrated that the carrier capture in ultrathin InAs layers occurs in a two-step process and that InAs monolayers give rise to the observation of switching of the hole relaxation from optical to acoustic phonon emission<sup>72</sup>. The capture times were measured by time-resolved two-wavelength pump-probe phototransmission, which allows utilization of excitation densities as low as  $10^8 \text{ cm}^{-2}$ . At those low densities the capture process is exclusively governed by phonons and not affected by carrier-carrier scattering. Using an average InAs thickness of 1.2 monolayers, we access the interesting situation where the hh and lh states are both

confined and their difference in confinement energy amounts to approximately one GaAs LO phonon. By measuring the spectral dependence of the capture times in the vicinity of the hh and lh exciton transitions, particular focus is put on the role of the confined lh state in the capture process. Within the lh exciton transition we find a constant capture time of 20 ps. As opposed to that, the capture time decreases abruptly from 50 ps to 22 ps within the hh exciton transition as the energy separation between hh and lh states exceeds the threshold for GaAs LO phonon emission. The combination of both characteristics provides strong evidence that the holes are captured rapidly by the weakly confined lh states and then cool down to the hh state. For a hh-lh separation larger than 36 meV the intersubband relaxation involves the emission of one LO phonon. This process occurs almost instantaneously leading to a capture time at the low energy side of the hh exciton transition as fast as the capture time at the lh exciton transition. The 2 ps we derive as an upper limit for the intervalence band relaxation time under LO phonon emission is in good agreement with recent experimental<sup>73, 74</sup> and theoretical<sup>74, 76</sup> results for GaAs/AlGaAs quantum wells, where intersubband relaxation times between 160 fs and 2 ps were found. At the high energy side of the hh exciton transition the hh-lh separation is smaller than 36 meV, so that the hole relaxation occurs by emission of acoustic phonons. This process is known to be slow requiring several tens of picoseconds<sup>77, 78</sup>. As a consequence, a small spectral detuning of the probe wavelength towards higher energies within the hh exciton transition leads to the observed abrupt increase of the capture time.

The pump-probe phototransmission technique used in the capture measurements exploits the bleaching of the excitonic absorption due to the population of the confined InAs states. Recently it has been demonstrated that the bleaching is not dependent on the distribution of the carriers among themselves in a confined level, but that it is solely determined by the occupation number in the confined level<sup>60, 79, 80</sup>. However, depending on the dominating bleaching mechanism the decrease in the excitonic absorption might be strongly non-linear dependent on the occupation number altering the observed rise and decay times with respect to the capture and recombination times of the true population. When using pump-probe phototransmission one therefore needs to clarify to what extent the observed transient bleaching reflects the true evolution of the confined states population. For that purpose we also calculate in Chapter 4 the transient

---

phototransmission in ultrathin InAs layers taking into account the contributions of both phase-space-filling<sup>81</sup> and exciton screening<sup>82, 83</sup>. The populations in the confined InAs states are derived from coupled rate equations. Calculation and experiments show in agreement that the transient phototransmission directly reflects the population in the confined states only for excitation densities lower than  $3 \times 10^8 \text{ cm}^{-2}$ . At higher excitation densities the measured and calculated phototransmission transients exhibit a saturation behaviour leading to diminished rise times and increased decay times with respect to the confined state population. This observation allows to conclude that the bleaching in ultrathin InAs layers is dominated by exciton screening<sup>84</sup>.

## References

- <sup>1</sup> K. v. Klitzing, G. Dorda, and M. Pepper, *Phys. Rev. Lett.* **45**, 494 (1980)
- <sup>2</sup> D.C.S. Tsui, H.L. Störmer, and A.C. Gossard, *Phys. Rev. Lett.* **48**, 1559 (1982)
- <sup>3</sup> L. Esaki, and L.L. Chang, *Phys. Rev. Lett.* **33**, 495 (1974)
- <sup>4</sup> R. Dingle, W. Wiegemann, and C.H. Henry, *Phys. Rev. Lett.* **33**, 827 (1974)
- <sup>5</sup> I. Hayashi, *IEEE Trans. Electron. Devices* **ED-31**, 1630 (1984)
- <sup>6</sup> G.W. Yoffe, J. Brübach, F. Karouta, and J.H. Wolter, *Appl. Phys. Lett.* **63**, 2318 (1993)
- <sup>7</sup> X. Leijtens, G.W. Yoffe, J.E.M. Haverkort, F. Karouta, J. Brübach, T. Eijkemans, L.M.F. Kaufmann, M.K. Smit, J.A.A. Stegemann, Y.C. Zhu, and J.H. Wolter, *Appl. Phys. Lett.* **66**, 2736 (1995)
- <sup>8</sup> A.F.J. Levi, R.N. Nottenburg, Y.K. Chen, and J.E. Cunningham, *Appl. Phys. Lett.* **54**, 2250 (1989)
- <sup>9</sup> G. Bastard, “Wave Mechanics Applied to Semiconductor Heterostructures”, *Monographies de Physique*, Les Ulis 1988
- <sup>10</sup> K.J. Ebeling, *Integrated Optoelectronics*, Springer Berlin Heidelberg 1989
- <sup>11</sup> S.S. Dosanjh, L.Hart, R. Nayak, and B.A. Joyce, *J. Appl. Phys.* **75**, 8066 (1994)
- <sup>12</sup> Z. Sobiesierski, S.A. Clark, R.H. Williams, A. Tabata, T. Benyattou, G. Guillot, M. Gendry, G. Hollinger, and P. Viktorovitch, *Appl. Phys. Lett.* **58**, 1863 (1991)
- <sup>13</sup> D.Y. Oberli, J. Shah, J.L. Jewell, and T.C. Damen, *Appl. Phys. Lett.* **54**, 1028 (1989)
- <sup>14</sup> M.C. Tamagaro, R. Hull, L.H. Greene, J.R. Hayes, and A.Y. Cho, *Appl. Phys. Lett.* **46**, 569 (1988)
- <sup>15</sup> P.J.A. Thijs, L.F. Tiemeijer, J.J.M. Binsma, and T. v. Dongen, *Philips J. Res.* **49**, 187 (1995)
- <sup>16</sup> R. People, and J.C. Bean, *Appl. Phys. Lett.* **47**, 322 (1985)
- <sup>17</sup> E.P. O’Reilly, *Semicond. Sci. Technol.* **4**, 121 (1989)
- <sup>18</sup> A. Sasaki, *J. Crystal Growth* **160**, 27 (1996)
- <sup>19</sup> S.L. Chuang, *Phys. Rev.* **B43**, 9649 (1991)
- <sup>20</sup> F. H. Pollak, *Semiconductors and Semimetals*, Vol. **32**, Academic Press, New York 1990

- 
- <sup>21</sup> T.Y. Wang, and G.B. Springfellow, *J. Appl. Phys.* **67**, 344 (1991)
- <sup>22</sup> P.J.A. Thijs, and T. van Dongen, *Electron. Lett.* **25**, 1735 (1989)
- <sup>23</sup> D. Gershoni, J.M. Vandenberg, R.A. Hamm, H. Temkin, and M.B. Panish, *Phys. Rev. B* **36**, 1320 (1987)
- <sup>24</sup> J.C. Woicik, J.G. Pellegrino, S.H. Southworth, P.S. Shaw, B.A. Karlin, C.E. Bouldin, and K.E. Miyano, *Phys. Rev. B* **52**, 2281 (1995)
- <sup>25</sup> C. Giannini, L. Tapfer, S. Lagomarsino, J.C. Boulliard, A. Taccoen, B. Capelle, M. Ilg, O. Brandt, and K.H. Ploog, *Phys. Rev. B* **48**, 11496 (1993)
- <sup>26</sup> P.D. Wang, N.N. Ledentsov, and C.M. Sotomayor Torres, *Phys. Rev. B* **50**, 1604 (1994)
- <sup>27</sup> O. Brandt, L. Tapfer, R. Cingolani, K.H. Ploog, M. Hohenstein, and F. Phillipp, *Phys. Rev. B* **41**, 12599 (1990)
- <sup>28</sup> M.I. Alonso, M. Ilg, and K.H. Ploog, *Phys. Rev. B* **50**, 1628 (1994)
- <sup>29</sup> K.A. Mäder, and A. Baldereschi, *Inst. Phys. Conf. Ser.* **123**, 341 (1992)
- <sup>30</sup> S. Wilke, and D. Hennig, *Phys. Rev. B* **43**, 12470 (1991)
- <sup>31</sup> P. Koenraad, F.A.P. Blom, C.J.G.M. Langerak, M. R. Leys, J.A.A.J. Perenboom, J. Singleton, S.J.R.M. Spermon, W. van der Vleuten, A.P.J. Voncken, and J.H. Wolter, *Semicond. Sci. Technol.* **5**, 861 (1990)
- <sup>32</sup> T.C. Damen, M. Fritze, A. Kastalsky, J.E. Cunningham, R.N. Pathak, H. Wang, and J. Shah, *Appl. Phys. Lett.* **67**, 515 (1995)
- <sup>33</sup> W. Czaja, *Festkörperprobleme XI*, 65, Pergamon Vieweg (1971)
- <sup>34</sup> P.D. Wang, N.N. Ledentsov, C.M. Sotomayor Torres, P.S. Kop'ev, and V.M. Ustinov, *Appl. Phys. Lett.* **64**, 1526 (1994)
- <sup>35</sup> M. Geddo, M. Capizzi, A. Patane, and F. Martelli, *J. Appl. Phys.* **84**, 3374 (1998)
- <sup>36</sup> F. Dujardin, N. Marréaud, and J.P. Laurenti, *Sol. State Communic.* **98**, 297 (1996)
- <sup>37</sup> S.S. Dosanjh, E.F. Bowser, and J.J. Harris, *Appl. Phys. Lett.* **64**, 2142 (1994)
- <sup>38</sup> G. Bastard, E.E. Mendez, L.L. Chang, and L. Esaki, *Phys. Rev. B* **26**, 1974 (1982)
- <sup>39</sup> O. Brandt, H. Lage, and K.H. Ploog, *Phys. Rev. B* **45**, 4217 (1992)
- <sup>40</sup> J. Brübach, J.E.M. Haverkort, J.H. Wolter, P.D. Wang, N.N. Ledentsov, C.M. Sotomayor Torres, A.E. Zhukov, P.S. Kop'ev, and V.M. Ustinov, *J. Opt. Soc. Am. B* **13**, 1224 (1996)

- 
- <sup>41</sup> R. Cingolani, O. Brandt, I. Tapfer, G. Scamarcio, G.C. La Rocca, and K.H. Ploog, *Phys. Rev.* **B42**, 3209 (1990)
- <sup>42</sup> M.G. Burt, *Appl. Phys. Lett.* **65**, 717 (1994)
- <sup>43</sup> J. Brübach, A. Yu. Silov, J.E.M. Haverkort, W. van der Vleuten, and J.H. Wolter, *Superlatt. Microstruc.* **21**, 527 (1996)
- <sup>44</sup> A. Yu. Silov, J.E.M. Haverkort, N.S. Averkiev, P.M. Koenraad, and J.H. Wolter, *Phys. Rev.* **B50**, 4509 (1994)
- <sup>45</sup> S.P. Kowalczyk, W.J. Schaffer, E.A. Kraut, and R.W. Grant, *J. Vac. Sci. Technol.* **20**, 705 (1982)
- <sup>46</sup> C. Priester, G. Allan, and M. Lannoo, *Phys. Rev.* **B38**, 9870 (1988)
- <sup>47</sup> M.V. Belousov, N.N. Ledentsov, M.V. Maximov, P.D. Wang, I.N. Yassievitch, N.N. Faleev, I.A. Kozin, V.M. Ustinov, P.S. Kop'ev, and C.M. Sotomayor Torres, *Phys. Rev.* **B51**, 14346 (1995)
- <sup>48</sup> J. Brübach, A. Yu. Silov, J.E.M. Haverkort, W. van der Vleuten, and J.H. Wolter, *Phys. Rev.* **B59**, 6488 (1999)
- <sup>49</sup> C.G. van der Walle, *Phys. Rev.* **B39**, 1871 (1989)
- <sup>50</sup> O. Brandt, R. Cingolani, H. Lage, G. Scamarcio, L. Tapfer, and K.H. Ploog, *Phys. Rev.* **B42**, 11396 (1990)
- <sup>51</sup> P.D. Wang, N.N. Ledentsov, and C.M. Sotomayor Torres, *J. Appl. Phys.* **79**, 7164 (1996)
- <sup>52</sup> R.L. Greene, *Phys. Rev.* **B29**, 1807 (1984)
- <sup>53</sup> R.P. Stanley, J. Hegarty, R. Fischer, J. Feldmann, E.O. Göbel, R.D. Feldman, and R.F. Austin, *Phys. Rev. Lett.* **67**, 128 (1991)
- <sup>54</sup> N.N. Ledentsov, R. Nötzel, P.S. Kop'ev, and K.H. Ploog, *Appl. Phys.* **A 55**, 533 (1992)
- <sup>55</sup> J.E. Zucker, A. Pinczuk, D.S. Chemla, A. Gossard, and W. Wiegemann, *Phys. Rev. Lett.* **51**, 1293 (1983)
- <sup>56</sup> A. Nakamura, M. Shimura, M. Hirai, and S. Nakashima, *Sol. State Communic.* **52**, 583 (1984)
- <sup>57</sup> P.F. Williams, D.L. Rosseau, and S.H. Dworesky, *Phys. Rev. Lett.* **32**, 196 (1974)
- <sup>58</sup> D.A. Kleinman, R.C. Miller, and A.C. Gossard, *Phys. Rev.* **B35**, 664 (1987)



- 
- <sup>59</sup> J. Brübach, J.E.M. Haverkort, J.H. Wolter, P.D. Wang, N.N. Ledentsov, and C.M. Sotomayor Torres, *Mat. Res. Soc. Symp. Proc.* **406**, 283 (1996)
- <sup>60</sup> P.W.M. Blom, C. Smit, J.E.M. Haverkort, and J.H. Wolter, *Phys. Rev.* **B47**, 2072 (1993)
- <sup>61</sup> J.A. Brum, and G. Bastard, *Phys. Rev.* **B33**, 1420 (1986)
- <sup>62</sup> H. Shichijo, R.M. Kolbas, N. Holonyak, J.J. Coleman, and P.D. Dapkus, *Sol. State Communic.* **27**, 1029 (1978)
- <sup>63</sup> J.Y. Tang, K. Hess, N. Holonyak, J.J. Coleman, and P.D. Dapkus, *J. Appl. Phys.* **53**, 6043 (1982)
- <sup>64</sup> M. Babiker, and B.K. Ridley, *Superlatt. and Microstruct.* **2**, 287 (1986)
- <sup>65</sup> R. Kersting, R. Schwedler, K. Wolter, K. Leo, and H. Kurz, *Phys. Rev.* **B46**, 1639 (1992)
- <sup>66</sup> P.W.M. Blom, J.E.M. Haverkort, P.J. van Hall, and J.H. Wolter, *Appl. Phys. Lett.* **62**, 1490 (1993)
- <sup>67</sup> P.W.M. Blom, J.E.M. Haverkort, J. Claes, P.J. van Hall, and J.H. Wolter, *SPIE* **2142**, 30 (1994)
- <sup>68</sup> R.A. Faulkner, *Phys. Rev.* **175**, 991 (1968)
- <sup>69</sup> A. Baldereschi, and J.J. Hopfield, *Phys. Rev. Lett.* **28**, 171 (1972)
- <sup>70</sup> H.P. Hjalmarson, P. Vogl, D.J. Wolford, and J.D. Dow, *Phys. Rev. Lett.* **44**, 810 (1980)
- <sup>71</sup> M. Lax, *Phys. Rev.* **119**, 1502 (1960)
- <sup>72</sup> J. Brübach, A. Yu. Silov, J.E.M. Haverkort, W. van der Vleuten, and J.H. Wolter, *Phys. Rev.* **B61**, 16833 (2000)
- <sup>73</sup> D.Y. Oberli, D.R. Wake, M.V. Klein, J. Klem, T. Henderson, and H. Morkoc, *Phys. Rev. Lett.* **59**, 696 (1987)
- <sup>74</sup> S. Hunsche, K. Leo, and H. Kurz, *Phys. Rev.* **B50**, 5791 (1994)
- <sup>75</sup> R. Ferreira, and G. Bastard, *Phys. Rev.* **B40**, 1074 (1989)
- <sup>76</sup> S. Rudin, and T.L. Reinecke, *Phys. Rev.* **B41**, 7713 (1990)
- <sup>77</sup> R.A. Höpfel, R. Rodrigues, Y. Iimura, T. Yasui, Y. Segawa, Y. Aoyagi, and S.M. Goodnick, *Phys. Rev.* **B47**, 10943 (1993)
- <sup>78</sup> J.A. Levenson, G. Dolique, J.L. Oudar, and I. Abraham, *Phys. Rev.* **B41**, 3688 (1990)

- 
- <sup>79</sup> S. Hunsche, K. Leo, H. Kurz, and K. Köhler, *Phys. Rev.* **B49**, 16565 (1994)
- <sup>80</sup> A.M.T. Kim, S. Hunsche, T. Dekorsky, and H. Kurz, *Appl. Phys. Lett.* **68**, 2956 (1996)
- <sup>81</sup> S. Schmitt-Rink, D.S. Chemla, and D.A.B. Miller, *Phys. Rev.* **B32**, 6601 (1985)
- <sup>82</sup> J.A. Brum, G. Bastard, and C. Guillemot, *Phys. Rev.* **B30**, 905 (1984)
- <sup>83</sup> J. Lee, H.N. Spector, and P. Melman, *J. Appl. Phys.* **58**, 1893 (1985)
- <sup>84</sup> M.J. Snelling, P. Perozzo, D.C. Hutchings, I. Galbraith, and A. Miller, *Phys. Rev.* **B49**, 17160 (1994)



## 2. *Electronic Structure in Ultrathin InAs/GaAs Quantum Wells*

### 2.1 Impact of Strain on the Band Alignment

Unlike conventional homojunctions, which result from selective doping of the same semiconductor, heterojunctions rely on compositional variation of the semiconductor material across the interface. The structural properties and the electronic structure of epitaxially grown InAs layers on GaAs substrate are governed by the large mismatch between the bulk lattice constants of InAs ( $g_e = 6.0584 \text{ \AA}$ ) and GaAs ( $g_s = 5.6533 \text{ \AA}$ )<sup>1</sup>. Such a large lattice mismatch can be accommodated in the InAs layer without the incorporation of defects by a uniform biaxial lattice strain only if the InAs layer is sufficiently thin. At the resulting so-called pseudomorphic interface the lattice parameter of the InAs layer parallel to the interface  $g_{\parallel}$  becomes equal to that of the substrate and remains the same throughout the whole structure. As depicted in Fig. 2.1 the lattice parameter perpendicular to the interface  $g_{\perp}$  responds by becoming equal to the value determined by the strain tensor due to a tetragonal distortion of the primitive unit cell. An epitaxial layer grown in this way is also called coherent.

Generally, the strain tensor depends on the crystal symmetry and the substrate orientation during growth. This thesis exclusively focuses on InAs layers grown on (001) substrate. With the [001] direction as the growth direction a simple strain tensor is obtained, since the off-diagonal elements vanish ( $\epsilon_{xy} = \epsilon_{xz} = \epsilon_{yz} = 0$ ). By taking  $x, y$  within, and  $z$  perpendicular to the InAs/GaAs interface, the remaining elements can be derived by macroscopic elasticity theory<sup>2</sup> to be

$$\epsilon_{xx} = \epsilon_{yy} = \epsilon_{\parallel} = \frac{g_{\parallel} - g_e}{g_e} \quad (2.1)$$

and

$$\epsilon_{zz} = \epsilon_{\perp} = \frac{g_{\perp} - g_e}{g_e} = -2 \frac{C_{12}}{C_{11}} \epsilon_{\parallel} \quad , \quad (2.2)$$

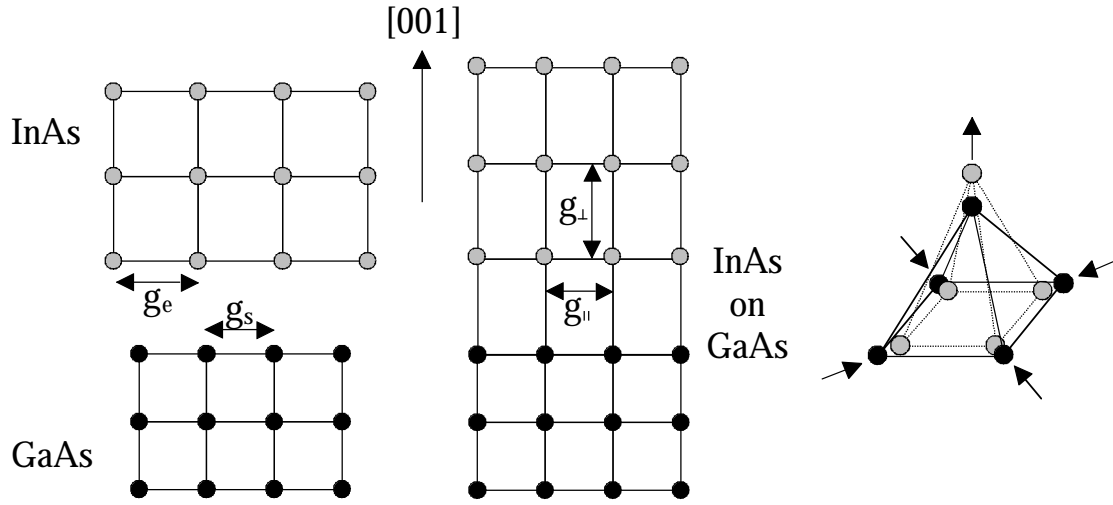


**Fig. 2.1:** Formation of a biaxially compressively strained InAs layer pseudomorphically grown on (001) GaAs substrate.  $g_e$  and  $g_s$  denote the lattice constants of the InAs and GaAs bulk material, whereas  $g_{\parallel}$  and  $g_{\perp}$  are the lattice constants of the strained InAs layer (left). Under pseudomorphic growth, the strain is accommodated by a tetragonal distortion of the unit cell (right).

where  $\epsilon_{\parallel}$  and  $\epsilon_{\perp}$  denote the lattice strain parallel and perpendicular to the interface, which are related by the elastic stiffness constants  $C_{12}$  and  $C_{11}$ . For a layer thickness below critical layer thickness, the InAs layer is coherent and  $g_{\parallel}$  can be replaced by the lattice constant of the GaAs substrate. Because the relaxed lattice parameter of bulk InAs is larger than the one of GaAs, the InAs layer is compressed in the (001) plane and expanded along the [001] direction. With the material parameters given in Tab. 2.1 the compressive in-plane strain in the InAs layer amounts to  $\epsilon_{\parallel} = -0.0669$  and the perpendicular strain to  $\epsilon_{\perp} = 0.0727$  leading to a perpendicular lattice constant in the coherent InAs layer of  $6.4988 \text{ \AA}$ . With regard to the discussion of band line-ups in strained InAs it is useful to decompose the total biaxial strain into a purely hydrostatic component given by<sup>3</sup>

$$\epsilon_{\text{hy}} = 2\epsilon_{\parallel} + \epsilon_{\perp} \quad (2.3)$$

and a pure shear component

$$\epsilon_{\text{sh}} = \epsilon_{\perp} - \epsilon_{\parallel} \quad (2.4)$$

Material parameter	InAs	GaAs
bulk lattice constant (Å)	6.0584	5.6533
$C_{11}$ ( $10^{11}$ dyn cm <sup>-2</sup> )	8.329	11.88
$C_{12}$ ( $10^{11}$ dyn cm <sup>-2</sup> )	4.526	5.38
Bandgap at 4.2 K (eV)	0.418	1.5177
spin-orbit split-off energy $\Delta_0$ (eV)	0.38	0.341
Interband deformation potential A (eV)	-6	-9.77
shear deformation potential B (eV)	-1.8	-1.7
Electron affinity $\chi$ (eV)	4.9	4.07

**Table 2.1:** Material parameters of InAs and GaAs used in this thesis (see Ref. 4, 5). For the sign of the deformation potentials the Bir-Pikus notation was used as given in Ref. 5.

Because strain accumulates with increasing thickness, an InAs layer cannot be grown coherently with a thickness up to any extent. From the critical layer thickness on, the relaxation of the epitaxial layer towards the strain free lattice constant starts by the formation of misfit dislocations. Among other theoretical models to calculate the critical layer thickness<sup>6</sup> the most commonly used one is the model of Matthews and Blakeslee<sup>7, 8</sup>. In their mechanical equilibrium model the critical layer thickness is determined by the thickness for which a segment of threading dislocations under the misfit strain bows and elongates to form a dislocation line. The critical layer thickness  $L_c$ , up to which the growth remains pseudomorphically, is given by<sup>9</sup>

$$L_c = \frac{g_e}{\sqrt{2\pi|\epsilon_{||}|}} \left( \frac{1 - \frac{1}{4}\nu}{1 + \nu} \right) \cdot \left[ \ln \left( \frac{\sqrt{2}L_c}{g_e} \right) + 1 \right], \quad (2.5)$$

where  $\nu$  is the Poisson's ratio which equals to  $C_{11}/(C_{11} + C_{12})$ . In Fig. 2.2 the calculation of the critical layer thickness as a function of the in-plane strain  $\epsilon_{||} = \epsilon$  is

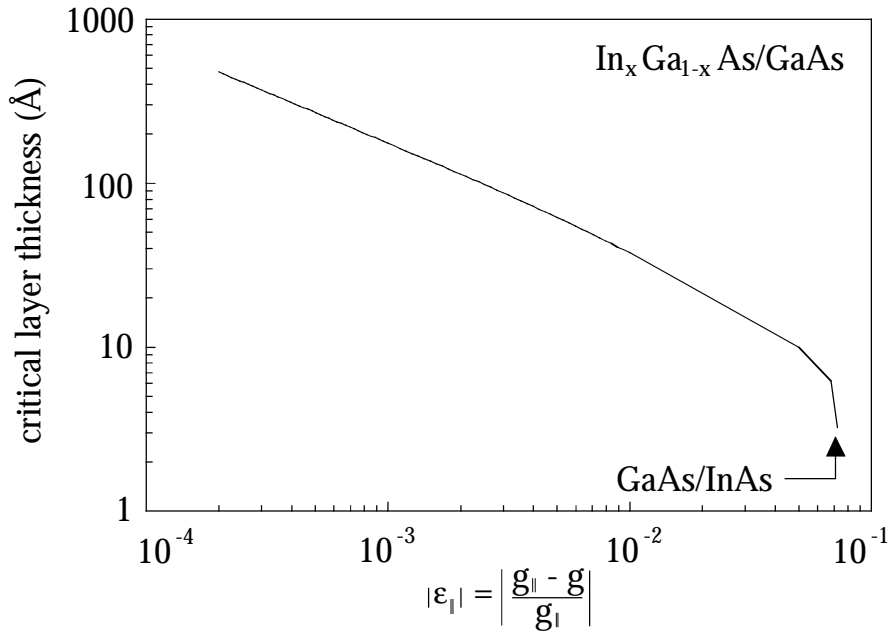


**Fig. 2.2:** Calculation of the critical layer thickness for the InGaAs/GaAs system using the model of Matthews and Blakeslee<sup>7,8</sup>.

shown for the  $\text{In}_x\text{Ga}_{1-x}\text{As}/\text{GaAs}$  system, where the in-plane strain corresponds to a certain In content of the epitaxial layer. From Fig. 2.2 it can be seen that for an InAs layer on GaAs the critical layer thickness amounts to 7 Å. This value agrees with recent experimental results of Sasaki<sup>10</sup>, who found a critical layer thickness of 3 ML. The only possibility to study the band alignment in coherently grown InAs on GaAs and the band offsets at the InAs/GaAs heterointerface are therefore ultrathin InAs layers of monolayer thickness. As a consequence, in ultrathin InAs layers strain induced band structure modifications and quantum size effects in the electronic structure are always superimposed.

At the heterointerface between two adjacent semiconductor materials possessing different bandgaps, band discontinuities (band offsets) are formed. In Fig. 2.3(a) the formation of a heterojunction is illustrated for the case of two undoped, lattice matched materials with the bandgaps  $E_{g,1}$  and  $E_{g,2}$ . For the sake of simplicity the positions of the intrinsic Fermi-levels, which for the achievement of the thermodynamic equilibrium can lead to additional band bending, are neglected. Furthermore, both semiconductors are characterized by their electron affinities  $\chi_1$  and  $\chi_2$ , which as their bandgaps are bulk material parameters. The electron affinity is the energy which is necessary to excite an electron from the conduction bandedge to the vacuum level and which can be

determined from photoemission experiments<sup>11, 12</sup>. From Fig. 2.3(a) it directly can be seen that the conduction band offset  $\Delta E_c$  is solely determined by the difference of the electron affinities of both materials

$$\Delta E_c = q|\chi_1 - \chi_2|. \quad (2.6)$$

The valence band offset  $\Delta E_v$  then is given by the simple relation

$$\Delta E_c + \Delta E_v = \Delta E_g = |E_{g,1} - E_{g,2}|. \quad (2.7)$$

From these considerations it is evident that the band alignment at the heterointerface of two different semiconductor materials is fully determined by their bulk electronic properties. In turn, the discussion of band offsets is restricted to the situation of two adjacent half-infinitely extended semiconductors. Any modifications in the electronic structure due to the formation of quantum wells rely on that band alignment, i.e. in any

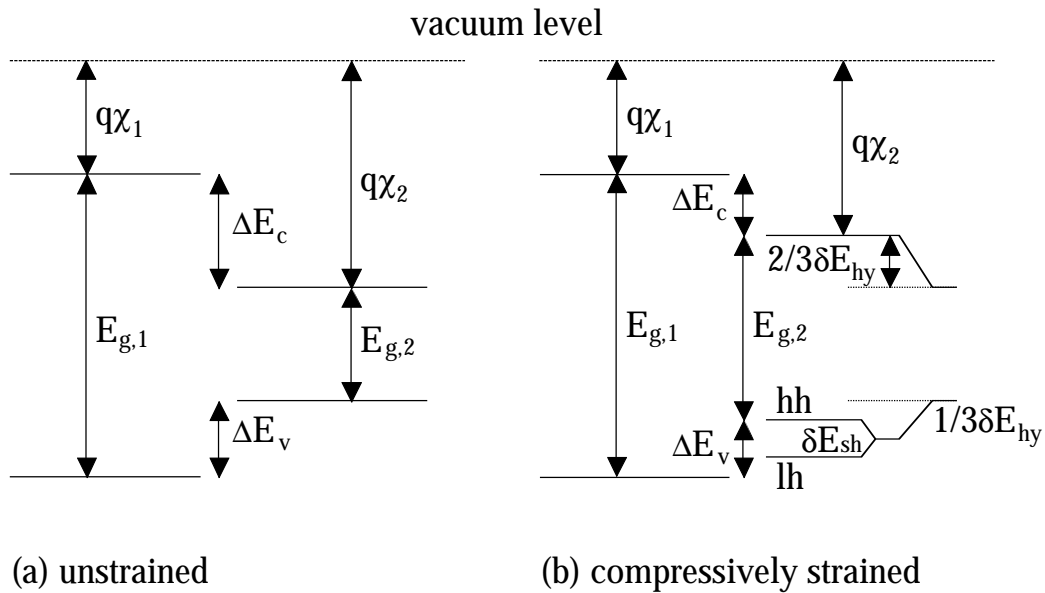


**Fig. 2.3:** Band diagram at the heterojunction of two half-infinitely extended semiconductors with different bandgaps and electron affinity. (a) lattice matched (b) under compressive strain.  $\delta E_{hy}$  and  $\delta E_{sh}$  denote the hydrostatic and shear strain energies.



quantization model (see Section 2.2) band offsets are introduced as known phenomenological parameters. Band offsets and quantization effects can therefore be treated separately.

Due to the incorporation of strain and the accompanying reduction in crystal symmetry, the band offsets drastically change when the two materials at the heterointerface are not lattice matched<sup>13-15</sup>. In Fig. 2.3(b) the situation under compressive strain as in the InAs/GaAs system is illustrated. The bandgap of the strained material is increased by the hydrostatic strain component, which leads to an energy shift of both the conduction and valence bandedges and subsequently to a decrease of the electron affinity with respect to the unstrained material. Near  $\vec{k} = 0$  the modifications of the electronic structure under the presence of strain can be described by deformation potential theory. As illustrated in Fig. 2.4, for zincblende semiconductors in the strain-free case the conduction band minimum is formed by two-fold degenerate s-like states  $|J = 1/2, \pm 1/2\rangle$ , and the valence band structure is decomposed by a four-fold degenerate multiple  $|J = 3/2, M_J = \pm 3/2, \pm 1/2\rangle$  at the top of the valence band, commonly known as hh and lh bands, and the spin-orbit split-off band  $|J = 1/2, M_J = \pm 1/2\rangle$ . Applying strain with an uniaxial component splits the  $J = 3/2$  states into a pair of Kramers degenerated levels. Using a representation for the above wavefunctions with the z-axis parallel to the [001] direction as the preferred (later: quantization) axis and neglecting the small strain dependence of the spin-orbit splitting itself, the combined strain dependent Hamiltonian reads<sup>17</sup>

$$\begin{array}{cccc}
 |1/2, \pm 1/2\rangle_c & |3/2, \pm 3/2\rangle & |3/2, \pm 1/2\rangle & |1/2, \pm 1/2\rangle_{so} \\
 E_g^0 + a_c \text{Tr}(\epsilon) & 0 & 0 & 0 \\
 0 & -a_v \text{Tr}(\epsilon) - \delta E_{sh} & 0 & 0 \\
 0 & 0 & -a_v \text{Tr}(\epsilon) + \delta E_{sh} & \sqrt{2} \delta E_{sh} \\
 0 & 0 & \sqrt{2} \delta E_{sh} & -a_v \text{Tr}(\epsilon) - \Delta_0
 \end{array} \tag{2.8}$$

Here,  $\text{Tr}(\epsilon)$  is the trace of the strain tensor,  $a_c$  and  $a_v$  are the hydrostatic deformation potential of the conduction and valence band, and  $\delta E_{sh}$ ,  $E_g^0$ ,  $\Delta_0$  denote the shear strain

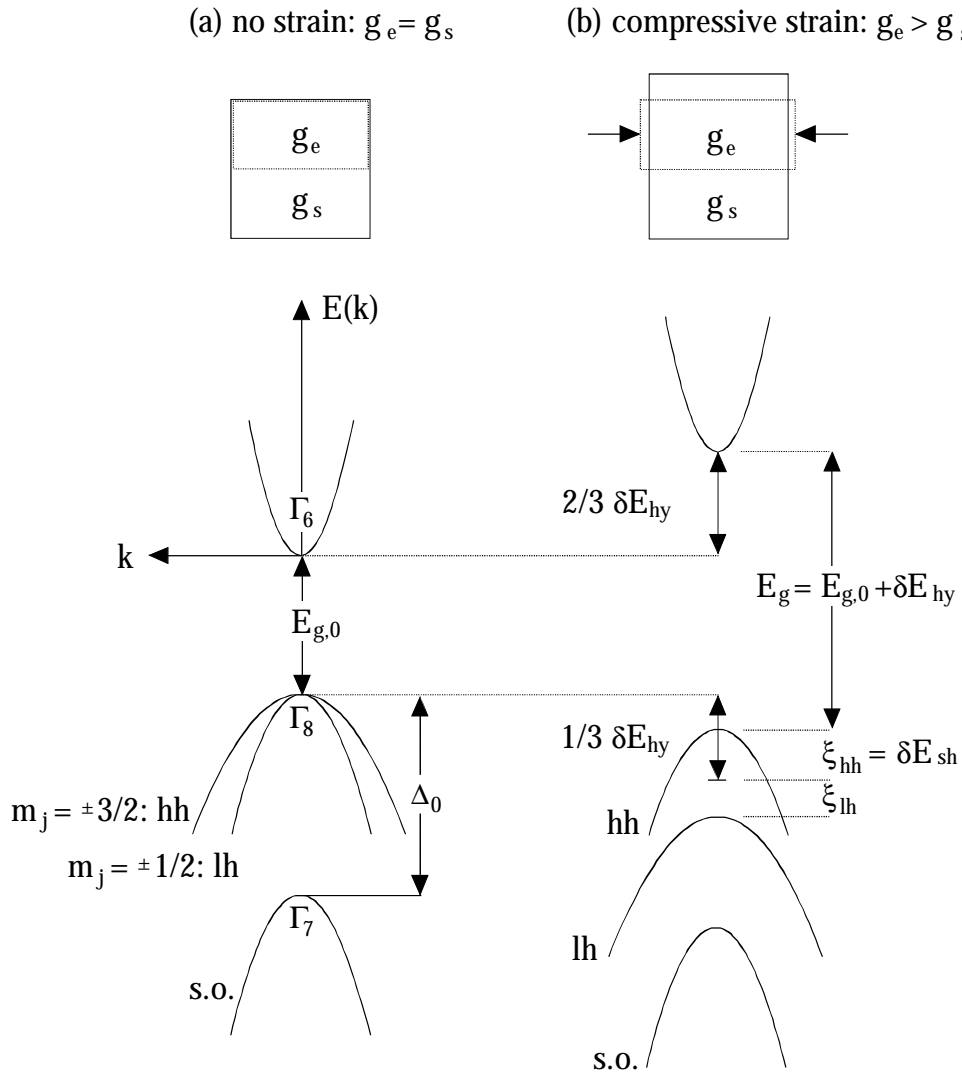


**Fig. 2.4:** Schematic band structure in momentum space for InAs under lattice matched conditions (a) and under compressive strain (b).  $\xi_{hh}$  and  $\xi_{lh}$  denote the amount of shear strain energy accommodated by the  $hh$  and  $lh$  subbands.

energy, the zero-strain bandgap and the spin-orbit split-off energy, respectively. In the case of the uniaxial strain component in [001] direction, the hydrostatic and shear strain energies are given by<sup>2, 3</sup>

$$\delta E_{hy} = 2A \left( 1 - \frac{C_{12}}{C_{11}} \right) \varepsilon$$

and

$$\delta E_{sh} = -B \left( 1 + \frac{2C_{12}}{C_{11}} \right) \varepsilon,$$

(2.9)

where A and B denote the interband hydrostatic and shear deformation potential, and the solution of the above Hamiltonian yields for the valence to conduction band transition energies<sup>16, 17</sup>

$$\begin{aligned}
 E_{v1} &= E_g^0 + \delta E_{hy} + \delta E_{sh} \\
 E_{v2} &= E_g^0 + \delta E_{hy} + \frac{1}{2}(\Delta_0 - \delta E_{sh}) - \frac{1}{2}\sqrt{\Delta_0^2 + 2\Delta_0\delta E_{sh} + 9\delta E_{sh}^2} \\
 E_{v3} &= E_{so} = E_g^0 + \delta E_{hy} + \frac{1}{2}(\Delta_0 - \delta E_{sh}) + \frac{1}{2}\sqrt{\Delta_0^2 + 2\Delta_0\delta E_{sh} + 9\delta E_{sh}^2}
 \end{aligned} \tag{2.10}$$

Regardless of whether the strain is compressive or tensile,  $E_{v3}$  always refers to the transition from the p-like spin-orbit split-off band to the conduction band, which therefore has the largest transition energy among all three valence bands. This, however, is different for the hh and lh bands. Taking the top of the valence bands of unstrained material as reference point, in the case of tensile strain, the shear strain component increases the energy of the  $|3/2, \pm 1/2\rangle$  states more than for the  $|3/2, \pm 3/2\rangle$  states. In addition, the energy of both types of states is increased by the hydrostatic strain component. In comparison with unstrained material the bandgap thus becomes smaller and the lowest lying transition has a lh character which provides both a  $\sigma$ - and  $\pi$ -polarization component followed by the hh transition, which contains a  $\sigma$ -component only. In the case of compressive strain an opposite behaviour is observed as depicted in Fig. 2.4: due to the hydrostatic strain the bandgap is increased, and the shear strain component lowers the energy of the lh states more than for the hh states so that the lowest lying transition exhibits a hh character.

Focussing on the relevant case of compressively strained InAs in a GaAs matrix, the analysis of the transition energies given in Eq. (2.10) yields the following results: the amount of hydrostatic strain energy is distributed according to the partition rule<sup>16, 17</sup> for the deformation potential A, i.e  $A = a_c + a_v$  and  $a_c = 2/3 A$ , so that the conduction bandedge is lifted by  $2/3 \delta E_{sh}$  whereas the top of the valence band is lowered by  $1/3 \delta E_{sh}$ . Subsequently the bandgap of the compressively strained material as observed in optical experiments is given by

$$E_g = E_g^0 + \delta E_{hy} + \delta E_{sh} . \tag{2.11}$$

For the later treatment of quantization effects in ultrathin InAs layers it is useful to incorporate the fact that already strain alone lifts the degeneracy of the  $|3/2, \pm 3/2\rangle$  (i.e. hh) states and  $|3/2, \pm 1/2\rangle$  (i.e. lh) states, into the band alignment at the heterointerface. As a motivation for this approach the observation may serve (as e.g. in polarized photocurrent measurements) that in strained semiconductor layers hh and lh valence bands provide different effective bandgaps<sup>18</sup>. Such an adaptation can be done by assigning the top of the hh and lh subbands an individual band offset  $\Delta E_v^{hh}$  and  $\Delta E_v^{lh}$  resulting in a band line-up as depicted in Fig. 2.3. Because in highly strained and therefore ultrathin layers the bandgap might not be directly experimentally accessible due to dominating size quantization effects, the use of different hh and lh band offsets has the advantage to represent the fundamental bandgap of the strained layer  $E_g$  by

$$E_g = E_g^{\text{GaAs}} - \Delta E_c - \Delta E_v^{hh} , \quad (2.12)$$

where  $\Delta E_c$  and  $\Delta E_v^{hh}$  can be determined individually (see Section 2.3). In addition, as can be seen from Fig. 2.3 and Fig. 2.4 the difference between the hh and lh band offset is identical with the strain induced splitting between the hh and lh valence bands due to the shear strain component. One should note that the usually made assumptions, namely that the strain induced splitting between hh and lh bands equals to  $\delta E_{sh}$  and that  $\delta E_{sh}$  is symmetrically accommodated in both valence bands, are only valid for an amount of strain which complies with  $\delta E_{sh} \ll \Delta_0$ . Taking the material parameters for InAs and GaAs as given in Tab. 2.1, the individual contributions of the hydrostatic and shear strain components to the energy shift of the hh and lh valence bands have been calculated for the InGaAs/GaAs system as a function of strain as displayed in Fig. 2.5. With increasing strain, the hydrostatic component lowers both the hh and lh valence band. In contrast, the shear strain component leads to a further reduction in energy of the lh band but to an energy increase for the hh band. Up to 1 % strain these energy shifts are proportional to the amount of strain and equal for the hh and lh band. However, when the strain exceeds 1 %, the shear strain, which is accommodated by the lh valence band, starts to saturate since the shear strain energy  $\delta E_{sh}$  starts to approach the magnitude of the spin-orbit split-off energy, i.e. the lh valence band feels a repulsive

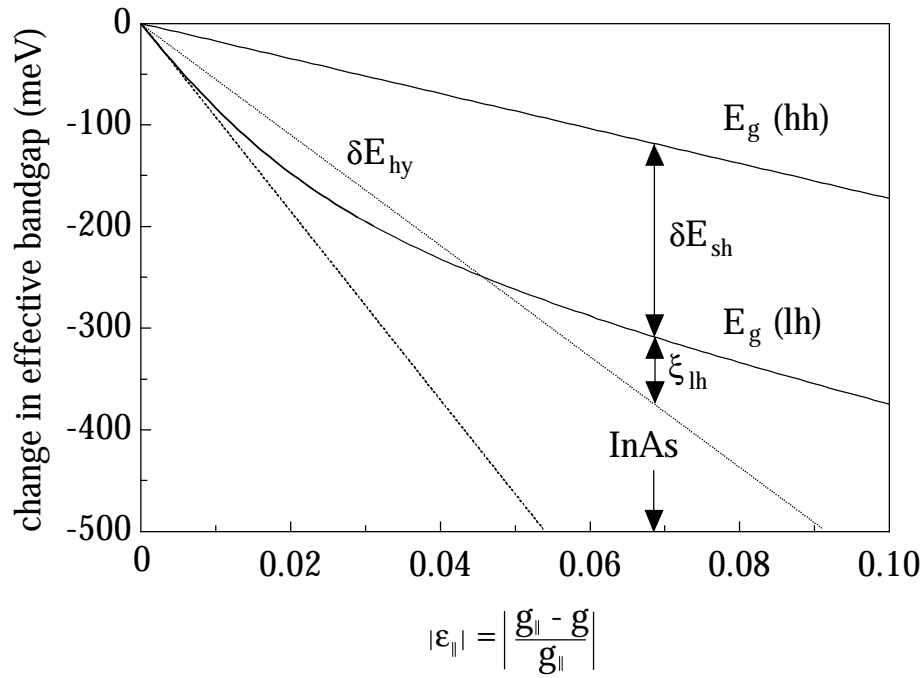


**Fig. 2.5:** Calculation of the change in the effective hh and lh bandgap as a function of compressive strain. The contributions to the energy shift of the hydrostatic (dotted line) and shear strain (dashed line) components are displayed individually. Note, that only for  $\epsilon < 1\%$  the shear strain energy is symmetrically distributed into the hh and lh band.

interaction with the spin-orbit split-off band. For the 6.8 % strained InAs/GaAs system the energy correction of the shear strain energy by the split-off band becomes even that significant, that the energy shift of the lh band due to the shear strain overcompensates the energy shift by the hydrostatic component. As a conclusion, in the InAs/GaAs system already from the viewpoint of bulk elasticity theory and not considering quantum size effects, the split-off band strongly influences the band alignment of the lh valence band. If the split-off band is not taken into account, the lh band offset and consequently the difference between hh and lh band offset would be highly overestimated. In Section 2.2, a second effect of the split-off band on the valence band alignment in the investigated InAs/GaAs structures is discussed. This effect is completely independent on the band structure modifications due to strain and results entirely from the fact, that the band alignment in the InAs/GaAs system can only be studied in very narrow InAs layers.

## 2.2 Quantum Size Effects in Ultrathin InAs Layers

Within the concept of band offsets, the InAs/GaAs system provides a unique situation. As mentioned above, band offsets are defined for the interface of two semi-infinitely extended layers of material. For lattice matched semiconductors this situation can be realized by means of very wide ‘quantum well’ structures, where quantum size effects are negligible. In the InAs/GaAs system, however, the situation is different. Due to the small critical layer thickness, the growth remains pseudomorphic only for a thickness of 2 - 3 monolayers. Beyond the critical layer thickness dislocations are incorporated, which may alter the band alignment at the heterointerface<sup>12</sup>, or the formation of self-assembled quantum-dots starts to dominate the growth process<sup>19</sup>. As a consequence, ultrathin InAs layers in a GaAs matrix seem to represent the only possibility to access the band offsets in the InAs/GaAs material system at all. Because the required InAs layer thickness is orders of magnitude smaller than the electron de Broglie wavelength in semiconductors, quantum size effects dominate the electronic structure in ultrathin InAs layers as observed e.g. in spectroscopic experiments. In order to get insight into the band alignment of the InAs/GaAs system, an appropriate description for size quantization effects is thus required, but which is also based on the concept of band offsets.

Due to the difference in electron affinity and bandgap of approximately 1 eV, the insertion of an InAs monolayer in a GaAs matrix produces a strong confining potential in the conduction and valence band on the length scale of the lattice constant, which introduces bound electron, hh and lh states in the GaAs bandgap<sup>20</sup>. Here, the lifting of the fourfold degeneracy of the valence band into hh and lh states is the consequence of the energy quantization, where the strain-induced splitting between hh and lh bands discussed above still needs to be superimposed. The confined electron, hh and lh states in turn give rise to the formation of hh and lh excitons (for a detailed discussion of excitons in ultrathin InAs layers see Chapter 3).

In previous work on ultrathin InAs layers<sup>21-24</sup>, the electronic structure has been described by a square well model. Even for monolayer and submonolayer coverages the quantum well width was identified as the average InAs layer thickness, and the depth of the confining potential for electrons and holes as the conduction and valence band

offsets, which were consistently used in the sense of bulk parameters<sup>25-27</sup>. In the square well model strain was considered either explicitly in an eight band  $k \cdot p$  type effective mass theory<sup>22, 27</sup> or implicitly by strain modified values for the band offsets and different band offsets for the hh and lh bands<sup>21, 24</sup>. Although the application of the quantum well model on ultrathin InAs layers provided reasonable quantitative agreement with the experiments, it is questionable whether the square well model is the physically correct approach. The dominant criterion for the validity of the square well model<sup>28, 29</sup> is that the envelope function is slowly varying on the scale of the lattice period. As a consequence, part of the envelope function is still localized inside the well, so that different effective masses in the direction of quantization have to be attributed to well and barrier. When increasing the well width, the square well model provides more than a single bound state. However, as illustrated in Fig. 2.6, these assumptions strongly contradict the situation in ultrathin InAs layers. The InAs layer modifies the atomic potential of the surrounding matrix on the length scale of the lattice constant, so that even the derivative of a particle-in-a-box envelope function has to change its sign within one lattice period, i.e. as rapid as the Bloch functions of the crystal. Apparently, this contradicts the major assumption of the square well model, and it suggests that an envelope function can only be constructed outside the InAs layer, which an alternative model for the description of the electronic structure in ultrathin InAs layers should imply. As a consequence, the confined conduction and valence band states of the InAs layer possess the effective masses of the GaAs barrier. In previous work applying the square well model on the electronic structure of ultrathin InAs layers, this fact was considered in order to achieve reasonable agreement between theory and experiment by artificially attributing the GaAs masses of the barrier to the InAs well. However, it represents a further violation of the assumptions of the square well model.

Generally, the insertion of an InAs monolayer into a GaAs matrix corresponds to the isoelectronic substitution of Ga atoms by In atoms, i.e. In and Ga have the same chemical properties but differ in their atomic level position. Since no additional charge is introduced by the InAs plane, it induces a confining potential on the length scale of the lattice constant. It should be noted that this situation of isoelectronic  $\delta$ -doping<sup>30-33</sup> is considerably different from the case of conventional  $\delta$ -doping<sup>34, 35</sup>. There, from the structural viewpoint indeed only monolayers of Si or Be are inserted in a bulk matrix.

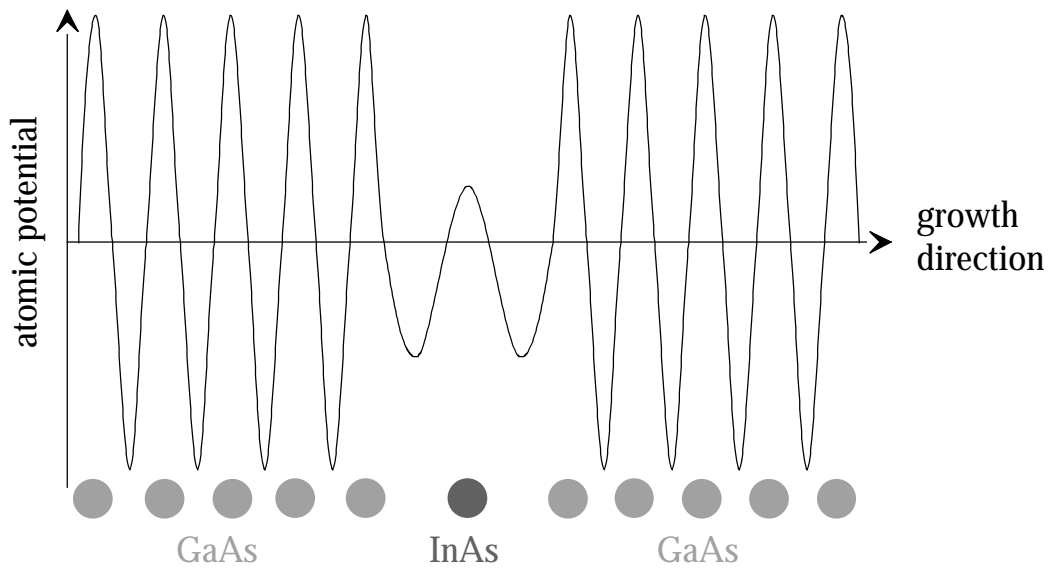


**Fig. 2.6:** Schematic picture for the alteration of the atomic potential by inserting an InAs monolayer in a GaAs matrix.

However, since those atoms act as a n- or p-dopant in GaAs, they create a Coulomb potential which extends over several tens of monolayers and which in turn provides more than single electron, hh and lh confined states.

Recently, Wilke et al.<sup>36</sup> described the situation of isoelectronic  $\delta$ -doping within the tight-binding scheme by using the Koster-Slater approach. One of the main conclusions of their work is, that as a consequence of the one dimensional character of the GaAs conduction band near the  $\Gamma$ -point the electronic structure of ultrathin InAs layer in GaAs can still be treated in an effective mass approach. They found that even for submonolayer coverages at least one In related defect level with a hh character exists, but also that this number is not exceeded for coverages larger than the critical layer thickness. However, a drawback of this model is that strain is only considered in the shift of the conduction band due to the hydrostatic component, but not the shift and splitting in the valence band due to the shear strain. Therefore, it does not provide information about the existence and degree of confinement of a confined lh state and the lh valence band alignment.

In this thesis an alternative model for the description of the electronic structure of ultrathin InAs layers is presented<sup>37</sup>, which still applies the concept of band offsets and which leads to the same qualitative and quantitative results as the model of isoelectronic



impurities. By modelling the confinement potential of the InAs layer with Dirac's  $\delta$ -function, the main properties of the electronic structure are inherently considered: the use of the  $\delta$ -potential implies that the envelope function can only be constructed outside the InAs layer, and it is actually this property which gives the  $\delta$ -potential a preference among the square well model when the potential width approaches the periodicity of the crystal Bloch wavefunctions. As a consequence, the effective masses in the direction of quantization for the confined electron, hh, and lh states are naturally fixed to the values of the GaAs matrix, and finally the  $\delta$ -potential provides for each carrier type only a single bound state regardless of the thickness of the InAs layer or the strength of the confining potential. This is consistent with the predictions of the work of Wilke<sup>36</sup>. The imponderability, that the  $\delta$ -potential is defined with a finite strength without a clear physical meaning in the first place, can be overcome by comparison of the eigenvalues of the  $\delta$ -potential with the eigenvalues of a (shallow) square well providing the same strength in the limiting case of a finite band offset and the well thickness approaching zero.

Within the  $\delta$ -potential model the confinement potential in the conduction and valence band can be expressed by  $V(z) = S_0 \delta(z)$  where  $S_0$  denotes the strength of the confining potential in the conduction and valence band respectively, and  $\delta(z)$  is the Dirac function. The physical meaning of the strength parameter  $S_0$  will be explained below. The calculation of the effective confinement energies of the confined valence band states, i.e. their energy position with respect to the valence bandedge of the surrounding GaAs matrix, is carried out using the two-band Luttinger-Hamiltonian<sup>38</sup> in spherical approximation ( $\gamma_2 = \gamma_3$ )

$$\hat{H} = -\frac{\hbar^2}{2m_0} \left( \gamma_1 + \frac{5}{2}\gamma_2 \right) k^2 + 2\gamma_2 (\hat{J} \cdot \hat{k})^2 - S_{\pm 3/2, \pm 1/2} \delta(z), \quad (2.13)$$

where the  $z$ -direction has been chosen along the growth direction as the axis of quantization. Due to the  $\delta$ -potential approach the Luttinger parameters  $\gamma_1$  and  $\gamma_2$  are fixed to values of the GaAs barrier ( $\gamma_1 = 6.85$ ,  $\gamma_2 = 2.10$ ). Furthermore, the use of the Luttinger-Hamiltonian not only yields the correct effective masses of the bound states in the direction of quantization, which is determined by the confinement potential of the

InAs layer, but it also allows to calculate the in-plane energy dispersion (see below). In order to incorporate the compressive strain of the InAs layer in this model, the strength parameter of the  $\delta$ -potential needs to be assumed to be different for the hh subband ( $S_{\pm 3/2}$ ) and lh subband ( $S_{\pm 1/2}$ ). Then, within the concept of band offsets,  $S_{\pm 3/2}$  and  $S_{\pm 1/2}$  both consider implicitly the same amount of hydrostatic strain as well as the strain induced splitting of the hh and lh subbands due to the uniaxial strain component, which is given by their difference. From Eq. (2.13) the effective confinement energies of the bound hh and lh states are derived as<sup>39</sup>

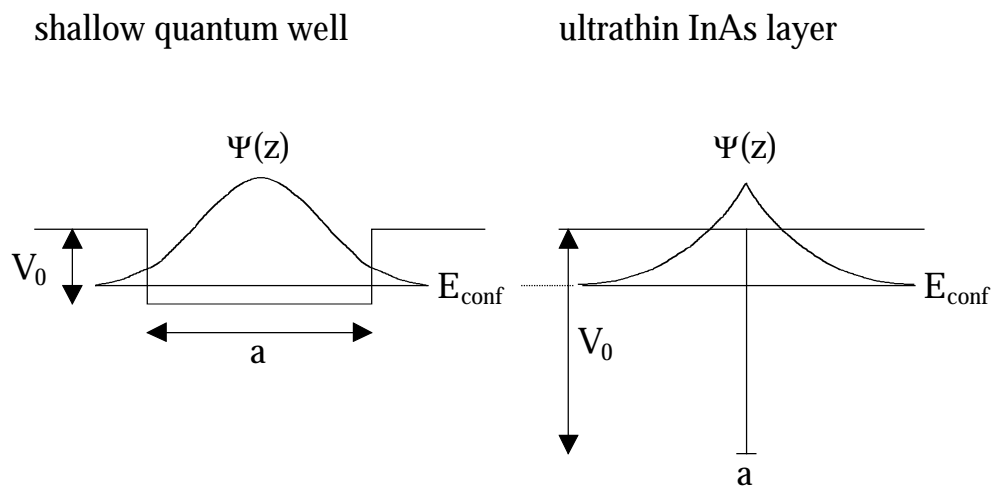
$$E_{\pm 3/2, \pm 1/2} = -\frac{m_0}{2\hbar^2(\gamma_1 \mp 2\gamma_2)} S_{\pm 3/2, \pm 1/2}^2. \quad (2.14)$$

The effective masses of the confined hh and lh states are identified as  $m_{\text{hh}}^* = m_0/(\gamma_1 - 2\gamma_2) = 0.3774 \times m_0$  and  $m_{\text{lh}}^* = m_0/(\gamma_1 + 2\gamma_2) = 0.0905 \times m_0$  for the direction of quantization, which are exactly the values of the GaAs barrier as the  $\delta$ -potential model predicts. For the conduction band, the calculation of the bound electron state yields the same expression as in Eq. (2.14), where one only has to replace  $S_{\text{hh, lh}}$  with the strength of the conduction band confinement potential  $S_e$ , and the effective mass with the electron effective mass for GaAs  $m_e^* = 0.0665 \times m_0$ . As a result, throughout the rest of this thesis we can proceed with the electron, hh, and lh effective masses as known, non-adjustable parameters.

In order to describe the electronic structure of ultrathin InAs layers in GaAs within the concept of band offsets by means of the  $\delta$ -potential approach, one needs to identify the physical meaning of the strength parameter  $S_0$  of the  $\delta$ -potential. A relation between  $S_0$  and the band offsets and the InAs layer thickness can be found from the comparison between the eigenvalues of the  $\delta$ -potential and the eigenvalues of a square well providing the same strength in the limit of a finite potential depth and the well width approaching zero. For a square well, the potential depth  $V_0$  can unambiguously be identified with the band offset  $\Delta E$ , and the well width is identical with the thickness of the quantum well layer, in the following denoted as  $a$ . For the limiting case  $a \rightarrow 0$  the effective confinement energy for the bound state of such a shallow well is given by

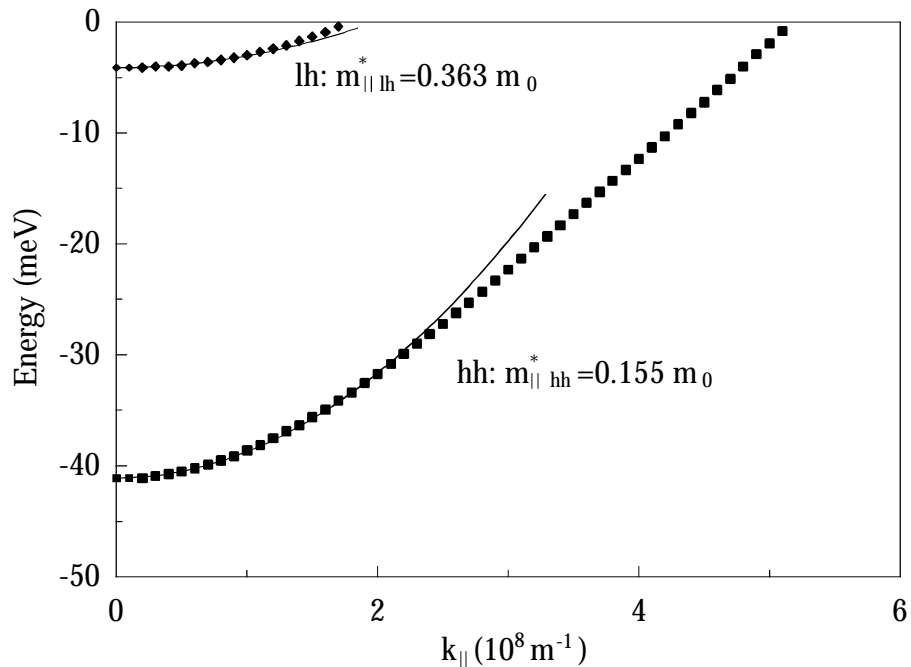
$$E = -\frac{m^*}{2\hbar^2} a^2 V_0^2 = -\frac{m^*}{2\hbar^2} a^2 \Delta E^2. \quad (2.15)$$

From the comparison of Eq. (2.15) with the eigenvalues of the  $\delta$ -potential in Eq. (2.14) it follows that the strength of the  $\delta$ -potential can be expressed by  $S_0 = aV_0 = a\Delta E$ . Thus, within the concept of band offsets, the effective confinement energies of the bound electron, hh, and lh states in ultrathin InAs layers can be correctly described by a  $\delta$ -potential, and they quadratically increase with the product of the corresponding band offset and the InAs layer thickness. Since the expression in Eq. (2.15) is well-known for shallow quantum wells it is worth noting the subtle difference with respect to ultrathin InAs layers: in the case of shallow quantum wells, the well is several tens of monolayers thick guaranteeing the validity of the particle-in-a-box model as explained above, but as depicted in Fig. 2.7 its shallow character results from the small band offset. In this case, the major part of the envelope function extends inside the well and in Eq. (2.15) one has to use the effective masses of the well material. In ultrathin InAs layers, however, as will be demonstrated below, the band offsets for all three types of carriers still amount to several hundreds of meV, and its shallow character results from its monolayer thickness, so that the confined state wavefunctions extend entirely into the barrier as a consequence of the breakdown of a quantum well model in the monolayer limit.

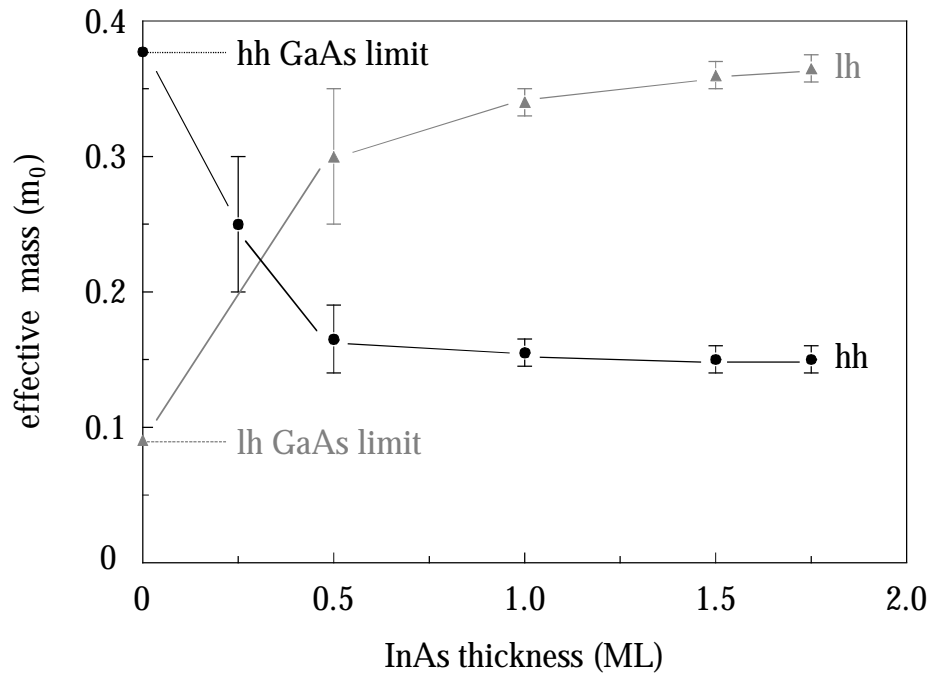


**Fig. 2.7:** Comparison between a shallow well (left) and an ultrathin InAs layer (right) both providing the same effective confinement energy.

For the discussion of excitons (see Chapter 3) and carrier capture (see Chapter 4) in ultrathin InAs layers it is important to know the correct in-plane effective masses. The in-plane energy dispersion relation  $E(k)$  for the subbands associated with the hh and lh confined states can be found numerically from Eq. (2.13). The result for a 1.1 ML thick InAs layer, as used later in the experiments, and its parabolic approximation at the top of the hh and lh valence bands, using the definition of an effective mass as  $m^* = \hbar^2 (\partial^2 E(k)/\partial k^2)^{-1}$ , is presented in Fig. 2.8. In this calculation strain is already considered by using strain modified band offsets for the hh and lh valence bands. As can be seen from the figure, the InAs monolayer provides both a confined hh and confined lh state with effective confinement energies of 42 meV and 4.5 meV, respectively. Up to  $k$ -values of the same order as the reciprocal exciton Bohr-radii one finds an in-plane effective mass of  $m_{||,hh}^* = 0.155 \times m_0$  for the hh subband and  $m_{||,lh}^* = 0.363 \times m_0$  for the lh subband. Ultrathin InAs layers thus exhibit an in-plane effective mass reversal in the hh and lh valence bands. The observed in-plane effective mass reversal is a direct consequence of the quantization introduced by the ultrathin InAs layer.



**Fig. 2.8:** Calculated in-plane dispersion of the hh and lh subbands in a 1.1 ML InAs layer (symbols) and its parabolic approximation by an in-plane effective mass (solid lines). The point of zero energy is taken at the GaAs valence bandedge and according to Eq. (2.14) negative energies refer to confinement in the GaAs bandgap.



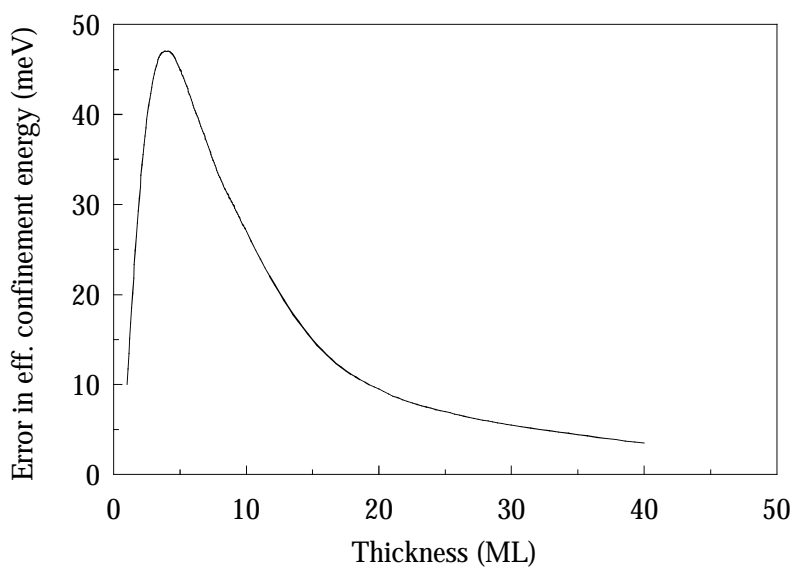
**Fig. 2.9:** Calculated hh and lh in-plane effective masses as a function of InAs thickness.

Figure 2.9 displays the hh and lh in-plane effective masses as a function of InAs layer thickness. At zero InAs thickness any quantization is absent and the effective masses approach the 3D GaAs bulk value. According to the  $\delta$ -potential model the effective mass reversal takes place at a thickness of approximately 0.25 ML. For thickness larger than 1 ML, hh and lh effective mass have saturated at the values given in Fig. 2.8.

The last part of this section is dedicated to the discussion of an additional effect of the spin-orbit split-off band, which influences the electronic structure of quantum wells being only a few monolayers wide quite considerably. This effect emerges even in unstrained quantum well structures and is a direct consequence of the small thickness of the quantum wells. It therefore clearly has to be distinguished from the modification of the shear strain energy accommodated in the valence band due to the spin-orbit split-off band as outlined in section 2.1. Like the ‘strain effect’ of the split-off band, also its ‘small thickness effect’ only modifies the confinement energy and energy dispersion of the lh valence band but does not have an impact on the hh valence band.

As mentioned above, at the Brillouin zone center of zincblende semiconductors the two upper valence bands are the hh and lh bands providing  $\Gamma_8$  symmetry. The third valence band ( $\Gamma_7$  symmetry) is lowered by spin-orbit coupling and corresponds to the

split-off band. When strain is applied, the strain causes an additional coupling between the  $\Gamma_8$  and  $\Gamma_7$  bands leading to the modifications in the lh transition energy as given by Eq. (2.10) as a result of the three-band Hamiltonian in Eq. (2.8). Disregarding strain, a two-band Hamiltonian neglecting the split-off band is a valid approach for lattice-matched quantum wells as long as the hole confinement energies are small in comparison with the spin-orbit splitting. However, for very narrow quantum wells, the hole confinement energies are comparable with the magnitude of the spin-orbit splitting, and then the split-off band has to be taken into account in a spin-degenerated  $3 \times 3$  Hamiltonian. Recently, Dujardin et al.<sup>40</sup> have performed these calculations for lattice matched InGaAs/InP quantum wells as shown in Fig. 2.10. Concerning the valence band offset entering the calculation this material system is similar to the InAs/GaAs system. Their study of the impact of the split-off band on the hh and lh effective confinement energy as a function of well width reveals that the hh confinement energies are not affected by the split-off band at all. On the contrary, the energy position of the confined lh states is affected considerably by the spin-orbit coupling. When the split-off band is taken into account, the lh level is pushed into the well, or in turn, neglecting the split-off band leads to an underestimate of the effective lh confinement energy. The calculations from Dujardin et al. reveal, that the change of the lh confinement energy due to the split-off band can be as large as 45 meV at maximum. On the other hand, for monolayer thickness, they find that the underestimate of the effective lh confinement energy is no larger than 10 meV.



**Fig. 2.10:** Error on the effective lh confinement energy in a lattice matched InGaAs/InP quantum well when spin-orbit coupling is neglected. The figure is taken from Ref. 40.

### 2.3 Coupling of Ultrathin InAs Layers: A New Method for the Determination of Band Offsets

As outlined in the previous section, the  $\delta$ -potential model provides a superior qualitative description of the electronic structure in ultrathin InAs layers, inherently including the correct values for the confined state effective masses in both the direction of quantization and the InAs layer plane. In order to achieve also good quantitative agreement with the experiments, the band offsets, as the only remaining unknown parameters in the  $\delta$ -potential model, need to be known with high precision. In turn, since the band offsets represent the band alignment at the highly strained InAs/GaAs heterointerface governed by bulk elasticity theory, their experimentally determined values allow a verification of the applicability of bulk elasticity theory in the monolayer limit.

The first experimental results on the band alignment at the InAs/GaAs heterointerface are reported in the pioneering work of Kowalczyk et al.<sup>12</sup>. Using X-ray photo-electron spectroscopy (XPS) they found a conduction band offset of  $\Delta E_c = 0.9$  eV and a valence band offset  $\Delta E_v = 0.17$  eV. Although the band offsets were determined with a remarkable accuracy of  $\pm 70$  meV, the applied measuring technique provides some questions about the validity of the reported band offsets due to the following reason: what is actually measured by XPS, is the relative energy position of three different core levels in InAs and GaAs, from which the valence band offset is extracted. Subsequently, the conduction band offset was derived from the fact, that, due to the continuity of the vacuum level at the heterointerface, the sum of the InAs bandgap, valence and conduction band offset has to be equal with the GaAs bandgap. However, in order to measure the three different core levels, samples of different thickness larger than the InAs critical layer thickness were required. Thus, the measured band offsets are affected by the incorporation of misfit dislocations. In addition, for the determination of the conduction band offset the value for the bandgap of unstrained InAs was used. In conclusion, the above band offsets seem to represent the (hypothetical) situation of unstrained InAs on GaAs but not the actual band alignment at the InAs/GaAs heterointerface.

In more recent papers about the determination of the band offsets in InAs/GaAs<sup>20-23</sup>, ultrathin InAs layers were investigated in order to stay below the critical layer thickness. The confined states were described by a quantum well model using strain modified band offsets, nevertheless violating its key assumptions in the monolayer and submonolayer limit. The procedure which subsequently was applied to determine the band offsets, was to measure the optical transition energies in samples with different InAs layer thickness by PL or PLE and to match the quantum well calculations of the transition energies as a function of InAs thickness with the experiments by fitting the band offsets. Despite the concern about the applicability of a particle-in-box-model on ultrathin InAs layers, already for unstrained quantum wells this procedure is questionable to provide reliable band offsets, because the transition energies depend on both the confinement energies of the electrons and hh' s or lh' s, which in this method cannot be separated. In the case of highly strained layers the situation becomes even more troublesome: due to the strain induced splitting of the hh and lh bands, one needs to independently determine three band offsets from only two optical transitions. This problem is reflected by the large spreading in the band offset values reported earlier although the same model and the same (incorrect) effective masses were used<sup>25-27, 41</sup>. In ultrathin InAs layers an additional complication arises since the transitions observed in PL or PLE are excitonic ones and the exciton binding energies were found to strongly depend on the InAs layer thickness<sup>24, 42</sup> (see Chapter 3). Thus, in the determination of the band offsets with the above procedure one had either to correct the measured transition energies by the exciton binding energies individually determined for each InAs thickness, or the calculations had to incorporate explicitly a model for the InAs layer width dependence of the exciton binding energies.

In this thesis an alternative spectroscopic method for the determination of the band offsets in ultrathin InAs layers has been developed, which inherently eliminates the complications as mentioned above. By employing the coupling between *two* ultrathin InAs layers of identical thickness embedded in a GaAs matrix and exploiting the large difference in electron and heavy hole effective mass of the confined states, the conduction, hh, and lh valence band offsets can be determined independently<sup>37, 43</sup>.

It is well-known, that in the case of two coupled quantum wells the confined two-fold degenerated electron, hh, and lh states of a single quantum well can split into a pair of



symmetric and antisymmetric states<sup>44-47</sup>. The magnitude of the splitting for each carrier type is determined by its effective mass, the corresponding band offset and by the well and barrier thickness. Due to its dependence on the effective mass, at a given well and barrier thickness the amount of splitting is an individual parameter for each carrier type. In turn, at a particular well and barrier width a situation can be created where only the carrier type with the smallest effective mass exhibits the coupling induced splitting into symmetric and antisymmetric states. With the effective mass and the sample parameters known, the splitting directly yields the corresponding band offset. If subsequently at a constant well thickness the barrier width is reduced, also the coupling of states with a larger effective mass is activated and the corresponding band offset can successively be determined. Consequently, this new method for band offset determination is explicitly sensitive to the band offset ratio.

Using the above method, the InAs/GaAs band offsets have been determined in a set of samples, where at a constant InAs layer thickness of 1.1 ML the GaAs barrier width was varied from 4 to 32 ML. The InAs layer and GaAs barrier thickness were accurately measured by high resolution X-ray diffraction. Subsequently, for all samples the splitting between the symmetric and antisymmetric states was measured using PLE. All transitions observed in PLE were identified with respect to their hh and lh character by cleaved side PLE. According to the model calculations of the confined states in coupled InAs layers (see Section 2.3.1), in the sample with a 32 ML barrier the splitting of the hh state is negligible due to its more than five times larger effective mass in comparison with the confined electron state. Consequently, the observed splitting of the hh exciton transition originates entirely from the splitting of the confined electron states, from which the conduction band offset is directly being deduced.

Once the conduction band offset is known, the lh valence band offset is derived from the coupling induced splitting of the lh exciton transition simultaneously emerging in the 32 ML barrier sample, since the observed splitting is simply given by the sum of the splitting of the confined electron and lh states. Finally, with the previously deduced conduction band offset the hh band offset is determined from the splitting of the hh exciton transition and accompanying strong red-shift of the symmetric hh exciton transition in the 16, 8 and 4 ML barrier samples. In these samples, the confined hh state

also splits off into symmetric and antisymmetric states and starts to contribute considerably to the observed red-shift and splitting.

An additional major advantage of this method for band offset determination is that uncertainties due to the excitonic character of the observed transitions are inherently eliminated. The dependence of the exciton binding energies on the InAs thickness is excluded since in all samples the InAs layer was fixed to a thickness of 1.1 ML. Moreover, the band offsets are extracted from the observed splitting, i.e. from the energy *difference* of the observed transitions rather than from their *absolute* spectral position, so that the exciton binding energies cancel out. That the underlying assumption, namely that the change of the exciton binding energy due to coupling is negligible, is met, will be shown in Chapter 3.

### 2.3.1 Confined States in Coupled Ultrathin InAs Layers

Applying the results from Section 2.2, the effective mass Hamiltonian for samples containing two identical InAs layers separated by a GaAs barrier of thickness  $L$  reads

$$\hat{H} = -\frac{\hbar^2}{2m^*} \frac{\partial^2}{\partial z^2} - aV_0 \delta\left(z - \frac{L}{2}\right) - aV_0 \delta\left(z + \frac{L}{2}\right), \quad (2.16)$$

where  $V_0$  represents the conduction, hh or lh valence band offset. In the limiting case of infinite  $L$  the potential of the coupled InAs layers provides only one single bound state, whose effective confinement energy is the same as for the single InAs layer but which is twofold degenerate. As displayed in Fig. 2.11, when  $L$  becomes finite its degeneracy is lifted and it splits into a symmetric and antisymmetric state. The symmetric state corresponds to the ground state of the confining potential and it has even symmetry, whereas the antisymmetric state corresponds to the first excited state with odd symmetry. By substituting  $\kappa_{\pm} = \sqrt{-2m^*E_{\pm}/\hbar^2}$ , where  $\kappa_{\pm}$  has the meaning of the barrier penetration depth of the wavefunctions of the coupled well problem, the energy eigenvalues  $E_+$  and  $E_-$  for the symmetric and antisymmetric state are given by the two solutions of the characteristic equation

$$\frac{2m^*aV_0}{\hbar^2} = \frac{2\kappa_{\pm}}{1 \pm \exp(-\kappa_{\pm}L)}. \quad (2.17)$$

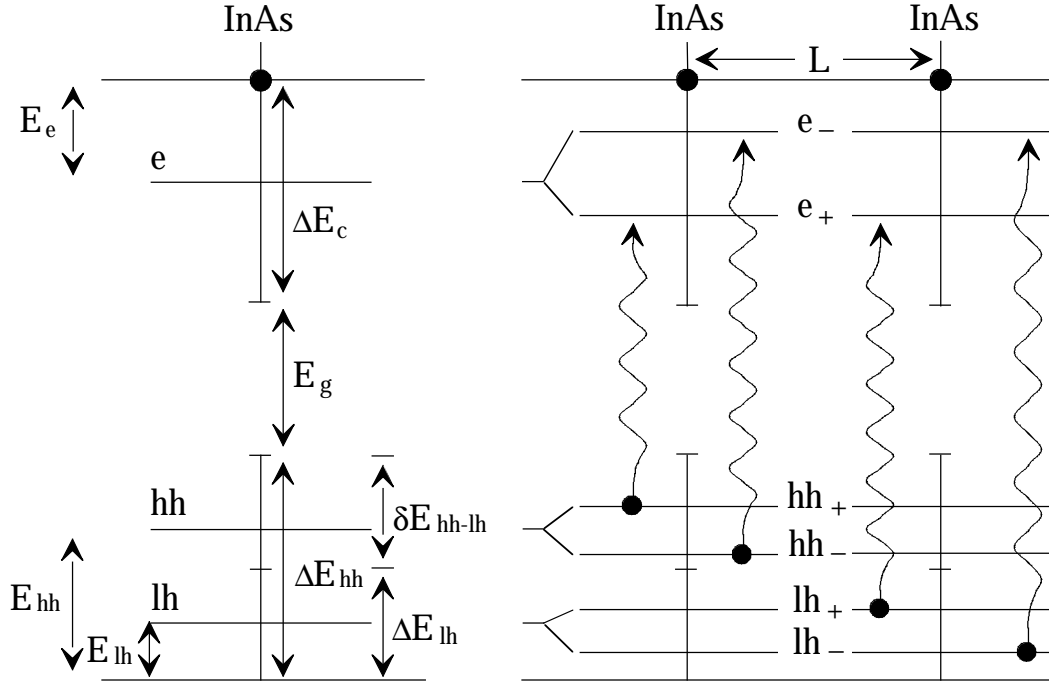


**Fig. 2.11:** Schematic real-space band alignment of a single ultrathin InAs layer of thickness  $a$ , embedded in a GaAs matrix (left part) and of two coupled InAs layers separated by a GaAs barrier (right part) of thickness  $L$ . The confined electron, hh, and lh states of the InAs layer are labelled as  $e$ , hh, and lh. Their effective confinement energies are denoted as  $E_e$ ,  $E_{hh}$ , and  $E_{lh}$ . The strength of the confining potential is determined by the conduction band offset  $\Delta E_c$  and the hh and lh band offset  $\Delta E_{hh}$  and  $\Delta E_{lh}$ , respectively. The strain induced splitting  $\delta E_{hh-lh}$  between the hh and lh subbands is considered by assuming different band offsets for the hh's and lh's. In the presence of coupling, each confined state splits into a symmetric state (labelled as +) and an antisymmetric state (labelled as -). The parity allowed transitions observed in PLE are indicated by the arrows.

In the limit of an infinite barrier width, the eigenvalues of the symmetric and antisymmetric state become equal and approach the value of a single  $\delta$ -potential. For the opposite limiting case of a zero thickness barrier, the confinement energy of the symmetric state equals to  $E_+ = -2m^*a^2V_0^2/\hbar^2$ , which is identical to the effective confinement energy for a single InAs layer of double thickness. Therefore, when

decreasing the barrier width, the symmetric state always remains bound and its effective confinement energy increases. In contrast, the effective confinement energy of the antisymmetric state diminishes with decreasing the barrier width, and at a critical barrier width of  $L_B = \hbar^2/m^*aV_0$  the antisymmetric states become unbound.

In order to illustrate the evolution of the symmetric and antisymmetric states, the effective confinement energy of the electron and hh states as a function of barrier width is displayed in Fig. 2.12. Predominantly due to the difference in their effective masses by more than a factor of five, both carrier types represent for the displayed barrier widths a different coupling regime. Calculating the barrier penetration width of a single  $\delta$ -potential  $\kappa = m^*aV_0/\hbar^2$ , yields a value of  $\kappa \approx 70 \text{ \AA}$  for the electrons corresponding to a 25 ML GaAs barrier, whereas the barrier penetration width of the hh amounts to less than  $20 \text{ \AA}$  (7 ML GaAs barrier). Thus, in Fig. 2.12 the electrons represent the regime of moderate coupling ( $\kappa \approx L$ ) and the heavy holes the situation for weak coupling ( $\kappa \ll L$ ). In the latter case it is characteristic that the splitting between the symmetric and antisymmetric states is very small and symmetrically distributed around the effective confinement energy of a single  $\delta$ -potential. For the electrons, however, the situation is different. The coupling induced shift of the symmetric and antisymmetric states is no longer symmetric with respect to the bound state of a single  $\delta$ -potential. As it can be seen from Fig. 2.12, the effective confinement energy of the antisymmetric state is already considerably altered whereas the one of the symmetric state has hardly changed. For later use it is also important to note, that at a barrier thickness of 32 ML the hh' s do not exhibit a splitting at all, whereas the splitting between the symmetric and antisymmetric electron states already amounts to 13 meV.

In PL or PLE one only observes optical transitions between states of equal parity. Thus, in the case of two coupled ultrathin InAs layers only the  $e_+hh_+$ ,  $e_-hh_-$ ,  $e_+lh_+$  and  $e_-lh_-$  transitions will emerge (see Fig. 2.11). Considering, that the observed transitions are excitonic ones, their transition energies are given by

$$\begin{aligned} E_{e_{\pm}hh_{\pm}} &= E_g^{\text{GaAs}} + E_{e_{\pm}} + E_{hh_{\pm}} - E_{hh}^x \\ E_{e_{\pm}lh_{\pm}} &= E_g^{\text{GaAs}} + E_{e_{\pm}} + E_{lh_{\pm}} - E_{lh}^x, \end{aligned} \quad (2.18)$$

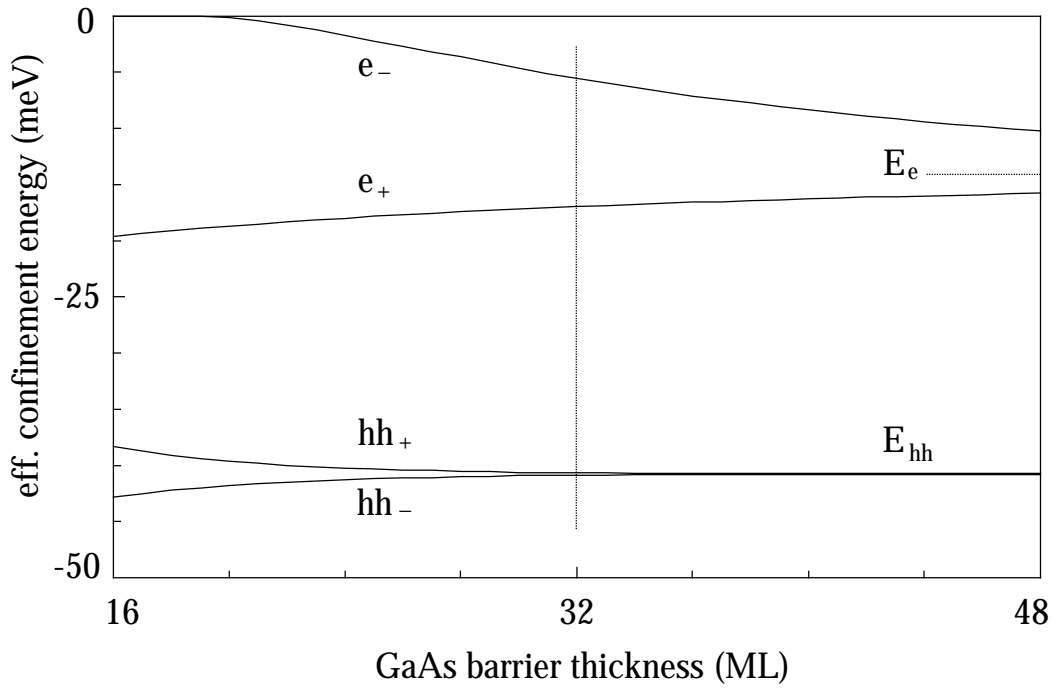


**Fig. 2.12:** Calculated electron and hh effective confinement energy for two coupled 1.1 ML thick InAs layers as a function of GaAs barrier width using  $\Delta E_c = 535$  meV and  $\Delta E_{hh} = 385$  meV. The point of zero energy is taken at the GaAs conduction and valence bandedges, respectively. Negative energies refer to confined states in the GaAs bandgap. Thickness are given in units of the unstrained lattice constants of GaAs (1 ML = 2.8266 Å) and InAs (1 ML = 3.0292 Å). At  $L = 32$  ML the splitting of the hh states is negligible, whereas the splitting of the electron states amounts to 13 meV. At approximately 20 ML the critical barrier thickness for the electrons is reached, where the  $e_-$  state becomes unbound.

where  $E_{hh}^x$  and  $E_{lh}^x$  denote the hh and lh exciton binding energies, and  $E_{hh\pm}$ ,  $E_{lh\pm}$ ,  $E_{e\pm}$  are the effective hh, lh, and electron confinement energies obtained from Eq. (2.15). From Eq. (2.18) it is evident that the observed splitting between the two hh and lh related transitions entirely depends on the band offsets  $\Delta E_c$ ,  $\Delta E_{hh}$  and  $\Delta E_{lh}$  once the effective masses, the thickness of the InAs layers and the GaAs barrier width are known. In turn, this provides the possibility to determine the values of the band offsets from the experimentally observed splitting. Moreover, extracting the band offsets from the coupling induced splitting is insensitive to excitonic effects. In earlier publications the band offsets were extracted from the dependence of the *absolute spectral position* of the hh and lh exciton transition on the thickness of a single InAs layer. Since e.g. the hh exciton binding energy was found to increase from 4 meV at zero InAs thickness to 12 meV at an InAs thickness of 1.6 ML, this method requires a sound knowledge of the

dependence of the hh and lh exciton binding energies on the InAs layer thickness, which was not considered earlier. In contrast, in this thesis the band offsets are deduced from the splitting of the excitonic  $e_{\pm}-hh_{\pm}$  and  $e_{\pm}-lh_{\pm}$  transitions, i.e. from their *difference in spectral position*, in a set of samples where the InAs thickness is kept constant. As it is evident from Eq. (2.18), in this approach the exciton binding energies cancel out. The only remaining uncertainty is a possible variation of the exciton binding energies as a function of barrier thickness. However, from calculations of the exciton binding energies as a function of barrier width for the regime of weak and moderate coupling (see Chapter 3), it is found that the changes in the exciton binding energies are smaller than 3 meV, which is small enough not to add significant uncertainty to the band offset values.

As can be seen from Eq. (2.18), the observed splitting between the symmetric and antisymmetric transitions depends on both the splitting in the conduction band and the splitting in the hh and lh valence band, respectively. In order to separate these contributions, and thus to have direct access to the band offset ratio, we developed a successive evaluation scheme for the band offset determination, which exploits the fact that the electron and hh effective masses differ by more than a factor of five. As discussed above, a barrier thickness of 32 ML corresponds to approximately the barrier penetration width of the electrons, whereas it is still more than four times larger than the barrier penetration width of the hh's. As a consequence, at 32 ML barrier width the  $hh_{+}-hh_{-}$  splitting is negligible as compared to the  $e_{+}-e_{-}$  splitting. Thus, in this situation the splitting between the  $e_{+}-hh_{+}$  and  $e_{-}-hh_{-}$  transitions observed in PLE is entirely due to the splitting in the conduction band, allowing a direct determination of the conduction band offset  $\Delta E_c$ . Once  $\Delta E_c$  is known, the lh valence band offset can be derived at the same barrier width from the splitting between the  $e_{+}-lh_{+}$  and  $e_{-}-lh_{-}$  transition, which is the sum of the splitting of the lh states and the previously determined splitting in the conduction band. Finally, the hh band offset can be determined from a sample where the barrier thickness becomes comparable to the hh barrier penetration width. Knowing the conduction band offset and thus from Eq. (2.17) the splitting in the conduction band at any barrier width, the additional red-shift of the  $e_{+}-hh_{+}$  transition or the enhanced splitting between the  $e_{+}-hh_{+}$  and  $e_{-}-hh_{-}$  transition directly yields  $\Delta E_{hh}$ .

### 2.3.2 Sample Growth and Structural Characterization

The samples designed for the band offset determination by means of coupling induced splitting contain two ultrathin InAs layers separated by a GaAs barrier with a nominal thickness of 4, 8, 16 or 32 ML. Within this set of samples an additional reference sample was grown comprising a single InAs layer only. The samples were synthesized by conventional molecular beam epitaxy (MBE) on exactly oriented CrO doped semi-insulating (001) GaAs substrate. Using CrO doped substrates suppresses any substrate related PL. After oxide desorption, a 0.4  $\mu\text{m}$  GaAs buffer layer was grown at a substrate temperature of 630  $^{\circ}\text{C}$ . Then the substrate temperature was lowered to 600  $^{\circ}\text{C}$  and the As-cracker temperature was set to 400  $^{\circ}\text{C}$  to grow with  $\text{As}_4$ . At this substrate temperature a 400  $\text{\AA}$  GaAs layer was grown first, followed by an additional 350  $\text{\AA}$  thick GaAs layer, within which the substrate temperature was lowered to 450  $^{\circ}\text{C}$ . The latter temperature ramp was found to be optimum to achieve a high optical quality GaAs matrix. Subsequently, the two ultrathin InAs layers and the GaAs barrier were deposited at 450  $^{\circ}\text{C}$ . Before and after the deposition of each InAs layer a 1 s growth interrupt was introduced to allow surface reconstruction and to suppress the formation of InAs clusters<sup>48-50</sup>. After the growth of the second InAs layer, 5 ML of GaAs were deposited. Subsequently, while growing a 565  $\text{\AA}$  GaAs cladding layer, the substrate temperature was increased to 630  $^{\circ}\text{C}$ . Finally, a 300  $\text{\AA}$   $\text{Al}_{0.33}\text{Ga}_{0.67}\text{As}$  window was grown to suppress surface electric fields, and the structures were capped by a 170  $\text{\AA}$  GaAs layer. To avoid any possible source of external strain the substrates were mounted In-free on the substrate holder, and for the X-ray diffraction and optical measurements the samples were held by paper frames on the sample holder.

As mentioned previously, the band offsets can only be derived from the coupling induced shift and splitting if the thickness of the InAs layers and the GaAs barrier are precisely known. Consequently, on each sample high-resolution double-crystal X-ray diffraction measurements were performed, which allow to determine the thickness of ultrathin InAs layers with an accuracy of better than 0.1 monolayer<sup>51</sup>. The X-ray experiments were performed in the symmetric (400) geometry utilizing the  $\text{CuK}\alpha_1$  line. The InAs layer and GaAs barrier thickness were found from comparison of the measured rocking curves and their simulations based on the dynamical theory.

Figure 2.13 displays the measured rocking curve and the simulations for the single InAs layer (a), the samples with the 16 ML (b), and 32 ML GaAs barrier (c), respectively. As indicated in the insert of Fig. 2.13(a), in the case of a single InAs layer the incident X-ray field is diffracted simultaneously from the underlying GaAs layer and from the cap layer comprising the upper GaAs layer and the AlGaAs window at identical Bragg angles. The interference between both contributions is observed by the Pendellösung oscillations, whose modulation amplitude and angular position is determined by the thickness of the InAs layer and the incorporated amount of strain. The feature in the rocking curve of the single InAs layer [Fig. 2.13(a)], which is most sensitive to the InAs layer thickness, is the position and shape of the Pendellösung fringe close to the substrate peak denoted as “ $\delta$ -well”. From the simulations one finds an average thickness of the InAs layer of  $1.10 \pm 0.05$  ML. The best fit was obtained with a zero in-plane strain and 6.8 % strain in (100) direction. This provides evidence, that the lattice mismatch is fully accommodated by an elastic distortion of the InAs unit cell, i.e. the InAs layer is grown pseudomorphically<sup>52</sup>.

The significant feature in the rocking curves of the coupled InAs layers [Fig. 2.13(b), (c)] is the appearance of a destructive interference of the Pendellösung oscillations. As depicted in the insert of Fig. 2.13(b), the X-ray field from the underlying GaAs layer can interfere with the X-ray field from the upper GaAs layer and AlGaAs window, as well as with the X-ray field, which is diffracted from the layer stack comprising the upper GaAs layer and the AlGaAs window plus the two InAs layers and the GaAs barrier. Both interferences lead to Pendellösung oscillations with a slightly different periodicity. The superposition of these Pendellösung oscillations gives rise to the observed beating. The simulations show, that a  $\pm 1$  ML change of the barrier thickness shifts the angular position of the beating in the Pendellösung by approximately  $\pm 50$  arcsec, whereas the feature close to the substrate peak (denoted as “ $\delta$ -well”) remains unchanged. In contrast, a small change in the InAs layer thickness, i.e. in the amount of totally deposited InAs, hardly changes the position of the beating in the Pendellösung, but considerably alters the feature near the substrate peak. Consequently, the simulations of the measured rocking curves for the coupled well samples allow to



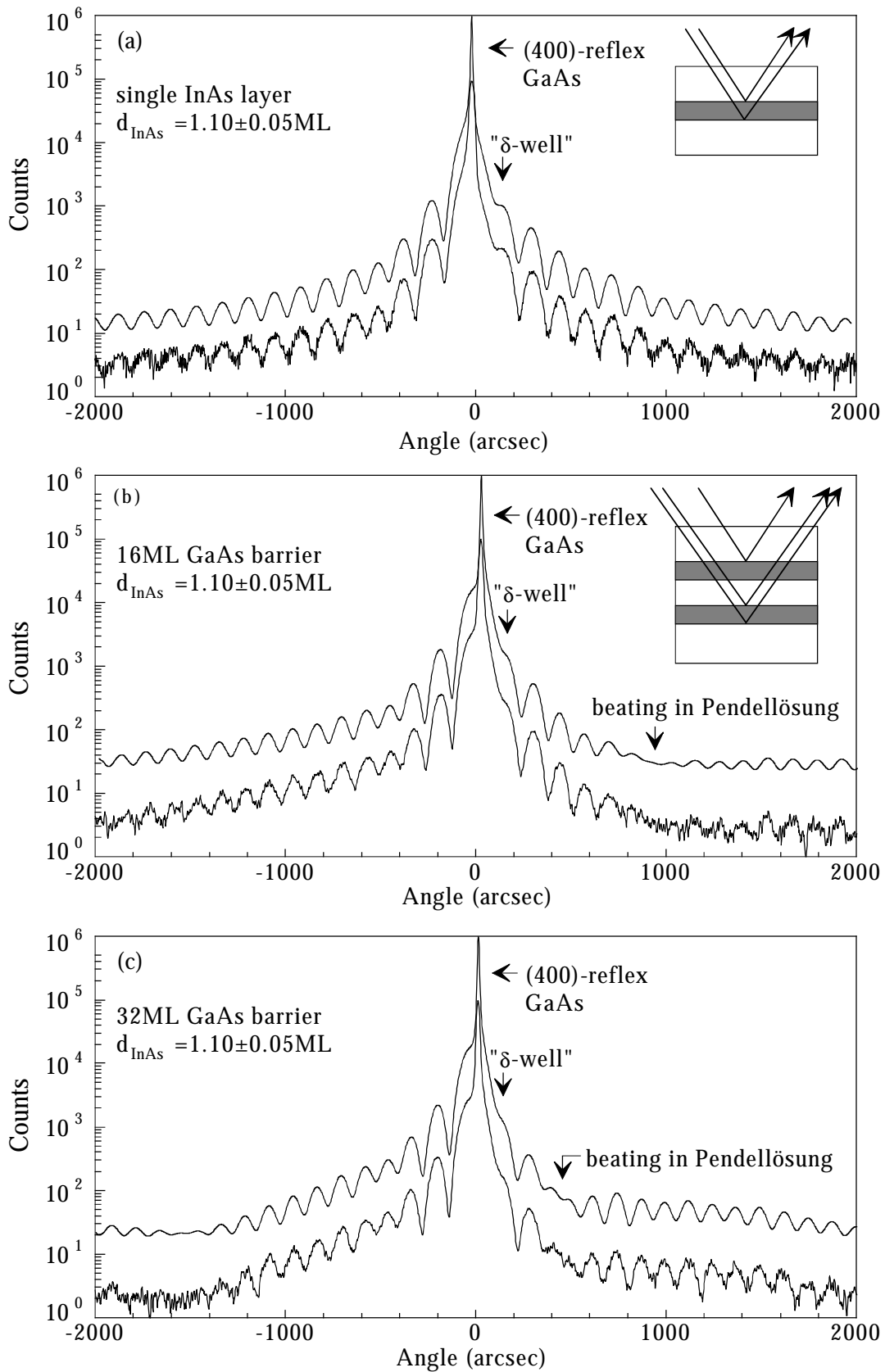


**Fig. 2.13:** Measured (lower curves) and simulated (upper curves) rocking curves of the reference sample (a) containing a single InAs layer and two samples with 16 ML (b) and 32 ML (c) GaAs barrier.

determine the thickness of the GaAs barrier and the InAs layers virtually independently. Consistently for the whole set of samples one finds an average thickness of the InAs layer of  $1.10 \pm 0.05$  ML. The barrier thicknesses were found to be 4, 8, 16 and 32 ML, respectively, with an uncertainty of  $\pm 0.5$  ML.

With respect to the above description of the electronic structure of the InAs layer by a  $\delta$ -potential and the question, over how many atomic layers the deposited InAs is distributed, the simulations of the measured rocking curves reveal the following results. The InAs layer thickness obtained above assumes a pure InAs layer. However, a similar quality of the simulation for the single InAs layer sample can be obtained when the InAs layer is decomposed into 1 ML InAs and 1 ML  $\text{In}_{0.05}\text{Ga}_{0.095}\text{As}$  on either side. This result is not too surprising since the angular position of the Pendellösung oscillations and the shape of the “ $\delta$ -well” feature depend on the product of the total amount of deposited InAs and the totally incorporated amount of strain<sup>43, 53</sup>. Thus, as long as the total InAs content in the simulations of the single InAs layer sample is kept constant within the  $\pm 5\%$  variation of the found layer thickness, the rocking curves do not provide accurate information about the distribution of the InAs over one or more atomic layers.

Nevertheless, an estimate about how much InAs is confined in a single atomic layer can be obtained from the rocking curves of the samples with 16 and 8 ML barrier thickness. In the simulations of these samples, the InAs layers was also decomposed into 2 or 3 adjacent  $\text{In}_x\text{Ga}_{1-x}\text{As}$  monolayers with different In contents by keeping the total amount of InAs constant. When the In contents in the InGaAs layers was brought towards an equidistribution, a shift of the beating in the Pendellösung oscillations by more than 200 arcsec towards the substrate reflection is observed. In order to match the simulations with the measured rocking curves, this shift could only be compensated by reducing the barrier thickness by 4 ML. However, as will be discussed in the following section, especially for small barriers (8, 16 ML) such a strong reduction of the barrier thickness would lead to a red-shift of the photoluminescence by more than 20 meV, which would be in contradiction to the optical experiments. In turn, if one allows the barrier thickness to be determined as 1 ML too wide (corresponding to less than 5 meV red-shift of the PL), one finds in agreement with the work of Woicik et al.<sup>52</sup> that still more than 80 % of the deposited InAs is confined in one atomic plane. Additional information, namely whether the residual InAs is symmetrically or asymmetrically

distributed around the layer containing more than 80 % of the deposited InAs, could not be found. Finally, it should be mentioned that the rocking curves do not show any indication for strain relaxation, although the total amount of InAs in our structures ( $2.2 \pm 0.1$  ML) is very close to the critical layer thickness of a single InAs layer.

### 2.3.3 Successive Band Offset Determination from the PL, PLE and Cleaved Side PLE Spectra of Coupled Ultrathin InAs Layers

With the effective electron, hh, and lh masses and the InAs layer and GaAs barrier thickness accurately known, in this section it is demonstrated how the conduction band offset, the hh and lh valence band offset, as well as the band offset ratio in ultrathin InAs layers in a GaAs matrix can be determined independently from the PL, PLE and cleaved side PLE spectra of the coupled InAs layer samples and the single InAs layer reference sample. The PL and PLE measurements were carried out in backscattering geometry using a tuneable Ti:Sapphire laser with a linewidth of less than 0.25 meV and a  $2 \times 0.85$  m double monochromator with a spectral resolution of better than 0.2 meV. In order to identify the observed transitions with respect to their hh and lh character<sup>23, 54, 55</sup>, cleaved side PLE measurements were performed. For the cleaved side PLE experiments, the freshly cleaved side of the samples was excited with either s- (perpendicular to the growth direction) or p- (parallel to the growth direction) polarized light and the PL emission ( $I_s$ ,  $I_p$ ) was detected in the direction perpendicular to the sample surface. By defining the degree of polarization (DOP) as  $(I_s - I_p)/(I_s + I_p)$ , positive values indicate that the valence band states involved in the transitions are hh-like whereas negative values indicate a lh character.

The 4.2 K PL spectra of the single and coupled InAs layer samples are shown in Fig. 2.14. The observed PL originates from the  $e_+hh_+$  exciton transition as the lowest lying transition of the InAs layers. The PL intensity and the peak intensity ratio between the PL from the InAs layers and the GaAs exciton of approximately 100 is almost equal for all samples, indicating a very efficient carrier capture by the InAs layers. It also shows that the carrier capture times as well as the oscillator strength of the exciton

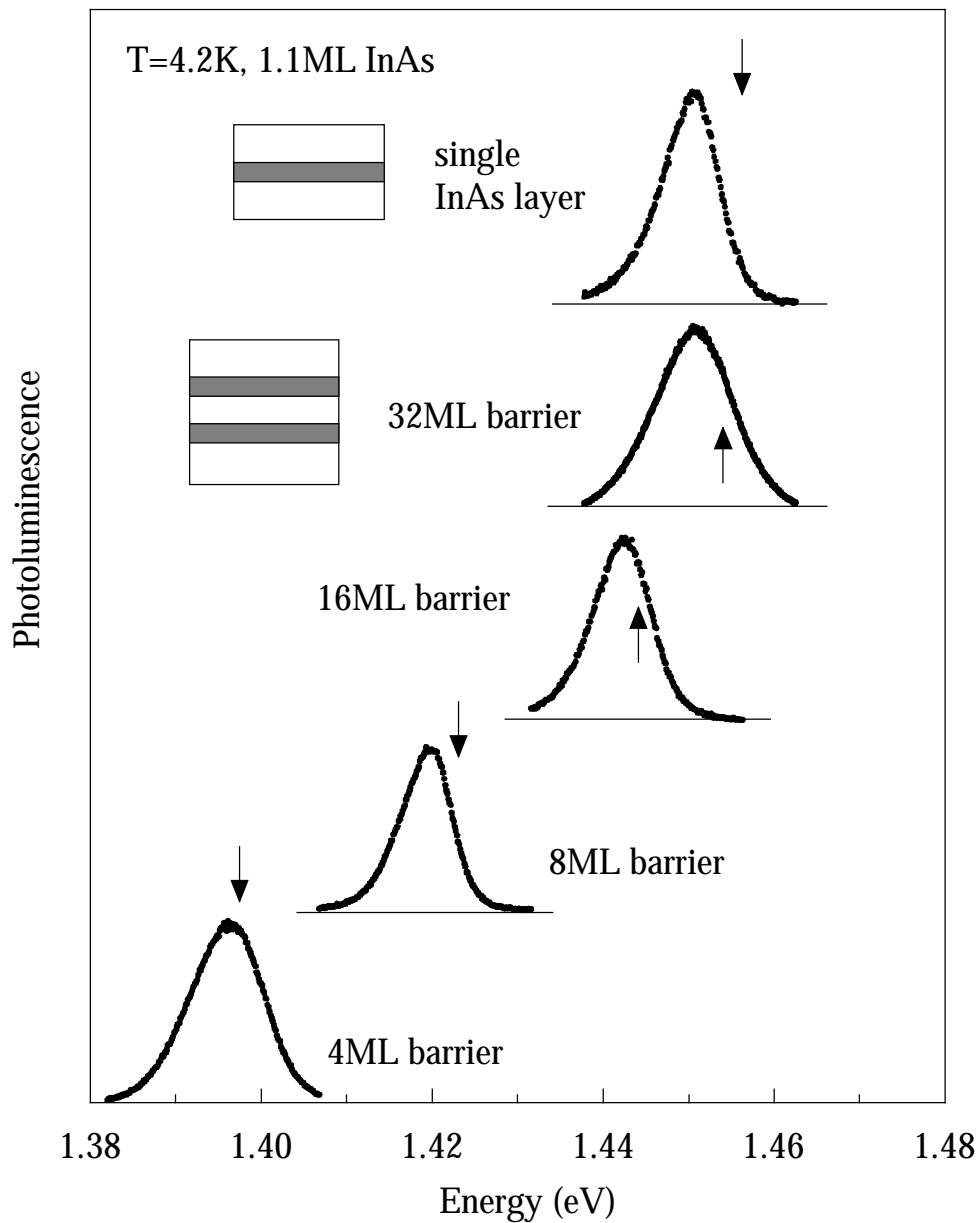


**Fig. 2.14:** 4.2 K photoluminescence spectra of the single and coupled InAs layer samples. Each spectrum was given an arbitrary offset. The arrows indicate the calculated transition energies using the  $\delta$ -potential model, without a correction for the hh exciton binding energy.

ground state and thus its exciton binding energy are hardly altered by the coupling of the InAs layers. The FWHM of the PL emission amounts to 8.5 meV in the single InAs layer and varies non-systematically between 5.9 meV and 8.4 meV for the coupled InAs layers. Thus, consistent with the X-ray analysis, the PL spectra do not exhibit excessive line broadening as an indication for strain relaxation, revealing that a 4 ML GaAs barrier is still thick enough to keep the growth of the second InAs layer pseudomorphic.

When the barrier thickness is reduced from 32 to 4 ML, one observes a red-shift of the PL line by 54 meV. Since the change in exciton binding energy of the lowest lying symmetric  $e_+-hh_+$  transition is smaller than 3 meV over the entire range of barrier widths (see Chapter 3), this red-shift originates predominantly from the increase in the effective confinement energies of the  $e_+$  and  $hh_+$  state due to the coupling. The observed red-shift is in excellent agreement with the model calculations of the effective confinement energies in coupled InAs layers (indicated by the arrows in Fig. 2.14) as well as with the tight-binding calculations of the isoelectronic  $\delta$ -doping model from Wilke et al.<sup>36</sup>, who predicted a red-shift of 50 meV.

With respect to the separation of the conduction and valence band offsets, it is important to note that the energy separation between the PL line of the single InAs layer and 32 ML barrier sample is less than 1 meV. However, this small energy separation in PL does not necessarily imply the absence of coupling. As Fig. 2.12 revealed already, at 32 ML barrier thickness the  $hh$  state is still not split-off so that the effective confinement energy of the  $hh$  state is not altered at all, and the effective confinement energy of the  $e_+$  state is hardly increased, whereas the effective confinement energy of the  $e_-$  state is decreased by almost 10 meV. As it will turn out from the PLE measurements, a 32 ML GaAs barrier leads to considerable coupling for the bound electron states which is almost completely accumulated in a blue-shift of the antisymmetric  $e_-$  state.

The PLE and cleaved side PLE measurements of the samples are shown in Fig. 2.15 and Fig. 2.16, respectively. In the PLE spectrum of the single InAs layer two peaks are visible, which are the  $hh$  exciton transition at 1.456 eV and the  $lh$  exciton transition at 1.493 eV. In particular, the origin of the latter was carefully checked, since it is close to the carbon related donor-to-acceptor transition in GaAs. The cleaved side PLE measurements show a strong p-polarization at this energy revealing a  $lh$  character of the transition at 1.493 eV, whereas Brandt et al.<sup>23</sup> found a  $hh$  character for the carbon related transition. The step-like structure with a peak on top between 1.4985 eV and 1.51 eV results from the two-dimensional density of states of the  $e$ - $lh$  band-to-band transition and the absorption by excited and unbound  $lh$  exciton states.

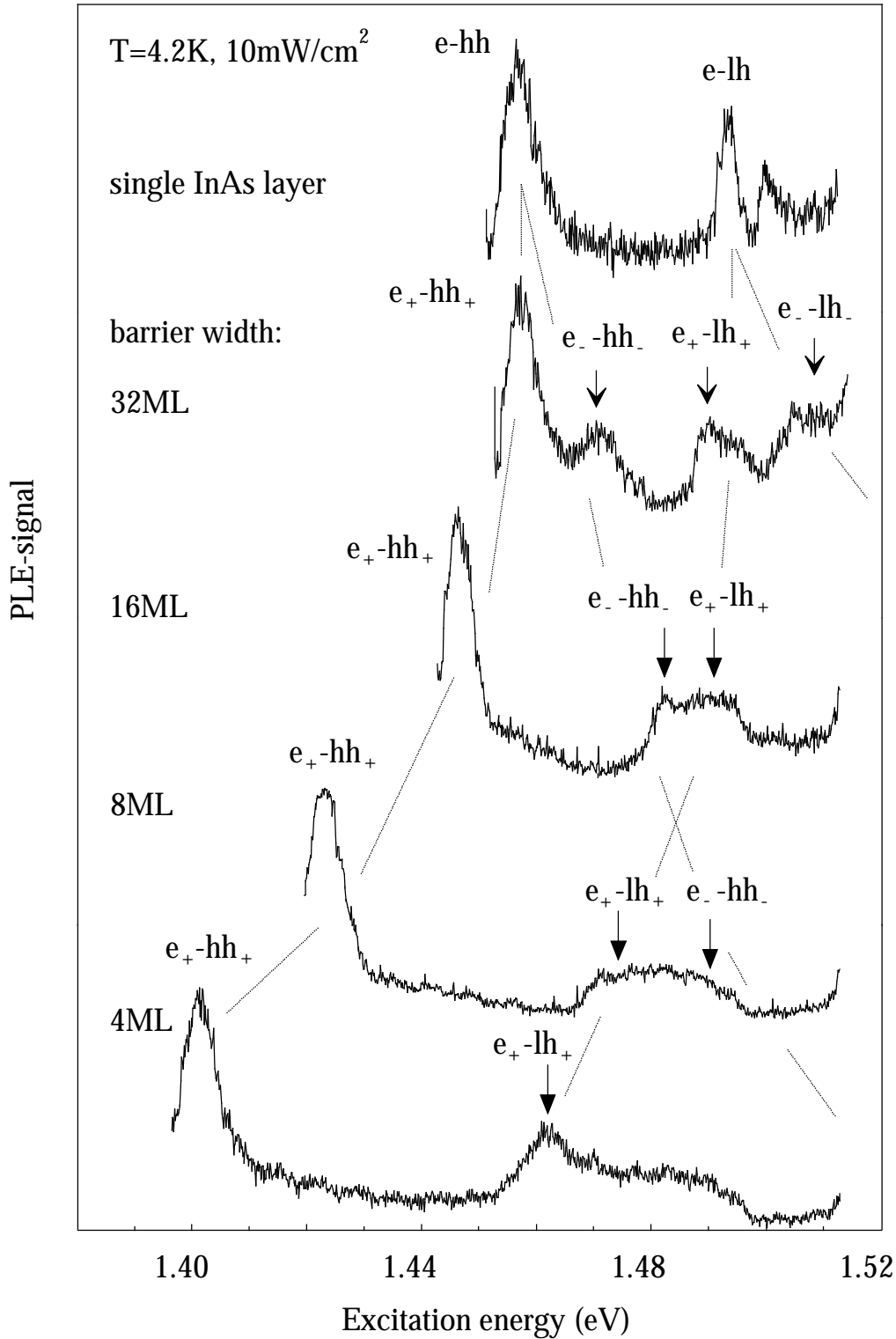


**Fig. 2.15:** PLE spectra of the single and coupled InAs layer samples measured at 4.2 K in near backscattering geometry. The transitions were identified with respect to their hh and lh character by cleaved side PLE. In the PLE spectrum of the single InAs layer the hh and lh exciton transitions (denoted as  $e-hh$  and  $e-lh$ ) are clearly visible. In the 32 ML barrier sample four parity allowed transitions emerge demonstrating the coupling between the InAs layers. Note that in the 32 ML barrier sample the  $e_+-hh_+$  transition emerges at almost the same spectral position as the  $e-hh$  transition in the single InAs layer.

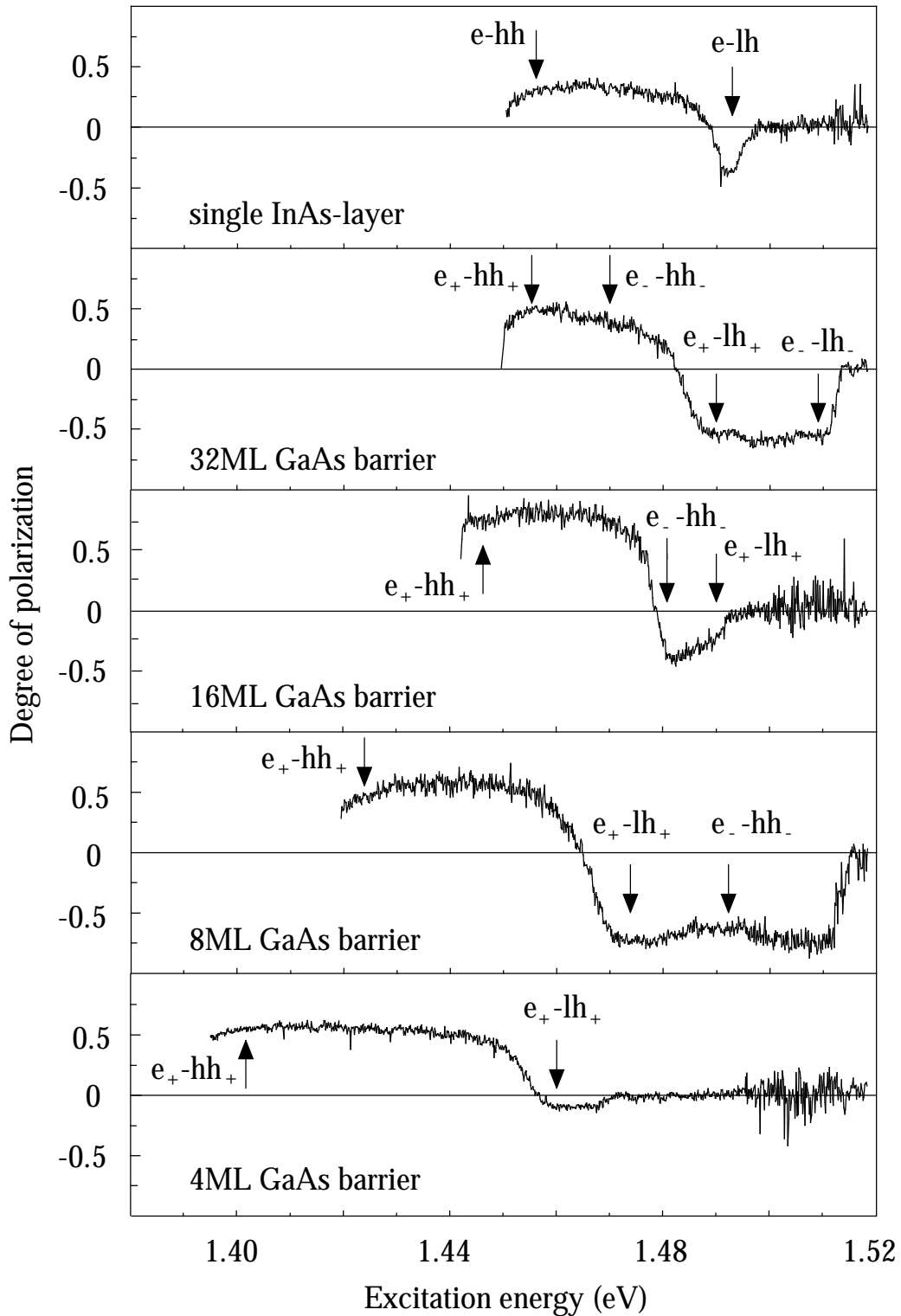


**Fig. 2.16:** Cleaved side PLE spectra of the samples measured at 4 K. For the single InAs layer sample and the 32 ML barrier sample a positive degree of polarization indicates a hh character of the valence band states involved in the transitions observed in PLE (indicated by the arrows), whereas negative values show the lh character. For the discussion of the degree of polarization in the 16, 8 and 4 ML barrier sample, see Section 2.5.

The coupling between the two InAs layers is clearly visible in the PLE spectrum of the 32 ML barrier sample, where one resolves four transitions. Considering that only transitions between states of equal parity are observed, they were identified by their polarization properties as the  $e_+-hh_+$ ,  $e_-hh_-$ ,  $e_+lh_+$  and  $e_-lh_-$  excitonic transitions. The observed splitting between the  $e_+-hh_+$  and  $e_-hh_-$  transition amounts to 13 meV, and 19 meV between the  $e_+lh_+$  and  $e_-lh_-$  transition, respectively.

According to Eq. (2.18), each of these splittings is the sum of the  $e_+-e_-$  splitting and the  $hh_+-hh_-$  or  $lh_+-lh_-$  splitting, respectively. The most important requirement for the separation of the contributions from the conduction and valence band and the successive determination of the band offsets was a negligible splitting between the  $hh_+$  and  $hh_-$  state in the regime of weak coupling. This assumption is justified by the following observations in the PL and PLE spectra of the 32 ML barrier sample:

- (i) In both the 32 ML barrier sample and single InAs layer sample, the energy difference between the  $e_+-hh_+$  or  $e_-hh_-$  exciton transition is the same, in PL as well as in PLE. This means that the  $hh$  exciton binding energies and the Stokes-shift are both either not altered at all, or their changes are small and exactly compensate each other. Thus, although the transitions are excitonic ones, the observed 13 meV splitting is only affected by the splitting of the confined electron and  $hh$  states and contributions of the exciton binding energy or Stokes shift cancel out.
- (ii) In both PL and PLE, the  $e_+-hh_+$  transition of the 32 ML barrier sample emerges at the same spectral position as the  $e_-hh_-$  transition of the single InAs layer sample. This observation is in agreement with the calculations of the effective electron and  $hh$  confinement energy as a function of barrier width which revealed, that at 32 ML barrier thickness the shift of the  $hh_+$  level with respect to the  $hh_-$  level is virtually zero and the shift of the  $e_+$  level with respect to the uncoupled case is very small.
- (iii) Figure 2.12 showed that the coupling induced shift of the antisymmetric  $e_-$  state is much larger than the shift of the symmetric  $e_+$  state and that most of the  $e_+-e_-$  splitting is accumulated in a shift of the  $e_-$  state since the confined electron states are in the regime of moderate coupling ( $\kappa_e \approx L$ ). In contrast, since the effective mass of the  $hh$ 's in the direction of quantization is five times higher than the one of the electrons, the  $hh$  states represent the regime of weak coupling ( $\kappa_{hh} \ll L$ ). Consequently, in the 32 ML barrier sample not only the shift of the  $hh_+$  state is negligible but also the  $hh_+-hh_-$  splitting.



From this discussion one can conclude that the observed 13 meV splitting between the  $e_+-hh_+$  and  $e_-hh_-$  transition originates entirely from the  $e_+-e_-$  splitting in the conduction band. Since the InAs layer thickness, the barrier thickness and the electron effective mass are known, by applying Eq. (2.17) one obtains from the 13 meV  $e_+-e_-$  splitting a conduction band offset of  $\Delta E_c = 535 \pm 15$  meV. The uncertainty in the conduction band offset results from the uncertainty in the InAs layer thickness ( $\pm 0.05$  ML) and the GaAs barrier thickness ( $\pm 0.5$  ML). Knowing the splitting of the confined electron states, the lh band offset can be extracted from the same PLE spectrum. Since the 19 meV splitting between the  $e_+-lh_+$  and  $e_-lh_-$  transitions is the sum of the  $e_+-e_-$  and  $lh_+-lh_-$  splitting, the  $lh_+-lh_-$  splitting alone amounts to 6 meV. Using the lh effective mass, Eq. (2.17) returns a lh valence band offset of  $\Delta E_{lh} = 225 \pm 25$  meV. The larger uncertainty in  $\Delta E_{lh}$  is due to the somewhat broader  $e_{\pm}-lh_{\pm}$  transitions. By performing similar calculations as displayed in Fig. 2.12 for the  $lh_+$  and  $lh_-$  state, one finds for a 32 ML barrier an increase of the effective  $lh_+$  confinement energy by 3 meV as compared to the uncoupled case. By comparing this value with the 3.5 meV red-shift of the  $e_+-lh_+$  transition observed in the 32 ML barrier sample, the magnitude of  $\Delta E_{lh}$  is verified. The fact that the  $lh_+-lh_-$  splitting is equally distributed in the shift of the  $lh_+$  and  $lh_-$  states is a consequence of the much weaker lh confinement as compared to the  $hh'$  s, in combination with the fact that the lh states are in regime of strong coupling ( $\kappa_{lh} \gg L$ ). With  $\Delta E_{lh} = 225$  meV and  $m_{lh}^* = 0.0905 m_0$  the lh barrier penetration length amounts to  $125 \text{ \AA}$  (44 ML), which is already considerably larger than the barrier width. Thus, in coupled ultrathin InAs layers the coupling of the  $lh'$  s is stronger than for the electrons and  $hh'$  s. It should be noted that the weak lh confinement is not only the result of the smaller lh effective mass. As outlined in Section 2.1, the shear strain component in the case of compressive strain leads to a diminishing of the band offset for the  $lh'$  s as compared to the  $hh$  band offset, so that in comparison with the  $hh'$  s the lh confinement is already reduced by the smaller lh band offset.

Finally, the  $hh$  valence band offset is determined from the observed 10 meV, 33 meV and 54 meV red-shift of the  $e_+-hh_+$  transition in the 16, 8 and 4 ML barrier samples with respect to uncoupled case. Since the barrier width in these samples reaches the value of the  $hh$  barrier penetration length, the red-shift of the  $e_+-hh_+$  transition is now due to the increase of the effective confinement energy of both, the  $hh_+$  and  $e_+$  states. With the

conduction band offset known from Eq. (2.17) for any barrier width, one obtains a hh valence band offset of  $385 \pm 15$  meV. With the values for the conduction and hh band offsets one experimentally finds a band offset ratio of  $Q_c = 0.58$ .

An overview of the transitions measured in the whole set of samples by PLE and the calculation of the transition energies as a function of barrier thickness using the  $\delta$ -potential model and the band offsets determined above, is displayed in Fig. 2.17. The agreement between experiment and theory supports the validity of the above determined band offsets and the  $\delta$ -potential approach.

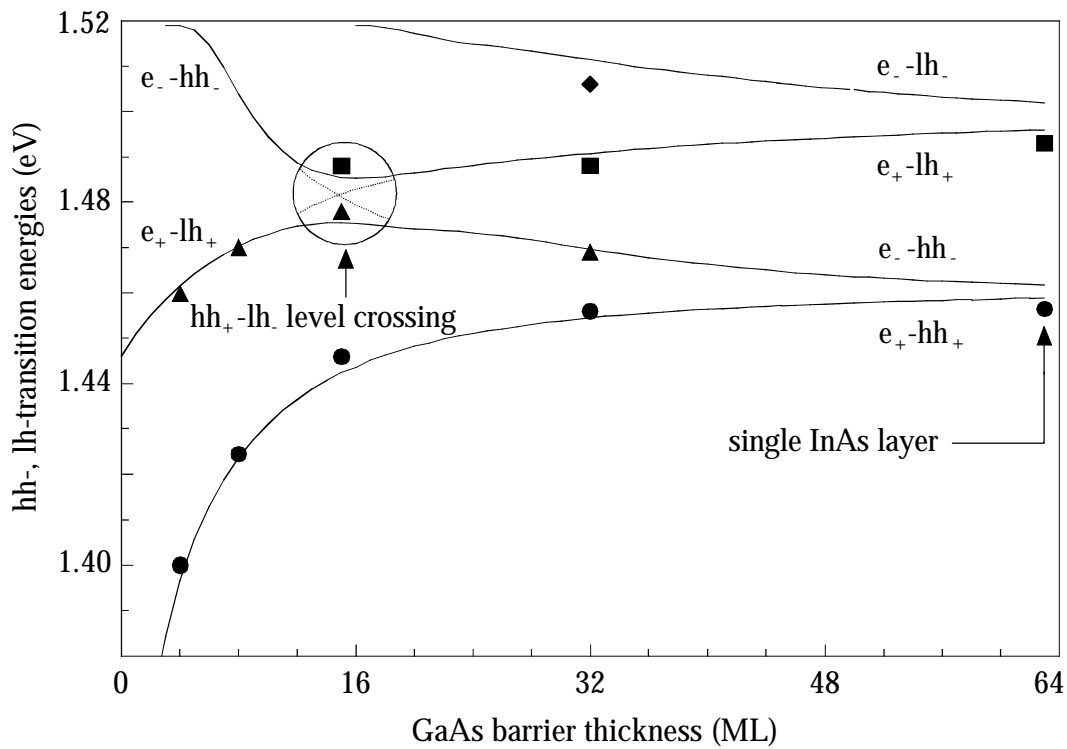


**Fig. 2.17:** Measured and calculated transition energies for the coupled InAs layer samples as a function of barrier width. The calculations were performed using  $\Delta E_c = 585$  meV,  $\Delta E_{hh} = 385$  meV, and  $\Delta E_{lh} = 225$  meV. The symbols at 64 ML represent the transitions observed in the single InAs layer. At approximately 16 ML one observes a crossover between the  $e_+ - lh_+$  and  $e_- - hh_-$  transitions.

## 2.4 Validation of the InAs/GaAs Band Offsets and Band Offset Ratio

In order to validate the band offsets determined in this work, they should be suitable to explain the experimental results of other groups. In addition, they need to be compared with the predictions of bulk elasticity theory. Applying Eq. (2.12), with the band offsets obtained above one finds a bandgap for strained InAs of  $E_g^{\text{InAs}} = 0.6$  eV. Since in the  $\delta$ -potential model this value is used in the sense of a bulk parameter, it has to be compared with the value derived from macroscopic elasticity theory given by Eq. (2.11). Assuming in accordance with the X-ray analysis, that the InAs layers are 6.8 % compressively strained, and taking the values for the hydrostatic and shear deformation potential and the stiffness constants given in Tab. 2.1, one finds a theoretical value for the InAs bandgap of 0.573 eV. Thus, the value for the bandgap of strained InAs derived from the experimentally determined band offsets is in good agreement with elasticity theory.

For the discussion of the strain induced splitting of hh and lh bands due to the shear strain one has to remember that in the  $\delta$ -potential model the strain induced hh-lh splitting is taken into account implicitly by assuming different band offsets  $\Delta E_{\text{hh}}$  and  $\Delta E_{\text{lh}}$ . As outlined in Section 2.2, in these values the strain induced modification of the hh-lh splitting by the split-off band is already incorporated. However, changes of the band structure due to strain fields in the surrounding GaAs matrix, as well as the ‘small thickness effect’ of the split-off band are neglected. According to Eq. (2.11), elasticity theory predicts a strain-induced separation between the hh and lh band offsets of

$$\delta E_{\text{hh-lh}} = \frac{1}{2} (3\delta E_{\text{sh}} - \Delta_0) + \frac{1}{2} \sqrt{\Delta_0^2 + 2\Delta_0\delta E_{\text{sh}} + 9\delta E_{\text{sh}}^2} \quad (2.19)$$

which yields a value for  $\delta E_{\text{hh-lh}}$  of 206 meV. From the band offsets determined above one finds an experimental value of  $\delta E_{\text{hh-lh}} = 160$  meV. Although both values are in reasonable agreement, one can at least qualitatively explain why the experimental value is too small. Firstly, by neglecting the split-off band in the calculation of the confined lh state in ultrathin quantum wells, the effective lh confinement energy will be underestimated. Thus, within the concept of band offsets, the lh band offset is slightly

overestimated in order to account for the increase of the lh effective confinement energy due to spin-orbit coupling. Estimating the impact of the ‘small thickness effect’ of the split-off band on the effective confinement energy of the lh’ s with 1 meV will result in a lh band offset of 200 meV and thus in a strain-induced hh-lh splitting of 185 meV. Secondly, an uncertainty in the magnitude of the lh band offset may result from the comparatively small effective lh confinement energy of 3.5 meV. For this weak confinement close to the GaAs valence band one has to expect repulsion between the confined lh level and the GaAs valence band due to their same symmetry. Effectively this would appear as a slightly stronger confinement of the lh’ s. However, since the confined lh level is used as a ‘probe’ for the lh band offset and because in the calculations of the effective lh confinement energy this repulsive interaction is not considered explicitly, it is compensated by an overestimate of the lh band offset.

From literature many experimental data are available about the spectral position of the hh and lh exciton transitions in single InAs layers of different thickness. In order to see whether the band offsets determined above and the  $\delta$ -potential model are suitable to describe the electronic structure of ultrathin InAs layers in a GaAs matrix over the whole range of the two-dimensional growth regime, the hh and lh transitions have been calculated as a function of the InAs layer thickness with the above band offsets. This calculation is displayed in Fig. 2.18 together with the experimental results of other groups<sup>21, 22, 24, 56</sup>. As can be seen from the figure, experiments and calculation are in good agreement. However, since the observed transitions are excitonic ones, the agreement can be further improved when the calculations include the dependence of the hh and lh exciton binding energy on the InAs layer thickness, as indicated by the dotted line in Fig. 2.18. Nevertheless, it should be noted that the dependence of the hh and lh interband transitions on InAs thickness is completely independent of the variation of exciton binding energies. In addition, it is worth pointing out that, for the dependence of the transition energies on InAs layer thickness, the same quality of agreement was achieved previously by other groups, but with different sets of band offsets, since they were used as a fitting parameter<sup>21, 22, 24</sup>. In contrast, in this thesis the band offsets were determined in a successive procedure from the shift and splitting of the optical transitions as a consequence of coupling in a set of samples where the InAs layer thickness was kept constant. Subsequently, they were used to give a prediction, how

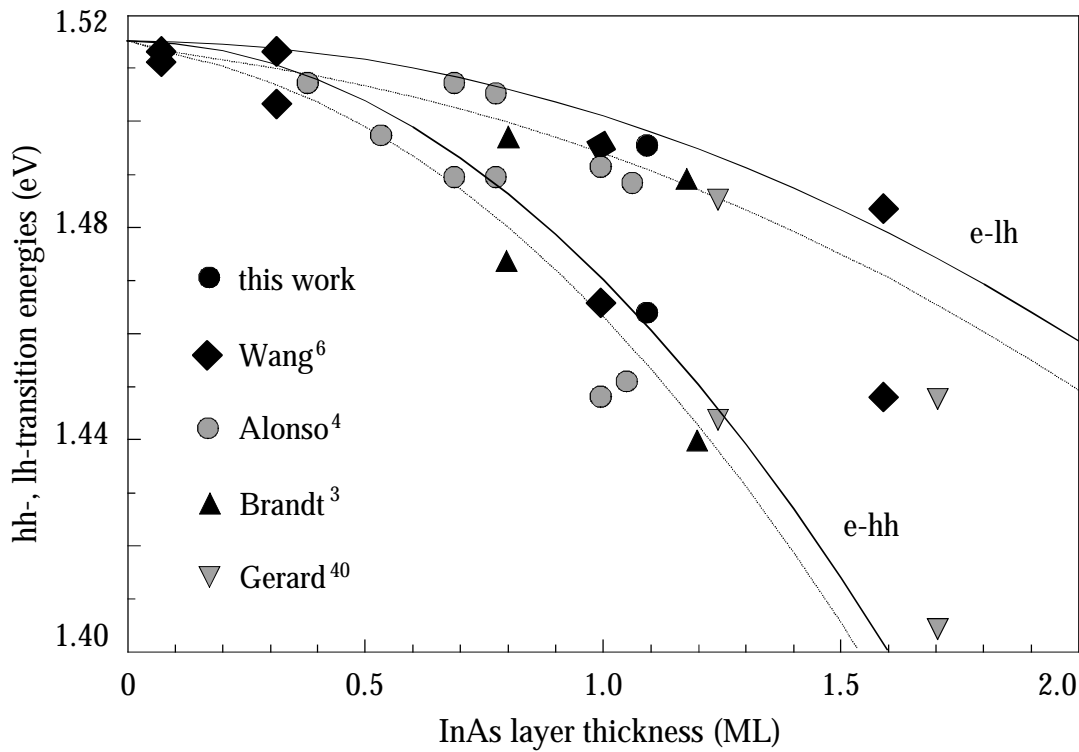


**Fig. 2.18:** Observed and calculated transition energies for a single InAs layer as a function of InAs thickness. The calculations (solid lines) are based on the  $\delta$ -potential model with the band offsets as determined in this thesis. The experimental data were taken from literature. The dotted lines show the calculations including the dependence of the exciton binding energy on InAs thickness as discussed in Chapter 3.

the hh and lh transition energies change with the InAs thickness.

Table 2.2 provides an overview of the band offsets, bandgap, band offset ratio and strain induced hh-lh splitting experimentally found by other groups or theoretically predicted<sup>20, 22, 24, 57-59</sup> and a comparison with the results of this thesis. The results of this work are in agreement with both the model solid theory of Van de Walle et al.<sup>15</sup> and macroscopic elasticity theory<sup>16, 17</sup>. Concerning the former, which provides reliable values for relative energy level positions, it turns out to be beneficial that the method for band offset determination presented in this thesis is explicitly sensitive to the band offset ratio. With respect to the latter, the experimental results of this work support the validity of elasticity theory in the monolayer limit. From the structural and geometrical viewpoint this has recently been proven by X-ray standing wave and X-ray absorption measurements of the In-As bond length in buried InAs monolayers grown on GaAs<sup>52</sup>.

other groups (exp.)	this work	Theory
$\Delta E_c = 689 \dots 711 \text{ meV}$	$\Delta E_c = 535 \text{ meV}$	$\Delta E_c = 526 \text{ meV}^{**)}$
$\Delta E_{hh} = 277 \dots 295 \text{ meV}$	$\Delta E_{hh} = 385 \text{ meV}$	
$\Delta E_{lh} = 30 \dots 89 \text{ meV}$	$\Delta E_{lh} = 225 \text{ meV}$	
$E_g = 0.531 \text{ eV}$	$E_g = 0.6 \text{ eV}$	$E_g = 0.573 \text{ eV}^{*})$
$Q_c = 0.72$	$Q_c = 0.58$	$Q_c = 0.53^{**)}$
$\delta E_{hh-lh} = 247 \text{ meV}$	$\delta E_{hh-lh} = 160 \text{ meV}$	$\delta E_{hh-lh} = 203 \text{ meV}^{*})$

\*) macroscopic elasticity theory

\*\*) local-density-functional pseudopotential approach

**Table 2.2:** Comparison of the values for the band alignment at the InAs/GaAs heterointerface found in previous experimental and theoretical work with the results of this work.

The main discrepancy between the band offsets determined in this work and the results from other groups concerns the magnitude of the lh band offset and thus the degree of confinement of the lh' s. With the values for the lh valence band offset reported by Wang<sup>24</sup> (89 meV) and Cingolani<sup>20</sup> (30 meV) one finds an effective lh confinement energy of 0.4 meV and 0.1 meV, respectively. Mistakenly, this small lh band offset has lead to the conclusion, that at 4 K the lh state is practically delocalized and the corresponding exciton is unbound. However, with the lh band offset determined above one finds a ten times higher effective lh confinement energy of 3.5 meV, which due to the 'small thickness effect' of the split-off band is even underestimated. At low temperatures this confinement energy is enough to maintain the lh state localized and to give rise to a bound lh exciton state. The existence of a bound lh exciton is directly visible in the PLE spectrum of the single InAs layer shown above as well as by its shift and splitting in the coupled InAs layers samples. Further experimental evidence for a bound lh exciton is provided by the observation of doubly resonant Raman scattering in ultrathin InAs layers discussed in the next chapter. The persistence of the doubly resonant Raman line at higher temperatures<sup>60</sup> demonstrates that the lh exciton remains bound up to temperatures of 18 K.

## 2.5 hh-lh level Crossing in Coupled Ultrathin InAs Layers

Returning to the overview of the measured transition energies in coupled InAs layers and the calculation of the transition energies as a function of barrier thickness displayed in Fig. 2.17, an interesting feature emerges at a barrier thickness of approximately 16 ML, which is denoted as “hh-lh<sub>+</sub> level crossing”. At this barrier thickness, in the PLE spectrum (see Fig. 2.15) between 1.48 eV and 1.495 eV only a broad band is visible rather than two separate peaks. In addition, the cleaved side PLE spectrum of this sample reveals a clear p-polarization for this band, thus a predominant lh character of the valence band states involved in these transitions.

The origin of this band can be explained as follows: when the barrier thickness is reduced, the effective confinement energy of the symmetric states is increased (observed as a red-shift of the corresponding transition) whereas the effective confinement energy of the antisymmetric states diminishes (observed as a blue-shift of the corresponding transition) until the critical barrier thickness is reached, where they become unconfined. An indication that the latter has certainly happened to the lh<sub>+</sub> state is the fact that the PLE spectrum of the 16 ML barrier sample above 1.495 eV is completely structureless and that the measured PL background is completely unpolarized. At a barrier thickness of approximately 16 ML the effective confinement energy of the blue-shifted lh<sub>+</sub> state and the red-shifted hh<sub>+</sub> state become equal so that both levels start to cross each other. At the cross-over point the energy separation between the e<sub>-</sub>-hh<sub>+</sub> and e<sub>+</sub>-lh<sub>+</sub> transition is entirely determined by the splitting between the e<sub>+</sub> and e<sub>-</sub> state, which according to Fig. 2.12 amounts to 19 meV. The DOP in the cross-over region is given by the superposition of the polarization properties of the e<sub>-</sub>-hh<sub>+</sub> and e<sub>+</sub>-lh<sub>+</sub> transition, i.e. it depends on the ratio between  $\sigma$ - and  $\pi$ -component of each transition weighted by their oscillator strength. As can be seen from the cleaved side PLE spectrum of the 32 ML or 8 ML barrier sample, the DOP for the hh transitions (see e.g. e<sub>+</sub>-hh<sub>+</sub> transition) is reduced from its theoretical value of +1 at the expense of a weaker  $\sigma$ -component, whereas the DOP of the lh transitions (see e.g. e<sub>+</sub>-lh<sub>+</sub> transition) is increased with respect to its theoretical value of  $-1/3$  in favour of the  $\pi$ -component. Assuming equal oscillator strengths for the e<sub>-</sub>-hh<sub>+</sub> and e<sub>+</sub>-lh<sub>+</sub> transitions, their superposition leads effectively to a negative DOP at the cross-over point. That the crossing of the hh<sub>+</sub> and

$lh_+$  levels indeed occurred, becomes evident from the comparison of the PLE and cleaved side PLE spectra of the 32 ML barrier sample with the ones of the 8 ML or 4 ML sample. For the 32 ML sample the second lowest lying transition is the  $e$ - $hh$  transition at 1.47 eV identified by its strong  $s$ -polarization. In contrast, in the 8 ML and 4 ML sample, where the  $e$ - $hh$  and  $e_+$ - $lh_+$  transitions are well spectrally separated again, the second lowest lying transition is predominantly  $p$ -polarized indicating that both transitions crossed each other and that the  $lh_+$  level has become the first excited valence band state of the two coupled InAs layers.

The remaining question, at which barrier thickness the antisymmetric electron state becomes unconfined, cannot be answered conclusively. The calculations in Fig. 2.12 reveal that the critical barrier thickness for the electrons is reached at approximately 20 ML. However, these calculations do not include a repulsive interaction between the antisymmetric electron state and the GaAs conduction band, which would shift the critical barrier thickness for the electrons towards smaller barrier widths. The broad band at 1.488 eV in the PLE spectrum of the 16 ML sample seems to contain the  $e_+$ - $lh_+$  as well as the  $e$ - $hh$  transition with both having equal oscillator strengths. This would indicate that the  $e$  state is at least still in strong resonance with the GaAs conduction band, but not completely unconfined.



## References

- <sup>1</sup> P. Bhattacharya, EMIS Data Review Series (INSPEC), 66 (1993)
- <sup>2</sup> E.P. O'Reilly, *Semicond. Sci. Technol.* **4**, 121 (1989)
- <sup>3</sup> T.Y. Wang and G.B. Springfellow, *J. Appl. Phys.* **67**, 344 (1990)
- <sup>4</sup> S. Adachi, *J. Appl. Phys.* **58**, R1 (1985)
- <sup>5</sup> Landolt-Börnstein, NS III **17(a)**, 218 (1982)
- <sup>6</sup> R. People, and J.C. Bean, *Appl. Phys. Lett.* **47**, 322 (1985)
- <sup>7</sup> J.W. Mathews, and A.E. Blakeslee, *J. Cryst. Growth* **27**, 118 (1974)
- <sup>8</sup> J.W. Mathews, and A.E. Blakeslee, *J. Cryst. Growth* **29**, 273 (1975)
- <sup>9</sup> J.W. Mathews, and A.E. Blakeslee, *J. Cryst. Growth* **32**, 265 (1976)
- <sup>10</sup> A. Sasaki, *J. Cryst. Growth* **160**, 27 (1996)
- <sup>11</sup> E.A. Kraut, R.W. Grant, J.R. Waldrop, and S.P. Kowalczyk, *Phys. Rev. Lett.* **44**, 1620 (1978)
- <sup>12</sup> S.P. Kowalczyk, W.J. Schaffer, E.A. Kraut, and R.W. Grant, *J. Vac. Sci. Technol.* **20**, 705 (1982)
- <sup>13</sup> C. Priester, G. Allan, and M. Lannoo, *Phys. Rev. B* **38**, 9870 (1988)
- <sup>14</sup> J.M. Moison, C. Guille, M. van Rompey, F. Barthe, F. Houzay, and M. Bensoussan, *Phys. Rev. B* **39**, 1772 (1989)
- <sup>15</sup> C.G. van de Walle, *Phys. Rev. B* **39**, 1871 (1989)
- <sup>16</sup> S. L. Chuang, *Phys. Rev. B* **43**, 9649 (1991)
- <sup>17</sup> F.H. Pollak, in *Effects of homogenous strain on the electronic and vibrational levels in semiconductors*, edited by T.P. Pearsall, *Semiconductors and Semimetals Vol. 32*, Academic Press, New York 1990
- <sup>18</sup> D. Gershoni, J.M. Vandenberg, R.A. Hamm, H. Temkin, and M.B. Panish, *Phys. Rev. B* **36**, 1320 (1987)
- <sup>19</sup> H. Kitabayashi, and T. Waho, *J. Cryst. Growth* **150**, 152 (1995)
- <sup>20</sup> R. Cingolani, O. Brandt, L. Tapfer, G. Scamarcio, G.C. LaRocca, and K. Ploog, *Phys. Rev. B* **42**, 3209 (1990)
- <sup>21</sup> O. Brandt, L. Tapfer, R. Cingolani, K. Ploog, M. Hohenstein, and F. Phillipp, *Phys. Rev. B* **41**, 12599 (1990)
- <sup>22</sup> M. I. Alonso, M. Ilg, and K. Ploog, *Phys. Rev. B* **50**, 1628 (1994)
- <sup>23</sup> O. Brandt, H. Lage, and K. Ploog, *Phys. Rev. B* **45**, 4217 (1992)

- <sup>24</sup> P.D Wang, N.N. Ledentsov, C.M. Sotomayor Torres, I.N. Yassievich, A. Pakhomov, A.Yu. Egovov, P.S. Kop'ev, and V.M. Ustinov, *Phys. Rev. B* **50**, 1604 (1994)
- <sup>25</sup> M. Nakayama, T. Fujita, I. Tanaka, H. Nishimura, and H. Terauchi, *Jpn. J. Appl. Phys.* **32**, 160 (1993)
- <sup>26</sup> K. Taira, H. Kawai, I. Hase, K. Kaneko, N. Watanabe, *Appl. Phys. Lett.* **53**, 495 (1988)
- <sup>27</sup> J. Meléndez, A. Mazuelas, P.S. Dominguez, M. Garriaga, M.I. Alonso, G. Armelles, L. Tapfer, and F. Briones, *Appl. Phys. Lett.* **62**, 1000 (1993)
- <sup>28</sup> M.G. Burt, *Appl. Phys. Lett.* **65**, 717 (1994)
- <sup>29</sup> M.G. Burt, *Phys. Rev. B* **50**, 7518 (1994)
- <sup>30</sup> K.A. Mäder and Alfonso Baldereschi, *Inst. Phys. Conf. Sc.* **123**, 341 (1991)
- <sup>31</sup> A. Baldereschi, and J.J. Hopfield, *Phys. Rev. Lett.* **28**, 171 (1972)
- <sup>32</sup> H.P Hjalmarson, P. Vogl, D.J. Wolford, and J.D. Dow, *Phys. Rev. Lett.* **44**, 810 (1980)
- <sup>33</sup> R.A. Faulkner, *Phys. Rev.* **175**, 991 (1968)
- <sup>34</sup> P. Koenraad, F.A.P. Blom, C.J.G.M. Langerak, M. R. Leys, J.A.A.J. Perenboom, J. Singleton, S.J.R.M. Spermon, W. van der Vleuten, A.P.J. Voncken, and J.H. Wolter, *Semicond. Sci. Technol.* **5**, 861 (1990)
- <sup>35</sup> T.C. Damen, M. Fritze, A. Kastalsky, J.E. Cunningham, R.N. Pathak, H. Wang, and J. Shah, *Appl. Phys. Lett.* **67**, 515 (1995)
- <sup>36</sup> S. Wilke, and D. Hennig, *Phys. Rev. B* **43**, 1240 (1991)
- <sup>37</sup> J. Brübach, A.Yu. Silov, J.E.M. Haverkort, W. van der Vleuten, and J.H. Wolter, *Phys. Rev. B* **59**, 6488 (1999)
- <sup>38</sup> J.M. Luttinger, *Phys. Rev.* **102**, 1030 (1956)
- <sup>39</sup> A.Yu. Silov, J.E.M. Haverkort, N.S. Averkiev, P.M. Koenraad, and J.H. Wolter, *Phys. Rev. B* **50**, 4509 (1994)
- <sup>40</sup> F. Dujardin, N. Marréaud, and J.P. Laurenti, *Solid State Commun.* **98**, 297 (1996)
- <sup>41</sup> O. Brandt, R. Cingolani, H. Lage, G. Scamarcio, L. Tapfer, and K. Ploog, *Phys. Rev. B* **42**, 11396 (1990)
- <sup>42</sup> I. Yassievitch, and U. Rössler, *J. Phys. C* **32**, 7927 (1994)
- <sup>43</sup> J. Brübach, A.Yu. Silov, J.E.M. Haverkort, W. van der Vleuten, and J.H. Wolter, *Superlatt. and Microstr.* **21**, 527 (1996)

- 
- <sup>44</sup> R.P. Leavitt, and J.W. Little, *Phys. Rev.* **B42**, 11774 (1990)
- <sup>45</sup> K.J. Moore, P. Dawson, and C.T. Foxon, *Phys. Rev.* **B38**, 3368 (1988)
- <sup>46</sup> M. Sato and Y. Horikoshi, *J. Appl. Phys.* **66**, 851 (1989)
- <sup>47</sup> S.S. Dosanjh, L. Hart, R. Nayak, and B.A. Joyce, *J. Appl. Phys.* **75**, 8066 (1994)
- <sup>48</sup> S.S. Dosanjh, P. Dawson, M.R. Fahy, B.A. Joyce, R.A. Stradling, and R. Murray, *J. Cryst. Growth* **127**, 579 (1993)
- <sup>49</sup> N.N. Ledentsov, P.D. Wang, C.M. Sotomayor Torres, A. Yu. Egorov, M.V. Maximov, V.M. Ustinov, A.E. Zhukov, and P.S. Kop'ev, *Phys. Rev.* **B50**, 12171 (1994)
- <sup>50</sup> P.D. Wang, N.N. Ledentsov, C.M. Sotomayor Torres, P.S. Kop'ev, and V.M. Ustinov, *Appl. Phys. Lett.* **64**, 1526 (1994)
- <sup>51</sup> C. Giannini, L. Tapfer, S. Lagomarsino, J.C. Boulliard, A. Taccoen, B. Capelle, M. Ilg, O. Brandt, and K. Ploog, *Phys. Rev.* **B48**, 11496 (1993)
- <sup>52</sup> J.C. Woicik, J.G. Pellegrino, S.H. Southworth, P.S. Shaw, B.A. Karlin, and C.E. Bouldin, *Phys. Rev.* **B52**, R2281 (1995)
- <sup>53</sup> T. Marschner, J. Brübach, M.R. Leys, C.A. Verschuren, and J.H. Wolter, *J. Appl. Phys.* **83**, 3630 (1998)
- <sup>54</sup> T. Shima, J.S. Lee, K. Undo, K. Tanaka, S. Niki, A. Yamada, and Y. Makita, *Appl. Surf. Sci.* **75**, 164 (1994)
- <sup>55</sup> M.V. Belusov, N.N. Ledentsov, M.V. Maximov, P.D. Wang, I. Yassievich, N.N. Faleev, I.A. Kozin, V.M. Ustinov, P.S. Kop'ev, and C.M. Sotomayor Torres, *Phys. Rev.* **B51**, 14346 (1995)
- <sup>56</sup> J.M. Gerard, and J.Y. Marzin, *Appl. Phys. Lett.* **53**, 568 (1988)
- <sup>57</sup> N. Tit, *J. Vac. Sci. Technol.* **A16**, 805 (1998)
- <sup>58</sup> R. Colombelli, V. Piazza, A. Badolato, M. Lazzarino, F. Beltram, W. Schoenfeld, and P. Petroff, *Appl. Phys. Lett.* **76**, 1146 (2000)
- <sup>59</sup> M. Di Ventra, and K.A. Mäder, *Phys. Rev.* **B55**, 13148 (1997)
- <sup>60</sup> J. Brübach, J.E.M. Haverkort, J.H. Wolter, P.D. Wang, N.N. Ledentsov, C.M. Sotomayor Torres, A.E. Zhukov, P.S. Kop'ev, and V.M. Ustinov, *J. Opt. Soc. Am* **B73**, 1224 (1996)

---

## 3. *Excitonic Effects in Ultrathin InAs/GaAs Quantum Wells*

### 3.1 Excitons in Ultrathin InAs Layers

Similar to conventional type I semiconductor quantum wells<sup>1</sup>, the optical properties of ultrathin InAs layers in a GaAs matrix are governed by the formation of excitons. The insertion of an InAs monolayer in a GaAs matrix strongly confines electrons and holes, which by mutual Coulomb interaction form excitons<sup>2</sup>. Due to the large dielectric constant of the host material, the exciton Bohr-radius amounts to several lattice constants, i.e. the excitons are Wannier excitons. The binding of the excitons to the InAs layer is reflected in the high photoluminescence efficiency, the associated red-shift of the exciton transitions with respect to the interband transitions and the enhancement of the exciton binding energy<sup>3, 4</sup>. Among excitons in quantum well structures, excitons in ultrathin InAs layers provide a unique situation, which in the past has led to contradicting conclusions about the exciton character, their dimensionality and the origin of the observed increase of the exciton binding energy<sup>3, 5-11</sup>. In conventional quantum wells the major part of the electron and hole wavefunctions are localized within the wells region, so that despite the increase of the exciton binding energy due to the confinement by the quantum well, the excitons have a well-like character. A good example is the hypothetical case of ideal 2D excitons associated with an infinitely deep quantum well, where the envelope functions are entirely confined to the well region. In the calculation of the 2D exciton binding energy this fact is considered by attributing electron and hole an infinite effective mass in the axis of quantization, and the in-plane well effective mass for the movement of electron and hole in the plane perpendicular to the quantization axis. As a result, the exciton has an entire well character expressed by the use of the well effective masses, but it is two-dimensional and possesses a binding energy of four times the bulk Rydberg energy. In ultrathin InAs layers the situation is different. The observed enhancement of the exciton binding energy manifests itself as

the reduction of the exciton dimensionality towards the two-dimensional case. However, as outlined in Chapter 2, the confined electron and hole wavefunctions extend entirely into the GaAs barrier, and the effective masses in both the quantization direction and the InAs plane are determined by the GaAs Luttinger parameters. Thus, regardless their dimensionality the excitons bound to the InAs layer are completely barrier-like. In the following the term dimensionality is used as a measure for the observed enhancement in the exciton binding energy with respect to the GaAs bulk value.

### 3.1.1 Ideal 3D and 2D Excitons

The ground state of a bulk semiconductor at zero temperature is built up from electrons occupying the valence band according to the dispersion relation and all conduction band states being empty. If a direct semiconductor is irradiated with light above the bandgap, an excited state is created by promoting an electron to the conduction band and leaving a hole behind in the valence band. If Coulomb interaction is neglected, the lowest lying excited state of the crystal is found at  $E = E_g$  and  $\vec{k} = 0$ . However, if the attractive Coulomb interaction between the electron in the conduction band and hole in the valence band is taken into account, a bound state below the bandgap is created, which is obtained by a linear combination of valence and conduction band states including the relative electron-hole motion<sup>1, 12</sup>. The exciton ground state with a finite binding energy  $R^*$  then represents the lowest lying excited state of the crystal. Without perturbations in the crystal, the exciton can move freely through the crystal.

In 3D, the eigenvalues of the exciton states with  $E < 0$  are found straightforwardly by solving the hydrogen problem with the Coulomb interaction reduced by the dielectric constant of the semiconductor. After separating centre-of-gravity and relative orbital motion of the electron-hole pair and solving the orbital Schrödinger equation, one obtains a series of discrete bound exciton states ( $n=1, 2, \dots$ ) located below the bandgap with the binding energies  $E_n^{x, 3D}$

$$E_n^{x,3D} = -\frac{R^*}{n^2}, n = 1, 2, \dots, \quad (3.1)$$

where  $R^*$  denotes the Rydberg energy given as  $R^* = \mu^* e^4 / 32\pi^2 \epsilon_0^2 \epsilon^2 \hbar^2$ , and  $\mu^*$  is the reduced effective mass. Unlike in 2D, the calculations are based on a complete isotropy of the effective electron and hole masses in all three crystal directions. For a better comparison with the results for 2D excitons it is worth providing the orbital wavefunction of the exciton ground state<sup>12</sup>

$$\Phi_{n=1}^{x,3D}(\mathbf{r}) = \frac{1}{\sqrt{\pi} a_0^{3/2}} \exp\left(-\frac{r}{a_0}\right) \quad (3.2)$$

with  $a_0 = 4\pi \epsilon_0 \epsilon \hbar^2 / \mu^* e^2$  being the exciton Bohr-radius and  $r = r_e - r_h$  the 3D relative electron-hole coordinate, as well as its k-representation<sup>12</sup>

$$\Phi_{n=1}^{x,3D}(\mathbf{k}) = \frac{\sqrt{8\pi} a_0^{3/2}}{(1 + a_0^2 k^2)^2}. \quad (3.3)$$

The latter expression is important for the bleaching of the excitonic absorption as discussed in Chapter 4, because Eq. (3.3) has the physical meaning of the volume of the exciton ground state in k-space. States in phase-space, which are already occupied, are no longer accessible in optical transitions and the filling of the phase-space under photoexcitation leads to diminishing of the exciton oscillator strength. In GaAs bulk material the Rydberg energy and exciton Bohr-radius amount to 3.8 meV and 90 Å, respectively.

For the discussion of absorption or PLE spectra and the bleaching of the excitonic absorption one also needs to consider the influence of correlated but unbound electron-hole states above the ionization limit ( $E > 0$ ). Although the calculations are rather complex, one can still find an analytical expression for the Coulomb enhancement or Sommerfeld-factor<sup>13</sup>

$$\alpha_{\text{CEF}}^{3\text{D}} = |\phi_{\text{E}>0}^{3\text{D}}(\mathbf{r} = 0)| = \frac{2\pi\sqrt{\mathbf{R}^*/\hbar\omega - E_g}}{1 - \exp(-2\pi\sqrt{\mathbf{R}^*/\hbar\omega - E_g})}. \quad (3.4)$$

This expression describes the enhancement of the absorption above the bandgap due to correlated electron-hole pairs beyond the square-root-like behaviour of band-to-band transitions. Since Eq. (3.4) diverges for  $\hbar\omega \rightarrow E_g$ , in pure bulk GaAs one observes the typical ‘tooth-like’ behaviour of the absorption at the bandgap.

The solution of the exciton problem in layered semiconductor structures was first presented by Shinada and Sugano<sup>14</sup>. In order to overcome the problem that the Coulomb interaction couples the electron-hole pair motion in growth direction and in the plane perpendicular, they used an infinite effective mass for the motion along the growth axis. Using this approach, they treated the hypothetical case of an ideally 2D exciton, i.e. the case of extreme anisotropy, with the well-known result, that the binding energy of the bound exciton states has increased with respect to the 3D value to

$$E_n^{\text{x},2\text{D}} = -\frac{\mathbf{R}^*}{(n - 1/2)^2}, \quad n = 1, 2, \dots \quad (3.5)$$

The exciton ground state orbital wavefunction and its Fourier transform can be derived as<sup>15</sup>

$$\phi_{n=1}^{\text{x},2\text{D}}(\mathbf{r}) = \left(\frac{2}{\pi}\right)^{1/2} \frac{2}{a_0} \exp\left(-\frac{2r}{a_0}\right) \quad (3.6)$$

and

$$\phi_{n=1}^{\text{x},2\text{D}}(\mathbf{k}) = \frac{\sqrt{2\pi} a_0}{(1 + a_0^2 \mathbf{k}^2 / 4)^{3/2}}, \quad (3.7)$$

respectively. Here,  $\mathbf{k}$  is the 2D wavevector corresponding to the relative electron-hole motion in the layer plane. Finally, one finds for the Sommerfeld-factor of the unbound exciton states in 2D<sup>15, 16</sup>

$$\alpha_{\text{CEF}}^{2\text{D}} = \left| \phi_{E>0}^{2\text{D}}(r=0) \right| = \frac{2}{1 + \exp\left(-2\pi\sqrt{R^*/\hbar\omega - E_g}\right)}. \quad (3.8)$$

Restricting the comparison of 3D and 2D excitons to the exciton ground state, yields the following results:

- (i) the binding energy in 2D is four times larger than in bulk material. Consequently, in quantum well structures excitonic resonances can be observed even at room temperature
- (ii) the oscillator strength of 2D excitons is strongly enhanced with respect to the 3D value with the well-known result that optical spectra of quantum well structures are governed by excitonic resonances
- (iii) the 2D exciton Bohr-radius given by the ground state wavefunction is two times smaller than in the 3D case
- (iv) according to Eq. (3.3), (3.7) and as depicted in Fig. 3.1, the volume in k-space, which significantly contributes to the exciton oscillator strength, is larger for 2D excitons than in 3D. As a consequence the bleaching of the excitonic absorption by phase-space-filling is more efficient for 2D excitons than for 3D excitons
- (v) as discussed later in Fig. 3.3, at the continuum edge the 3D Sommerfeld-factor leads to a strong, ‘tooth-like’ enhancement of the absorption, whereas in the 2D case the enhancement of the absorption is structureless and amounts only to a factor of 2. As opposed to that, at photon energies ten Rydbergs above the bandgap, the enhancement of the absorption due to unbound electron-hole pairs is virtually zero in 3D, whereas in 2D the absorption is still enhanced by 30 %.

Although the above 2D exciton model qualitatively describes excitonic effects in quantum well structures and also leads to reasonable numerical results for the exciton binding energy, there are two major reasons why it cannot be strictly applied for excitons in ultrathin InAs layers both resulting from the assumption of an extreme effective mass anisotropy. Firstly, by using an infinite effective mass in the direction of the anisotropy, the exciton is fully characterized by the in-plane effective mass of the (hypothetical) 2D layer in which the electron-hole pair can move freely. Thus, when describing excitons in quantum wells by ideally 2D excitons, one has to replace the



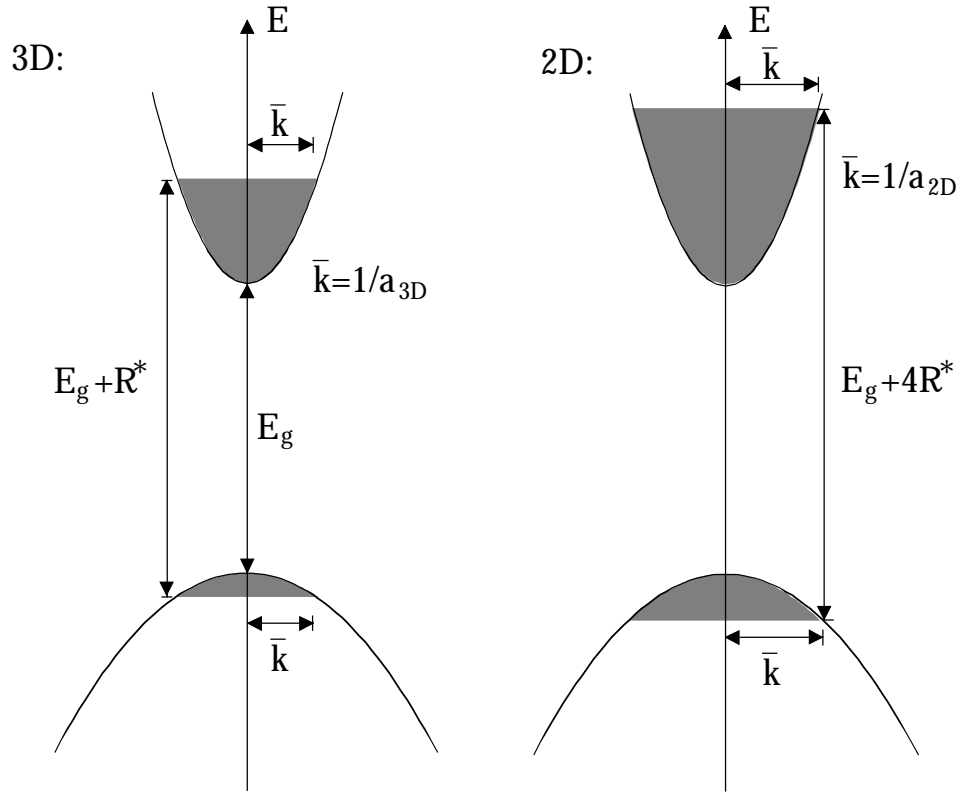


**Fig. 3.1:** Schematic representation of the conduction and valence band states that contribute to the formation of the exciton ground state in 3D and 2D. The volume in  $k$ -space, which contributes significantly to the exciton oscillator strength, is given by  $\bar{k} = 1/a_0$ .

bulk effective masses by the in-plane effective masses of the well material in  $R^*$ . However, the 2D exciton model assumes a non-degenerate ellipsoidal valence band, i.e. the in-plane effective hole mass equals to the 3D bulk value and no distinction between hh and lh excitons is made. This problem can be overcome by extending the exciton Hamiltonian with the potential of an infinitely deep well. Solving this problem in the limit of zero well thickness yields with  $E_{n=1}^x = 4 \times R^*$  the same binding energy as the 2D exciton model. Due to the infinitely high barrier, the excitons maintain their entire well character. In the infinitely deep quantum well, the degeneracy of the hh and lh subbands is lifted and hh and lh excitons associated with the confined hh and lh states are formed. For infinitely high barriers, the in-plane effective masses are independent of the well width given by  $m_{hh}^* = m_0/(\gamma_1 + \gamma_2)$  and  $m_{lh}^* = m_0/(\gamma_1 - \gamma_2)$ , respectively. As a consequence of the reversal of the in-plane effective mass, 2D lh excitons have a larger binding energy than 2D hh excitons. Although this property qualitatively reflects the

reality in quantum wells for thickness larger than 50-100 Å, it contradicts the observations when the well thickness approaches zero, revealing another limitation of using the 2D exciton model for excitons in ultrathin InAs layers. At finite barrier height, with decreasing well thickness an increasing part of the confined state wavefunctions leaks into the barrier indicated by the decreasing effective confinement energies. As a consequence, electrons and holes become less localized in the plane of the well according to the barrier penetration length and thus become increasingly more barrier-like. In spite of the reasonable numerical agreement for the exciton binding energies it is actually due to this argument, that the 2D exciton model cannot be used in ultrathin InAs layers. As discussed in Chapter 2, the electronic states in InAs layers are solely determined by the parameters of the surrounding GaAs matrix, and consequently both hh and lh excitons have an entirely barrier-like character.

In conventional quantum wells the change from a well-like character to a barrier-like character of the excitons when reducing the well thickness is combined with an increase in the exciton dimensionality from almost 2D excitons to a 3D character. With the increasing leakage of the confined state wavefunctions into the barrier, the probability to find an electron and hole at a given place in the direction of quantization is smeared out so that the spatial anisotropy in the carrier movement is weakened<sup>17, 18</sup>. As a result of the reduced confinement the gain in electrostatic energy in the electron-hole pair is decreased leading to a smaller binding energy. The unique situation for excitons in ultrathin InAs layers arises from the fact that here the change in exciton dimensionality when varying the InAs layer thickness is decoupled from the change in their well or barrier character. For all InAs thicknesses within the two-dimensional growth regime hh and lh excitons have a GaAs barrier character. However, when the InAs thickness is increased from zero to 2 ML, the hh exciton binding energy increases from the Rydberg energy of GaAs to almost the 2D limit of  $4 \times R^*$ . The separation of the material properties and the dimensionality of excitons in ultrathin InAs layers is also expressed by the coexistence of almost ideally 2D hh excitons and the 3D lh excitons, but both being GaAs-like, as will be discussed below.

## 3.1.2 Excitons in Single Ultrathin InAs Layers

### 3.1.2.1 Calculation of the Exciton Binding Energy and Exciton Dimensionality

A model for excitons in ultrathin InAs layers has to consider the strict separation between the material properties and dimensionality of the excitons, i.e. the excitons are always GaAs-like, whereas their dimensionality is independently determined by the strength of the confining potential of the InAs layer. In analogy to the  $\delta$ -potential model for the calculations of the effective confinement energy of electron, hh, and lh states of the InAs layer, the binding energies of the hh and lh excitons bound to the InAs layer can be calculated with the zero-radius potential model<sup>19</sup>. In this model the InAs layer is regarded as a sheet of isoelectronic impurities inserted in the GaAs matrix. The electrically neutral substituent In first traps a single charge carrier, whereupon the second charge carrier of opposite sign becomes bound via the Coulomb field leading to the formation of an exciton state. The first particle is bound to the InAs layer by its non-Coulombic short-range potential. The InAs layer thus can be viewed to bind excitons which can freely move along the InAs layer. The validity of the zero-radius potential model is limited to the range where the localization length of the first particle is large compared to the width of the confining potential<sup>10, 19</sup>.

With these assumptions, the exciton binding energy can be found in a variational approach by solving the Schrödinger equation

$$\left( \begin{array}{l} -\frac{\hbar^2}{2\mu^*} \Delta_{x,y} - \frac{\hbar^2}{2m_e^*} \Delta_{z,e} - \frac{\hbar^2}{2m_h^*} \Delta_{z,h} \\ -\frac{e^2}{4\pi \epsilon \epsilon_0 \sqrt{r^2 + (z_e - z_h)^2}} + \frac{\hbar^2}{m_e^*} \kappa_e \times \delta(z_e) + \frac{\hbar^2}{m_h^*} \kappa_h \times \delta(z_h) \end{array} \right) \Psi_\lambda = E_\lambda \Psi_\lambda \quad (3.9)$$

with the trial wavefunction

$$\Psi_\lambda = \frac{1}{N} \exp\left(-\frac{r}{\lambda} - \kappa_e |z_e| - \kappa_h |z_h|\right), \quad (3.10)$$

where  $N$  is the normalization factor and  $r$  denotes the in-plane radial coordinate. Minimizing the energy eigenvalue  $E_\lambda$  with respect to the variational parameter  $\lambda$  leads to the dependence of the hh and lh exciton binding energy as a function of InAs thickness, as displayed in Fig. 3.2. For the inverse barrier penetration length  $\kappa_e = \kappa_h = 0$ , i.e. when electrons and holes are not confined at all, the calculations reveal the 3D exciton binding energy  $E_x = R^*$ . For the opposite limiting case  $\kappa_e, \kappa_h \rightarrow \infty$ , electrons and holes are completely confined to  $z = 0$ . Since this corresponds to the situation of a quantum well with infinitely high barriers in the limit of zero thickness, one finds for  $E_x$  the 2D result of  $E_x = 4R^*$ .

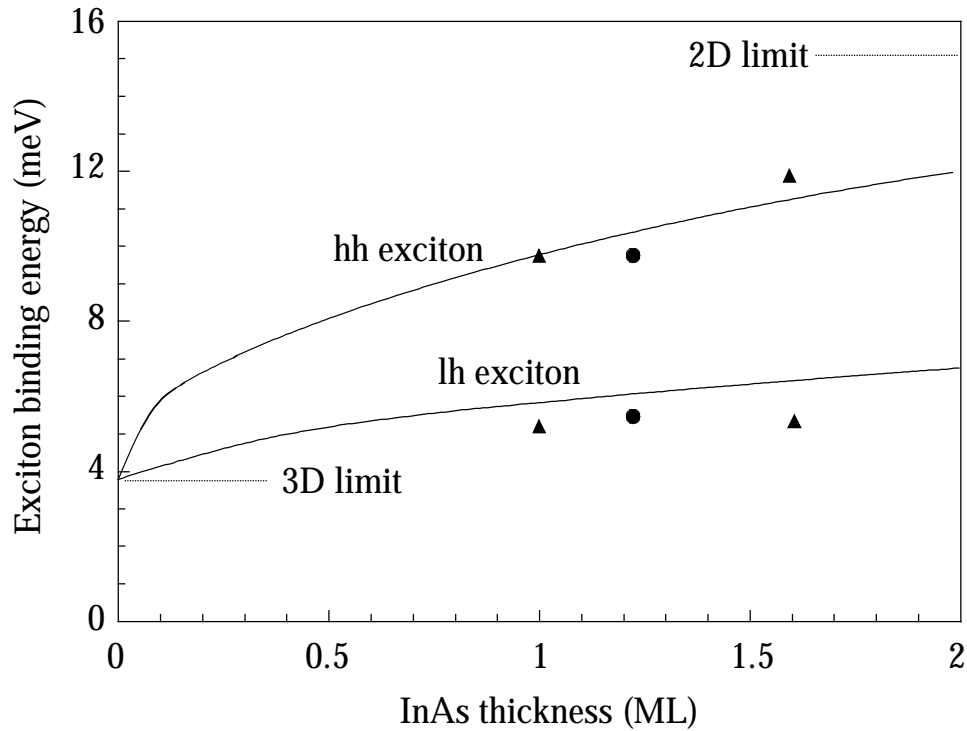


**Fig. 3.2:** Calculated hh and lh exciton binding energy in a single ultrathin InAs/GaAs quantum well as a function of InAs thickness. The symbols (●) represent the values for a 1.2 ML thick InAs layer determined in this work. The symbols (▲) are the results taken from Ref. 10.

For InAs thickness of 1.1 - 1.4 monolayers, the calculations in Fig. 3.2 yield a hh exciton binding energy of 11 meV and 6.5 meV for the lh exciton binding energy. This result is in agreement with the 10 meV and 5.5 meV found experimentally. The discrepancy between the hh and lh exciton binding energy at a given InAs thickness is explained by the much weaker confinement of the lh as compared to the hh.

For later use, an alternative treatment for the exciton binding energies is to translate the enhanced exciton binding energy with respect to the effective Rydberg energy into the dimensionality of the excitons. For this purpose one uses the results for an ideal 2D exciton and corrects the deviation with respect to the measured exciton binding energy  $E_x$  by means of the dimensionality parameter  $D$  according to the expression  $E_x = 4D \times R^*$ . With this definition,  $D$  ranges from  $1/4$  in the pure 3D case to  $1$  in the ideal 2D case. From the measured hh and lh exciton binding energies of  $10$  meV and  $5.5$  meV, one finds  $D = 0.66$  for the hh exciton, and for the lh exciton  $D = 0.3$ . This result demonstrates, that the hh excitons have an almost 2D character, whereas the lh excitons are 3D. With the dimensionality parameter known, the effective Bohr-radius  $a^*$  can be calculated according to  $a^* = a_0 / 2\sqrt{D}$  yielding  $90$  Å and  $115$  Å for the hh and lh exciton, respectively.

The striking coexistence of 2D hh and 3D lh excitons in ultrathin InAs layers at a thickness larger than  $1$  ML can be understood as follows: the gain in exciton binding energy, and consequently the reduction in dimensionality, is determined by the degree of localization of electron and hole around the InAs layer. Since the electron is involved in the formation of both hh and lh excitons, the difference in dimensionality is given by the difference of the hh and lh barrier penetration length, which is determined by the hh and lh effective mass and the strength of the confining potential hh and lh experience. In conventional unstrained quantum wells the confinement potential is the same for hh and lh, and the difference in exciton binding energy is solely produced by the difference in hh and lh effective mass. As opposed to that, in ultrathin InAs layers, as a consequence of the compressive strain, the depth of the hh confinement potential is  $2.5$  times larger than for the lh. Therefore, due to the difference in hh and lh band offsets, the difference in hh and lh exciton dimensionality is much more pronounced.

### 3.1.2.2 Experimental Determination of the Exciton Binding Energy

The most effective and direct spectroscopic technique for the determination of the exciton binding energy is PLE. In this absorption-like measurement the transition of the exciton ground state appears one exciton binding energy below the corresponding band-to-band transition. Therefore, as clearly visible in Fig. 3.3 for the lh exciton, the exciton

binding energy can directly be taken from the PLE spectrum as the energy difference between the discrete exciton line and the step-like absorption band of the band-to-band transition superimposed by the Sommerfeld-factor for the absorption of unbound exciton states. From Fig. 3.3 one finds a lh exciton binding energy of 5.5 meV. However, for the hh exciton no similar feature at the hh band-to-band transition is found for two reasons. When the inhomogenous broadening of the hh exciton transition reaches the magnitude of the exciton binding energy, the PLE signal of the exciton ground state transition merges with the PLE from excited exciton transitions ( $n \geq 2$ ) and the PLE originating from band-to-band transitions enhanced by the Sommerfeld-factor for unbound excitons. Another reason why the band-to-band transition is observed for the lh's but not for the hh's, is the 2D character of the hh excitons as opposed to the 3D character of the lh excitons. In 2D, unbound electron-hole pairs create only a weak, structureless enhancement of the absorption above the bandedges, whereas unbound electron-hole pairs in 3D lead to a spectrally sharp, diverging absorption enhancement at the continuum edge. Since the 3D Sommerfeld-factor, as expressed in Eq. (3.4), applies only to strictly 'free' excitons, its observation in PLE not only provides additional evidence for the coexistence of 2D hh and 3D lh excitons in ultrathin InAs layers, but also indicates only weak interface or alloy scattering. Furthermore one should note in Fig. 3.3, that the band-to-band absorption is weaker for the hh related transitions than for the lh related transitions. The magnitude of the band-to-band absorption is proportional to the reduced in-plane effective mass and the reduced barrier penetration depth of the hole states involved. Because hh and lh effective masses are reversed in ultrathin InAs layers, and since the barrier penetration depth is 5 times larger for the lh than for the hh, the band-to-band absorption for lh transitions is effectively by a factor 3 stronger than for the hh transitions.

For the experimental determination of the hh exciton binding energy there are two alternative methods. One previously used by Wang is magneto-PLE<sup>10</sup>, where a magnetic field is applied parallel to the growth direction of the sample. In the magnetic field, Landau levels equidistantly separated by the cyclotron resonance frequency emerge at the high energy side of the zero-field exciton ground state transition. Varying the magnetic field, the exciton binding energy can subsequently be extracted from the

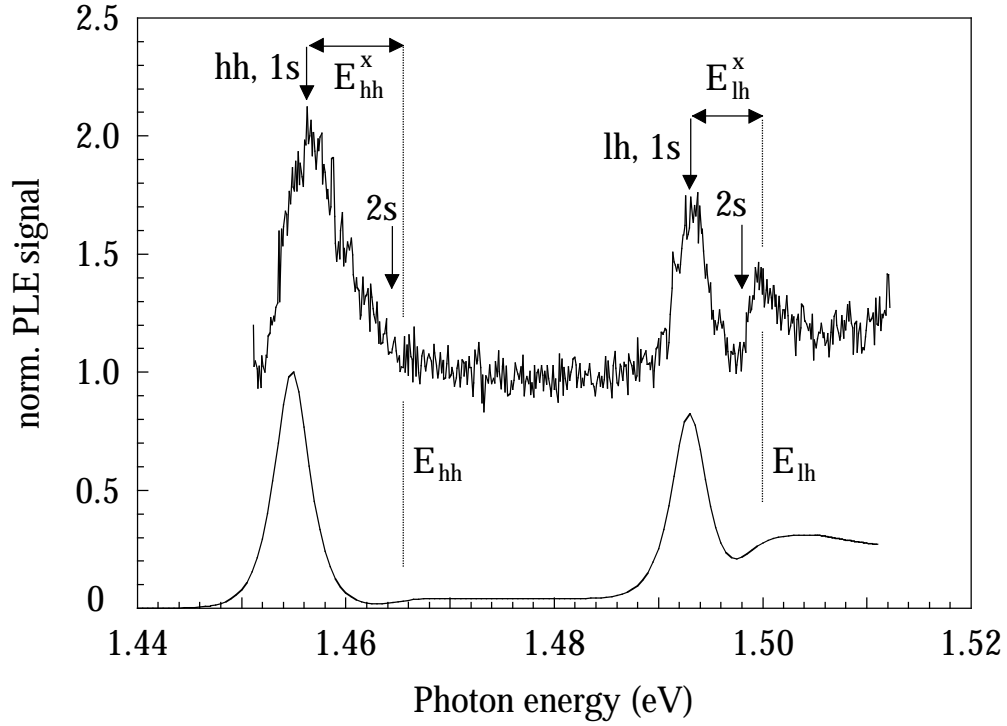


**Fig. 3.3:** Calculated (bottom) and measured (top) PLE spectrum for 1.1 ML InAs. In the calculation of the PLE spectrum no fitting parameters were used but the results for the confined state wavefunctions, confinement energies, exciton binding energies and effective masses as derived in this thesis. For the matrix element of the band-to-band transitions the Kane matrix element for GaAs of 23 eV as reported in Ref. 1 was used. The only free parameter in the calculation is the linewidth of the excitonic absorption due to inhomogeneous broadening, which was derived from the measurement and with which the spectrum was convolved.

extrapolation of the observed change in diamagnetic shift of the Landau-levels to the zero-field limit. The other technique, used in this thesis, is to derive the exciton binding energy from temperature dependent PL measurements. This method is based on the observation that with increasing temperature, the excitonic PL intensity decreases rapidly. Assuming that the PL efficiency is determined by the competition between radiative recombination and non-radiative recombination due to the emission of phonons, the temperature dependent PL efficiency is given by<sup>20, 21</sup>

$$\eta = \frac{p_r}{p_r + p_{nr}} . \quad (3.11)$$

With increasing temperature, the probability increases that the exciton is not in its ground state but in an excited state, whose occupation probability is given by the Boltzmann-distribution. Once an exciton is activated into an excited state, it recombines non-radiatively under the emission of phonons and the PL of the exciton ground state becomes thermally quenched. With the temperature-independent probability  $p_r = p_{r,0}$  for radiative recombination from the exciton ground state, and the temperature-dependent probability for non-radiative recombination after activation into an excited state  $p_{nr} = p_{nr,0} \times \exp(-E_A/kT)$ , the temperature dependent PL efficiency reads

$$\eta = \frac{p_{r,0}}{p_{r,0} + p_{nr,0} \exp(-E_A/kT)}. \quad (3.12)$$

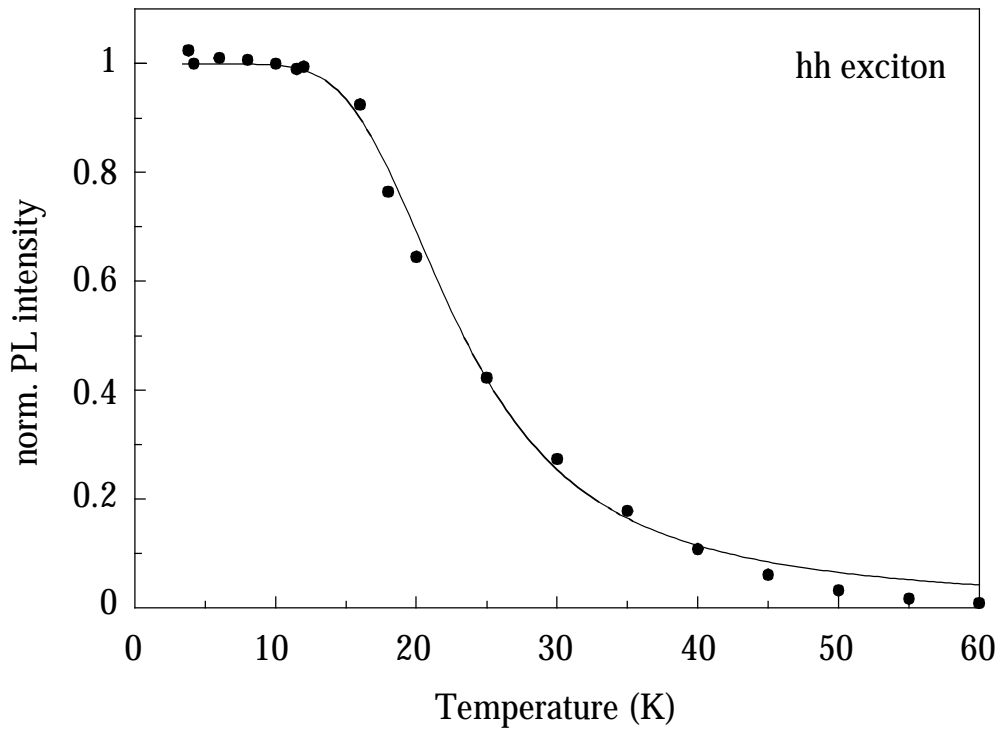


**Fig. 3.4:** Measured hh exciton photoluminescence as a function of temperature. The fit to the data (solid line) yields a hh exciton binding energy of 10 meV.

Here,  $E_A$  denotes the activation energy to thermally activate an exciton from the ground state into an excited state. Since the excited 2s, 3s, ... exciton states are located close to the band-to-band transition,  $E_A$  corresponds to the exciton binding energy. Hence, the



exciton binding can be derived from a least square fit of Eq. (3.12) to the measured temperature dependency of the PL efficiency. From Fig. 3.4 one finds a value for the hh exciton binding energy of 10 meV. This value is in good agreement with results obtained by magneto-PLE by Wang, who found a hh exciton binding energy of 8 meV and 12 meV for a 1 ML and 1.6 ML InAs layer, respectively.

### 3.1.3 Excitons in Coupled Ultrathin InAs Layers

One of the assumptions used for the band offset determination by means of coupling of two InAs layers was, that the observed shift and splitting of the excitonic transitions originates predominantly from a change of the effective confinement energies of the symmetric and antisymmetric states due the coupling, but that changes in the exciton binding energies due to coupling are negligible<sup>22</sup>. A straightforward way to calculate the exciton binding energies for two coupled InAs layers is to replace in the Hamiltonian of Eq. (3.9) the confinement potential  $V(z) = -\hbar^2/m \times \kappa \delta(z)$  of a single InAs layer by the confinement potential of two coupled InAs layers separated by a GaAs barrier of thickness  $L$ , i.e. by  $V(z) = -\hbar/m \times \kappa [\delta(z - L/2) + \delta(z + L/2)]$ . Although this approach is exact, its solution turns out to be quite complex yielding only a numerical solution<sup>23-25</sup>. A physically direct approach to the exciton-in-coupled-wells-problem is found by the following argument: as the discussion of 2D and 3D excitons revealed, the magnitude of the exciton binding energy is determined by the degree of confinement of the electron and hole. For a *single* InAs layer, the exciton binding energy increases with increasing InAs thickness or vice versa with increasing effective electron and hole confinement energy according to Fig. 3.2. This scaling behaviour of the exciton binding energy in a *single* InAs layer can be used to determine the change in exciton binding energy in *coupled* InAs layers. Due to the coupling, each pair of confined symmetric and antisymmetric electron and hole states can lead to the formation of an exciton, in the following denoted as  $X^+$ -exciton (formed by electrons and holes in a symmetric state) and  $X^-$ -exciton (formed by electrons and holes in an antisymmetric state). At infinite barrier width, the exciton binding energy of  $X^+$  and  $X^-$  are identical, since both confined symmetric and antisymmetric states have the same effective confinement energy. With

decreasing barrier width, according to Eq. (2.17) the confinement of the symmetric states increases, whereas the confinement of the antisymmetric states decreases. Consequently, the exciton binding energy of the  $X^+$ -exciton is expected to increase and the exciton binding energy of the  $X^-$ -exciton diminishes. At the critical barrier thickness  $L = L_B$  the antisymmetric state becomes unconfined. Hence, at this barrier thickness the exciton binding energy of the  $X^-$ -exciton will reach the 3D value of  $R^*$ . Another limit value is provided by zero barrier thickness. This case corresponds to a single InAs layer of two times the width and a four times larger confinement. Consequently, the binding energy of the  $X^+$ -exciton is increased up to a value of 13 meV derived from Fig. 3.2 by replacing the InAs thickness  $a$  with  $a' = 2 \times a$ .

Using this approach, the exciton binding energy in coupled InAs layers as a function of barrier width was calculated in the following sequence: firstly, for each barrier width the effective confinement energies of the symmetric and antisymmetric electron states  $E_e^+$  and  $E_e^-$ , respectively, were determined according to Eq. (2.17). Subsequently,  $E_e^+$  and  $E_e^-$  were transformed into an effective width  $a'$  of a *single* InAs layer providing the same effective confinement energy as the *coupled* InAs layer by means of

$$E_e^\pm = -\frac{m_e^* a'^2 V_0^2}{2\hbar^2}. \quad (3.13)$$

Finally, with  $a'$  as a result for the symmetric and antisymmetric state, the exciton binding for the  $X^+$  and  $X^-$  exciton was calculated with the zero-radius potential model as discussed in Section 3.1.2.1.

The following discussion of the coupling induced change of the exciton binding energy can be restricted to the hh excitons since the enhancement of their binding energy with respect to the 3D value is larger and more sensitive to changes in the effective carrier confinement (see Fig. 3.2). Furthermore, according to the zero-radius potential model one can assume, that the hh's are much stronger localized by the confinement potential of the InAs layer than the electrons and that therefore the change of exciton binding in coupled InAs layers is governed by the coupling induced change of the effective confinement energy of the symmetric and antisymmetric electron states.

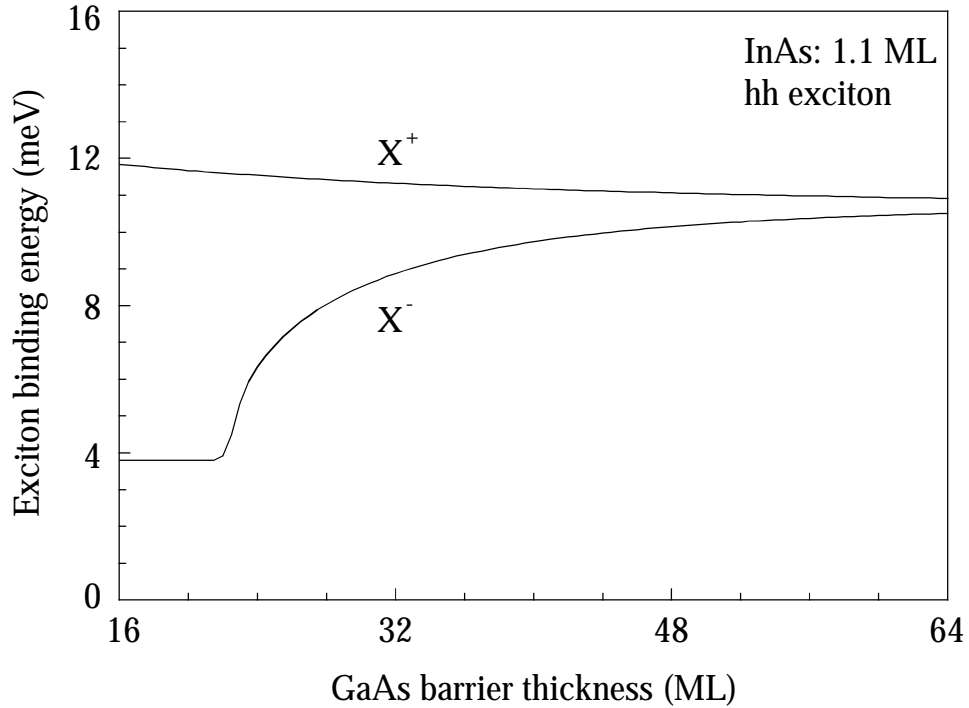


**Fig. 3.5:** Coupling induced change of the hh exciton binding energy as a function of GaAs barrier width. The calculations were performed using a thickness of 1.1 ML for both InAs layers.

As shown in Fig. 3.5, at a barrier thickness of 64 ML, the difference in exciton binding energy between the  $X^+$  and  $X^-$  exciton is smaller than 0.5 meV. This small difference in exciton binding energy reflects the weak interaction of the  $X^+$  and  $X^-$  excitons at distances only slightly smaller than overlapping Bohr-radii ( $L \approx 2 \times a_0$ ). With decreasing barrier thickness, the overlap between both types of excitons increases and, according to the change in effective confinement energy of the symmetric and antisymmetric electron state, the  $X^+$  exciton binding energy increases, whereas the one of the  $X^-$  exciton diminishes. At approximately 20 ML barrier thickness, the  $X^-$  exciton binding energy reaches the 3D value of 4.5 meV, since the barrier thickness amounts to the critical barrier thickness  $L_B$  for a monolayer thick InAs layer where the antisymmetric electron state becomes unbound. At zero barrier thickness, the  $X^+$  exciton binding energy approaches the limit value of 13 meV associated with a single InAs layer of an effective thickness of  $a' = 2 \times a = 2$  ML. For the determination of the hh band offset from the coupling induced red-shift of the lowest lying  $hh_+$  transition as discussed in Chapter 2 it is important to note, that over the whole range of barrier thickness the variation of the  $X^+$  exciton binding energy is smaller than 2.5 meV. Hence, from the

totally observed red-shift of 54 meV only 4 % can be attributed to the change in exciton binding energy. In addition, for a 32 ML barrier sample, the difference in the exciton binding energy of the  $X^+$  and  $X^-$  exciton is smaller than 2 meV. For this sample a coupling induced splitting of the  $hh_+$  and  $hh_-$  transition of 13 meV was measured. The subsequently derived conduction band offset may thus be overestimated by maximum 10 %.

### 3.2 Doubly Resonant Raman Scattering and Resonant Luminescence

With the effective electron,  $hh$ , and  $lh$  confinement energies and the  $hh$  and  $lh$  exciton binding energies known as a function of InAs layer thickness, a particularly interesting situation can be created when the InAs layer thickness lies between 1.2 ML and 1.6 ML. At this thickness, electron,  $hh$ , and  $lh$  states are well confined and the energy separation between the  $hh$  and  $lh$  exciton transitions amounts to one GaAs LO phonon. Under resonant excitation of the  $lh$  exciton transition, this configuration of optical transitions gives rise to the observation of resonant excitonic effects such as hot exciton relaxation (HER), resonant luminescence (RL) and doubly resonant Raman scattering (DRRS), seen as sharp emission lines additional to the ordinary PL<sup>26, 27</sup> since exciting and detected photons are both resonant with a real state of the sample. Those effects have been observed before in GaAs/ $Al_xGa_{1-x}As$  quantum wells, where the incoming and outgoing photons were either resonant with two  $hh$  transitions<sup>28, 29</sup> or with a  $lh$  transition and a  $hh$  transition<sup>30</sup>, and both transitions were separated by one or an integer multiple of the LO phonon energy.

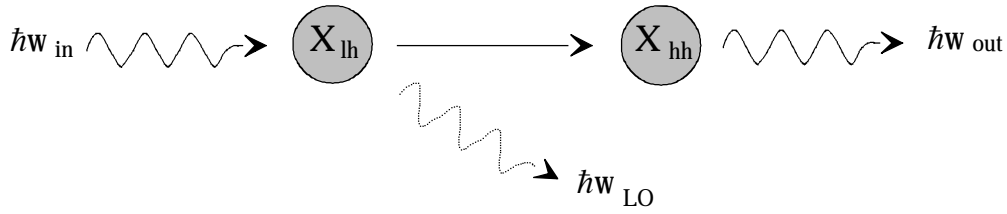
As illustrated in Fig. 3.6, the resonant excitonic effects, HER, RL and DRRS, can be distinguished as follows:

HER is the incoherent succession of two single photon processes [see Fig. 3.6(a)]. The exciting photon is absorbed and creates a  $lh$  exciton. The  $lh$  exciton subsequently relaxes under emission of one LO phonon to an unoccupied  $hh$  exciton state and recombines within the  $hh$  exciton lifetime. From rate equation analysis it follows that this process only leads to a sharp emission line of reasonable intensity if the relaxation time is much faster than the  $hh$  exciton lifetime and the time required for the further

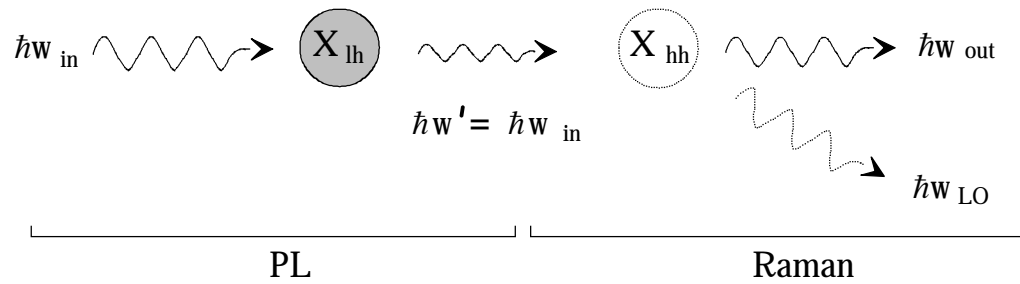
thermalization of the hh excitons by acoustic phonons. The fast relaxation of the lh excitons in turn leads to an efficient depopulation of the lh exciton state, so that the lifetime, which one measures for the lh excitons, is basically as short as the relaxation time. Furthermore, due to the fast relaxation of the lh excitons, the narrow spectral distribution of created lh excitons, which is entirely determined by the spectrum of the exciting laser beam, is transformed into a narrow spectral population of hh exciton states, which within the hh exciton lifetime will be subsequently broadened. If a sharp emission line originates from HER, its transient behaviour will be determined by the hh exciton lifetime and the time required for thermalization of the hh excitons by acoustic phonon scattering, whereas the lh exciton lifetime will be measured to be much shorter than the hh exciton lifetime. The emission intensity of the sharp line depends on the excess density pumped into the lh exciton state, i.e. on the absorption at the particular excitation energy, and its spectral width is determined by the LO phonon broadening and the broadening due to acoustic phonon scattering.

In a three level system like ultrathin InAs layers, which provide a single confined electron, hh, and lh state, two RL processes are possible [see Fig. 3.6(b)]: in one RL process an incoming photon is absorbed by creating a lh exciton. The lh exciton subsequently recombines within its lifetime under emission of a photon at the same energy. This emitted photon can be efficiently scattered by one LO phonon, because the emitted photon and the scattered photon are both resonant with a lh and hh exciton state, respectively. In another RL process the created lh exciton recombines under emission of one LO phonon and a photon, which is resonant with a hh exciton state. In both cases RL is the incoherent succession of two single photon processes, which occurs over the lh exciton lifetime. As for HER, both RL processes depend on the absorption of the lh transition. If either of the RL processes produces a sharp emission line one LO phonon below the excitation energy, its decay time should be identical with the lh exciton lifetime. Its spectral width is determined by the broadening of the spectral narrow population pumped into the lh exciton state due to thermalization by acoustic phonons, which can occur within the lh exciton lifetime, and by LO phonon broadening. Because both RL processes have the same spectral and transient behaviour, they will not be discussed separately in the following.

i. resonant "hot" exciton relaxation (HER):



ii. resonant luminescence (RL):



iii. double resonant Raman scattering (DRRS):

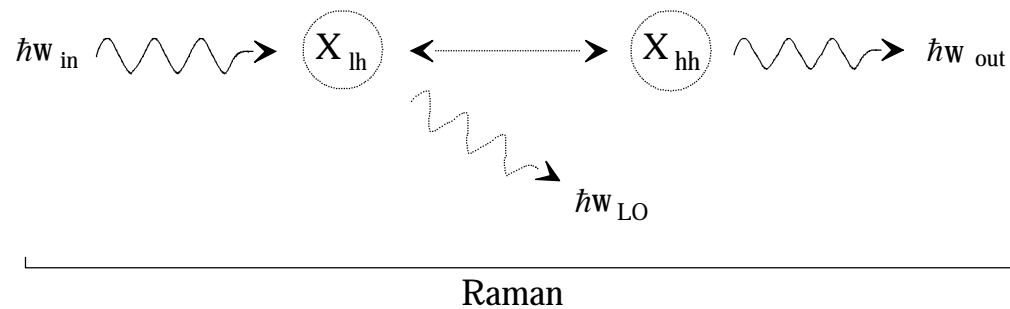


**Fig. 3.6:** Schematic representation of hot exciton relaxation (HER), resonant luminescence (RL) and doubly resonant Raman scattering (DRRS). All three processes lead to a sharp emission line besides ordinary photoluminescence. Filled circles indicate population of the hh and lh exciton states.

As opposed to RL, DRRS is a single coherent two-photon process, which does not involve any population of the lh and hh exciton states and which is, for that reason, independent of the absorption of the lh exciton transition<sup>31</sup> [see Fig. 3.6(c)]. The incoming photon is in resonance with the lh exciton state, and therefore it can be efficiently scattered in a Raman process by creation or annihilation of a LO phonon. The outgoing, scattered photon is also in resonance with the hh exciton state, which further enhances the scattering efficiency. As a Raman process, DRRS occurs over the

dephasing time of the lh exciton<sup>28</sup>. Thus, if DRRS produces a sharp emission line one LO phonon below the excitation energy, its decay time is identical to the lh exciton dephasing time, and its spectral width is determined by LO phonon broadening only.

### 3.2.1 Sample Growth and Characterization

In order to investigate whether ultrathin InAs layers embedded in a GaAs matrix exhibit HER, RL or DRRS, a single InAs layer structure similar to the one described in Chapter 2 was synthesized by MBE with a designed InAs thickness between 1.2 and 1.6 ML to meet the requirement for the observation of resonant excitonic effects, i.e. the energy separation between hh and lh exciton transition amounts to one LO phonon. The sample was grown on semi-insulating (100) GaAs substrate. After oxide desorption a 300 nm thick GaAs layer was grown at 600 °C, followed by a 40 period 25 Å / 25 Å GaAs/Al<sub>0.4</sub>Ga<sub>0.6</sub>As superlattice. After growing a 200 nm thick GaAs layer, the substrate temperature was lowered down to 450 °C and the arsenic beam equivalent pressure was increased from  $3 \times 10^{-6}$  to  $10^{-5}$  Torr to grow 100 Å of GaAs and the InAs layer. After growing 20 Å of GaAs, the substrate temperature was increased to 600 °C and the arsenic pressure reduced to  $3 \times 10^{-6}$  Torr to grow a 200 nm thick GaAs layer followed by a 40 period 25 Å / 25 Å GaAs/Al<sub>0.4</sub>Ga<sub>0.6</sub>As superlattice. The low substrate temperature and the high arsenic pressure were used to minimize In segregation<sup>32, 33</sup>. The two superlattices avoid surface or substrate traps and suppress surface or substrate related electric fields. The structure was grown without growth interrupts. In order to eliminate any possible external strain, the substrate was chemically polished and the sample was held by paper frames on the actual sample holder. The thickness of the InAs layer was subsequently determined by comparing the measured rocking curve of the (400) reflection using double crystal X-ray diffraction with simulations based on the dynamical theory. For this sample an InAs layer thickness of 1.4 ML was found.

The sample was characterized by standard PL in near backscattering geometry at 4.2 K using a HeNe-laser at 1.96 eV and a cooled CCD detector. Around the GaAs bandgap the spectra show between 1.5154 eV and 1.5128 eV a well-resolved GaAs free exciton and two donor bound exciton lines. Below the GaAs bandgap the PL line of the

InAs hh exciton transition is observed at 1.445 eV, which is about 650 times stronger than the GaAs exciton line. The comparatively large 7.9 meV FWHM of the hh exciton PL, indicating inhomogeneous broadening, will be discussed in detail at the end of this Chapter. According to the calculations in Fig. 2.18, the observed spectral position of the hh exciton transition is consistent with the InAs thickness determined by X-ray suggesting the lh exciton transition to emerge around 1.485 eV.

### 3.2.2 Observation of Resonant Excitonic Effects in CW Experiments

As depicted in Fig. 3.7, in the doubly resonant cw experiments the sample was excited by a tuneable Ar<sup>+</sup> pumped Ti:sapphire laser with a measured FWHM of the laserline of 0.25 meV. The excitation wavelength was tuned on the lh transition and the emission spectrum around the hh transition was measured using a 2×0.85 m double monochromator with a spectral resolution of better than 0.1 meV and a cooled photomultiplier in the single-photon-counting mode.

Fig. 3.8(a) shows the emission spectra of the 1.4 ML InAs layer recorded in near back-scattering geometry under  $z(x,x)\bar{z}$  configuration at 4.2 K for different excitation energies within the lh exciton transition. The polarization in the plane of the InAs layer is defined as  $x \parallel [100]$ ,  $y \parallel [010]$ ,  $x' \parallel [110]$ ,  $y' \parallel [1\bar{1}0]$  with  $z \parallel [001]$  as growth direction. Under excitation of the lh exciton transition an additional sharp line on the high energy side of the hh exciton PL appears, which shifts in energy by the same amount as the excitation energy is shifted. As shown in Fig. 3.8(b), when the excitation energy is tuned through the lh exciton transition, at the high energy side the intensity of the sharp line follows the same lineshape as observed by the PLE signal of the ordinary hh exciton transition. At the low energy side the intensity of the sharp line falls off slower than the PLE signal, however, the sharp line disappears when the laser is completely detuned from the lh transition. When increasing the excitation density by four orders of magnitude, the intensity of the sharp line increases strictly linear with the excitation density. Furthermore, the sharp line has a FWHM of  $0.5 \pm 0.06$  meV, which does not change noticeable by varying the excitation energy or by increasing either the excitation density or the temperature. From the narrow linewidth and the fact, that the



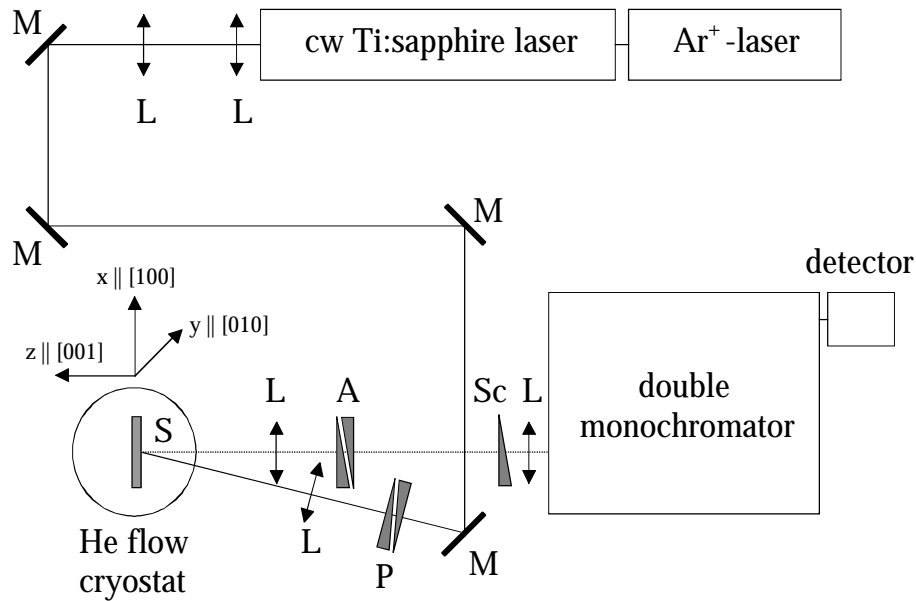


**Fig. 3.7:** Experimental set-up for resonant excitation cw experiments. L: lens, M: mirror, A: analyzer, P: polarizer, Sc: scrambler.

excitation occurs at the low energy side of the donor-to-acceptor-transition, a phonon replica or selective pair luminescence line<sup>34, 35</sup> can be excluded as the origin of the sharp line. For clarity, Fig. 3.9 displays the peak position of the hh exciton PL and of the sharp line versus the excitation energy, which shows that the sharp line appears consistently  $36.56 \pm 0.12$  meV below the excitation energy. This suggests, that the three distinct processes described earlier, namely hot exciton relaxation (HER), resonant luminescence (RL) or doubly resonant Raman scattering (DRRS), can be responsible for the sharp line since they all involve one GaAs LO phonon. The interaction with GaAs LO phonons rather than InAs phonons in all three processes can be understood by the fact that the lh and hh excitons, bound to the InAs layer, extend entirely in the GaAs matrix, whereas the GaAs phonon mode is only weakly perturbed by the thin InAs layer<sup>26, 36-38</sup>. Because the excitons are bound to the InAs layer,  $k$  is not strictly a good quantum number anymore and the excitons can also interact with phonons having a momentum slightly higher than  $q=0$ . Taking the GaAs LO phonon dispersion over the inverse exciton Bohr-radius leads to an effective phonon mode with an energy spread of approximately 0.1 meV. In combination with the results of the transient properties of the sharp line presented below, this phonon broadening is likely to be the origin of the slightly larger width of the sharp line in excess of the linewidth of the exciting laser.

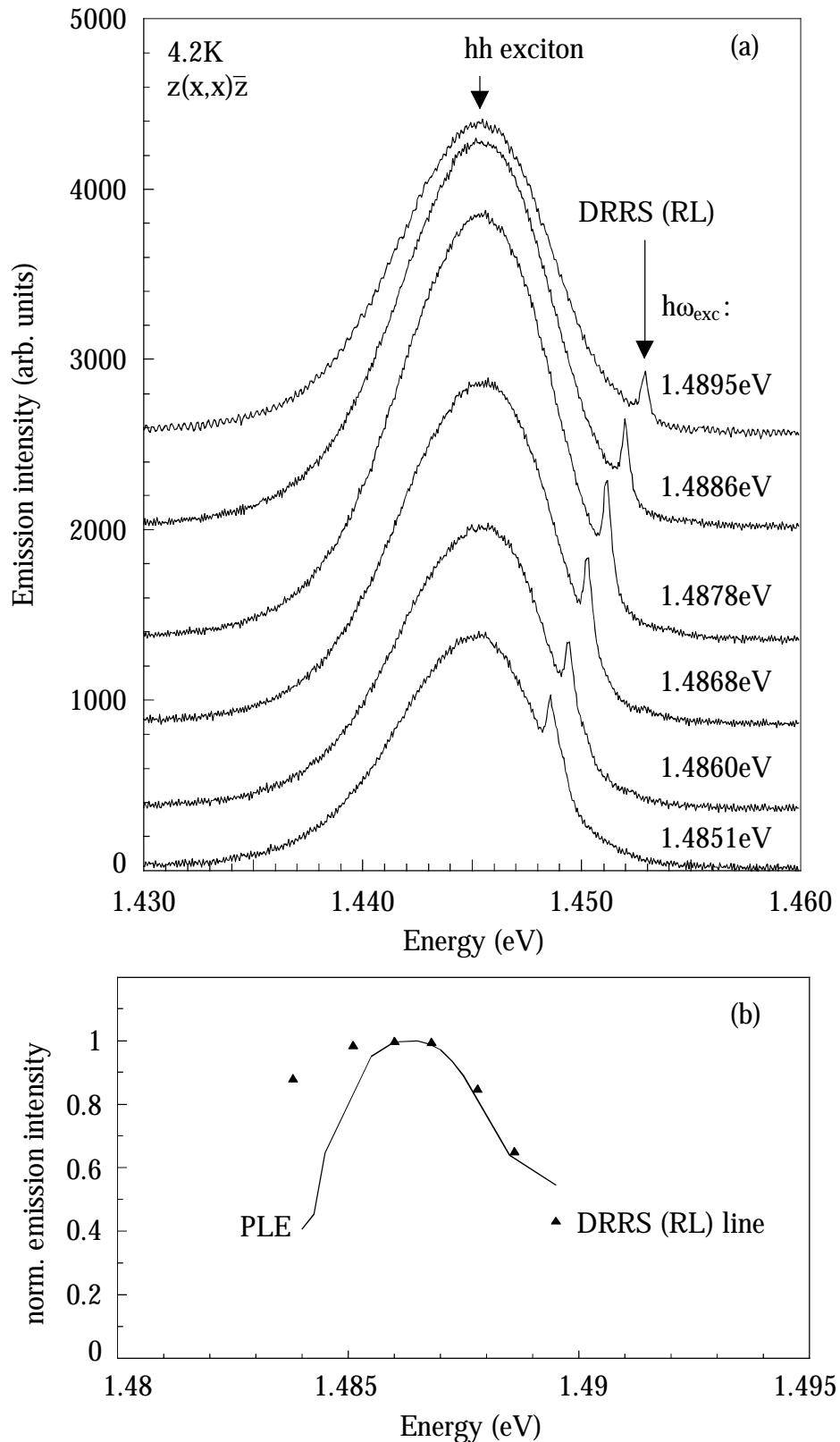


**Fig. 3.8:** (a) Emission spectra of the 1.4 ML InAs layer under excitation on the lh exciton transition for different excitation energies recorded at 4.2 K and near-backscattering geometry. Under excitation of the lh exciton transition a sharp line labelled as DRRS (RL) appears on the high energy side of the ordinary hh exciton PL. (b) Comparison of the lh exciton PLE and the DRRS (RL) line intensity.

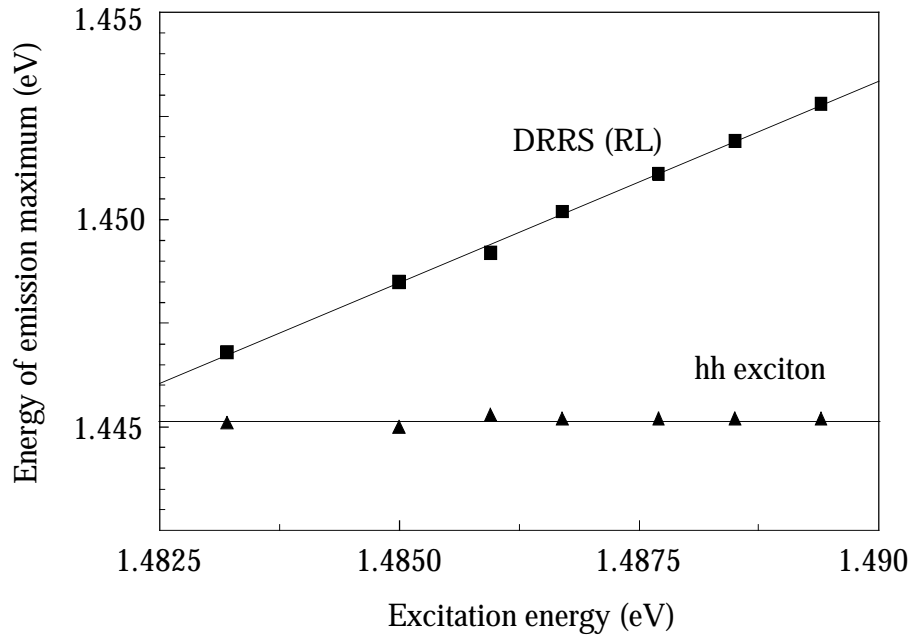


**Fig. 3.9:** Energy position of the emission maximum of the hh exciton PL and the DRRS (RL) line as a function of excitation energy. No shift of the hh PL line is observed, whereas the DRRS (RL) line always appears  $36.56 \pm 0.12$  meV below the excitation.

### 3.2.3 Distinction of the Resonant Excitonic Effects by Time-Resolved Experiments

Although HER, RL and DRRS are distinct processes, they can be simultaneously present<sup>31, 39-41</sup>, and they all lead to the observed sharp emission line with similar spectral properties when hh and lh exciton transitions are resonantly coupled by LO phonons. From the above description of the three processes it can be seen, that they can hardly be distinguished by the properties of that sharp emission line in cw experiments, especially when they involve the same number and type of phonons<sup>31, 39, 42</sup>, because the only parameter, which reflects the individual process, is the linewidth of the sharp emission line. However, each process has an individual impact either on the decay time of the sharp emission line or on the lh exciton lifetime, thus the transient behaviour of the sharp emission line acts as a fingerprint for each individual process.

In order to investigate whether the origin of the sharp line is DRRS (occurring over the dephasing time), RL (occurring over the lh exciton lifetime) or HER (occurring over the hh exciton lifetime accompanied by a short lh exciton lifetime), time-resolved

measurements on the decay time of the sharp line and the hh exciton lifetime were performed using time-correlated-single-photon-counting (TCSPC). Because no lh exciton PL was observed, the lh exciton lifetime was measured by two-wavelength time-resolved pump-probe phototransmission, which will be described in detail in Chapter 4.

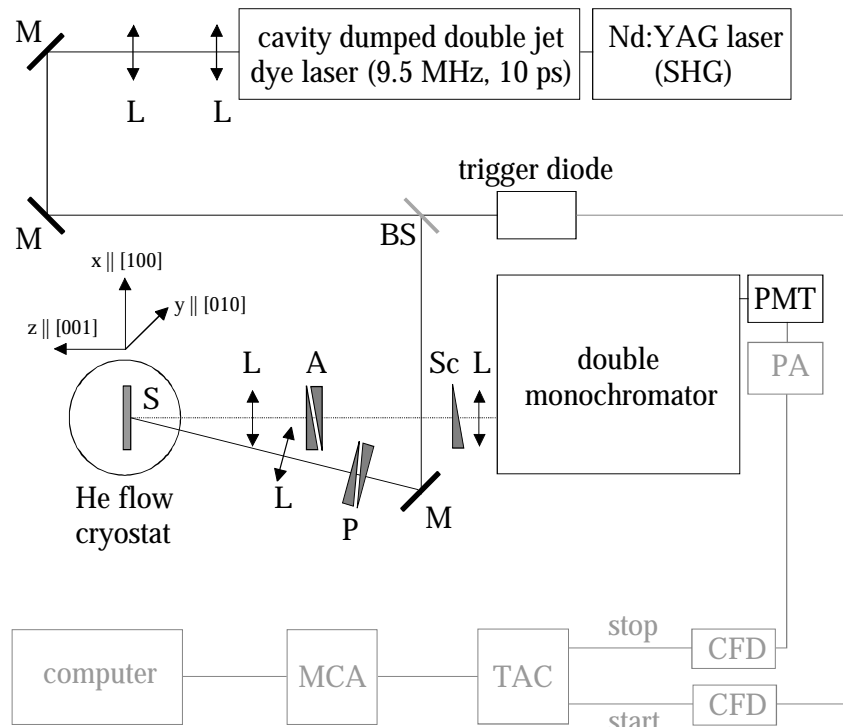


**Fig. 3.10:** Time-correlated single photon counting (TCSPC) set-up for the measurements of the decay time of the sharp DRRS (RL) line. PMT: photomultiplier, PA: pulse amplifier, CFD: constant fraction timing discriminator, TAC: time-to-amplitude converter, MCA: multi-channel analyzer.

As depicted in Fig. 3.10, in the TCSPC experiments the sample was excited with a Styryl 8 laser equipped with a cavity dumper and a 3-plate birefringent filter pumped by a mode-locked frequency doubled Nd:YAG laser. To achieve the best compromise between pulse width and spectral width, 10 ps pulses (FWHM) with a spectral linewidth of 0.32 meV were used. In comparison with the cw measurements the slightly wider laser line results in a somewhat larger 0.6 meV FWHM of observed sharp DRRS (RL) line. In order to avoid local heating of the sample, but to get a reasonable signal-to-noise ratio, all measurements were performed with an unfocussed laser beam with 10 mW cw power at a repetition frequency of 9.5 MHz. The time response of the standard TCSPC set-up, determined by the time response of the trigger diode and the transit time spread

in the monochromator and photomultiplier tube, had a risetime of 225 ps and the minimum detectable decay time was 275 ps.

Firstly, the hh exciton lifetime was measured under excitation above the GaAs bandgap with the monochromator set to different detection energies within the hh exciton PL, and subsequently under resonant excitation of the lh exciton transition with the detection energy set to the maximum of the hh exciton PL. As displayed in Fig. 3.11, the hh exciton lifetime amounts to 485 ps regardless of the excitation energy and no variation is found for detection energies within the hh exciton PL line.

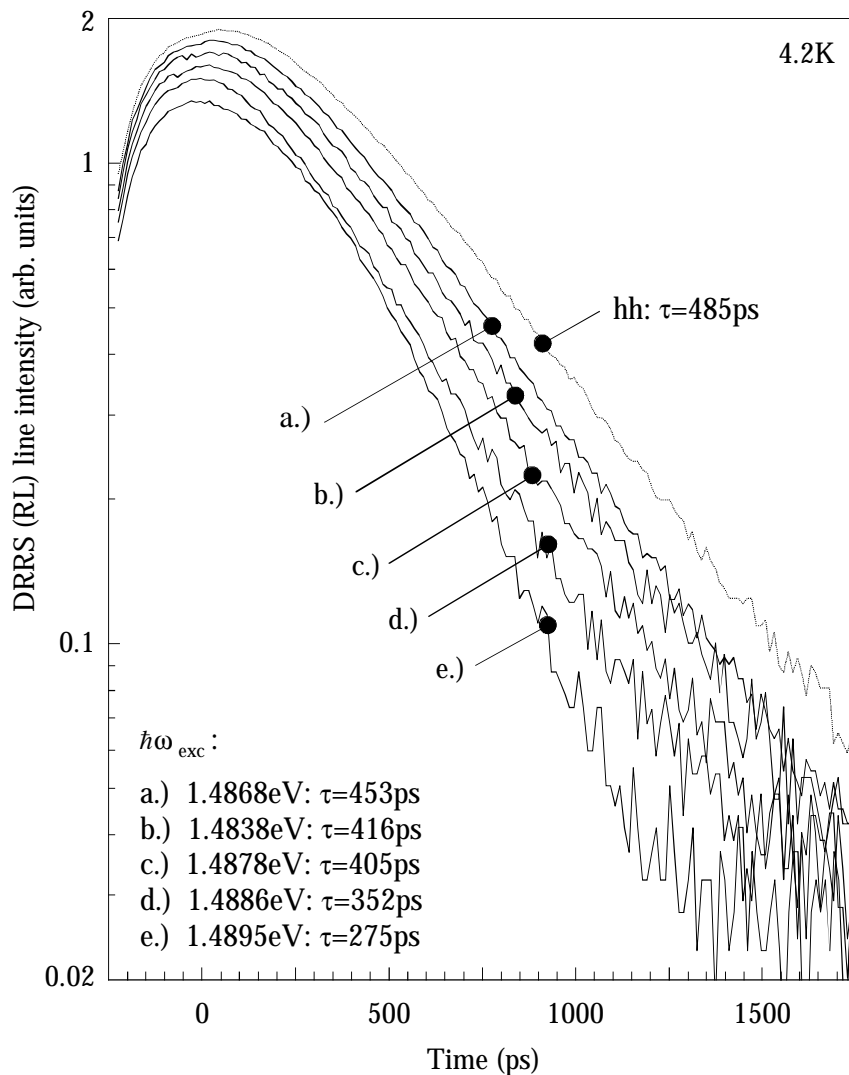


**Fig. 3.11:** Transients of the decay of the hh exciton PL (dotted) and the DRRS (RL) emission line (solid) at different excitation energies. During the transient measurements the excitation energy was set to the values as given in the figure, and the detection energy was set to the actual maximum of the hh exciton PL or the DRRS (RL) line. Since the hh PL decay time turned out to be independent of the excitation energy, only the measurement with an excitation of 1.4868 eV is shown.

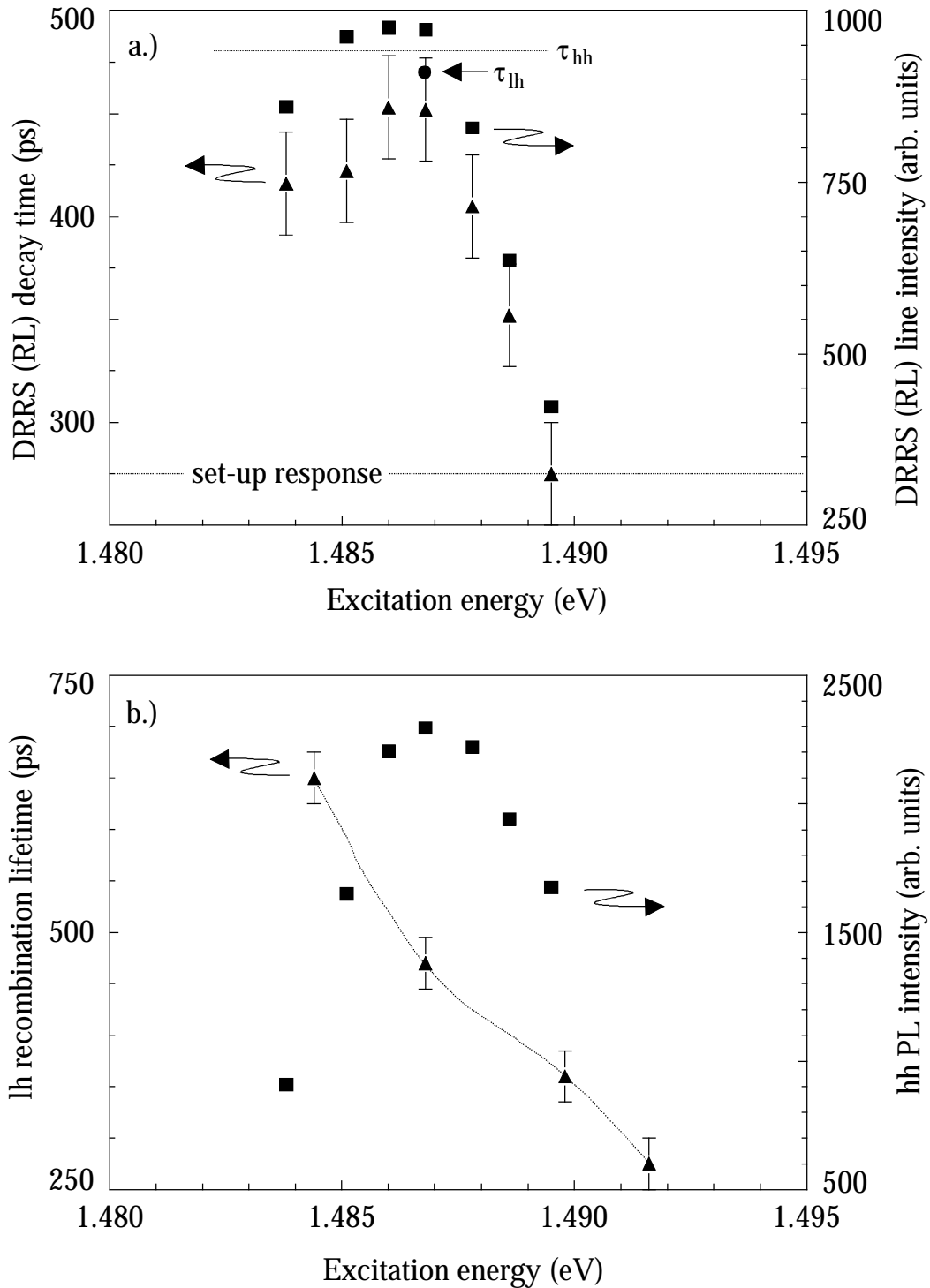


**Fig. 3.12:** (a) Decay time (▲) and maximum intensity (■) of the DRRS (RL) line as a function of excitation energy. On resonance at 1.4868 eV the measured decay time of the DRRS (RL) line equals the lh exciton lifetime (●)  $\tau_{lh}$ . Off resonance at 1.4895 eV the measured decay time is basically the set-up response corresponding to a decay time as short as the laser pulse. The hh exciton lifetime  $\tau_{hh}$  is independent of the excitation energy (dotted line). (b) lh exciton lifetime (▲) and maximum of the hh exciton PL (■) as a function of excitation energy. Off resonance at 1.4895 eV the lh exciton lifetime is 100 ps larger than the decay time of the DRRS (RL) line shown in (a).

Secondly, the lh exciton lifetime was measured with the photon energy of the pump beam set above the GaAs bandgap and the detection energy of the probe beam set to different values within the lh exciton transition. As shown in Fig. 3.12(b), the lh exciton lifetime decreases monotonically from 650 ps at 1.4844 eV to 370 ps at 1.4895 eV. This result already suggests that HER is unlikely to be the origin of the sharp emission line for the following reason: the occurrence of HER requires a pair of hh and lh exciton states separated by the GaAs LO phonon energy. The observation of the sharp line at any excitation energies within the lh exciton transition indicates that this condition is fulfilled over the whole width of the lh exciton transition. Because a relaxation of the lh excitons by LO phonon emission leads to a fast depopulation of the lh exciton state, the lh exciton lifetime is limited by the exciton relaxation time, and therefore it should be much shorter than the hh exciton lifetime over the *whole width* of the lh exciton transition. In turn, the increase of the lh exciton lifetime towards lower energies could indicate a blocking of the fast exciton relaxation by e.g. the lack of hh exciton states with an energy separation of 36 meV or their pre-occupation by captured holes. However, if HER was the origin of the sharp line, this blocking should be accompanied with the disappearance of the sharp line at excitation energies where no pairs of unoccupied hh exciton and populated lh exciton states with an energy separation of 36 meV are found. An additional argument against HER as the origin of the sharp line results from the observed linewidth of 0.5 meV, which is only 0.25 meV broader than the exciting laser beam. With typical exciton relaxation times of several 100 fs to 1 ps<sup>43, 44</sup> leading to a transform limited broadening of more than 0.7 meV, one should expect a linewidth in the case of HER of more than 1 meV.

The origin of the decrease of the lh exciton lifetime towards higher photon energies is twofold: on one hand, as explained in detail in Chapter 4, in a 1 - 1.4 ML thick InAs layer the holes are captured in a two-step process with the confined lh levels acting as an intermediate capture state, from which captured holes can relax to the confined hh levels. Depending on whether the energy separation between occupied lh levels and unoccupied hh levels is smaller or larger than the GaAs LO phonon energy, the hole relaxation occurs either in an acoustic phonon cascade requiring several tens of ps or within approximately 1-2 ps by the emission of one LO phonon. As shown in the rate equation analysis in Chapter 4, in the latter case the fast hole relaxation leads to a

depletion of the hole reservoir, which can participate in the formation of lh excitons, which is observed as a decrease of the measured phototransmission decay time towards the high energy side of the lh exciton transition. The other reason for the decrease in the lh exciton lifetime is related to the 3D character of the lh excitons and relatively weak confinement of the lh. With an effective confinement energy of 4.5 meV, lh's can escape from the lh state by thermal emission. Probing the lh transition at higher photon energies involved lh states with a confinement energy closer to the thermal activation energy, and consequently leads to an increasing thermally activated depopulation of lh exciton states. A similar process is applicable for the lh excitons itself. With an exciton binding energy of 5 meV and the 3D character, only 2.5 meV are required to thermally activate a lh exciton from its ground state to the first excited state. According to Section 3.1.2.2, this leads to an increase of the non-radiative recombination rate, and thus to a decrease of the non-radiative lifetime. Since the observed lifetime for the exciton ground state  $\tau_{lh}$  is related to the intrinsic radiative lifetime  $\tau_r$  and the non-radiative lifetime  $\tau_{nr}$  by  $1/\tau_{lh} = 1/\tau_r + 1/\tau_{nr}$  the thermal activation into an excited exciton state is observed as a decrease of the measured exciton lifetime.

In order to further separate RL from DRRS, the decay time of the sharp emission line was measured at different excitation energies within the lh exciton transition. The results are shown in Fig. 3.11 and Fig. 3.12(a), where the decay time of the sharp line is plotted together with the maximum intensity of the sharp line for different excitation energies. The first striking result is that the decay time of the sharp line changes drastically when the excitation energy is tuned through the lh exciton transition. This again proves that HER cannot be the origin of the sharp line, because otherwise the decay time should equal to the hh exciton lifetime. Moreover, at higher excitation energies the decay time of the sharp line decreases even more strongly than the lh exciton lifetime.

If one compares the maximum emission intensity of the sharp line and of the hh exciton PL, which is shown in Fig. 3.12(b) and which as an ordinary PLE spectrum is a measure for the absorption around the lh exciton transition, one may conclude that the sharp line is entirely due to RL. Since the population in the lh exciton state is governed by the absorption, it serves in a RL process as a source of photons for the subsequent emission process. Nevertheless, in a RL process the decay time of the sharp line should



be equal to the lh exciton lifetime at any excitation energy. From a comparison of Fig. 3.12(a) and Fig. 3.12(b), it follows that this is only the case for an excitation energy of 1.4868 eV, which in the following is referred to as excitation on resonance. There the lh exciton lifetime was found to be 470 ps and the decay time of the sharp line amounts to 455 ps. In contrast, the more the excitation energy is tuned off resonance, the more the decay time of the sharp line decreases. When the laser is tuned 3 meV off resonance towards higher energies, the decay time of the sharp line reaches its minimum detectable value of 275 ps, whereas the lh exciton lifetime is still 100 ps higher. By tuning the excitation off resonance towards lower energies, where the lh exciton lifetime increases up to 650 ps, also a decrease of the decay time of the sharp line is observed, although not as clear as on the high energy side. This is simply due to the experimental fact, that the RL or DRRS spectrum is superimposed on the ordinary hh exciton PL, i.e. the closer the RL or DRRS line lies at the maximum of the hh exciton PL, the more the detected signal contains photons from the ordinary recombination of the hh excitons with a lifetime of 485 ps. Since RL and DRRS are always simultaneously present, the experimental results suggest, that the sharp line is predominantly due to RL for excitation on resonance, whereas off resonance its origin is DRRS.

Additional evidence for the result that in the case of excitation on resonance the sharp line originates from RL is provided by a recent polarization analysis of the sharp line for the special case of the excitation on resonance reported by Wang et al.<sup>26, 28</sup>. One of their main results was, that for excitation on resonance, the exciton-phonon interaction via the deformation potential is negligible. Then the ratio between the fluorescence and Raman component, expressed by the lifetime  $\tau_{lh}$  and the dephasing time  $T_2$  of the lh excitons, amounts to<sup>8,16</sup>

$$\frac{T_2}{\tau_{lh}} = \frac{1 - 2I(y', x')}{2I(y', x')} = 0.089, \quad (3.14)$$

where  $I(y', x')$  was normalized according to  $I(+, +) + I(+, -) = 1$ . Consequently, the Raman component of the sharp line is insignificant compared to the resonant luminescence component. Moreover, with the above determined lh exciton lifetime of

470 ps for excitation on resonance from Eq. (3.14) the lh exciton dephasing time is found to be  $T_2 \approx 40$  ps at this particular energy. This result will be discussed below.

For the discussion of the origin of the sharp line under excitation off resonance, it is important to remember that the RL process entirely depends on the excess population pumped into the lh exciton state, whereas the DRRS process does not. When the excitation energy is tuned off resonance, the excess population in the lh exciton state decreases according to the absorption at the lh exciton transition, whereas the contribution from DRRS does not change, since the incoming and outgoing photons are still in resonance with bound lh and hh exciton states, respectively. Consequently, the RL component decreases with respect to the DRRS component, and the sharp line becomes predominantly Raman-like. Moreover, the RL process decays with the lh exciton lifetime, whereas the DRRS decays with the dephasing time of the lh exciton, which according to Eq. (3.14) is in the order of 40 ps. At an excitation energy of 1.4895 eV the measured decay time of the sharp line is basically the set-up response, which on one hand is already considerably smaller than the lh exciton lifetime at this energy, and which on the other hand corresponds to a real decay time much smaller than 275 ps. The fact that, while going off resonance, the sharp line continuously changes its origin from RL to DRRS, and that additionally the lh exciton lifetime decreases, explains the experimental observation that all transients show a single exponential decay.

### 3.2.4 Temperature Dependence of the Resonant Excitonic Effects

For the observation of RL and DRRS it is essential that both intermediate states coincide with real, bound states. If one of the states becomes a scattering or continuum state, only either the incoming or the outgoing photon is in resonance with a bound state and the scattering efficiency decreases to the value of usual resonant Raman scattering. In addition, since the scattering efficiency of the RL and DRRS processes depends on the time during which the phase of the bound state wavefunctions is preserved, it is important if the hh and lh exciton states are localized<sup>45, 46</sup> or delocalized<sup>42, 47-49</sup>. Generally, in the case of a localized state, the exciton is ‘trapped’ into a valley of local

potential fluctuations originating from local strain fields or lateral fluctuations in the In concentration from which it cannot escape. Since an exciton in a localized state cannot contribute to energy transfer, the state is undamped yielding a large coherence volume and a large scattering efficiency. Localized excitons can also interact efficiently with the crystal lattice by means of Fröhlich interaction. A localized exciton produces a local polarization of the lattice through Coulomb interaction between electron and hole. When the exciton recombines or the exciton state collapses the lattice polarization is removed under emission of a LO phonon. In contrast, an exciton in a delocalized state is characterized by a non-vanishing probability for leaving the local potential, by e.g. absorption of acoustic phonons or thermal activation. Therefore, it can contribute to energy transport by means of a hopping process. Because each hopping event breaks the phase of the state, the state becomes damped which reduces the scattering efficiency.

The transition between localized and delocalized states is not abrupt. As described in Ref. 50, the hopping or escape rate from a localized state is a continuous function of the localization energy, i.e. the closer a localized state is located to the mobility edge, the more the character of the state becomes delocalized. Even a small temperature rise can thus weaken the exciton localization and reduces the intensity of the sharp line.

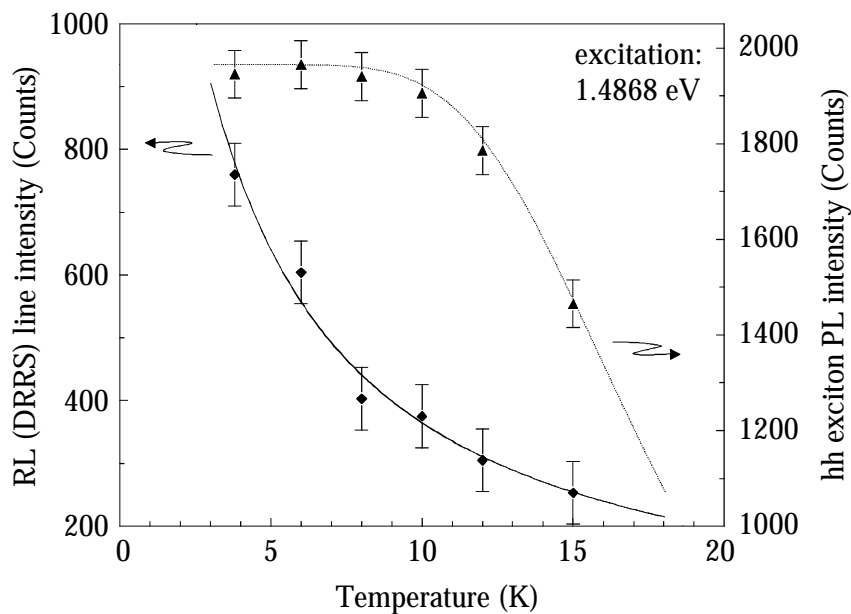


**Fig. 3.13:** Maximum intensity of the DRRS (RL) line (●) at different temperatures recorded under excitation on resonance at 1.4868 eV. At 18 K the sharp line was no longer detectable. The solid line shows the best fit to the data assuming thermal activation of excitons from their localized state. For comparison, the temperature dependent hh PL as measured (▲) and calculated (dotted line) is shown.

The maximum intensity of the sharp line under excitation on resonance at 1.4868 eV for different temperatures is shown in Fig. 3.13. The intensity of the sharp line decreases dramatically without any line shift or noticeable line broadening by increasing the temperature from 3.8 to 18 K, where the line was not detectable anymore. A possible effect of thermal detuning of the exciton transitions was eliminated experimentally by compensating the possible changes in lh and hh exciton transition energies due to the temperature rise with a detuning of the excitation energy by an amount of  $k_B\Delta T$  to lower energies, whereby no subsequent increase of the line intensity was observed. For comparison, the maximum intensity of the ordinary hh PL is also plotted in Fig. 3.13. Up to 10 K, where the disappearance of the RL line is almost completed, the hh PL remains virtually constant. At larger temperatures the decrease in the hh PL is due to the increase of the probability for non-radiative recombination as discussed in Section 3.1.2.2.

For the explanation of the striking temperature behaviour of the RL line intensity one needs to consider that in the given temperature range, the LO phonon energy  $\hbar\omega_{LO}$  is much larger than  $kT_B$ , so that the number of phonons available for phonon emission, given by the Bose-Einstein factor, is constant. Therefore, the coupling of hh and lh excitons by LO phonons is unaffected by the temperature rise, and the drop of the RL line intensity must originate from a change in the nature of the exciton states itself. From the constancy of the ordinary hh PL intensity one can further conclude that the drop in the RL line intensity reflects an increase of the dephasing rate in the initial or final state of the RL process with increasing temperature.

The contribution from elastic and inelastic scattering to the dephasing rate in localized and delocalized states is as follows<sup>51-53</sup>: the phase of a delocalized state, originating from the presence of elastic scattering by local potential fluctuations, can only be destroyed by additional inelastic scattering. However, since photons can only interact with excitons at  $k = 0$ , an exciton scattered into a state with the same energy but  $k \neq 0$  is no longer resonant with the incoming photons. Consequently, the dephasing rate in a delocalized state needs to be identified with the elastic scattering rate provided by the local potential fluctuations or exciton-exciton interaction, which is only weakly temperature dependent. In contrast, besides the radiative decay, phonon scattering is the only contribution to the dephasing rate in a localized state. A phonon with sufficient

energy can excite an exciton from its localized state up to the mobility edge, making a contribution to the dephasing rate  $\propto \exp(-\Delta E/k_B T)$  so that the intensity of the sharp line decreases with temperature as<sup>50, 54</sup>

$$I(T) = I(T = 0) \left[ 1 - \exp\left(-\frac{\Delta E}{k_B T}\right) \right] \quad (3.15)$$

Here,  $\Delta E$  denotes localization energy, i.e. the energy position of the exciton state with respect to the mobility edge, and  $I(T = 0)$  is the dephasing rate at zero temperature where all scattering mechanisms are frozen out. Using Eq. (3.15), the best fit to the data in Fig. 3.13 reveals a localization energy of  $\Delta E = 0.3 \pm 0.05$  meV. Thus, for the selective excitation at 1.4868 eV the excitons are in a localized state 0.3 meV below the mobility edge. This small localization energy for excitation on resonance coincides very well with classical percolation theory and the quantum mechanical theory of localization by Anderson, Mott and Davis, which predicts the mobility edge to occur at the line center of the exciton absorption curve. At the low energy side the exciton states are localized leading to a low dephasing rate and therefore to a high RL or DRRS efficiency, whereas above the mobility edge the exciton states are delocalized, thus the excitons experience a larger dephasing rate due to elastic scattering at local potential fluctuations leading to a smaller RL or DRRS line intensity.

The fact that the coupling between two localized exciton states, rather than a localized and a delocalized exciton state, indeed leads to a smaller dephasing rate and thus a stronger DRRS or RL line, becomes visible from the comparison of the emission spectra of the sample discussed so far (sample A) and another part of the wafer, where the InAs layer turns out to be somewhat thinner shifting the hh and lh exciton transitions observed in PLE by 3 meV towards higher energies (sample B). These measurements are displayed in Fig. 3.14(a). Using the same excitation energy of 1.4868 eV reveals that the intensity of the DRRS or RL relative to the hh PL emission is enhanced because, as depicted in Fig. 3.14(b), the initial state of the RL or DRRS process coincides with an exciton state at the low energy side of the PLE spectrum, and thus with a state which is stronger localized. Similar evidence is provided by Fig. 3.8(b): for excitation energies at the high energy side of the lh exciton transition the intensity of the sharp line follows the

PLE intensity reflecting that the initial state is delocalized and that therefore the intensity of the sharp line is determined by the density of states. On the other hand, for excitation energies on the low energy side of the lh exciton transition, the intensity of the sharp line is enhanced, because the lh exciton states are localized.

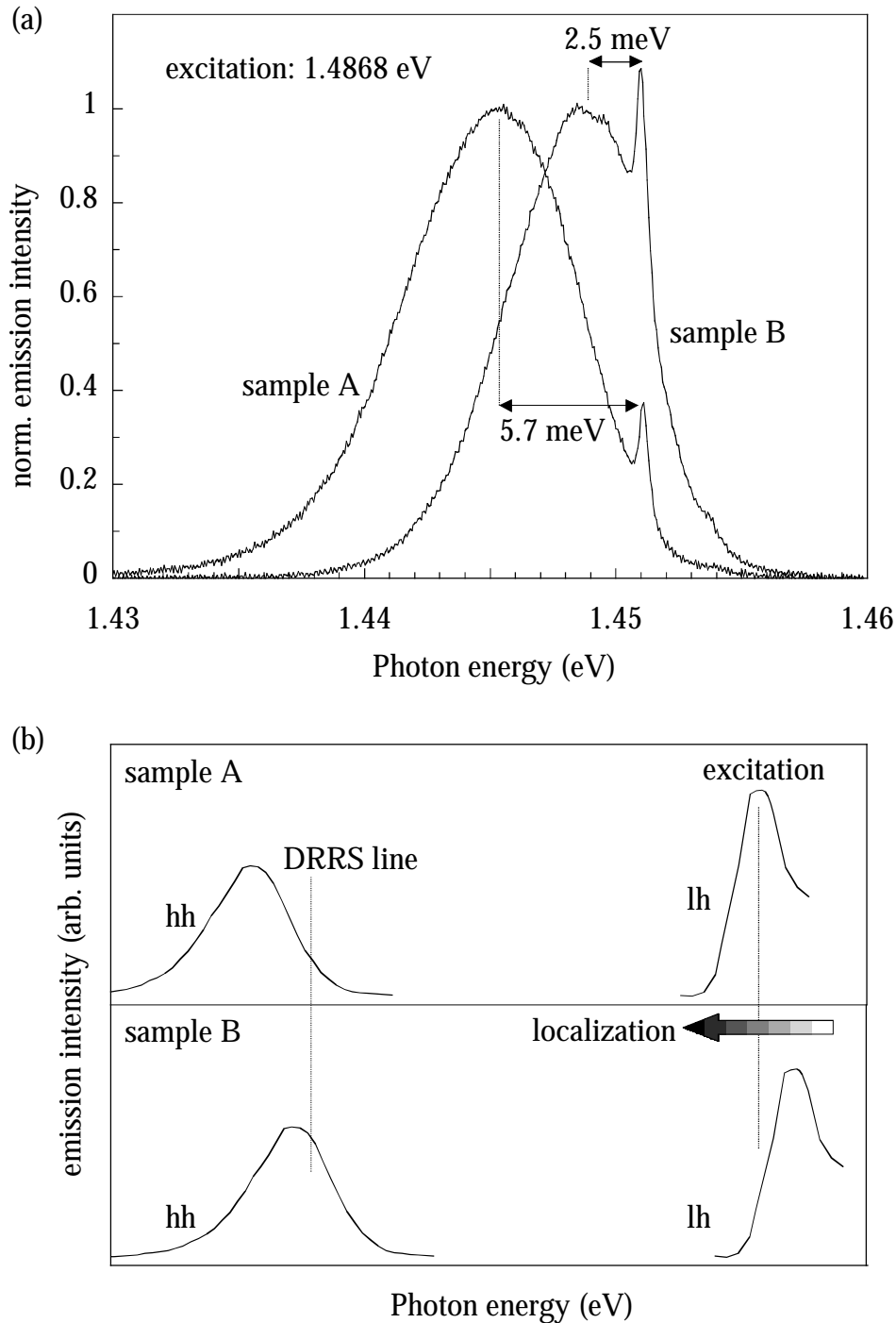


**Fig. 3.14:** (a) Comparison of the emission spectra of two different samples from the same wafer at the same excitation energy. (b) Schematic representation of the PL and DRRS (RL) emission for both samples with respect to the localization of the lh exciton.

The interpretation of the dramatic drop in the intensity of the sharp line when increasing the temperature from 4 to 16 K is thus as follows: at 4 K, ingoing and outgoing photons are both resonant with localized hh and lh exciton states producing a sharp line according to

$$\hbar\omega_{\text{in}} \xrightarrow{\text{A}\cdot\text{p}} (X_{\text{lh}}) \xrightarrow{\text{F}} (X_{\text{hh}} + \hbar\omega_{\text{LO}}) \xrightarrow{\text{A}\cdot\text{p}} \hbar\omega_{\text{out}} + \hbar\omega_{\text{LO}}, \quad (3.16)$$

where  $X_{\text{lh}}$ ,  $X_{\text{hh}}$ ,  $\hbar\omega_{\text{in}}$ ,  $\hbar\omega_{\text{out}}$ ,  $\hbar\omega_{\text{LO}}$  denote excitons, photons and the LO phonon, A·p is the photon-exciton interaction and F is the Fröhlich interaction. Since hh and lh exciton states are localized at 4 K, they provide a low dephasing rate and thus a large RL or DRRS efficiency. With respect to the localization of the lh exciton, one has to consider that despite of its 3D character given by the orbital wavefunctions, it is still bound to the InAs layer. Only along the InAs plane the lh excitons can move freely (determined by the centre of mass wavefunction) and thus the localization is logarithmically weak<sup>50</sup>, as in 2D. The small localization energy of 0.3 meV for excitation on resonance is consistent with the relatively long dephasing time of 40 ps and the observation of the 3D Sommerfeld-factor, both indicating that interface or alloy scattering of the lh excitons is present but weak.

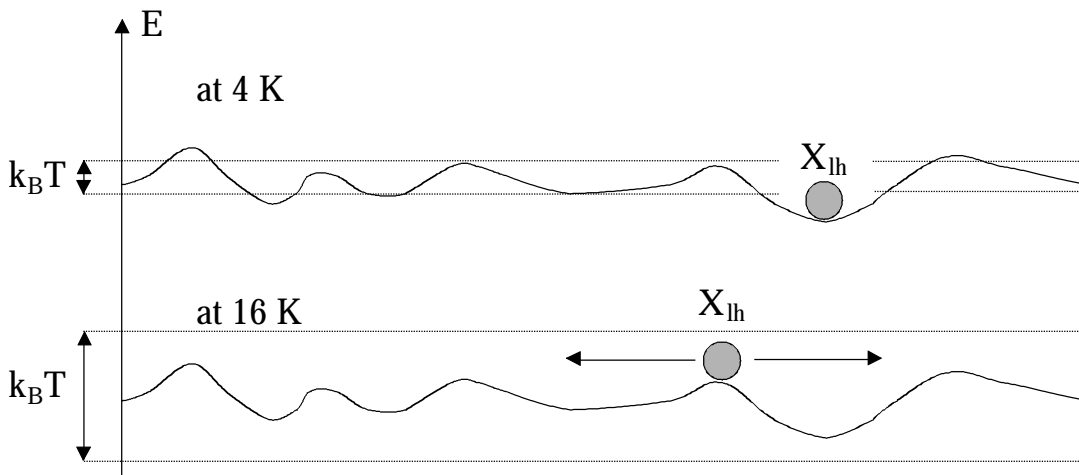


**Fig. 3.15:** Schematic picture for the delocalization of the lh excitons with increasing temperature.

As depicted in Fig. 3.15, due to the temperature rise scattering with predominantly acoustic phonons thermally activates lh excitons into a delocalized state where the dephasing rate is enhanced and Fröhlich interaction is reduced so that the RL or DRRS efficiency decreases. An equivalent explanation is - by taking the magnitude of the dephasing as a measure for the degree of localization of the exciton states - that the temperature rise transforms the character of the lh exciton states from a predominantly localized state at low temperatures to a delocalized state at higher temperatures.

### 3.2.5 Linewidth of Exciton Transitions in Ultrathin InAs Layers

In the literature on the optical properties of ultrathin InAs layers linewidth of the hh PL between 3 meV and more than 20 meV have been reported for InAs layer thickness of 0.3 to 1.6 ML. Recently, an increase of the PL linewidth has been observed for a 1 ML thick InAs layer when the growth interruption time was increased, which was accompanied by emerging PL and PLE features from a 0.3 ML wetting layer consisting of anisotropically elongated InAs clusters. In contrast, PL linewidths of less than 0.2 meV were found at an InAs thickness of less than 0.1 ML. The single InAs layer samples investigated in this work, with a thickness between 1.1 and 1.4 ML, show a PL linewidth between 7.5 and 8.5 meV, respectively. A review of the available linewidth data for samples grown under similar circumstances<sup>2-11, 22</sup> (substrate orientation, growth temperature, duration of the growth interrupt) shown in Fig. 3.16 reveals the tendency that the PL linewidth decreases with decreasing InAs thickness and that the reduction in linewidth is accompanied by a reduced Stokes shift.

The observed linewidth is often explained by fluctuations in the InAs layer thickness by 1 ML leading to the formation of 2 ML thick InAs islands with different lateral size. In this model, the change in electron and hole effective confinement energy at the monolayer steps leads to different transition energies according to the  $dE_{\text{eff}}/dL$ . If the change of effective confinement energy is small enough, the variation of the transition energies appears as line broadening. Additional averaging occurs when the steps in well thickness occur over the exciton Bohr-radius so that the excitons experience an effective confinement potential for electrons and holes. Furthermore, changes in the exciton



binding energy are negligible for  $dL/L \ll 1$ . For conventional quantum wells down to a thickness of 50 Å this model<sup>55, 56</sup> satisfactorily explains the observed increase in linewidth with decreasing well thickness because here thickness variations of one or two monolayers only cause changes of the transition energies of a few meV.

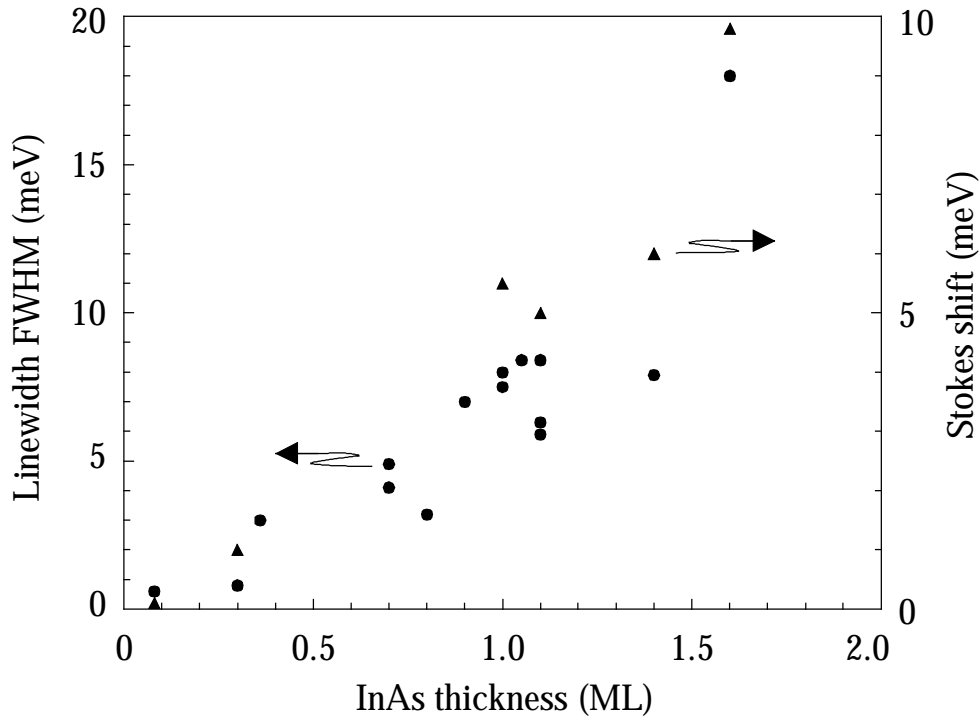


**Fig. 3.16:** Overview (literature and this work) of the observed PL linewidth and Stokes shift in ultrathin InAs/GaAs quantum wells as a function of well width (●: FWHM, ▲: Stokes shift).

For quantum well structures on a monolayer scale, however, this model has to be rejected for the following reasons: according to Chapter 2, in ultrathin InAs layers a monolayer step leads to a shift of the transition energies by more than 60 meV. Consequently, steps in the InAs layer thickness would be observed as a line splitting rather than a line broadening. Because the change in the InAs thickness amounts to the thickness itself, also changes in the exciton binding energy, as displayed in Fig. 3.6, need to be considered contributing to another few meV of splitting rather than broadening. Moreover, the application of the well width fluctuation model on monolayer thick InAs layers only leads to a quantitative agreement with the experimental data when the lateral extension of the InAs islands is assumed to be 2 - 4 times smaller than the exciton Bohr-radius. This, however, would imply that the hh excitons and - because of

their larger Bohr-radius - in particular the lh excitons experience short-range potential fluctuations leading to a small dephasing time, which clearly contradicts the observation of RL and DRRS and the dephasing time of  $T_2 \approx 40$  ps for the lh exciton derived above.

A more realistic explanation of the observed PL linewidth and the relatively long lh dephasing time enabling the observation of RL and DRRS can be obtained within the framework of the contribution of localized and delocalized states to the density of states<sup>57-59</sup>. Disorder as a consequence of local strain fields or variations in the InAs layer thickness, interpreted as the formation of thicker InAs islands of different lateral extension or an alloy-like InGaAs layer with a laterally inhomogeneous In content, leads to local fluctuations of the lateral potential of the InAs layer and subsequently to a localized exciton state. If the perturbation of the confinement potential is deep enough, or the distance between perturbation centres is large enough, electron and hole can establish coherent wavefunctions over the area of the exciton Bohr-radius. As a result the exciton is immobile, but the dephasing time of its wavefunction is long, only limited by the presence of phonons. If, additionally, further energy relaxation is omitted, the dephasing is entirely determined by the interaction of the exciton with acoustic phonons via the deformation or piezoelectric potential. Since localization acts as an attractive potential, the energy of the excitons is lowered with respect to the binding energy of an exciton which can freely move in the InAs layer plane. Therefore, as shown in Fig. 3.17, localized states deliver a contribution to the density of states below the exciton binding energy of a free exciton bound to the InAs layer, which is observed as a low energy tail in PL. In turn, when adjacent localizing potential fluctuations are located within the exciton Bohr-radius, the exciton states can couple. This coupling enhances the mobility in the InAs layer plane, but it destroys the phase of the exciton wavefunction, and  $T_2$  for those delocalized states becomes as short as 1 ps. The relatively long dephasing time of 40 ps therefore suggests that short-range potential fluctuations on a length scale smaller than the lh exciton Bohr-radius of approximately 120 Å are absent in the investigated sample. In fact, the observation of this long dephasing time for excitation on resonance proves that the low energy side of the lh exciton transition consists of localized states, and its extension to lower energies can be mapped out by measuring the localization energy  $\Delta E$ , hence the temperature dependence of the DRRS, or  $T_2$  as function of the excitation energy.

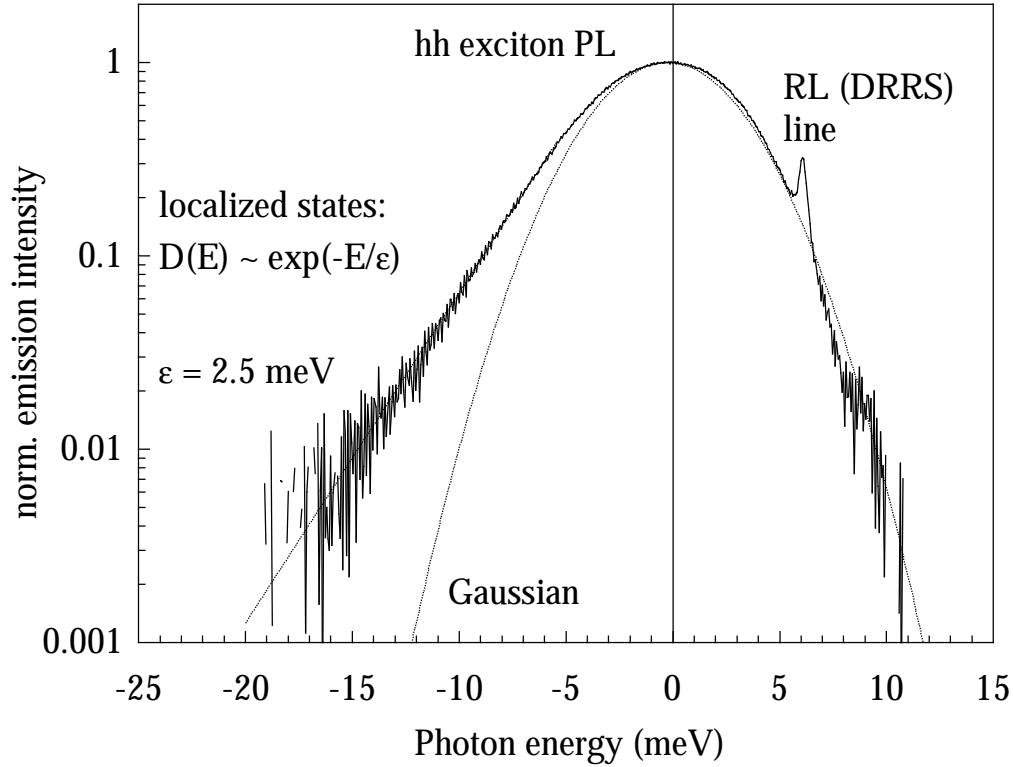


**Fig. 3.17:** Observation of the tail of localized states at the low energy side of the hh exciton PL.

Broadening of the PL and PLE at the high energy side requires an additional explanation in the delocalized state regime, i.e. for exciton states with an in-plane wavevector  $k = k_e - k_v \geq 0$ . Strictly speaking they should not be observed as excitons have to obey the same selection rules as band-to-band transitions, thus only exciton states with  $k = 0$  can be observed in optical experiments. However, due to the confinement of electrons and holes by the InAs layer, scattering at potential fluctuations experienced by migrating excitons and the localization of electron and hole in the exciton,  $k$  is not strictly a good quantum number and the  $k = 0$  selection rule is weakened. For an estimate of the broadening by these ‘forbidden’ transitions, and the knowledge that short-range potential fluctuations within the Bohr-radius are absent, one can identify as a supremum the uncertainty of the exciton wavevector with the inverse exciton Bohr-radius. Using the above electron and hole in-plane effective masses yields that ‘forbidden’ transitions can account for 1 - 2 meV broadening.

## References

- <sup>1</sup> G. Bastard, E. E. Mendez, L.L. Chang, and L. Esaki, *Phys. Rev. B***26**, 1974 (1982)
- <sup>2</sup> R. Cingolani, O. Brandt, L. Tapfer, G. Scarmaccio, G.C. LaRocca, and K.Ploog, *Phys. Rev. B***42**, 3209 (1990)
- <sup>3</sup> O. Brandt, R. Cingolani, H. Lage, G. Scarmarcio, L. Tapfer, and K. Ploog, *Phys. Rev. B***42**, 11396 (1990)
- <sup>4</sup> O. Brandt, L. Tapfer, R. Cingolani, K. Ploog, M. Hohenstein, and F. Phillipp, *Phys. Rev. B***41**, 12599 (1991)
- <sup>5</sup> M.V. Belousov, N.N. Ledentsov, M.V. Maximov, P.D. Wang, I.N. Yassievitvh, N.N. Faleev, I.A. Kozin, V.M. Ustinov, P.S. Kop'ev, and C.M. Sotomayor Torres, *Phys. Rev. B***51**, 14346 (1995)
- <sup>6</sup> M. I. Alonso, M. Ilg, and K. Ploog, *Phys. Rev. B***50**, 1628 (1994)
- <sup>7</sup> P.D. Wang, N.N. Ledentsov, C.M. Sotomayor Torres, P.S. Kop'ev, and V.M. Ustinov, *Appl. Phys. Lett.* **64**, 1526 (1994)
- <sup>8</sup> O. Brandt, H. Lage, and K. Ploog, *Phys. Rev. B***45**, 4217 (1992)
- <sup>9</sup> N.N. Ledentsov, P.D. Wang, C.M. Sotomayor Torres, A.Yu. Egorov, M.V. Maximov, V.M. Ustinov, A.E. Zhukov, and P.S. Kop'ev, *Phys. Rev. B***50**, 12171 (1994)
- <sup>10</sup> P.D. Wang, N.N. Ledentsov, I.N. Yassievich, A. Pakhonov, A.Yu. Egorov, P.S. Kop'ev, and V.M. Ustinov, *Phys. Rev. B***50**, 1604 (1994)
- <sup>11</sup> S.S. Dosanjh, E.F. Bowser, J.J. Harris, *Appl. Phys. Lett.* **64**, 2142 (1994)
- <sup>12</sup> John O. Dimmock, in *Semiconductors and Semimetals Vol. 3*
- <sup>13</sup> R.J. Elliott, *Phys. Rev.* **108**, 1384 (1957)
- <sup>14</sup> M. Shinada, and S. Sugano, *J. Phys. Soc. Japan* **21**, 1936 (1966)
- <sup>15</sup> D.S. Chemla, D.A.B. Miller, and S. Schmitt-Rink, in *Optical non-linearities and instabilities*, ed. H. Haug, Academic Press 1988
- <sup>16</sup> S. Schmitt-Rink, D.S. Chemla, and D.A.B. Miller, *Phys. Rev. B***32**, 6601 (1985)
- <sup>17</sup> R.P Leavitt, and J.W. Little, *Phys. Rev. B***42**, 11774 (1990)
- <sup>18</sup> R.L Greene, K. Bajaj, and D.E. Phelps, *Phys. Rev. B***29**, 1807 (1984)
- <sup>19</sup> I. Yassievitch, and U. Rössler, *J. Phys. Condens. Matter*, 7927 (1994)
- <sup>20</sup> G. Bacher, C. Hartmann, H. Schweizer, T. Held, G. Mahler, and H.Nickel, *Phys. Rev. B***47**, 9545 (1993)

- 
- <sup>21</sup> D. Curie, *Luminescence in Crystals*, London 1963
- <sup>22</sup> J. Brübach, A.Yu. Silov, J.E.M. Haverkort, W. van der Vleuten, and J.H. Wolter, *Pys. Rev. B* **59**, 6488 (1999)
- <sup>23</sup> K.J. Moore, P. Dawson, and C.T. Foxon, *Phys. Rev. B* **38**, 3368 (1988)
- <sup>24</sup> J.W. Little, and R.P. Leavitt, *Phys. Rev. B* **39**, 1365 (1989)
- <sup>25</sup> R.P. Leavitt, J.W. Little, and S.C. Horst, *Phys. Rev. B* **40**, 4183 (1989)
- <sup>26</sup> P.D. Wang, N.N. Ledentsov, C.M. Sotomayor Torres, A.E. Zhukov, P.S. Kop'ev, and V.M. Ustinov, *J. Appl. Phys.* **79**, 7164 (1996)
- <sup>27</sup> J. Brübach, J.E.M. Haverkort, J.H. Wolter, P.D. Wang, N.N. Ledentsov, C.M. Sotomayor Torres, A.E. Zhukov, P.S. Kop'ev, and V.M. Ustinov, *J. Optc. Soc. Am.* **B13**, 1224 (1996)
- <sup>28</sup> D.A. Kleinman, R.C. Miller, and A.C. Gossard, *Phys. Rev. B* **35**, 664 (1987)
- <sup>29</sup> R.C. Miller, D.A. Kleinman, and A.C. Gossard, *Sol. State Communic.* **60**, 213 (1986)
- <sup>30</sup> R.C. Miller, D.A. Kleinman, C.W. Tu, and S.K. Sputz, *Phys. Rev. B* **34**, 7444 (1986)
- <sup>31</sup> Y.R. Shen, *Phys. Rev. B* **9**, 622 (1974)
- <sup>32</sup> K. Muraki, S. Fukata, Y. Shiraki, and R. Ito, *J. Cryst. Growth* **127**, 546 (1993)
- <sup>33</sup> C. Giannini, L. Tapfer, S. Lagomarsino, J.C. Boulliard, A. Taccoen, B. Capelle, M. Ilg, O. Brandt, and K.H. Ploog, *Phys. Rev. B* **48**, 11496 (1993)
- <sup>34</sup> J.C.M. Henning, Y.A.R.R. Kessener, P.M. Koenraad, M.R. Leys, W. van der Vleuten, J.H. Wolter, and A.M. Frens, *Semicond. Sci. Technol.* **6**, 1079 (1991)
- <sup>35</sup> R. Ulbrich, *Phys. Rev. Lett.* **27**, 1512 (1971)
- <sup>36</sup> S.Y. Tong, and A.A. Maradudin, *Phys. Rev.* **181**, 1318 (1969)
- <sup>37</sup> P.D. Wang, and C.M. Sotomayor Torres, *J. Appl. Phys.* **74**, 5047 (1993)
- <sup>38</sup> M.J. Yang, R.J. Wagner, B.V. Shanabrook, W.J. Moore, J.R. Waterman, C.H. Yang, and M. Fatemi, *Appl. Phys. Lett.* **63**3434 (1993)
- <sup>39</sup> M.V. Klein, *Phys. Rev. B* **8**, 919 (1973)
- <sup>40</sup> P.F. Williams, D.L. Rousseau, and S.H. Dweretsky, *Phys. Rev. Lett.* **32**, 196 (1974)
- <sup>41</sup> A. Nakamura, M. Shimura, M. Hirai, and S. Nakashina, *Sol. State Communic.* **52**, 583 (1984)
- <sup>42</sup> R. Stanley, Hegarty, R. Fischer, J. Feldmann, E.O. Göbel, R.D. Feldman, and R.F. Austin, *Phys. Rev. Lett.* **67**, 128 (1991)

- <sup>43</sup> S. Hunsche, K. Leo, H. Kurz, and K. Köhler, *Phys. Rev. B* **50**, 5791 (1994)
- <sup>44</sup> M.C. Tatham, J.F. Ryan, and C.T. Foxon, *Phys. Rev. Lett.* **63**, 1637 (1989)
- <sup>45</sup> Z.L. Yuan, Z.Y. Xu, B.Z. Zheng, J.Z. Xu, S.S. Li, W. Ge, Y. Wang, J. Wang, L.L. Chang, P.D. Wang, C.M. Sotomayor Torres, and N.N. Ledentsov, *Phys. Rev. B* **54**, 16919 (1996)
- <sup>46</sup> P. Paki, R. Leonelli, L. Isnard, and R.A. Masut, *J. Vac. Sci. Technol. A* **18**, 956 (2000)
- <sup>47</sup> S. Wilke, H. Stolz, W. von der Osten, and G. Weimann, *Superlatt. & Microstruc.* **10**, 389 (1991)
- <sup>48</sup> H. Stolz, D. Schwarze, W. von der Osten, and G. Weiman, *Superl. and Microstruc.* **9**, 511 (1991)
- <sup>49</sup> U.Siegner, D. Weber, E.O. Göbel, D. Bennhardt, V. Heuckeroth, R. Saleh, H. Schwab, C. Klingshirn, J.M. Hvam, and V.G. Lyssenko, *Phys. Rev. B* **46**, 4564 (1992)
- <sup>50</sup> J. Hegarty, and M.D. Sturge, *J. Opt. Soc. Am. B* **2**, 1143 (1985)
- <sup>51</sup> J. Hegarty, L. Goldner, and M.D. Sturge, *Phys. Rev. B* **30**, 7346 (1984)
- <sup>52</sup> J. Hegarty, M.D. Sturge, C. Weisbuch, A.C. Gossard, and W. Wiegmann, *Phys. Rev. Lett.* **49**, 930 (1982)
- <sup>53</sup> T. Takagahara, *Phys. Rev. B* **31**, 6552 (1985)
- <sup>54</sup> D. Brinkmann, F. Rossi, S.W. Koch, and P.Thomas, *Phys. Rev. B* **54**, 2561 (1996)
- <sup>55</sup> C. Weisbuch, R. Dingle, A.C. Gossard, and W. Wiegmann, *Sol. State Communic.* **38**, 709 (1984)
- <sup>56</sup> G. Bastard, D. Delalande, M.H. Meynadier, P.M. Frijlink, and M.Voos, *Phys. Rev. B* **29**, 7042 (1984)
- <sup>57</sup> A. Pinczuk, J. Shah, R.C. Miller, A.C. Gossard, and W.Wiegmann, *Sol. State Communic.* **50**, 735 (1984)
- <sup>58</sup> R. Küchler, G. Abstreiter, G. Böhm, and G. Weimann, *Semicond. Sci. Technol.* **8**, 88 (1993)
- <sup>59</sup> K. Leo, W.W. Rühle, and K. Ploog, *Phys. Rev. B* **38**, 1947 (1988)



---

## ***4. Carrier Capture in Ultrathin InAs/GaAs Quantum Wells***

One of the most striking optical properties of ultrathin InAs layers embedded in a GaAs matrix is the appearance of a strong photoluminescence (PL) line below the GaAs bandgap<sup>1-4</sup>. This PL is known to arise from the recombination of hh excitons bound to the InAs layer<sup>5, 6</sup>. In high quality pseudomorphically grown InAs layers the peak intensity of the InAs PL was found to be higher than the excitonic PL of the GaAs matrix<sup>7-9</sup> by a factor 100-500. Since the absorption of the InAs layer itself cannot account for such a high luminescence efficiency even if one identifies the effective absorption length with the barrier penetration length of the confined states, this suggests a very efficient carrier capture by the InAs layer. According to literature<sup>1-9</sup> the magnitude of the InAs PL hardly depends on the thickness of the InAs layer. This result is quite striking because a variation of the InAs thickness by 1 ML corresponds to a change in the effective confinement energy by more than 60 meV which in conventional GaAs/AlGaAs quantum wells leads to a modulation of the PL efficiency by one order of magnitude<sup>10</sup>. In ultrathin InAs layers, the formation of wire- or dot-like InAs clusters results in a drastic decrease of the PL efficiency<sup>3, 11</sup>.

The capture times as discussed in the following are defined as the time delay between the generation of an electron-hole pair in the GaAs and the moment when electrons or holes reach the corresponding confined electron, hh or lh state in the InAs layer. This so-called overall capture time is different from the local capture time used in the classical diffusion<sup>12, 13</sup> model for the description of the capture process. In that model the capture is treated as the succession of two distinct processes, namely the diffusion of the photogenerated carriers within the barrier into the crystal volume of the quantum well followed by the scattering of the carriers from three-dimensional barrier states, which are spatially confined in the well region but energetically above the well, into the two-dimensional levels of the quantum well. The scattering from the barrier into the well is expressed by the local capture time<sup>13</sup>, which is as short as 100 fs.



For overall capture times in relatively thin heterostructures only a few comparable values are available. Calculations from Brum and Bastard<sup>14</sup>, based on their state-of-the-art quantum mechanical capture model for electrons and holes, show a capture time of 45 ps for a shallow 50 Å wide GaAs quantum well with 500 nm Al<sub>0.18</sub>Ga<sub>0.82</sub>As barriers. A recent adaptation of their theory by Heller and Bastard<sup>15</sup> for exciton capture reveals capture times less than 1.2 ps for a shallow but 200 Å wide GaAs/AlGaAs quantum well. Blom<sup>16</sup> et al. found an ambipolar capture time of 22 ps for a 26 Å GaAs quantum well centred in a 100 nm wide Al<sub>0.3</sub>Ga<sub>0.7</sub>As separate confinement heterostructure, and recently capture times below 1 ps were reported in a 25 Å wide Be δ-doped structure<sup>17</sup>. For ultrathin InAs/GaAs quantum wells, the only published carrier capture time is an estimate from Brandt et al.<sup>18</sup>. Neglecting the absorption of the InAs layer itself and assuming a flux of photogenerated carriers from the GaAs to the InAs layer expressed by the overall capture time  $\tau_{\text{cap}}$ , the ratio of the PL intensity of the InAs layer  $I_{\text{InAs}}$  and of the GaAs exciton emission  $I_{\text{GaAs}}$  is given by<sup>18</sup>

$$\frac{I_{\text{InAs}}}{I_{\text{GaAs}}} = \frac{\tau_{\text{exc}}}{\tau_{\text{cap}}} . \quad (4.1)$$

With an exciton lifetime  $\tau_{\text{exc}}$  of 3 ns for high quality GaAs<sup>19</sup>, the capture time can be estimated to be  $\tau_{\text{cap}} \approx 10\text{-}20$  ps. Experimental data for the capture times in ultrathin InAs layers, however, are still lacking.

In this work for the first time an experimental study of the carrier capture in a single ultrathin InAs layer embedded in a GaAs matrix was performed. The capture times were measured by time-resolved two-wavelength pump-probe phototransmission in order to have direct spectral control of both the initial and final states involved in the capture process. In addition to obtaining experimental data for the capture times in ultrathin InAs layers, the choice of a 1.2 ML thick InAs layer in the experiments targeted the interesting situation where hh and lh states are both confined, and their difference in confinement energy amounts to approximately one GaAs LO phonon. By measuring the spectral dependence of the capture times in the vicinity of the hh and lh exciton transitions, the role of the confined lh state in the capture process was investigated in particular.

## 4.1 Sample Growth and Characterization

The sample under investigation was synthesized by conventional Molecular Beam Epitaxy on CrO doped semi-insulating (001) GaAs substrate. After oxide desorption, the layer sequence started with a 0.4  $\mu\text{m}$  GaAs buffer layer, followed by a 350  $\text{\AA}$  GaAs layer, within which the substrate temperature was lowered from 630  $^{\circ}\text{C}$  to 450  $^{\circ}\text{C}$ . At this lower temperature the InAs layer, and subsequently 5 ML of GaAs, were deposited. Before and after the InAs layer a 1 s growth interruption was introduced. While growing the next 565  $\text{\AA}$  of GaAs, the substrate temperature was returned to 630  $^{\circ}\text{C}$ . Finally, the structure was capped with a 300  $\text{\AA}$   $\text{Al}_{0.33}\text{Ga}_{0.67}\text{As}$  window and a 170  $\text{\AA}$  GaAs layer.

The thickness of the InAs layer was determined by high-resolution X-ray diffraction in (004) geometry<sup>20</sup>. From simulations of the rocking-curves based on the dynamical theory we found an InAs layer thickness of  $1.2 \pm 0.1$  ML, assuming 6.8 % compressive strain. The X-ray study also revealed that more than 80 % of the deposited InAs is confined within a single atomic plane.

The sample was characterized with standard PL measurements at 4.2 K. Below the GaAs bandgap at 1.445 eV the strong PL line of the InAs hh exciton transition was observed. The peak intensity ratio between the InAs hh exciton emission and the GaAs exciton at 1.515 eV was approximately 650, demonstrating the efficient trapping of carriers by the InAs layer.

## 4.2 Time-Resolved Two-Wavelength Pump-Probe Phototransmission

A direct method to study the carrier capture is time-resolved two-wavelength pump-probe phototransmission. This technique exploits the bleaching of the excitonic absorption by photogenerated carriers populating the confined states of the InAs layer to which the excitons are bound. As illustrated in Fig. 4.1, the carriers are photogenerated in the GaAs matrix by tuning the pump pulses above the GaAs bandgap. The probe pulses are tuned on either the hh or lh transition of the InAs layer and the change in the excitonic absorption due to the captured carriers is measured as a function of the delay between pump and probe pulses. Since ultrathin InAs layers provide only a single

confined electron state but a confined hh and a confined lh state, this technique allows to trace the capture of the holes to the hh and lh state independently.

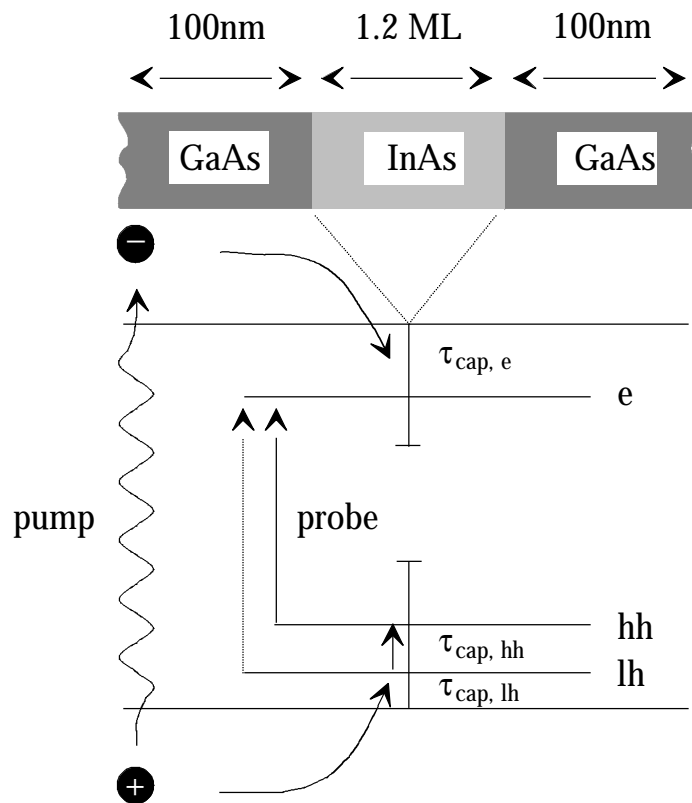


**Fig. 4.1:** Basic principle of the two-wavelength pump-probe phototransmission technique to measure capture times in a single ultrathin InAs/GaAs quantum well.

In comparison with single wavelength upconversion-, correlation- or pump-probe techniques<sup>21-23</sup>, two-wavelength pump-probe phototransmission has two further advantages: when optical non-linearities are excited and probed at the same wavelength, coherent effects like phase relaxation (dephasing) and polarization relaxation (e.g. spin relaxation) and incoherent effects such as carrier relaxation, carrier capture and carrier thermalization are superimposed. Since in ultrathin InAs layers the capture times can be expected to be similar as the dephasing time, it would be very difficult to unambiguously separate both effects. Additionally, in upconversion experiments excitation densities of  $10^{11} \text{ cm}^{-2}$  or more are required to obtain a reasonable signal-to-noise ratio. At those high excitation densities, however, the carrier capture is already severely influenced by carrier-carrier scattering, and any features in the capture times

due to the exclusive interactions with polar optical phonons may already be washed out<sup>24, 25</sup>.

During this thesis a picosecond time-resolved two-wavelength pump-probe photo-transmission set-up was realized, which is schematically shown in Fig. 4.2. The laser system consists of a mode-locked Coherent Antares Nd:YAG laser and two Coherent 702 double jet dye lasers, which both are equipped with a cavity dumper. The dye lasers were synchronously pumped by the frequency doubled pulse train of the Nd:YAG laser at 532 nm with a pulse width of 80 ps and a repetition rate of 76 MHz. The output of the Nd:YAG laser was typically 3 W equally shared by both dye lasers. The Nd:YAG laser was equipped with a temperature controller for the frequency doubling crystal and a feedback controlled, piezoelectric driven cavity end mirror to achieve optimum intensity, position and pointing stabilization of the Nd:YAG beam. The laser, which was used for the excitation of the GaAs barrier in the samples, was operated with DCM Special as the gain medium and DDTC as the saturable absorber at a fixed excitation wavelength of 682 nm (1.818 eV). At a maximum output power of 100 mW the temporal pulse width (FWHM) was better than 1 ps. For the generation of the probe pulses in the second dye laser, a mixture of Styryl 8 and Styryl 9 was used as gain medium and HITCI as saturable absorber. The probe wavelength was tuned on either the hh or lh exciton transition. Although the usage of a mixture of Styryl 8 and Styryl 9 leads to 50 % shorter dye-lifetime, the spectral tunability was extended from 780 nm to 900 nm and the pulse width was kept below 1.5 ps over the whole range. All four dye jets were cooled down to an average temperature of 10 °C, which lead to a drastic reduction of phase and time jitter between the pump and probe pulses and to an improvement in the stability and temporal width of the cross-correlation by more than 300 %. To achieve the best compromise between spectral and temporal resolution in the capture experiments, both dye lasers were operated with single-plate birefringent filters giving a sufficient spectral resolution of 0.8 meV.

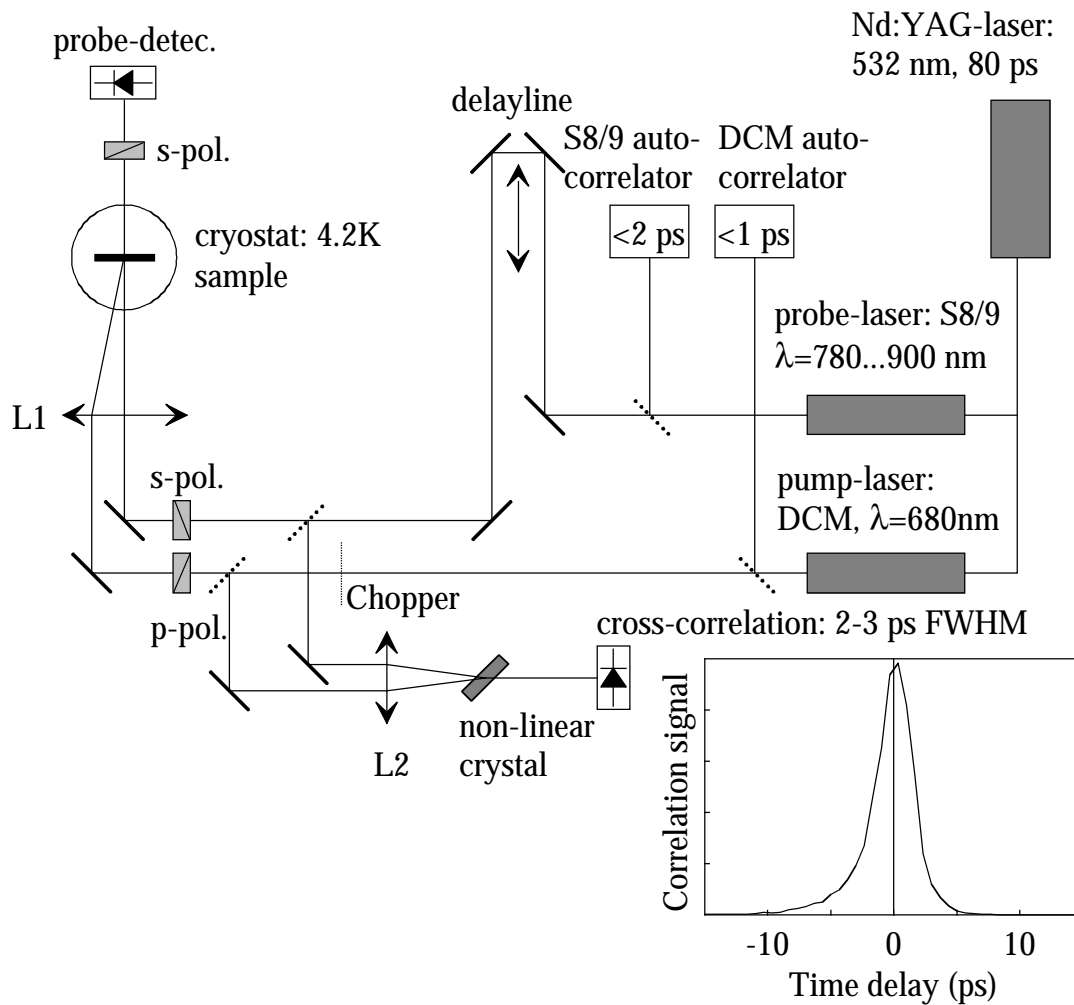


**Fig. 4.2:** Time-resolved two-wavelength pump-probe phototransmission set-up. The insert shows the cross-correlation between pump and probe pulses.

After pump and probe beams passed a variable delayline, they were focused onto the sample in near backscattering geometry with the spotsize of the probe beam being 4 times smaller than the pump beam. Consequently, the excitation density can be assumed as homogenous and systematic errors due to lateral carrier diffusion can be excluded. Pump and probe beam were used in crossed polarizations. By placing a third polarizer in the probe beam behind the sample background signal due to scattered pump light and unpolarized photoluminescence was considerably reduced. The sample was mounted in a He flow cryostat and held by paper frames to avoid any possible source of external strain. By modulating the pump beam, the induced transmission change was measured as a function of pump and probe delay utilizing a conventional Si pin-diode and

standard lock-in technique. During the experiments the cross-correlation of pump and probe beam, which marks the position of zero delay and whose temporal width equals to the time resolution of the set-up, was monitored in-situ using a LiIO<sub>3</sub> crystal. In daily operation the cross-correlation was limited to a FWHM of 2 - 3 ps due to residual jitter of the pump and probe beam. Finally, the intensity ratio between pump and probe beam was kept below 50.

### 4.3 Phototransmission in Ultrathin InAs/GaAs Quantum Wells

The most common criticism with respect to the interpretation of carrier capture experiments is the query over the extent to which the measured transients directly reflect the evolution of the population in the states associated with the optical transition. When using time-resolved phototransmission (PT) the population in the InAs layer affects all three absorption mechanisms, namely the interband absorption by the subbands of the confined electron, hh, and lh state, the absorption by bound hh and lh excitons and the absorption due to unbound exciton states, which are simultaneously present and which exhibit different changes under photoexcitation. By tuning the probe wavelength to the hh and lh exciton transitions, however, the observed PT originates entirely from the bleaching of the excitonic absorption, and the evolution of the population in the confined InAs layer states is transformed into the PT transients through the reduction in exciton oscillator strength as a function of excitation density. Depending on the dominating bleaching mechanism, the decrease in excitonic absorption might have a strong non-linear dependence on the carrier concentration, altering the observed rise and decay times with respect to the capture and recombination times of the true population. In addition, the amount of bleaching differs for hh and lh excitons due to their different in-plane effective masses. In general, one therefore has to assume that the observed PT transients do *not* represent the evolution of the population in the InAs layer in the first place. For a solid interpretation of PT experiments with respect to carrier capture and recombination times it is thus important to find a model which correlates the temporal evolution of the population in the confined InAs states with the transient PT of the

associated excitonic transitions or, alternatively, experimental conditions where the measured PT transients directly reflect the population.

Experimentally, rise and decay times of the population are conserved in the PT transients for excitation densities which provide a linear change in the magnitude of the PT. Figure 4.3(a) displays the PT transients at the peak position of the hh exciton transition at 1.451 eV, measured at different excitation densities, and Fig. 4.3(b) shows the magnitude of the PT observed in the maximum of the transient as a function of excitation density. The solid line in Fig. 4.3(b) represents the calculation of the transient PT discussed below. As can be seen from Fig. 4.3(b), for excitation densities of up to  $3 \times 10^8 \text{ cm}^{-2}$  the magnitude of the PT increases proportional with the excitation density, and consequently the PT transients in Fig. 4.3(a) exhibit virtually the same rise and decay times. In contrast, at excitation densities larger than  $10^9 \text{ cm}^{-2}$  the magnitude of the PT starts to saturate. At these excitation densities the PT transients show a slightly diminished rise time whereas the decay time appears to be increased. For the largest excitation density of  $7 \times 10^{10} \text{ cm}^{-2}$  the maximum of the transient evolves into a broad plateau. From these measurements it can be concluded that the PT transients in the investigated InAs layer directly reflect the population in the confined states only for excitation densities up to  $3 \times 10^8 \text{ cm}^{-2}$ .

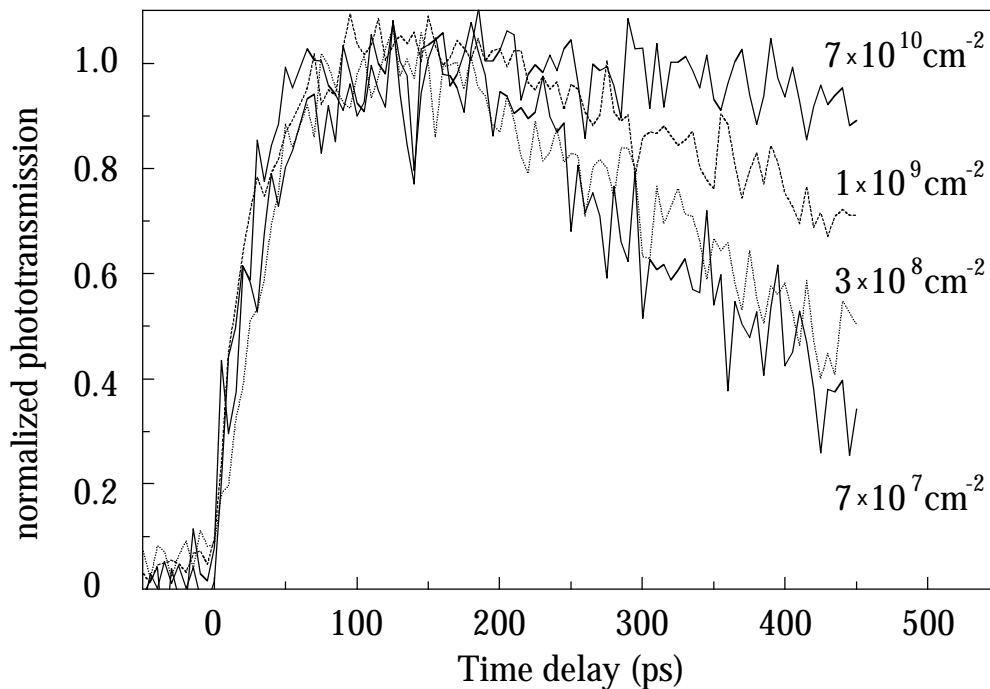


**Fig. 4.3(a):** Normalized phototransmission at the hh exciton transition for different excitation densities.

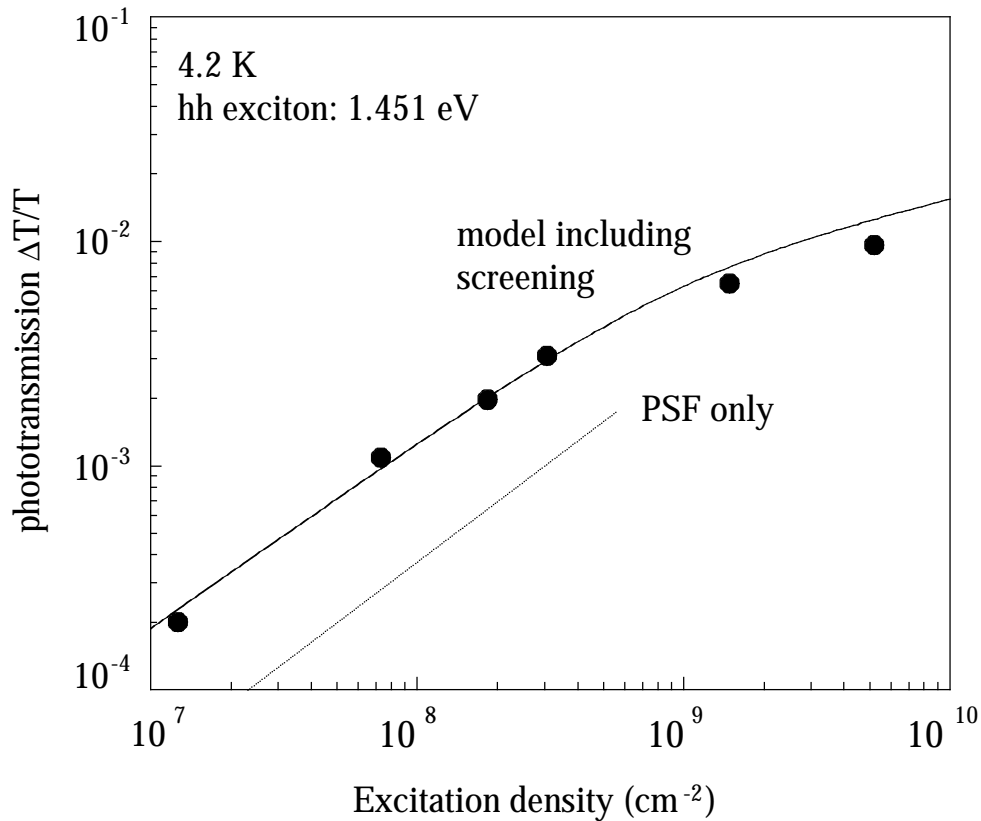


**Fig. 4.3(b):** Measured (symbols) and calculated (solid line) magnitude of the phototransmission at the maximum of the transient as a function of excitation density. The individual contribution of phase-space-filling (PSF) is indicated by the dotted line.

For a theoretical treatment of the observed PT behaviour, it is assumed that the insertion of the InAs layer in the GaAs matrix introduces single electron, hh, and lh states in the GaAs bandgap. The confined states give rise to the formation of hh and lh excitons bound to the InAs layer, and their population by photogenerated carriers  $N(t)$  leads to a bleaching of the excitonic absorption  $\alpha(N)$ , which for the ground state is given by [Eq. (4.2)]

$$\alpha(N) = \frac{4\pi e^2 E_p}{\epsilon_0 c_0 n m_0 \omega} \left| \langle \chi_h | \chi_e \rangle \right|^2 \times \left| \phi(r=0, N) \right|^2 \times \delta[\hbar\omega - E_g + E_e + E_h + E^x(N)].$$

Here,  $\chi_e, \chi_h$  denote the confined electron and hole state wavefunctions,  $\phi(r)$  is the exciton orbital wavefunction,  $E_g, E_e, E_h$  are the GaAs bandgap and the electron and hole



effective confinement energies, and  $E^x$  is the exciton binding energy. Exploiting that for the exciton oscillator strength  $|\varphi(\mathbf{r})|^2 \propto 1/a_0^2$  holds and using  $E^x = 2D \hbar^2 / \mu^* a_0^2$  one finds that the change in excitonic absorption scales in the same way as the exciton binding energy as a function of excitation density. In the absence of photogenerated carriers, the confined InAs layer states and the hh and lh exciton are characterized by the effective masses, in-plane effective masses, effective confinement energies, exciton binding energies, Bohr-radii and dimensionality parameters as derived in the previous chapters (see Table 4.1). According to Eq. (4.2), the calculation of the transient change of the excitonic absorption requires on one hand a description for the evolution of the population in the confined InAs layer states. In the following this is done by coupled rate equations. Since the InAs layer provides only one confined electron level, but two confined hole levels, in between which cooling of holes can take place, this model also takes into account the relaxation of holes from the lh to the hh level. On the other hand, one needs to translate the population in the confined InAs states into a bleaching of the excitonic absorption. For ultrathin InAs layers, there are two bleaching mechanisms relevant, namely phase-space-filling and exciton-screening. This is motivated by the observation that even at high excitation densities there is at least one bound exciton state. Additionally, for both hh and lh excitons only a bleaching of the excitonic absorption is observed, but no noticeable broadening or shift of the excitonic resonances. The latter is explained by the fact, that under photoexcitation the single particle states of the system are changed leading to a bandgap renormalization which is compensated by the decrease of the exciton binding energy due to screening<sup>26-28</sup>.

Parameter	hh	lh
effective mass $m^*$	$0.3774 \times m_0$	$0.0905 \times m_0$
in-plane effective mass $m_{\parallel}^*$	$0.155 \times m_0$	$0.363 \times m_0$
exciton binding energy $E_x$	10 meV	5.5 meV
Dimensionality factor D	0.66	0.3
Bohr-radius $a^*$	90 Å	115 Å

**Table 4.1:** Parameters used for the calculation of the absorption bleaching in a 1.2 ML InAs layer.

### 4.3.1 Phase-Space-Filling

Phase-space-filling describes the diminishing of the exciton oscillator strength due to the reduction of the number of single particle states that contribute to the bound electron-hole state. In analogy with bandfilling in bulk material, it is a consequence of the exclusion principle which results in a blocking of transitions in k-space under photoexcitation, but the single particle fermion states are unchanged. Bleaching of the excitonic absorption due to phase-space-filling increases linearly as a function of the excitation density  $N$  as long as  $N$  is smaller than the saturation density  $N_s$ , whose reciprocal value represents an area occupied by a photogenerated electron-hole pair which cannot sustain more excitons. For the relevant case of a non-degenerate electron-hole population, the bleaching due to phase-space-filling is given by<sup>29</sup>

$$\frac{\Delta\alpha(N)}{\alpha} = -\frac{N}{N_s} = -\int (f_e(\mathbf{k}) + f_h(\mathbf{k})) \times \frac{\varphi^x(\mathbf{k})}{\varphi^x(\mathbf{r}=0)} d\mathbf{k}, \quad (4.3)$$

where  $f_e$  and  $f_h$  denote the electron and hole distributions and  $\varphi^x(\mathbf{k})$  is the Fourier transform of the orbital exciton wavefunction.  $\varphi^x(\mathbf{k})$  represents the distribution according to which electron and holes states build-up the exciton by linear combination, and Eq. (4.3) therefore has the meaning that states in k-space, which are already occupied by electrons or holes, are no longer available for the formation of excitons. Because the Bohr-radius is smaller and the binding energy is larger for 2D excitons than for 3D excitons, Eq. (4.3) also explains why phase-space-filling is much more significant for 2D excitons than for 3D excitons. A simplification of Eq. (4.3) can be obtained by considering that in GaAs an electron and hole distribution within one LO phonon energy  $\hbar\omega_{LO}$  above the bandedges is established in less than 1 ps. Since this is faster than the temporal resolution in the experiments, the saturation parameter amounts to  $1/N_s = 8\pi a^{*2} E^x/\hbar\omega_{LO}$ . For the hh excitons  $N_s$  can be estimated with  $1.7 \times 10^{11} \text{ cm}^{-2}$ , and  $N_s$  amounts to  $2 \times 10^{11} \text{ cm}^{-2}$  for the lh excitons. Thus, if phase-space-filling would be the only bleaching mechanism, the measured PT transients should directly reflect the population in the confined InAs states for excitation densities up to these values for  $N_s$ .

The excitation density dependent measurements of the PT shown in Fig. 4.3(a) and 4.3(b), however, already exhibit a deviation from linear behaviour for excitation densities larger than  $3 \times 10^8 \text{ cm}^{-2}$ . This behaviour can only be explained when screening of the Coulomb interaction is taken into account.

### 4.3.2 Exciton Screening

Bleaching of the excitonic absorption due to screening describes the effect that in the presence of photogenerated carriers, electrons and holes do not interact via a Coulomb potential but by a screened potential<sup>30</sup>

$$V_s(r) = -\frac{e^2}{4\pi \epsilon \epsilon_0 r} \left\{ 1 - \frac{1}{2\pi \kappa_s} [H_0(\kappa_s r) - J_0(\kappa_s r)] \right\}, \quad (4.4)$$

where  $\kappa_s$  denotes the inverse screening length, and  $H_0$  and  $J_0$  are the Struve function and Bessel function of second kind, respectively. For distances  $r \ll \kappa_s^{-1}$  this potential behaves like a Coulomb potential, whereas for  $r \gg \kappa_s^{-1}$  it falls off as  $r^{-3}$ , i.e. the core of the potential is preserved whereas its long-range part is suppressed. Following Ref. 31, with this potential the change in exciton binding energy and oscillator strength of the hh and lh excitons was calculated in a variational approach. Using a trial wavefunction for the exciton ground state  $\phi^x(r) = \lambda/\sqrt{2\pi} \times \exp(-\lambda r/2)$ , the energy expectation value was minimized with respect to the variational parameter  $\lambda$ . The exciton binding energies were subsequently corrected by the dimensionality parameter in order to match the results for the limiting case  $N \rightarrow 0$  with  $E_x$  as found by the zero-radius potential model in the absence of photogenerated carriers. The inverse screening length entering Eq. (4.4) was obtained from the Debye model for 2D semiconductors<sup>31, 32</sup> as [Eq. (4.5)]

$$\kappa_s = \frac{2}{a^*} \left\{ \frac{m_{|,e}^*}{\mu_{||}^*} \left[ 1 - \exp\left(-n_e \pi \hbar^2 / m_{|,e}^* k_B T\right) \right] + \frac{m_{|,h}^*}{\mu_{||}^*} \left[ 1 - \exp\left(-p_h \pi \hbar^2 / m_{|,h}^* k_B T\right) \right] \right\},$$

where  $n_e$  and  $p_h$  denote the carrier concentrations and  $\mu_{||}^*$  is the reduced in-plane effective mass. As can be seen from Eq. (4.5), the inverse screening length consists of two independent contributions for the holes and the electrons weighted by their in-plane effective mass. Therefore, a photogenerated electron and hole lead to a different amount of exciton screening and at an equal population of electrons and holes the amount of screening differs for hh and lh excitons.

The inverse screening parameters as a function of excitation density for hh and lh excitons is displayed in Fig. 4.4. For both hh and lh excitons it increases linearly up to excitation densities of approximately  $1 \times 10^9 \text{ cm}^{-2}$ . In this range the inverse screening length becomes independent on the effective masses, i.e. the contributions to screening from captured electrons and holes are equal. For larger excitation densities the inverse screening length starts to deviate from linear behaviour, and at  $5 \times 10^{10} \text{ cm}^{-2}$  it reaches the saturation limit of  $\kappa_s = 2/a^*[(m_{||,e}^* + m_{||,h}^*)/\mu_{||}^*]$ . In the non-linear regime of  $\kappa_s$  the individual contributions of captured electrons and holes to the screening diverge, with the result that the PT becomes more sensitive to the electron capture than to the capture of a hole.

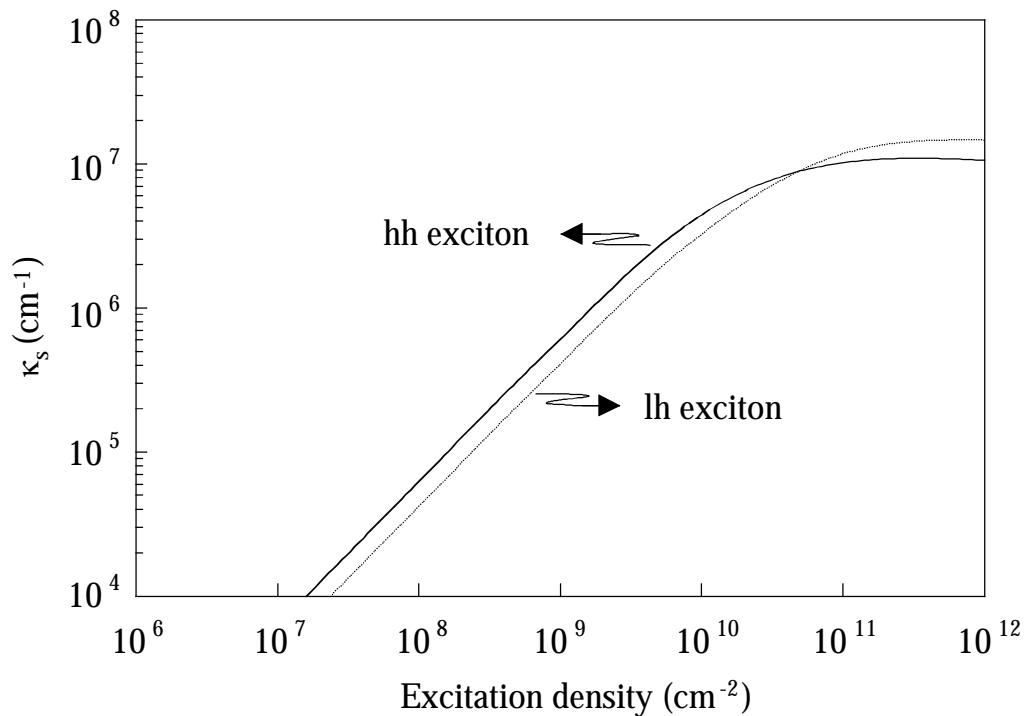


**Fig. 4.4:** Inverse screening length for the hh and lh excitons as a function of excitation density. The calculations were performed at equal electron and hole populations ( $n_e = p_h$ ).

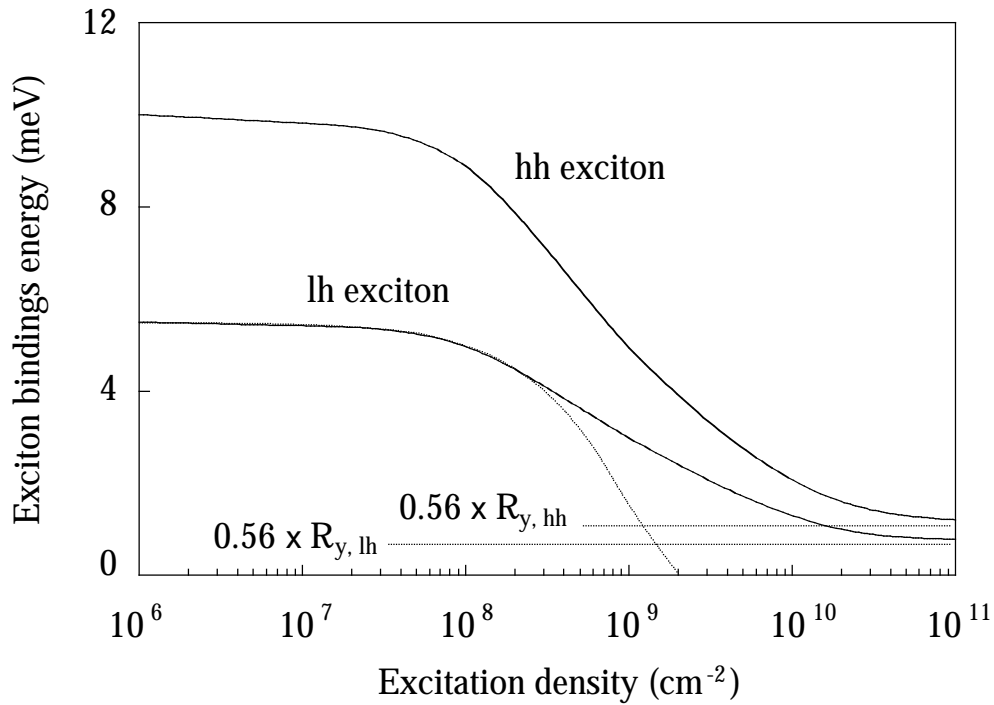


**Fig. 4.5:** Calculated exciton binding energies as a function of excitation density. For the hh exciton the 2D screened potential was used. The calculations for the lh exciton were performed with the 2D (solid line) and 3D (dotted line) screened potential.

The results of the calculations for the hh and lh exciton binding energies in the presence of screening as a function of excitation density are plotted in Fig. 4.5. For the lh exciton the change of the exciton binding energy due to screening was also calculated for the ideal 3D case using analytical expressions<sup>28</sup> by approximating the Coulomb-potential with a Hulthén-potential  $V_s(r) = -\left\{\frac{e^2 \kappa_s}{4\pi \epsilon \epsilon_0}\right\} \times \exp(-\kappa_s r) / [1 - \exp(-\kappa_s r)]$  in the exciton Hamiltonian. Up to electron and hole concentrations of  $10^8 \text{ cm}^{-2}$  one observes a linear decrease of the exciton binding energy. In addition, in this low density regime the 2D and 3D screening potentials provide the same results for the lh exciton. For excitation densities larger than  $10^8 \text{ cm}^{-2}$  the change in the exciton binding energies starts to deviate from the linear behaviour. At these carrier concentrations the inverse screening length still increases proportional with the carrier concentration, and the observed behaviour results from a non-linear dependence of the exciton binding energy on  $\kappa_s$ . For the lh exciton, the exciton binding energy in the 3D case starts to decrease more rapidly than in the 2D case demonstrating that screening for 3D excitons is more

efficient. In particular, at approximately  $3 \times 10^9 \text{ cm}^{-2}$  the inverse screening length reaches the magnitude of the Bohr-radius and the 3D screened potential does not provide a bound exciton state anymore. As opposed to that, in the regime where screening becomes density independent, i.e. for excitation densities of  $10^{10} \text{ cm}^{-2}$  and larger, the 2D hh exciton binding energy starts to saturate at a value of  $0.56 \times R^*$ , as predicted by random-phase-approximation<sup>33</sup>, reflecting the persistence of the 2D exciton ground state even at high carrier concentrations<sup>34</sup>.

The calculations of the PT incorporating both phase-space-filling and exciton screening are displayed in Fig. 4.3(b) and 4.6, respectively. To facilitate direct comparison with the experiments shown in Fig. 4.3(a) and 4.3(b), the calculations were performed at the peak position of the hh exciton transition. The solid lines in Fig. 4.3(b) represent the calculated PT in the maximum of the transient as a function of excitation density. Calculations and measurements show in agreement, that up to  $3 \times 10^8 \text{ cm}^{-2}$  the bleaching increases linearly with excitation density, but starts to saturate at higher densities. This behaviour is caused by the non-linear dependence of the exciton binding energy on the inverse screening length and the saturation of the  $\kappa_s$  at higher excitation densities suggesting that the bleaching results predominantly from exciton screening. It can be seen from Fig. 4.3(b), that at excitation densities below  $10^9 \text{ cm}^{-2}$  the contribution from phase-space-filling is 2-4 times smaller than the contribution from exciton screening. This is in agreement with the work of Snelling et al.<sup>35</sup>, who found that for excitation densities  $N < N_c = \mu^* \hbar \omega_{LO} / \hbar^2$ , the reduction of the exciton oscillator strength due to phase-space-filling is a factor of two smaller than due to exciton screening. In ultrathin InAs layers  $N_c$  can be estimated as  $2.4 \times 10^{10} \text{ cm}^{-2}$ .

The non-linearities due to the dominance of screening also become obvious in the calculations of the PT transients at different excitation densities, as shown in Fig. 4.6. For electron and hole concentrations of up to  $3 \times 10^8 \text{ cm}^{-2}$  rise and decay times of the transient PT and the population are virtually identical, thus reflecting the linear dependence of the bleaching on excitation density. At excitation densities larger than  $10^{10} \text{ cm}^{-2}$ , a plateau rather than a sharp maximum starts to emerge in the transient PT at time delays where the PT reaches its maximum. This plateau indicates that the saturation level of the inverse screening length and the exciton binding energy has been reached, where a further increase of the carrier density does not lead to a further

bleaching of the absorption. At these high excitation densities, the rise time of the transient PT becomes significantly shorter than the rise time of the population, whereas the decay time of the PT transient appears to be increased. For this reason, lifetimes would be substantially overestimated, and capture times would be determined as too short if the screening contribution to the bleaching is not considered.

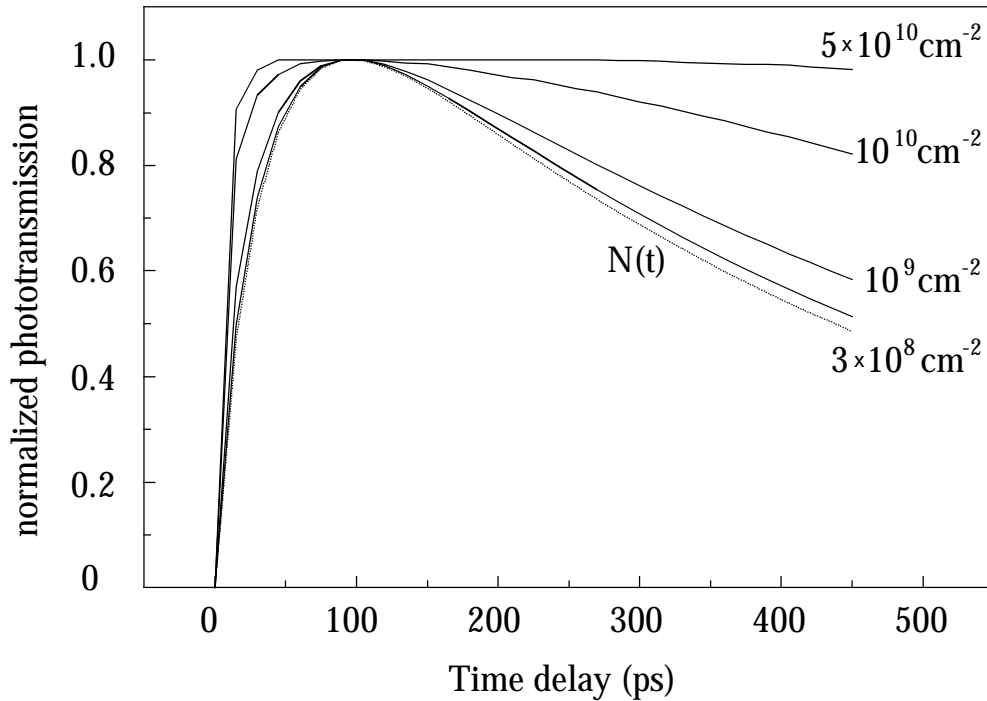


**Fig. 4.6:** Calculated phototransmission transients at the hh exciton transition for different excitation densities (solid lines). For comparison, the transient of the assumed population  $N(t)$ , which scales with the excitation density, is also shown (dotted line). For excitation densities  $\leq 3 \times 10^8 \text{ cm}^{-2}$  the phototransmission transients directly reflect the population within 5 % accuracy.

### 4.3.3 Coupled Rate Equation Model

The population in the confined electron, hh, and lh states of the InAs layer can be described by coupled rate equations. In this approach all coherent effects which originate from the evolution of the particle wavefunctions are neglected and all time constants which influence the carrier dynamics like capture, relaxation and recombination times are introduced as phenomenological parameters. As depicted in Fig. 4.7, the exciting laser pulse at 1.818 eV creates a spectrally narrow distribution of

electrons and holes, whose excess energy (electrons: 260 meV, holes: 39 meV) is distributed according to the effective masses in the GaAs conduction and valence band. After excitation, electrons and holes relax predominantly under LO phonon emission towards the GaAs bandedges. During the relaxation, electrons and holes also thermalize, i.e. electrons and holes establish a quasi-Fermi distribution with the thermal energy of the particles being still close to their initial excess energy. For that reason, the hole distribution is much cooler than the electron distribution. In parallel to this process a reduction of the carrier temperature towards the lattice temperature takes place. Recently it was found theoretically and experimentally<sup>26, 36, 37</sup>, that in GaAs carrier relaxation and thermalization occurs within approximately 200 fs. In addition, for the relevant case of low carrier concentrations, within less than 1 ps the carrier temperature is decreased to less than 450 K corresponding to a carrier kinetic energy being smaller than one LO phonon energy above the GaAs bandedges<sup>14, 38</sup>. Considering the 2 ps time-resolution of the capture experiments it is therefore justified to conclude that the carrier cooling in the GaAs matrix will not influence the capture times one measures: within the duration of the pump-pulse a reservoir of thermalized electrons and holes is established one LO phonon above the GaAs bandedges. The temporal carrier generation function entering the rate-equations can thus be approximated by a  $\delta$ -function. In addition one has to make an assumption to what extent the capture times are affected by a carrier thermalization within the LO phonon energy towards the lattice temperature. A quasi-equilibrium is reached by predominantly acoustic phonon scattering, which requires several tens to hundreds ps. Since this is much longer than the expected capture times, one can assume a steady-state situation for the energy dependence of the electron and hole occupation numbers in the GaAs. The electron and hole distribution functions are constant for all continuum states within the LO phonon energy, and zero elsewhere.

With this assumptions the temporal evolution of the electron and hole population in the GaAs barrier  $n_b(t)$  and  $p_b(t)$ , respectively, can then be described as

$$\frac{dn_b}{dt} = n_0 \times \delta(t) - \frac{n_b}{\tau_{\text{rec}}^{\text{GaAs}}} - \frac{n_b}{\tau_{\text{cap}}^e} \quad (4.6)$$



$$\frac{dp_b}{dt} = p_0 \times \delta(t) - \frac{p_b}{\tau_{\text{rec}}^{\text{GaAs}}} - \frac{p_b}{\tau_{\text{cap}}^{\text{lh}}} - \frac{p_b}{\tau_{\text{cap}}^{\text{hh}}}, \quad (4.7)$$

where  $n_0, p_0$  denote the number of electrons and holes initially pumped into the barrier. For the sake of consistency, in the following all populations are given in units of  $\text{cm}^{-2}$ . As a depopulation mechanism for the barrier states, we consider radiative and non-radiative recombination in  $\tau_{\text{rec}}^{\text{GaAs}}$  and the direct capture of electrons and holes to the confined electron, hh, and lh states of the InAs layer, expressed by the capture times  $\tau_{\text{cap}}^e, \tau_{\text{cap}}^{\text{lh}}$  and  $\tau_{\text{cap}}^{\text{hh}}$ , respectively.

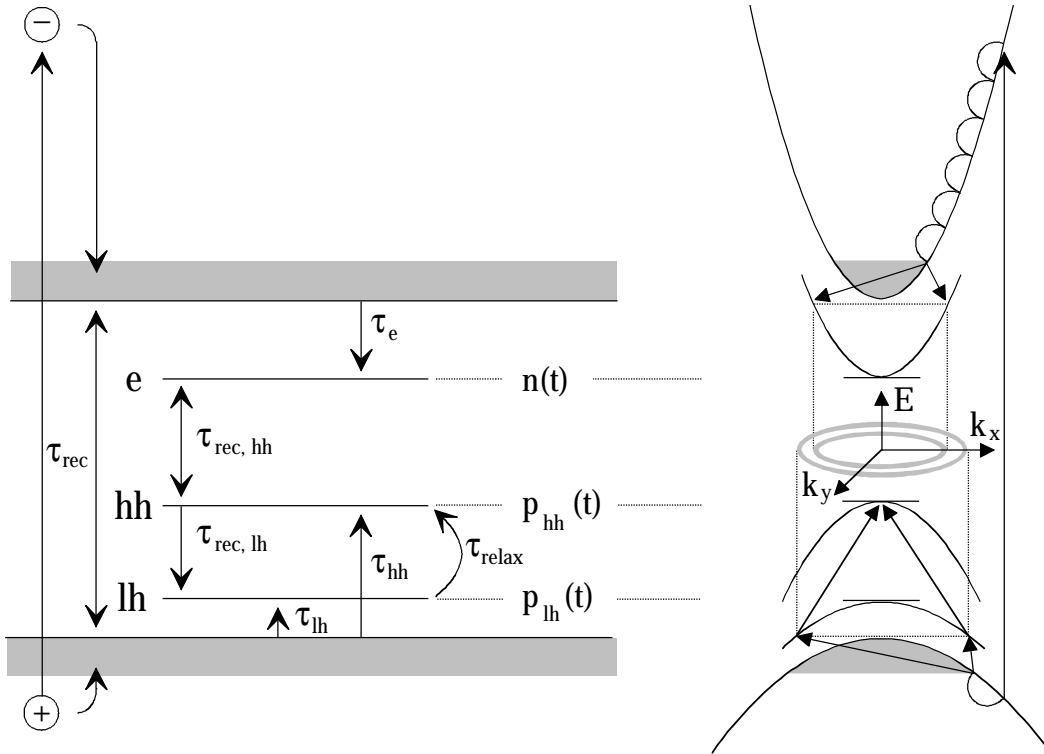


**Fig. 4.7:** Schematic representation of the carrier dynamics and band diagram used in the rate equation model. The shaded area above the bandedges represents the LO phonon energy.

Neglecting thermal carrier escape, for the confined electron, hh, and lh states of the InAs layer the rate equations can be derived in a similar way as

$$\frac{dn}{dt} = \frac{n_b}{\tau_{cap}^e} - \frac{n}{\tau_{rec}^{e-hh}} - \frac{n}{\tau_{rec}^{e-lh}} \quad (4.8)$$

$$\frac{dp_{hh}}{dt} = \frac{p_b}{\tau_{cap}^{hh}} + \frac{p_{lh}}{\tau_{relax}^{lh-hh}} - \frac{p_{hh}}{\tau_{rec}^{e-hh}} \quad (4.9)$$

$$\frac{dp_{lh}}{dt} = \frac{p_b}{\tau_{cap}^{lh}} - \frac{p_{lh}}{\tau_{relax}^{lh-hh}} - \frac{p_{lh}}{\tau_{rec}^{e-lh}} \quad (4.10)$$

All three subbands are populated by the direct capture of electron and holes, whereas the depopulation occurs via band-band recombination, which may differ for hh' s ( $\tau_{rec}^{e-hh}$ ) and lh' s ( $\tau_{rec}^{e-lh}$ ). In addition, it is assumed that the population of the hh level and the depopulation of the lh level can occur via intersubband relaxation from the lh state to the hh state taking place within the intersubband relaxation time  $\tau_{relax}^{lh-hh}$ . This approach is motivated by the results for the carrier capture<sup>14, 39</sup> and intersubband relaxation in GaAs quantum wells<sup>40</sup>. The capture rates to the ground state are highest when the confinement potential of the quantum well provides a bound state close to the barrier continuum and when the relaxation to the ground state can occur rapidly via LO phonon emission.

The system of coupled rate equations [Eq. (4.6) - (4.10)] can be solved analytically by finding the homogenous solution, subsequently performing a variation of the constants and calculating the Wronskian. Using  $\tau_{cap}^e, \tau_{cap}^{hh}, \tau_{cap}^{lh} \ll \tau_{rec}^{e-h}$  and substituting

$$a_n = -\frac{1}{\tau_{cap}^e}; b_n = -a_n; c_n = -\left(\frac{1}{\tau_{rec}^{e-hh}} + \frac{1}{\tau_{rec}^{e-lh}}\right);$$

$$a_p = -\left(\frac{1}{\tau_{cap}^{hh}} + \frac{1}{\tau_{cap}^{lh}}\right); b_p = \frac{1}{\tau_{cap}^{lh}}; c_p = -\left(\frac{1}{\tau_{rec}^{e-lh}} + \frac{1}{\tau_{relax}^{lh-hh}}\right); \quad (4.11)$$

$$d_p = \frac{1}{\tau_{\text{cap}}^{\text{hh}}}; e_p = \frac{1}{\tau_{\text{relax}}^{\text{lh-hh}}}; f_p = -\frac{1}{\tau_{\text{rec}}^{\text{e-hh}}}$$

to calculate the rate coefficients for  $t=0$

$$A_n = -\frac{b_n}{c_n - a_n} \quad (4.12)$$

$$A_p = -\frac{b_p}{c_p - a_p}; B_p = \frac{b_p e_p}{(f_p - a_p)(c_p - a_p)} - \frac{b_p e_p}{f_p - a_p}; C_p = \frac{b_p e_p}{(f_p - c_p)(c_p - a_p)}$$

the solutions for the population in the GaAs conduction and valence band  $n_b(t)$  and  $p_b(t)$  and in the InAs electron, hh, and lh levels  $n(t)$ ,  $p_{\text{lh}}(t)$  and  $p_{\text{hh}}(t)$ , respectively, read

$$n_b(t) = n_0 \exp\left(-\frac{t}{\tau_{\text{cap}}^e}\right) \quad (4.13)$$

$$p_b(t) = p_0 \exp\left(-\frac{\tau_{\text{cap}}^{\text{hh}} + \tau_{\text{cap}}^{\text{lh}}}{\tau_{\text{cap}}^{\text{hh}} \tau_{\text{cap}}^{\text{lh}}} t\right) \quad (4.14)$$

$$n(t) = A_n \left[ \exp\left(-\frac{t}{\tau_{\text{cap}}^e}\right) - \exp\left(-\frac{\tau_{\text{rec}}^{\text{e-hh}} + \tau_{\text{rec}}^{\text{lh}}}{\tau_{\text{rec}}^{\text{hh}} \tau_{\text{rec}}^{\text{lh}}} t\right) \right] \quad (4.15)$$

$$p_{\text{lh}}(t) = A_p \left[ \exp\left(-\frac{\tau_{\text{cap}}^{\text{hh}} + \tau_{\text{cap}}^{\text{lh}}}{\tau_{\text{cap}}^{\text{hh}} \tau_{\text{cap}}^{\text{lh}}} t\right) - \exp\left(-\frac{\tau_{\text{rec}}^{\text{e-lh}} + \tau_{\text{relax}}^{\text{lh-hh}}}{\tau_{\text{rec}}^{\text{e-lh}} \tau_{\text{relax}}^{\text{lh-hh}}} t\right) \right] \quad (4.16)$$

$$p_{\text{hh}}(t) = B_p \left[ \exp\left(-\frac{\tau_{\text{cap}}^{\text{hh}} + \tau_{\text{cap}}^{\text{lh}}}{\tau_{\text{cap}}^{\text{hh}} \tau_{\text{cap}}^{\text{lh}}} t\right) - \exp\left(-\frac{t}{\tau_{\text{rec}}^{\text{e-hh}}}\right) \right] + C_p \left[ \exp\left(-\frac{t}{\tau_{\text{rec}}^{\text{e-hh}}}\right) - \exp\left(-\frac{\tau_{\text{rec}}^{\text{e-lh}} + \tau_{\text{relax}}^{\text{lh-hh}}}{\tau_{\text{rec}}^{\text{e-lh}} \tau_{\text{relax}}^{\text{lh-hh}}} t\right) \right]. \quad (4.17)$$

From the above expressions it is evident, that the description of the population in quantum well structures comprising more than one bound state in the conduction or valence band with two exponential functions and a single capture and recombination lifetime is in general not correct. In ultrathin InAs layers this approach only holds for the population in the confined electron level. In contrast, for the hh and lh population the situation is more complex. Rise and decay times are both dependent on the hh and lh capture times and the relaxation and recombination times, respectively, and their impact on the temporal evolution on the total hh and lh population is weighted by the rate coefficients.

#### 4.4 Experimental Results for the Carrier Capture

The carrier capture measurements at the hh and lh exciton transition of the InAs layer were performed at a fixed excitation density of  $2 \times 10^8 \text{ cm}^{-2}$ . As demonstrated in Section 4.3.2, at this excitation density the PT transients still directly reflect the evolution of the population in the confined InAs states. The pump wavelength was set above the GaAs bandgap to 1.818 eV. Figure 4.8 displays the PT transients in the vicinity of the lh exciton transition [Fig. 4.8(a)] and hh exciton transition [Fig. 4.8(b)]. For the measurements in the vicinity of the lh exciton transition the probe wavelength was tuned from the high energy side of the lh transition at 1.492 eV to its low energy side at 1.484 eV. As can be seen in Fig. 4.8(a), both transients exhibit the same rise time of  $20 \pm 2 \text{ ps}$ , but the decay time is 200 ps shorter at 1.492 eV. In the vicinity of the hh exciton transition the opposite behaviour is observed. With the probe wavelength tuned to the low energy side of the hh exciton transition at 1.445 eV the rise time amounts to  $22 \pm 2 \text{ ps}$ . In contrast, the rise time increases to  $50 \pm 2 \text{ ps}$  at the high energy side of the hh exciton transition at 1.458 eV, but both transients show the same decay time.

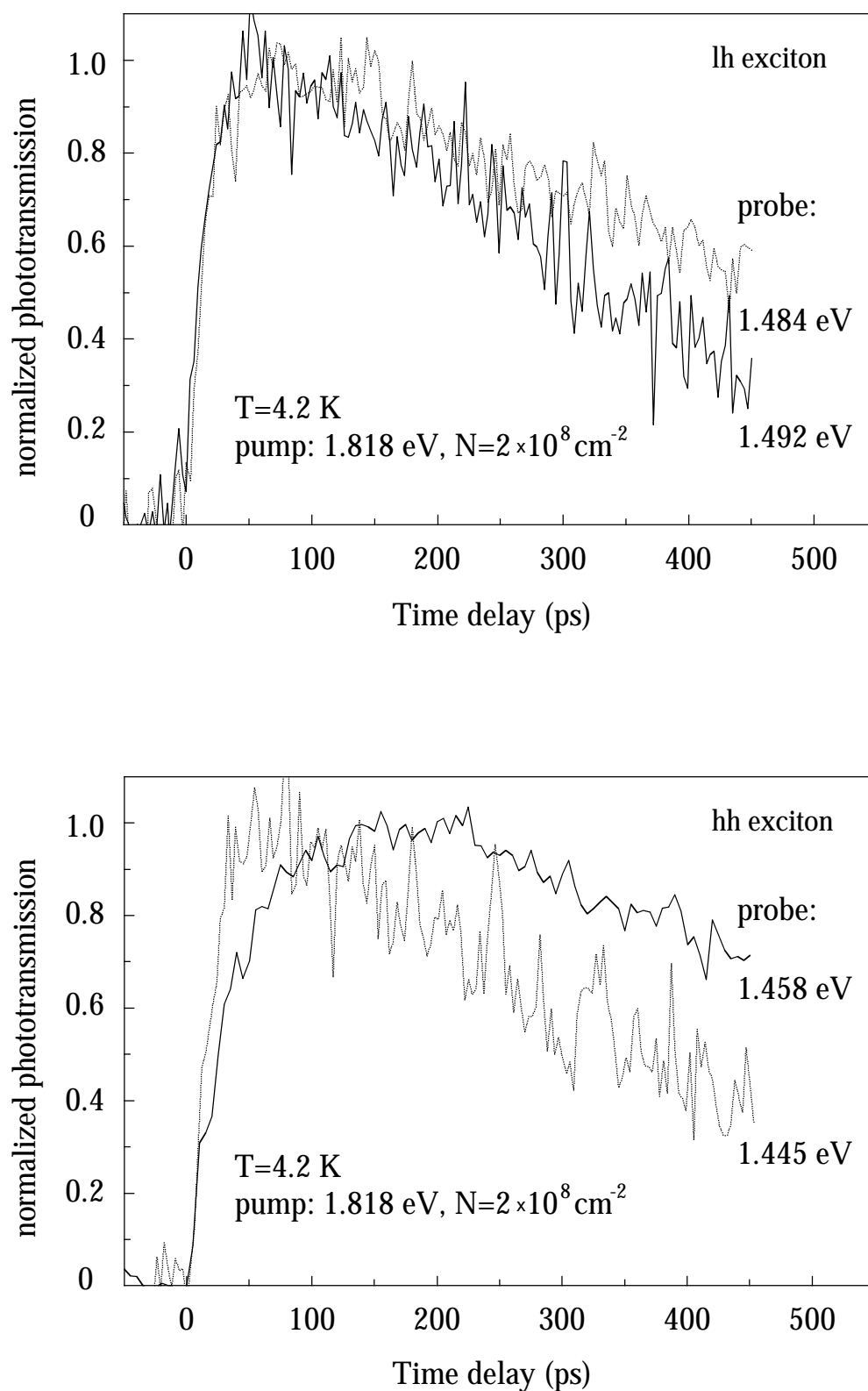


**Fig. 4.8:** Measured transient phototransmission in the vicinity of the lh (top) and hh exciton transition (bottom). The probe beam was tuned from the high energy side of the excitonic transition (solid line) to the low energy side (dotted line).

Figure 4.9 summarizes the results for the PT rise times when tuning the probe wavelength through the hh and lh exciton transitions<sup>41</sup>. Within the lh exciton transition one finds a constant rise time of 20 ps. In contrast, within the hh exciton transition, a steep increase of the PT rise time from 22 ps to 50 ps is observed. In addition, the line shape of the PT spectra indicates that one observes only a bleaching of the excitonic absorption but no noticeable broadening or shift of the excitonic resonances.

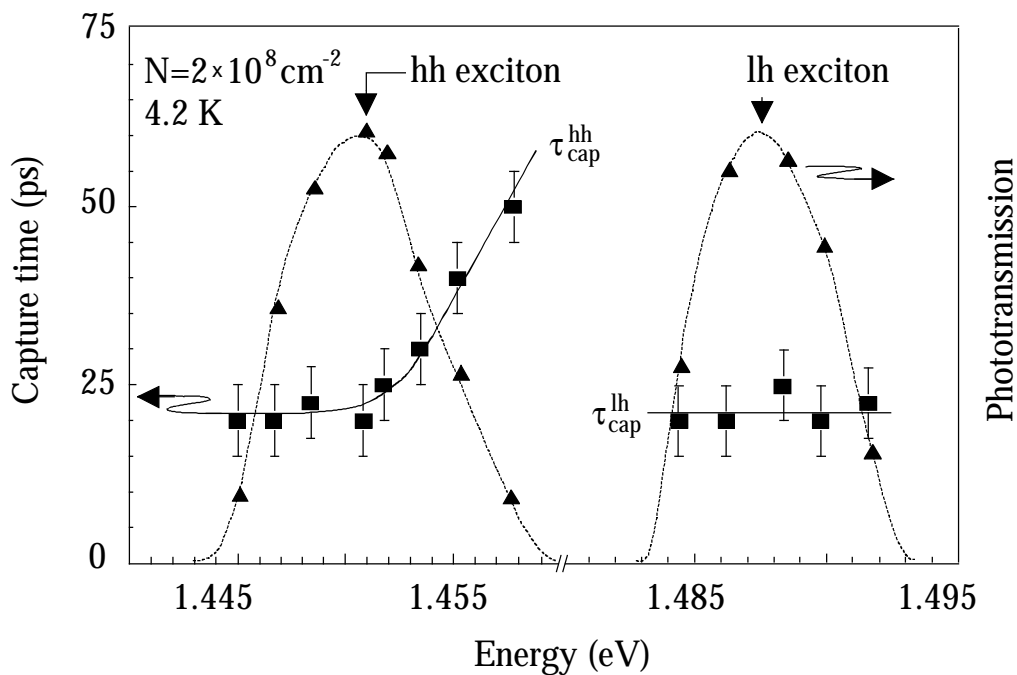


**Fig. 4.9:** Measured phototransmission rise times (■) in the vicinity of the hh and lh exciton transitions. The solid lines are a guide to the eye. Within the lh exciton transition a constant rise time of 20 ps is observed. At the hh exciton transition the rise time increases abruptly from 22 ps at the low energy side to 50 ps at the high energy side. The dotted lines and the symbols (▲) indicate the phototransmission spectrum.

In order to explain the observed increase by more than a factor of two of the PT rise time within the hh exciton transition in combination with the constant PT rise time at the lh exciton transition, one needs to consider that the insertion of a 1.2 ML thick InAs layer in a GaAs matrix leads to a confined lh state only 4.5 meV below the GaAs continuum, whereas the effective confinement energy of the hh state amounts to 42 meV<sup>42</sup>. Thus, the energy separation between hh and lh subbands amounts to approximately the GaAs LO phonon energy of 36 meV. When the hh-lh level separation

is larger than 36 meV the hole relaxation can occur rapidly via LO phonon emission. As the wavefunctions of the confined InAs layer states extend *entirely* into the GaAs matrix, the capture process and the intersubband relaxation are well described by assuming GaAs bulk phonons. Both properties should therefore give rise to a fast relaxation of carriers from a lh level to a hh level by GaAs LO phonon emission<sup>40, 43</sup> within less than 1-2 ps. In contrast, when the hh-lh level separation becomes smaller than the LO phonon energy,  $\tau_{\text{relax}}^{\text{lh-hh}}$  should increase to several tens of picoseconds<sup>44-46</sup>.

#### 4.5 Evaluation of the Capture Times by Rate Equation Analysis

In order to demonstrate that a change of  $\tau_{\text{relax}}^{\text{lh-hh}}$  from 1-2 ps to several tens of picoseconds is responsible for the observed increase of the PT rise time within the hh exciton transition, a systematic analysis of the rate-equations has been performed. This is necessary because rise and decay times of the populations  $p_{\text{hh}}(t)$  and  $p_{\text{lh}}(t)$  as given in Eq. (4.16) and (4.17) are determined by a combination of the individual hole capture times to the hh and lh level, the relaxation time for intersubband relaxation from the lh to the hh level, and the band-band recombination time. Changes in the electron capture time need not to be considered in this parameter study. Since the InAs layer provides only a single bound electron state, alterations of  $\tau_{\text{cap}}^e$  would change the capture times at the hh and lh exciton transition in the same way. Furthermore, for the hh and lh recombination lifetime in the following a value of 485 ps is assumed, which was found by the time-correlated single photon counting experiments presented in Chapter 3.

In the rate-equation analysis one must consider four cases, which are related to the observed steep increase of the PT rise time at the hh exciton transition:

(i) Direct hole capture by the hh and lh levels, but negligible relaxation from the lh level to the hh level. Assuming a constant electron capture time, the increase of the PT rise time within the hh exciton transition would then originate from an increase of  $\tau_{\text{cap}}^{\text{hh}}$  from 20 ps to more than 50 ps within a 10 meV change in the hh effective confinement energy. The calculated PT transients at the hh and lh exciton transition for this case are displayed in Fig. 4.10(a) and Fig. 4.11(a), respectively. The increase of  $\tau_{\text{cap}}^{\text{hh}}$  would be

motivated by a capture time oscillating as a function of effective confinement energy, as in the case of usual quantum wells before the well provides the next confined state<sup>14, 39</sup>.

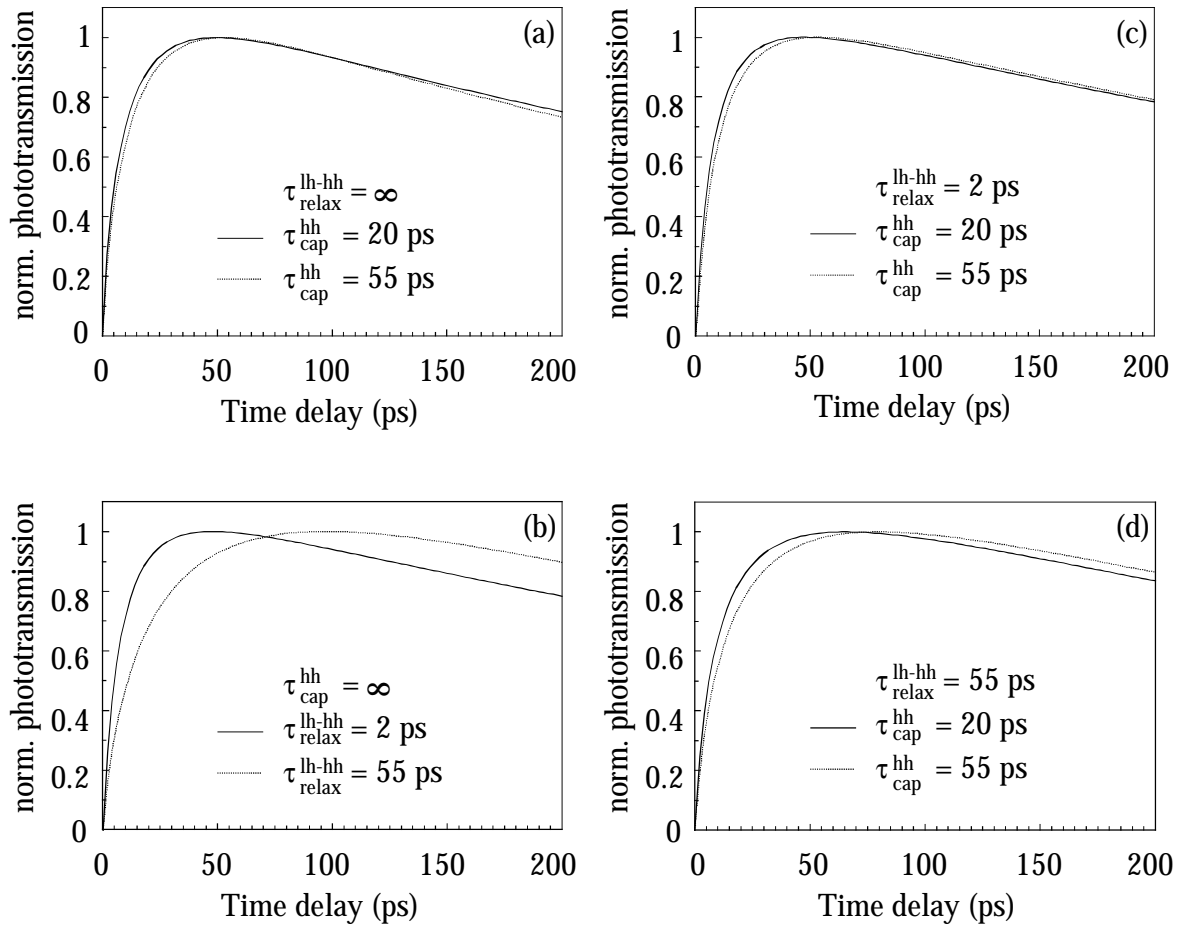


**Fig. 4.10:** Calculated transient phototransmission at the hh exciton transition according to the rate-equation analysis. The capture and relaxation times used in the calculations are given in the figure. The comparison of (a) - (d) reveals, that only a negligible direct capture of holes to the confined hh state accompanied with a change of the relaxation time from 2 ps to 55 ps leads to an increase of the phototransmission rise time from 22 ps to 50 ps.



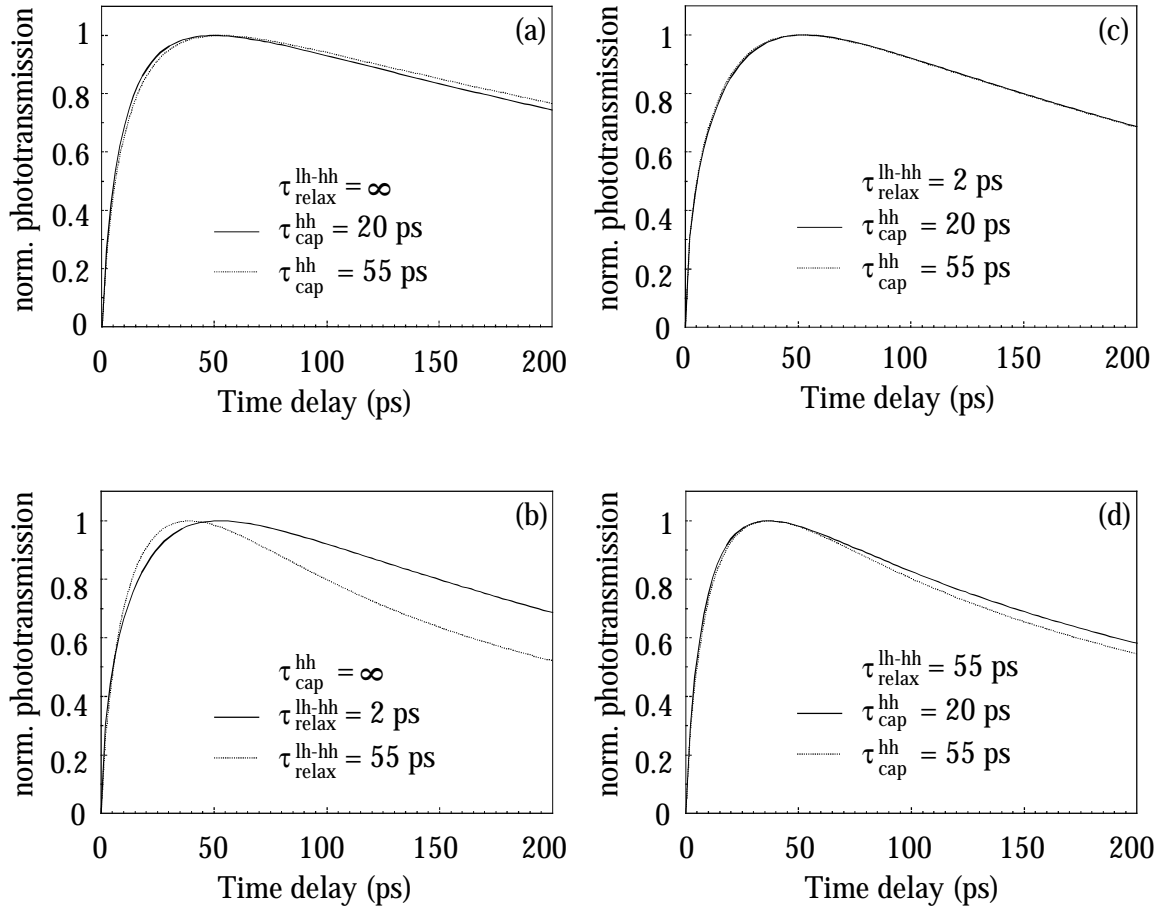


**Fig. 4.11:** Calculated transient phototransmission at the lh exciton transition using the same parameters as in Fig. 4.10. The comparison with Fig. 4.10 shows, that an increase of the relaxation time from 2 ps to 55 ps leading to an increase of the hh phototransmission rise time, correlates with a reduction of the decay time of the phototransmission at the lh exciton transition.

(ii) Direct capture of holes to the confined lh level, but negligible direct capture of holes to the hh level, accompanied with a change in the hole intersubband relaxation time from 2 ps to 55 ps. The calculated PT for this case is given in Fig. 4.10(b) and Fig. 4.11(b). The drastic change in relaxation time is a consequence of the change in relaxation mechanism from GaAs LO phonon emission to an acoustic phonon cascade.

(iii) Direct capture of holes to the confined hh and lh levels, where  $\tau_{\text{cap}}^{\text{hh}}$  increases from 20 ps to more than 50 ps towards the high energy side of the hh exciton transition, combined with a fast carrier relaxation by LO phonon emission with  $\tau_{\text{relax}}^{\text{lh-hh}} \leq 2$  ps [see Fig. 4.10(c) and 4.11(c)].

(iv) Direct capture of holes to the confined hh and lh levels, where  $\tau_{\text{cap}}^{\text{hh}}$  increases from 20 ps to more than 50 ps at the high energy side of the hh exciton transition, combined with a slow carrier relaxation via acoustic phonon emission with  $\tau_{\text{relax}}^{\text{lh-hh}} \geq 50$  ps [see Fig. 4.10(d) and Fig. 4.11(d)]. The comparison between (iii) and (iv) also treats the case that holes are captured by the hh level as fast as by the lh level ( $\tau_{\text{cap}}^{\text{hh}} \approx \tau_{\text{cap}}^{\text{lh}} = 20$  ps), and that the relaxation mechanism changes from LO phonon emission to an acoustic phonon cascade.

The comparison of the calculated PT transients at the hh and lh exciton transitions displayed in Fig. 4.10 and Fig. 4.11 reveals the following conclusions: firstly, the rise time of the lh PT transient is completely insensitive to any changes of the time constant for a direct capture to the confined hh level and the intersubband relaxation time. Therefore, the measured rise time of the PT transient at the lh exciton transition directly yields a capture time to the lh level of 20 ps. This is surprisingly short for such a thin layer, which provides a confinement potential on the length scale of the lattice constant. Secondly, with this value known, there are only two cases left which lead to a significant increase of the PT rise time at the hh exciton transition. In the first case, the PT rise time increases from 20 ps to 35 ps when  $\tau_{\text{cap}}^{\text{hh}}$  increases from 20 ps to 55 ps, combined with an increase of the lh to hh level relaxation time from 2 ps to 55 ps [see Fig. 4.10(c) and (d)]. This, however, leads to equal decay times in the PT transients of the lh exciton [see Fig. 4.11(c) and (d)]. In the second case, direct capture of holes to the hh level is assumed to be absent. From Fig. 4.11(b), it can be seen that the increase in the hh PT rise time is then accompanied by a decrease of the lh transient decay time and a constant hh transient decay time, as both observed in the experiments.

The carrier capture experiments and the rate-equation analysis therefore suggest the following carrier dynamics in the investigated 1.2 ML InAs layer. At the low energy side of the hh exciton transition, the associated hh states are populated within less than 2 ps by a fast relaxation of holes from the lh states via emission of GaAs LO phonons. This finding is in agreement with experimental and theoretical studies of the intersubband relaxation in GaAs/AlGaAs quantum wells, which revealed relaxation times as short as 160 fs to 2 ps when the subband splitting became larger than the threshold energy for LO phonon emission<sup>40, 43</sup>. In accordance with the results in Chapter 3, the fast relaxation

via GaAs phonons rather than InAs phonons is explained by the fact that the GaAs phonon modes are only weakly perturbed by the thin InAs layer and that the wavefunctions of the confined hh and lh states extend entirely into the GaAs matrix.

At the high energy side of the hh exciton transition the relaxation of holes from lh to hh levels is slowed down to more than 50 ps, but the direct capture of holes by the hh states is still not significant. The slower relaxation time is consistent with the energy separation between lh states and these hh states being smaller than the threshold energy for LO phonon emission. In such a case relaxation occurs via a cascade of acoustic phonons<sup>44-46</sup> with relaxation times larger than 40 ps. A change in the relaxation mechanism from LO phonon emission to an acoustic phonon cascade at the threshold energy of 36 meV, which is probed by a small spectral detuning of the probe wavelength towards higher energies within the hh exciton transition, is therefore sufficient to explain the observed steep increase of the hh transient rise time accompanied by the decrease of the lh transient decay time and a constant decay time of the hh transient.

The efficient capture of holes<sup>47</sup> by the confined lh state within 20 ps, and the relative unimportance of a direct capture by the confined hh state, can be understood as follows: in general it is assumed that the capture process takes place between an initial three-dimensional barrier state and a final two-dimensional state by the emission of a LO phonon under energy and momentum conservation. The capture probability is the largest when the overlap integral is maximum. In conventional quantum wells the overlap integral must be separated into a contribution from the overlap between barrier and confined state wavefunction in the well region and a contribution due to transitions in the barrier layer. The smallest capture times are found for those wells, which provide a bound state close to the barrier continuum edge, because then the overlap of the wavefunctions involved in the capture process is larger in the barrier region than that in the well region. In ultrathin InAs layers, the contribution of the well region to the overlap integral vanishes since the confined state wavefunctions extend entirely in the barrier. The capture process therefore occurs solely in the barrier layer and the capture probability simply increases with the barrier penetration length and the density-of-states of the confined InAs layer states. For the 1.2 ML thick InAs layer, the 4.5 meV effective confinement energy of the lh yields a lh barrier penetration length of 120 Å, whereas the barrier penetration length of the hh amounts to only 25 Å. In addition, the lh level

possesses a larger in-plane effective mass than the hh level leading to a more than two times larger density-of-states for the lh. The efficient capture to the lh state results from its large barrier penetration length and its in-plane effective mass being the largest among all three confined states. In turn, the capture probability for the hh state is more than 10 times smaller than that for the lh level. Additionally, since the effective hh confinement energy of 42 meV exceeds the LO phonon energy, transitions from a GaAs barrier state to the hh level can only occur at large final state momentum values, which further reduces the hh capture probability.

## References

- <sup>1</sup> M. Alonso, M. Ilg, and K. Ploog, *Phys. Rev. B* **50**, 1628 (1994)
- <sup>2</sup> M.V. Belousov, N.N. Ledentsov, M.V. Maximov, P.D. Wang, I.N. Yassievitch, N.N. Faleev, I.A. Kozin, V.M. Ustinov, P.S. Kop'ev, and C.M. Sotomayor Torres, *Phys. Rev. B* **51**, 14346 (1995)
- <sup>3</sup> P.D. Wang, N.N. Ledentsov, C.M. Sotomayor Torres, I.N. Yassievitch, A. Pakhomov, A.Yu. Egorov, P.S. Kop'ev, and V.M. Ustinov, *Phys. Rev. B* **50**, 1604 (1994)
- <sup>4</sup> P.D. Wang, N.N. Ledentsov, C.M. Sotomayor Torres, P.S. Kop'ev, and V.M. Ustinov, *Appl. Phys. Lett.* **64**, 1526 (1994)
- <sup>5</sup> R. Cingolani, O. Brandt, L. Tapfer, G. Scarmaccio, G.C. LaRocca, and K. Ploog, *Phys. Rev. B* **42**, 3209 (1990)
- <sup>6</sup> O. Brandt, H. Lage, and K. Ploog, *Phys. Rev. B* **45**, 4217 (1992)
- <sup>7</sup> N.N. Ledentsov, P.D. Wang, C.M. Sotomayor Torres, A.Yu. Egorov, M.V. Maximov, V.M. Ustinov, A.E. Zhukov, and P.S. Kop'ev, *Phys. Rev. B* **50**, 12171 (1994)
- <sup>8</sup> M. Sato, and Y. Horikoshi, *J. Appl. Phys.* **66**, 851 (1989)
- <sup>9</sup> M. Nakayama, T. Fujita, I. Tanaka, H. Nishimura, and H. Terauchi, *Jpn. J. Appl. Phys.* **32**, 160 (1993)
- <sup>10</sup> Y. Murayama, *Phys. Rev. B* **34**, 2500 (1986)
- <sup>11</sup> J. Marzin, *Phys. Rev. Lett.* **56**, 3221 (1986)
- <sup>12</sup> H. Shichijo, R.M. Kolbas, N. Holonyak, J.J. Coleman, and P.D. Dapkus, *Solid State Commun.* **27**, 1029 (1978)
- <sup>13</sup> J.Y. Tang, K. Hess, N. Holonyak, J.J. Coleman, and P.D. Dapkus, *J. Appl. Phys.* **53**, 6043 (1982)
- <sup>14</sup> J.A. Brum and G. Bastard, *Phys. Rev. B* **33**, 1420 (1986)
- <sup>15</sup> O. Heller and G. Bastard, *Phys. Rev. B* **54**, 5629 (1996)
- <sup>16</sup> P.W.M. Blom, C. Smit, J.E.M. Haverkort, and J.H. Wolter, *Phys. Rev. B* **47**, 2072 (1993)
- <sup>17</sup> T.C. Damen, M. Fritze, A. Kastalsky, J.E. Cunningham, R.N. Pathak, H. Wang, and J. Shah, *Appl. Phys. Lett.* **67**, 515 (1995)

- <sup>18</sup> O. Brandt, L. Tapfer, K. Ploog, M. Hohenstein, and F. Phillipp, *Phys. Rev.* **B41**, 12599 (1990)
- <sup>19</sup> G.W. 't Hooft, W.A.J.A. van der Poel, C.W. Molenkamp, and C.T. Foxon, *Phys. Rev.* **B35**, 8281 (1982)
- <sup>20</sup> C. Giannini, L. Tapfer, S. Lagomarsino, J.C. Bouillard, A. Taccoen, B. Capelle, M. Ilg, O. Brandt, and K. Ploog, *Phys. Rev.* **B48**, 11496 (1993)
- <sup>21</sup> H. Mahr, and M.D. Hirsch, *Opt. Commun.* **13**, 96 (1985)
- <sup>22</sup> C.V. Slank, R.C. Fork, R.F. Leheny, and J. Koch, *Phys. Rev. Lett.* **42**, 112 (1979)
- <sup>23</sup> D. Rozen, A.G. Pouka, Y. Budansky, H. Katz, and R.R. Alfano, *Appl. Phys. Lett.* **39**, 935 (1981)
- <sup>24</sup> M. Mosko, A. Moskova, and V. Cambel, *Phys. Rev.* **B51**, 16860 (1995)
- <sup>25</sup> M. Preisl, J. Mork, and H. Haug, *Phys. Rev.* **B44**, 14478 (1994)
- <sup>26</sup> S. Hunsche, H. Hessel, A. Ewertz, H. Kurz, and J.H. Collet, *Phys. Rev.* **B48**, 17818 (1993)
- <sup>27</sup> J. Nunnenkamp, J.H. Collet, J. Klebniczki, J. Kuhl, and K. Ploog, *Phys. Rev.* **B43**, 14047 (1991)
- <sup>28</sup> L. Bányai, and S.W. Koch, *Z. Phys.* **B63** (Condensed Matter), 283 (1986)
- <sup>29</sup> S. Schmitt-Rink, D.S. Chemla, and D.A.B. Miller, *Phys. Rev.* **B32**, 6601 (1985)
- <sup>30</sup> F. Stern and W.E. Howard, *Phys. Rev.* **163**, 816 (1967)
- <sup>31</sup> J. Lee, H.N. Spector, and P. Melman, *J. Appl. Phys.* **58**, 1893 (1985)
- <sup>32</sup> O. Hipolito and V.B. Campos, *Phys. Rev.* **B19**, 3083 (1979)
- <sup>33</sup> J.A. Brum, G. Bastard, and C. Guillemot, *Phys. Rev.* **B30**, 905 (1984)
- <sup>34</sup> R. Zimmermann, *phys. stat. sol. (b)* **146**, 371 (1988)
- <sup>35</sup> M.J. Snelling, P. Perozzo, D.C. Hutchings, I. Galbraith, and A. Miller, *Phys. Rev.* **B49**, 17160 (1994)
- <sup>36</sup> W.M. Knox, C. Hirliman, D.A.B. Miller, J. Slank, D.S. Chemla, and C.V. Shank, *Phys. Rev. Lett.* **56**, 1191 (1986)
- <sup>37</sup> W.M. Knox, R.L. Fork, M.C. Downer, D.A.B. Miller, D.S. Chemla, C.V. Shank, A.C. Gossard, and W. Wiegmann, *Phys. Rev. Lett.* **54**, 1306 (1985)
- <sup>38</sup> M. Pugnet, J. Collet, and Corret, *Solid State Commun.* **38**, 531 (1981)
- <sup>39</sup> S.V. Kozyrev and A. Ya. Shik, *Sov. Phys. Semicnd.* **19**, 1024 (1986)
- <sup>40</sup> S. Hunsche, K. Leo, H. Kurz, and K. Köhler, *Phys. Rev.* **B50**, 5791 (1994)

- 
- <sup>41</sup> J. Brübach, A. Yu. Silov, J.E.M. Haverkort, W. van der Vleuten, and J.H. Wolter, Phys. Rev. **B61**, 16833 (2000)
- <sup>42</sup> J. Brübach, A. Yu. Silov, J.E.M. Haverkort, W. van der Vleuten, and J.H. Wolter, Phys. Rev. **B59**, 6488 (1999)
- <sup>43</sup> M.C. Tatham, J.F. Ryan, and C.T. Foxon, Phys. Rev. Lett. **63**, 1637 (1989)
- <sup>44</sup> J.A. Levenson, G. Dolique, J.L Oudar, and I. Abram, Phys. Rev. **B41**, 3688 (1990)
- <sup>45</sup> R.A. Höpfel, R. Rodrigues, Y. Iimura, T. Yasui, Y. Segawa, Y. Aoyagi, and S.M. Goodnick, Phys. Rev. **B47**, 10943 (1993)
- <sup>46</sup> A. Seilmair, H.-J. Hübner, G. Abstreiter, G. Weimann, and W Schlapp, Phys. Rev. Lett. **59**, 1345 (1987)
- <sup>47</sup> S.J. Chua, S.J. Xu, X.H. Zhang, and X. Zhang, Microelectronic Engineering **43**, 287 (1998)

---

## 5. Summary

In this thesis a comprehensive experimental and theoretical study of the electronic structure, excitonic effects, and the carrier capture in ultrathin InAs layers embedded in a GaAs matrix is presented. Ultrathin InAs layers have recently attracted strong interest from both the application and fundamental point of view. Based on their unique optical properties, such as a strong photoluminescence line below the GaAs bandgap, they represent a novel concept for optoelectronic devices with an operation wavelength widely tuneable around 980 nm but employing the well-established GaAs process technology. Evidently, for an efficient device optimization reliable data about the band alignment are absolutely necessary and a fundamental understanding of the optical properties and the carrier and exciton dynamics is desirable. In turn, the tremendous fundamental interest in monolayer thick InAs layers itself is motivated by the fact that they represent the ideal case of a two-dimensional direct semiconductor system as the intermediate state between the usual quantum well and isolated isoelectronic impurities. Moreover, since the growth of InAs on GaAs is governed by the large lattice mismatch, InAs layers of a thickness below 5 Å are the only possibility to study the band alignment at the highly strained InAs/GaAs heterointerface. However, according to the contradictory results in literature concerning effective masses, confinement energies, and localization of the confined states related to the InAs layer, or the dimensionality and binding energies of the bound excitons, there seemed to be a problem in the understanding of their basic properties. This culminated e.g. in a debate about the existence of a localized lh state and the validity of elasticity theory in ultrathin highly strained layers. Beyond that, experimental data for the capture times and a detailed knowledge about the capture mechanism of photogenerated carriers or the relaxation of excitons, which are important to explain the strong photoluminescence from ultrathin InAs layer, were simply lacking.

For the calculation of the *electronic structure* in pseudomorphically grown ultrathin InAs layers a new model was developed, which is based on the concept of band offsets but which does not have the general limitations of the quantum well model. By describing the confinement potential of the InAs with a  $\delta$ -potential it is naturally



considered that the wavefunctions of the confined states extend entirely in the GaAs barrier. As a consequence the effective masses in the direction of quantization ( $m_e^*(z) = 0.0665 \times m_0$ ,  $m_{hh}^*(z) = 0.3774 \times m_0$ ,  $m_{lh}^*(z) = 0.0905 \times m_0$ ) as well as in the plane of the InAs layer ( $x$ ,  $y$ -direction), which were derived from the two-band Luttinger-Hamiltonian in spherical approximation, are solely determined by the barrier material. Due to the confinement a reversal in the heavy- and light-hole in-plane effective masses is observed ( $m_{hh}^*(x,y) = 0.155 \times m_0$ ,  $m_{lh}^*(x,y) = 0.363 \times m_0$ ).

By using the  $\delta$ -potential approach and employing the controlled coupling between two ultrathin InAs layers of identical thickness separated by a GaAs barrier of different widths a novel spectroscopic technique for the determination of *band offsets* was developed. The band offsets were extracted independently from the photoluminescence excitation measurements of the coupling induced splitting between the symmetric and antisymmetric states, exploiting the large difference between the electron and heavy-hole effective masses in growth direction. The major advantage of this method is that it is explicitly sensitive to the *band offset ratio* and that it eliminates substantial errors due to excitonic effects. The band offsets and the band offset ratio for the highly strained InAs/GaAs heterointerface determined in this work ( $\Delta E_c=535$  meV,  $\Delta E_{hh}=385$  meV,  $\Delta E_{lh}=225$  meV,  $E_g=0.6$  eV,  $\delta E_{hh-lh}=160$  meV,  $Q_c=0.58$ ) agree for the first time with elasticity theory and theoretical predictions from LDA calculations. In turn, the good agreement between the experimental and theoretical values demonstrates that continuum elasticity theory and the concept of band offsets are suitable approaches even for InAs layers of monolayer thickness. Moreover, the magnitude of the light-hole band offset unambiguously provides a localized light-hole state at cryogenic temperatures.

*Excitonic effects* in monolayer thick InAs layers, which dominate their optical properties, were investigated both experimentally and theoretically. Due to the strong confinement potential, the InAs layer binds heavy-hole (hh) and light-hole (lh) excitons. These excitons are GaAs-like because the wavefunctions of the confined states of the InAs layer extend entirely into the GaAs barrier. The exciton binding energies, determined by PLE and temperature dependent PL measurements, were found to be 10 meV for the hh exciton and 5.5 meV for the lh exciton. With the exciton binding energies and the in-plane effective masses known, the dimensionality of the excitons was clarified. The hh excitons were found to be almost two-dimensional. In contrast, the

lh excitons turned out to be almost three-dimensional, reflecting the weak confinement of the lh state. The question arising over whether ultrathin InAs layers at low temperatures provide a bound lh exciton, was unambiguously answered in cw and time-resolved resonant excitation experiments. Under selective excitation of the lh exciton transition a sharp emission line was discovered, which emerges close to the hh exciton photoluminescence line exactly one GaAs LO phonon below the excitation energy. By studying the transient behaviour of the sharp line it was found that its origin continuously transforms from resonant luminescence for excitation on resonance into doubly resonant Raman scattering for off resonant excitation. Relaxation of hot excitons as a third possible mechanism to account for the sharp line, could be ruled out by additional measurements of the hh exciton lifetime. Since in the regime of doubly resonant Raman scattering the observation of the sharp line requires the existence of both a bound hh and lh exciton state, the dramatic decrease of the intensity of the sharp line due to a temperature rise from 4 K to 18 K directly proves the existence of a well bound lh exciton. For the special case of excitation on resonance, a polarization analysis of the sharp line revealed a negligible exciton-phonon interaction by deformation potential coupling. Based on this fact, our measurements of the lh exciton lifetime yield a lh exciton dephasing time of 40 ps. This relatively long dephasing time provides strong evidence that short-range potential fluctuations due to local strain fields, or the growth of InAs islands with a lateral extension smaller than the  $120\text{\AA}$  lh exciton Bohr-radius, is absent. This is in excellent agreement with the results of the structural characterization by X-ray diffraction, which shows that the InAs layers are coherently strained and that more than 80 % of the deposited InAs is confined in one atomic plane.

In order to explain the giant photoluminescence from ultrathin InAs layers a detailed experimental study of the *carrier capture* was performed. To our knowledge, these are the first experimental data for capture times ever reported for quantum well structures thinner than  $25\text{\AA}$ . The capture times were determined by picosecond time-resolved two-wavelength pump-probe phototransmission. Since this method utilizes two synchronously pumped pulse lasers operating at different wavelengths, it allows a direct spectral control over the initial and final states of the capture and relaxation process. Due to the high sensitivity of this time-resolved modulation technique the low excitation regime becomes accessible. This range is of particular interest, because in the absence of

carrier-carrier scattering the capture process is exclusively governed by interaction with optical and acoustical phonons. Around the lh exciton transition the capture time was found to be 20 ps, which is fast for such a thin layer whose confinement potential is localized within one lattice constant. However, according to the quantum mechanical interpretation of the carrier capture, which firstly was applied to the trapping of electrons by Brum, Bastard and Blom, this efficient capture is explained by the large barrier penetration depth of the confined lh state, and subsequently by its large overlap with resonant barrier states, in excellent agreement with the results for the band alignment. In contrast to that, the capture time significantly increases from 22 ps to 55 ps towards higher photon energies within the hh exciton transition. Since in monolayer thick InAs layers the energy separation between hh and lh states amounts to one GaAs LO phonon, this feature demonstrates that a direct capture of the holes by the hh state is suppressed, but that the capture occurs in a two-step process with the lh level as intermediate capture state. After the capture by the lh state, the holes almost instantaneously cool down to the hh state under LO phonon emission when the energy separation between an occupied lh state and an unoccupied hh state is larger than the phonon threshold. However, when the energy separation is smaller than 36 meV, the cooling from the lh states occurs via acoustic phonons and the capture time increases. The efficient capture by the lh state in combination with the two-step capture mechanism satisfactory explains the strong photoluminescence from ultrathin InAs layers. Moreover, the capture time of 20 ps is in excellent agreement with the observed photoluminescence intensity ratio between the GaAs exciton and the hh exciton related to the InAs layer. Finally, in order to investigate whether time-resolved phototransmission indeed represents the evolution of the population in the InAs layer, a model for the excitonic absorption of a two-dimensional system in the presence of photogenerated carriers was developed. By considering both phase-space-filling and exciton screening, it has been shown for the first time that the rise and fall times in transient phototransmission only represent the capture and recombination times for excitation densities below  $3 \times 10^8 \text{ cm}^{-2}$ .

---

## *Samenvatting*

In dit proefschrift wordt een uitgebreide experimentele en theoretische studie van de elektronische structuur, excitonische effecten en de invang van ladingsdragers in ultradunne InAs lagen, die in een GaAs matrix ingesloten zijn, gepresenteerd. Ultradunne InAs lagen hebben recentelijk grote belangstelling aangetrokken, zowel vanuit toepassings- als ook fundamenteel oogpunt. Gebaseerd op hun unieke optische eigenschappen, zoals bijvoorbeeld een zeer sterke fotoluminescentielijn onder de GaAs bandgap, representeren zij een nieuw concept voor optoelektronische devices met een instelbare golflengte in een breed bereik rond 980 nm, maar gebruikmakend van de gangbare GaAs proces technologie. Voor de optimalisatie van deze devices zijn betrouwbare data met betrekking tot het band alignment vanzelfsprekend absoluut noodzakelijk, en het fundamenteel begrip van de optische eigenschappen en van de dynamica van de ladingsdragers en excitonen is wenselijk. De grote belangstelling vanuit fundamenteel gezichtspunt voor InAs lagen met een monolaag dikte is gemotiveerd door het feit, dat zij het ideale geval van een twee-dimensionaal, direct halfgeleidersysteem vertonen als tussentoestand tussen gebruikelijke quantumputten en geïsoleerde isoelektronische verontreinigingen. Bovendien, omdat de groei van InAs op GaAs door het grote verschil in de roosterconstante bepaald wordt, zijn InAs lagen met een dikte van minder dan 5 Å de enige mogelijkheid om het band alignment aan het “hooggespannen” InAs/GaAs hetero-interface te bestuderen. Niettemin, volgens de tegenstrijdige resultaten in de literatuur betreffende effectieve massa's, opsluitingenergieën en lokalisatie van de gebonden toestanden, die door de InAs laag geïntroduceerd worden, of met betrekking tot de dimensionaliteit en bindingsenergieën van de excitonen, leek er een probleem te bestaan in het begrip van hun fundamentele eigenschappen. Dit werd onder andere zichtbaar in het debat over het bestaan van een gelokaliseerde ‘light-hole’ toestand en over de principiële toepasbaarheid van de elasticiteitstheorie in ultradunne, “hooggespannen” lagen. Verder waren tot nu toe experimentele gegevens over de ladingsdragerinvangtijd en kennis over het invangmechanisme van fotogegeneerde ladingsdragers of over de relaxatie van

excitonen, die belangrijk zijn voor de verklaring van de sterke fotoluminescentie uit ultradunne InAs lagen, gewoon niet aanwezig.

Voor de berekening van de *elektronische structuur* in pseudomorphisch gegroeide ultradunne InAs lagen wordt in dit proefschrift een nieuw model ontwikkeld, dat gebaseerd is op het concept van band offsets, maar dat niet de algemene beperkingen van het quantumput model heeft. Door de beschrijving van het opsluitingspotentiaal van de InAs laag met een  $\delta$ -potentiaal wordt er intrinsiek rekening mee gehouden dat de golffuncties van de gebonden toestanden zich uitsluitend in de GaAs barrière uitstrekken. Als gevolg hiervan, worden de effectieve massa's, zowel in de richting van kwantisatie ( $m_e^*(z) = 0.0665 \times m_0$ ,  $m_{hh}^*(z) = 0.3774 \times m_0$ ,  $m_{lh}^*(z) = 0.0905 \times m_0$ ) alsook in het vlak van de InAs laag (x, y-richting), die rechtstreeks van de twee-bands Luttinger Hamiltoniaan in sferische benadering afgeleid kunnen worden, alleen door het barrière materiaal bepaald. Als gevolg van de opsluiting van de toestanden, neemt men een omkering van de 'heavy'- en 'light-hole' effectieve massa in het InAs vlak waar ( $m_{hh}^*(x, y) = 0.155 \times m_0$ ,  $m_{lh}^*(x, y) = 0.363 \times m_0$ ).

Door toepassing van de  $\delta$ -potentiaal benadering en gecontroleerd koppelen van twee identieke ultradunne InAs lagen met een GaAs barrière van variabele dikte ertussen, werd een nieuwe spectroscopische techniek voor de bepaling van *band offsets* ontwikkeld. Door gebruik te maken van het grote verschil in de effectieve massa van elektron en 'heavy hole' in groei richting, kunnen de band offsets onafhankelijk van elkaar bepaald worden uit de splitsing van symmetrische en antisymmetrische toestanden, die door de koppeling tot stand komt en die door middel van fotoluminescentie excitatie metingen bepaald kan worden. Het grote voordeel van deze methode is dat de *band offset ratio* direkt bepaald kan worden en dat systematische fouten door excitonische effecten inherent worden voorkomen. De band offsets en de band offset ratio voor het InAs/GaAs heterointerface die in dit proefschrift bepaald zijn ( $\Delta E_c=535$  meV,  $\Delta E_{hh}=385$  meV,  $\Delta E_{lh}=225$  meV,  $E_g=0.6$  eV,  $\delta E_{hh-lh}=160$  meV,  $Q_c=0.58$ ), komen voor het eerst overeen met de elasticiteitstheorie en theoretische voorspellingen van LDA berekeningen. Omgekeerd toont de goede overeenstemming tussen gemeten en theoretische waarden aan, dat de continuüm elasticiteitstheorie en het concept van band offsets ook in het geval van slechts monolaag dikke InAs lagen nog

---

steeds bruikbare benaderingen zijn. Bovendien zorgt de grootte van het 'light-hole' band offset er voor, dat er bij lage temperaturen een gebonden 'light-hole' toestand bestaat.

Excitonische effecten, die de optische eigenschappen van ultradunne InAs lagen domineren, worden in dit proefschrift zowel experimenteel en alsook theoretisch onderzocht. Door de sterke opsluitingspotentialen bindt de InAs laag 'heavy-hole' (hh) en 'light-hole' (lh) excitonen. Deze excitonen hebben een GaAs-achtige karakter, omdat de golf functies van de gebonden toestanden van de InAs laag zich uitsluitend in de GaAs barrière uitstrekken. De excitonbindingsenergieën werden met behulp van PLE en temperatuurafhankelijke fotoluminescentie metingen bepaald. Voor de hh excitonen bedraagt de bindingsenergie 10 meV, en voor de lh excitonen 5.5 meV. Met deze waarden en de bekende in-plane effectieve massa's, kon de dimensionaliteit van de excitonen opgehelderd worden. De hh excitonen zijn vrijwel tweedimensionaal, in tegenstelling tot de lh excitonen, die vrijwel driedimensionaal zijn, hetgeen de relatief zwakke opsluiting van de lh toestand weergeeft. De vraag die zich stelt, of ultradunne InAs lagen bij lage temperaturen een gebonden lh exciton vertonen, kon zonder enige twijfel door cw en tijdsopgeloste, resonante excitatie experimenten beantwoord worden. Bij selectieve excitatie van de lh exciton overgang, werd in de buurt van de gewone hh luminescentie lijn een spectraal zeer scherpe emissie lijn waargenomen, die precies één GaAs LO phonon onder de excitatie energie verschijnt. Het bestuderen van het transiënte gedrag van deze scherpe lijn leverde het resultaat op, dat het veroorzakende mechanisme geleidelijk verandert van resonante luminescentie bij excitatie on resonance tot dubbel resonante Raman verstrooiing voor excitatie off resonance. Relaxatie van hete excitonen, wat ook als oorzaak van de scherpe lijn in aanmerking zou kunnen komen, kon door meting van de levensduur van lh excitonen worden uitgesloten. Omdat het optreden van de scherpe lijn in het regime van dubbel resonante Raman verstrooiing het bestaan van zowel een gebonden hh toestand alsook van een gebonden lh toestand vereist, toont het dramatisch afnemen van de intensiteit van de scherpe lijn bij een temperatuurverhoging van 4 K naar 18 K duidelijk de aanwezigheid van een gebonden lh exciton aan. Voor het speciale geval van excitatie on resonance, laat een polarisatie analyse van de scherpe lijn blijken, dat exciton-phonon interactie via deformatie potentialen koppeling verwaarloosbaar is. Met dit feit bekend, kan van de gemeten lh exciton levensduur een lh exciton dephasingstijd van 40 ps worden

afgeleid. Deze relatief lange dephaseringstijd suggereert, dat fluktuaties van de potentiaal op een schaal kleiner dan de lh exciton Bohr straal, dus kleiner dan zo'n 120 Å, die veroorzaakt worden door lokale strain velden of de groei van InAs eilanden, niet aanwezig zijn. Dit is in goede overeenstemming met de resultaten van de karakterisatie van de monsters met behulp van hoge resolutie Röntgen diffractie, die aangeven, dat de InAs lagen coherent gespannen zijn, en dat meer dan 80 % van het gedeponeerde InAs in een atomaire laag opgesloten is.

Om de gigantische fotoluminescentie uit ultradunne InAs lagen te kunnen verklaren, wordt in dit proefschrift een gedetailleerd experimenteel onderzoek aan de *ladingsdragerinvang* verricht. Naar ons weten, zijn dit de eerste meetdata voor invangtijden in quantumput structuren met een dikte onder de 25 Å. De invangtijden werden gemeten met behulp van tijdsopgeloste twee-golflengte pump-probe fototransmissie met picoseconde resolutie. Omdat deze methode gebruikmaakt van twee synchroon gepompte pulse lasers, die verschillende golflengten emitteren, heeft men directe spectrale controle over zowel de begin toestand alsook de eind toestand van het invang of relaxatie proces. Verder wordt door de hoge gevoeligheid van deze tijdsopgeloste modulatietechniek het regime van lage excitatiedichtheden toegankelijk. Dit bereik is van bijzondere interesse, omdat, in de afwezigheid van carrier-carrier verstrooiing, het invangproces uitsluitend door akoestische en optische fononen bepaald wordt. In het bereik van de lh exciton overgang vindt men een konstante invangtijd van 20 ps. Dit is zeer kort voor een dunne laag, waarvan de opsluitingspotentiaal zich slechts over een roosterkonstante uitstrekt. Niettemin, kan volgens de quantum mechanische interpretatie van de ladingsdragerinvang, die voor het eerst door Brum, Bastard en Blom voor elektronen werd toegepast, deze efficiënte invang door de grote barrière penetratiediepte van de lh toestand en vervolgens de grote overlap met resonante barrière toestanden verklaard worden. Dit is in goede overeenstemming met de resultaten voor het band alignment in ultradunne InAs lagen. In het bereik van de hh exciton overgang loopt de invangtijd van 22 ps aan de laagenergetische zijde op naar 55 ps aan de hoogenergetische zijde. Omdat in InAs lagen met een monolaag dikte de afstand tussen de hh en de lh toestand overeenkomt met de energie van een GaAs phonon, toont dit feit aan, dat een directe invang van gaten naar de hh toestand nauwelijks aanwezig is, maar dat de invang in een twee-staps

---

proces gebeurt met de lh toestand als tussenliggende invangtoestand. Na invang door de lh toestand, relaxeren de gaten bijna instantaan naar de hh toestand onder emissie van een GaAs LO phonon als de energetische afstand tussen een bezette lh en een onbezette hh toestand groter is dan de LO phonon drempel. In tegenstelling, als de lh-hh afstand kleiner is dan 36 meV, dan gebeurt de relaxatie van de lh naar de hh toestand slechts door akoestische phononen, en de invangtijd word groter. De efficiënte invang door de lh toestand in combinatie met het twee-staps invang mechanisme verklaart de sterke fotoluminescentie uit ultradunne InAs lagen op een bevredigende manier. Verder is de gemeten 20 ps invangtijd in goede overeenstemming met de waargenomen verhouding van de intensiteit van de fotoluminescentie van het GaAs exciton en het aan de InAs laag gerelateerde hh exciton. Om afsluitend te onderzoeken, of de transiënte fototransmissie daadwerkelijk ook de populatie in de gebonden toestanden van de InAs laag weergeeft, werd er een model voor de excitonische absorptie van een tweedimensionaal systeem in aanwezigheid van fotogegenereerde ladingsdragers ontwikkeld. Door het in aanmerking nemen van zowel phase-space-filling als ook exciton screening kon voor het eerst worden aangetoond, dat de stijg- en vervaltijden, die in de transiënte fototransmissie worden waargenomen, alleen dan de invang- en recombinatietijden weergeven, als de excitatiedichtheid kleiner is dan  $3 \times 10^8 \text{ cm}^{-2}$ .





---

## *Acknowledgements*

Heartfelt thanks go first to my promotor, Prof. Dr. Joachim Wolter, who expertly guided me through graduate school and who was patient enough to give me time and space to find my own research topic. Resisting the temptation to create quick publications by telling his students what to do, he instead advised us in methods to bundle our creativity and ideas. With his boundless energy he created a remarkable network of contacts as well as a superbly equipped Lab, and with growth and characterization facilities, a transport group, theoretical support and an optical Lab under one roof, it is the kind of place where one might want to spend four good years.

Many thanks go also to Prof. Dr. G. Döhler, my associate advisor. The critical questions and fruitful discussions with him and his enthusiastic group members certainly contributed to find a consistent understanding of ultrathin InAs layers.

I am very thankful that my PhD time coincided with the stay of Dr. Gideon Yoffe and Dr. Andrei Yu. Silov. By patiently and cheerfully sharing their broad knowledge on optical devices, semiconductor physics, processing and calculation tricks they largely contributed to my education during my PhD as well as to the success of this work. Beyond that, when after 6 pm it got a little quieter, it has always been a pleasure to discuss anything from valence band subband mixing, the latest gossips on University politics to Mongolian literature.

The experimental work would have been unthinkable without the commitment and enthusiasm of Willem van der Vleuten, the MBE ‘guru’ during my PhD time. He was always open to discuss less standard growth menus and recipes, optimize MBE process parameters for the ‘odd’ InAs samples and, thanks to his endurance when others might have given up, we finally succeeded in the ‘illegal’ project of realizing self-assembled quantum dot samples, which gave at least one further generation of PhD students loads of ‘nutrition’.

Special thanks also to Jos van Reuven and Frans van Setten without whose technical support and expertise concerning cryogenics, electronics and computerization the realization of the time-resolved two-wavelength pump-probe set-up would have been considerably more time-consuming. Much appreciation also to Tom Eijkemans and Cees van Es for introducing me to the PL and HRXRD characterization set-up and

allowing me to work with it independently, and to Peter Nouwens for making the superb contacts on the nipi modulator samples and the InAs LED structures.

Thanks go also to Dr. John Hopkins and Dr. Thomas Marschner for the fruitful discussions on MBE growth and their encouragement to understand the subtleties in the interpretation of the X-ray diffraction results.

Finally I like to thank Prof. Dr. Acket and Prof. J.I. Dijkhuis for critical revision of the manuscript of my thesis as well as all group members and my graduate students, Marcel Heemskerk, Ingrid Janssen and Arthur Minnaert, for making my stay at TUE so enjoyable.

---

***List of publications***

J. Brübach, A.Yu. Silov, J.E.M. Haverkort, W. van der Vleuten, and J.H. Wolter, “Carrier capture in ultrathin InAs/GaAs quantum wells”, *Phys. Rev.* **B61**, 16833 (2000)

J. Brübach, A.Yu. Silov, J.E.M. Haverkort, W. van der Vleuten, and J.H. Wolter, “Coupling of ultrathin InAs layers as a tool for band offset determination”, *Phys. Rev.* **B59**, 6488 (1999)

J. Brübach, A.Yu. Silov, J.E.M. Haverkort, W. van der Vleuten, and J.H. Wolter, “Coupled ultrathin InAs layers in GaAs as a tool for the determination of band offsets”, *Superlattices and Microstructures* **21**, 527 (1996)

J. Brübach, J.E.M. Haverkort, and J.H. Wolter, P.D. Wang, N.N. Ledentsov, and C.M. Sotomayor Torres, A.E. Zhukov, P.S. Kop’ev, and V.M. Ustinov, “Dynamics of double resonant Raman scattering and resonant luminescence in ultrathin InAs/GaAs quantum wells”, *J. Opt. Soc. Am.* **B73**, 1224 (1996)

J. Brübach, J.E.M. Haverkort, and J.H. Wolter, P.D. Wang, N.N. Ledentsov, and C.M. Sotomayor Torres, “Exciton dynamics in ultrathin InAs/GaAs quantum wells”, *Mat. Res. Soc. Symp. Proc.* **406**, 283 (1996)

J. Brübach, A.Yu. Silov, J.E.M. Haverkort, W. van der Vleuten, and J.H. Wolter, “Two-step carrier capture and exciton screening in ultrathin InAs layers embedded in a GaAs matrix”, *Proc. Int. Conf. Phys. Semicond.* **XXIII**, 1963 (1996)

T. Marschner, J. Brübach, C.A. Verschuren, M.R. Leys, and J.H. Wolter, “X-ray interference effect as a tool for the structural investigation of GaInAs/InP multiple quantum wells”, *J. Appl. Phys.* **83**, 3630 (1998)

G.W. Yoffe, J. Brübach, F. Karouta, W. van der Vleuten, L.M.F. Kaufmann, and J.H. Wolter, “Low voltage hetero nipi waveguide modulators with GaAs/AlAs quantum wells”, *Appl. Phys. Lett.* **63**, 1456 (1993)

G.W. Yoffe, J. Brübach, F. Karouta, and J.H. Wolter, “Single wavelength all-optical phase modulation in a GaAs/AlAs hetero-nipi waveguide: towards an optical transistor”, *Appl. Phys. Lett.* **63**, 2318 (1993)

G.W. Yoffe, J. Brübach, F. Karouta, and J.H. Wolter, “A single wavelength all-optical GaAs/AlAs phase modulator: towards an optical transistor”, *Inst. Phys. Conf. Ser.* **136**, 823 (1994)

J. Hopkins, M.R. Leys, J. Brübach, W. van der Vleuten, and J.H. Wolter, “A RHEED study of the dynamics of GaAs and AlGaAs growth on a (001) surface by MBE”, *Appl. Surf. Sci.* **84**, 299 (1995)

X. Leijtens, G.W. Yoffe, J.E.M. Haverkort, F. Karouta, J. Brübach, T. Eijkemans, L.M.F. Kaufmann, M.K. Smits, A.A. Stegemann, Y.C. Zhu, and J.H. Wolter, “2×2 Mach-Zehnder interferometric switch based on hetero-nipi quantum wells”, *Appl. Phys. Lett.* **66**, 2736 (1995)

J. Brübach, J.E.M. Haverkort, and J.H. Wolter, “Dynamics of doubly resonant Raman scattering and resonant hot luminescence in ultrathin InAs/GaAs quantum wells grown by MBE”, *Proc. Ger. Phys. Soc.* **VI**, 1404 (1996)

J. Brübach, J.E.M. Haverkort, and J.H. Wolter, “Carrier capture in ultrathin InAs/GaAs quantum wells”, *Proc. Ger. Phys. Soc.* **VI**, 1405 (1996)

J. Brübach, A.Yu. Silov, J.E.M. Haverkort, and J.H. Wolter, “Structural and optical properties of coupled ultrathin InAs/GaAs quantum wells”, *Proc. Ger. Phys. Soc.* **VI**, 1581 (1996)

## *Curriculum Vitae*

*Jörg Brübach, born March 15<sup>th</sup>, 1965 in Hannover, Germany*

In 1984 I completed high school at the Matthias-Claudius Gymnasium, Gehrden with great honor. After my military service I started in 1985 studying Physics at the University of Technology in Braunschweig. During my study I focussed in particular on semiconductor physics and communication technology as well as on superconductivity. I finished my master thesis in 1992 under supervision of Prof. F.R. Kessler at the Institute for Semiconductor Physics and Optics. The master thesis deals with the optical and magneto-optical properties of amorphous, polycrystalline and crystalline Ge and Si. Most of the experimental work was carried out at the high magnetic field facility. In 1992 my diploma was awarded with 'summa cum laude'.

Between 1992 and 1996 I carried out my PhD work at the COBRA Inter-University Research Institute of the Eindhoven University of Technology in the group of Prof. Dr. J.H. Wolter. Starting with spectroscopic and time-resolved investigations of the optical non-linearities of GaAs/AlAs hetero-nipi structures and their application in optical modulators, after 1½ years I developed a strong interest for highly strained ultrathin InAs/GaAs quantum wells. Besides the MBE growth and the structural characterization I focussed in particular on the electronic structure, excitonic effects and carrier dynamics of these structures.

In 1996 I started as senior designer at ASML being responsible for DUV lasers and optical materials research. Since 1999 I am project manager for 193 nm and 157 nm dose control of advanced imaging systems.

# *Stellingen*

bijhorende bij het proefschrift van

Jörg Brübach

*Ultrathin InAs/GaAs Quantum Wells:  
Electronic Structure, Excitonic Effects  
and Carrier Capture*

1. The quantum well model is not suitable to describe the electronic structure of ultrathin InAs layers embedded in a GaAs matrix.

This thesis.

2. As opposed to the interpretation of Dosanjh and Wang, the effective mass reversal observed in ultrathin InAs layers results from the strong quantization and not from the hh-lh subband mixing due to compressive strain.

S.S. Dosanjh et al., Appl. Phys. Lett. **64**, 2142 (1994)

P.D. Wang et al., Phys. Rev. **B50**, 1604 (1994)

3. So far, the lh confinement in ultrathin InAs layers had been underestimated by one order of magnitude.

O. Brandt et al., Phys. Rev. **B45**, 4217 (1992)

This thesis.

4. Controlled coupling between two quantum wells by means of varying barrier width allows to experimentally determine band offsets and the band offset ratio in any semiconductor heterostructure provided that the difference in electron and hole mass is sufficiently large.

This thesis.

5. In quantum wells bleaching due to exciton screening may be as large or even larger than phase-space-filling.

S. Schmitt-Rink et al., Phys. Rev. B **32**, 6601 (1985)

M.J. Snelling et al., Phys. Rev. **B49**, 17160 (1994)

6. Resonant luminescence and Raman scattering become indistinguishable when lifetimes and dephasing times are equal.

R.P. Stanley et al., Phys Rev. Lett. **67**, 128 (1991)



7. The usually made assumption, that shear strain is equally accommodated in the hh and lh subbands, is only valid for strain of less than 1% regardless whether it is compressive or tensile.
8. As opposed to conventional quantum wells, the linewidth of the optical transitions in ultrathin InAs layers cannot be explained by monolayer well-width fluctuations but originates from a different exciton localization strength of the lateral potential.
9. Despite the entertaining value, the use of 'watermodels' for the explanation of physical phenomena becomes questionable when they either distract from the core of the phenomenon or when they lead to discussions in how far the used model represents indeed the phenomenon.
10. Tolerance should be clearly distinguished from carelessness. As a measure for distinction the amount of energy put into the continuation of a controversial dialogue may serve.